Thomas Førde

Theoretical and Experimental Studies of Metal Hydride Storage Units

Thesis for the degree of philosophiae doctor

Trondheim, December 2007

Norwegian University of
Science and Technology
Faculty of Engineering Science and Technology
Department of Energy and Process Engineering

NTNU
Norwegian University of
Science and Technology

NTNU
Norwegian University of Science and Technology

Thesis for the degree of philosophiae doctor

Department of Energy and Process Engineering

ISBN 978-82-471-5630-8 (printed ver.)
ISBN 978-82-471-5644-5 (electronic ver.)
ISSN 1503-8181

Theses at NTNU, 2007:252

Printed by Tapir Uttrykk

Preface

The work presented in this thesis has been carried out at department of Energy Systems (ENSYS) at Institute for Energy Technology (IFE), Kjeller. Part of the work was performed at NTNU – Norwegian University of Science and Technology in Trondheim. The scope of this Ph.D. study is to design, build and thermally integrate a metal hydride storage unit with a water cooled Proton Exchange Membrane (PEM) fuel cell.

This work would never have been accomplished without the contribution from a number of people. I would like to thank my supervisor, Professor Otto K. Sønju for his support and encouragement throughout this work. I would also like to thank Professor Volodymyr. A. Yartys, a supervisor of my work, for his precise and constructive criticism throughout this work. I would like to thank Professor Erling Næss for careful revision of part two of this thesis. Furthermore Dr Øystein Ulleberg and Dr Ronny Glöckner must be thanked for their help within the system part of this thesis. Dr Michael Lototsky also deserves a great thank for finding time to help me through the material characterisation. A very special thanks goes to Dr Jan Petter Mæhlen and Dr Jon Eriksen for their invaluable help with the experimental work and their interest in proof reading this thesis. I would also like to thank Per Finden for helping me finding a professor in the beginning of this study.

Financial support from the Norwegian Research Council, Norsk Hydro and Statkraft is gratefully acknowledged. However, there was little money on my project for double housing. I am therefore greatly indebted to Helge Huser, who let me stay almost for free during my visits to Trondheim. While Helge provided me with a place to sleep in Trondheim, Daniel Stanghelle shared his office with me and Monica made us delicious dinners.

Finally I would like to thank my parents for their many encouragements and my dear Elin for her active assistance in the work and for her attractive distraction from the work. With my little daughter Linnea's arrival, I am glad it was soon completed.

Abstract

The main objective of this work was in experimental studies and modelling of the metal hydride (MH) storage materials and their performances in different types of the MH storage units. The obtained results were further used as a background for the optimisation of the design of the MH storage unit developed within this project, which was thermally connected to a water-cooled proton exchange membrane fuel cell (PEM FC).

The content of the work is divided into three parts:

1. MATERIAL PROPERTIES. Characterisation of the kinetics of hydrogen exchange, thermodynamic (Pressure-Concentration-Temperature isotherms) and micro-structural analyses of the selected for applications alloys.
2. METAL HYDRIDE STORAGE SYSTEMS. The behaviour of the different storage units was studied through experimental work and numerical simulations for the chosen alloys loaded into the units.
3. SYSTEM INTEGRATION. Interactions between the MH storage unit and a fuel cell / electrolyser were studied, through the experimental work and system simulations.

The main results obtained in the work and presented in the thesis are summarised below.

Because of high cycle stability, ability to endure gas impurities and fast kinetics of hydrogen exchange, the AB_5-type $La_{0.83}Ce_{0.10}Pr_{0.04}Nd_{0.03}Ni_{4.40}Al_{0.60}$ alloy was selected as an H storage material. Kinetic studies showed that nucleation and growth or diffusion mechanisms are the rate limiting steps in the interaction of the intermetallic alloy with hydrogen. Enthalpy of formation of the corresponding hydride $La_{0.83}Ce_{0.10}Pr_{0.04}Nd_{0.03}Ni_{4.40}Al_{0.60}H_{5.4}$ was determined as $\Delta H_{absorption}$=-27 kJ/mol H_2 in the PCT thermodynamic studies. A semi-empirical expression describing the reaction rate of the gas-solid reaction for both absorption and desorption was proposed and experimentally verified. The proposed expression was suitable for use in heat and mass transfer modelling and yielded the values of activation energies and Avrami pre-exponential factors in good agreement with the available reference data.

Zero-dimensional, one-dimensional and two-dimensional models describing the heat and mass transfer processes in the metal hydride storage units were developed and experimentally verified. Three different MH-storage units filled with the same alloy were tested; the reactors differed in their heat management. The simplest reactor was a cylindrical reactor made of

stainless steel with no internal heat exchanger, and with heat transferred through the external walls. The second reactor was made from aluminium and had a replaceable heat exchanger. Two types of heat exchangers were tested; a brush type and a tube type. The third reactor was also made of aluminium and had an internal heat exchanger consisting of a tube with radial fins.

The numerical models were used to identify the parameters controlling the dynamic charge-discharge behaviour of the metal hydride storage units. It was found that both the activation energy and effective thermal conductivity are the most important parameters. Analysis of the experimental data collected during charge and discharge experiments showed that, in addition to the pressure of the hydrogen during loading or release of hydrogen, the overall heat transfer number and heat transfer surface had the most significant effect on the charge and discharge time.

Studies of interaction between three main components of a hydrogen energy system, including an electrolyser, a PEM FC and a MH storage unit, were performed. The zero-dimensional model of the MH store was implemented during a system simulation. The simulations were aimed at considering the case of large fluctuations in energy price, when energy can be bought for a low cost, stored as hydrogen for the required time and sold with a higher price as electricity produced by a FC. The results from the performed simulations and experiments were utilised to design a MH storage unit able to serve a 1.2 kW PEM FC with hydrogen for approximately two hours. Data acquisition and control programs were developed to efficiently operate these two components.

TABLE OF CONTENTS

1 INTRODUCTION 11

1.1 Hydrogen as an energy carrier 12

1.2 Hydrogen storage 14
1.2.1 Compressed hydrogen 15
1.2.2 Liquid hydrogen 15
1.2.3 Hydrogen stored in hydrogen rich liquids 15
1.2.4 H_2 storage in solids 15

1.3 Thesis background and objectives 16

1.4 Outline of thesis and structure of work 17

Part 1: Equilibrium and Kinetic Behaviour of Metal Hydride Powder 21

2 METAL HYDRIDES: BACKGROUND AND THEORY 22

2.1 Introduction 23

2.2 Thermodynamics of metal hydrogen interactions 25

2.3 Kinetics of metal hydrides 27

2.4 Experimental methods 28

2.5 Preliminary experiments 30

3 INFLUENCE OF INTRINSIC HYDROGENATION/DEHYDROGENATION KINETICS ON THE DYNAMIC BEHAVIOUR OF METAL HYDRIDES: A SEMI EMPIRICAL MODEL AND ITS VERIFICATION 34

3.1 Abstract 34

3.2 Introduction 34

3.3 Theoretical and experimental description 35
3.3.1 Theoretical background 35

3.4 Experimental details 38
3.4.1 Treatment of the experimental data 39
3.4.2 Derivation of kinetic expression 40

3.5 Results and discussion 42
3.5.1 Analysis of experimental data 43
3.5.2 Modelling 45

3.6 Discussion 46

3.7 Conclusions 46

Part 2: Modelling and Experimental Work with Storage Units 49

4 METAL HYDRIDE STORAGE UNITS: BACKGROUND, THEORY AND EXPERIMENTAL SET UP 50

4.1 Introduction 52

4.2 Theoretical background 54
4.2.1 Momentum equation 54
4.2.2 Energy conservation 56

4.3 Heat transfer parameters 59
4.3.1 Heat transfer, thermal conductivity, particle and size distribution 59
4.3.2 Particle surface area, and solid/gas heat transfer coefficient 65
4.3.3 Permeability coefficient and porosity 65
4.3.4 Heat transfer coefficients 67
4.3.5 Heat capacity and swelling 71

4.4 Experimental set up 73

4.5 Test geometries 73
4.5.1 Unit#A 74
4.5.2 Unit#B 75
4.5.3 Unit#C and Unit#D 76

4.6 Preliminary results 77

5 HEAT TRANSFER CHARACTERISATION OF A METAL HYDRIDE STORAGE CONTAINER DURING HYDROGEN CHARGE AND DISCHARGE 82

5.1 Abstract 82

5.2 Introduction 85

5.3 Mathematical model 85

5.4 Modelling parameters 86

5.5 Initial and boundary conditions 89

5.6 Experimental set up 90

5.7 Experimental and modelling results 91
5.7.1 Experimental results 91
5.7.2 Numerical results and their discussion 95

5.8 Conclusions 99

6 CHARGING AND DISCHARGING TIMES OF HYDROGEN FOR A METAL HYDRIDE STORAGE TANK 102

6.1 Abstract 102

6.2 Introduction 105

6.3 Experimental set up 106
6.3.1 The test reactor 106

6.4 Results and discussion 109
6.4.1 Hydrogen charging discharging experiments 109

6.5 Numerical predictions 113
6.5.1 Brush type heat exchanger mathematical model 113
6.5.2 Boundary conditions 116
6.5.3 Results 116
6.5.4 Tube type heat exchanger mathematical model 119
6.5.5 Modelling parameters 120
6.5.6 Boundary conditions 122
6.5.7 Results 123

6.6 Conclusions 128

7 EXPERIMENTAL STUDIES AND THEORETICAL COMPARISON OF FOUR DIFFERENT METAL HYDRIDE STORAGE UNITS 132

7.1 Abstract 132

7.2 Introduction 134

7.3 Theory 134

7.4 Experimental set up 136

7.5 Results and discussion 139

7.6 Conclusions 144

APPENDIX A7.1: UNCERTAINTY 147

Part 3: Behaviour of Metal Hydrides in Hydrogen Systems 153

8 METAL HYDRIDES SYSTEM INTEGRATION: BACKGROUND AND PRELIMINARY EXPERIMENTS 154

8.1 Introduction 155

8.2 Renewable energy hydrogen system laboratory 158

8.3 Preliminary experiments 160

8.4 Design of storage unit and control program 162
8.4.1 Design of MH storage unit 162
8.4.2 Control program 166

8.5 Conclusions 167

9 MODELLING AND SIMULATION OF A THERMALLY COUPLED ELECTROLYSER/METAL HYDRIDE/FUEL CELL SYSTEM 170

9.1 Abstract 170

9.2 Introduction 172

9.3 System description 172

9.4 System simulation tools and methodology 173

9.5 Results and discussion 175

9.6 Conclusions 180

10 THERMAL INTEGRATION OF A METAL HYDRIDE HYDROGEN STORAGE UNIT AND A PEM FUEL CELL STACK 183

10.1 Abstract 183

10.2 Introduction 186

10.3 Experimental set up 187
10.3.1 Metal hydride storage unit 187
10.3.2 Characterisation 188
10.3.3 PEM fuel cell system 188
10.3.4 Operation and characterisation 189

10.4 Renewable hydrogen energy system 189
10.4.1 Characterisation and operation 191

10.5 Results and discussion 191
10.5.1 Metal hydride 191

10.6 PEM fuel cell system 193

10.7 Integration of metal hydride H_2 storage unit and PEM fuel cell 194

10.8 Conclusions 197

APPENDIX A10.1: KINETICS AND THERMAL EQUATIONS 202

APPENDIX A10.2: WATER BALANCES 203

PART 4: Conclusions and Recommendation for Further Work 209

11 MAIN RESULTS, SUMMARY AND RECOMMENDATIONS FOR FURTHER WORK 210

11.1 Main results 210

11.2 Summary 212

11.3 Recommendations for further work 213

1 INTRODUCTION

Modern societies are dependent on safe access to energy. Energy is required for cooling and heating of buildings and to produce goods and services that surround us. If we look at the earth in perspective, we know this is a very complex and vulnerable system. Our historical development and efforts for a better life has resulted in a considerable encroachment on the fragile natural balance. Today, the energy consumption is mainly based on the limited reserves of fossil fuels like oil, natural gas and coal. If the production rate continues at today's level, the estimated reserves [1] of oil in the entire world will end in 41 years while the reserves of natural gas will end in 63 years, Figure 1.1.

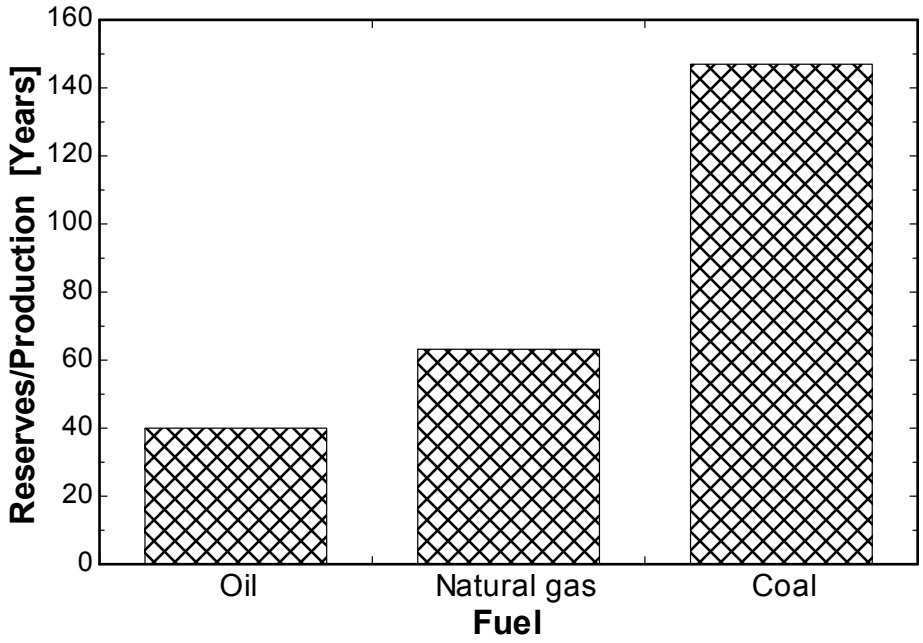

Figure 1.1 The remaining reserves in the world at the end of 2006 are divided by the production the same year[1].

The consumption of fossil fuels also leads to environmental consequences such as emissions of the climatic gas carbon dioxide (CO_2) and nitrous gases (NO_X). This is an increasing pollution problem in cities and villages and a hazard to health.

[1] Proven reserves are generally regarded to be the quantities that geological and engineering information indicates with reasonable certainty can be recovered in the future from known reservoirs under existing economic and operation conditions.

Consequently where are two main reasons to investigate other energy carriers than fossil fuels:

1. Limited reserves of fossil fuels on earth.

2. Environmental problems due to consumption of fossil fuels.

The energy system of the future will probably and hopefully be based on renewable energy like hydropower, wind power, photovoltaic cells and bio-energy. However, as most of these energy resources are intermittent and, a way of storing energy is required. Only a few countries have the same opportunity as Norway to adjust the power production to the power consumption by draining and filling the water reservoars.

1.1 HYDROGEN AS AN ENERGY CARRIER

Since the transition to new sources of energy is expected to proceed gradually, the best way to replace the fossil fuel may be to look for energy sources that will be able to fit into the consumption patterns of today. That is at the consumer end about 25% of the primary energy is used as electricity while about 75% is used as fuel [2]. A number of energy sources, such as, nuclear energy, hydropower, solar energy, wind energy, geothermal energy, tidal energy and energy from ocean waves are available, but in contrast to fossil fuels none of these energy sources can directly be utilized as a fuel. Hence, the energy sources must be used to manufacture a fuel or fuels, as well as to generate electricity. The challenge is to select a versatile energy carrier for the future with high utilization efficiency and costs acceptable. In general, there are several possible energy carriers for the future such as electricity, synthetic gasoline, synthetic natural gas (methane), methanol, ethanol and hydrogen. However, from the criteria given below, two energy carriers are considered more favourable than the others.

1. Storability (storage between product and end use)
2. Mobility (for transportation purposes)
3. Versatility (convertible with other energy carriers/ cover different user demand)
4. Utilization efficiency (overall efficiency through all necessary stages of conversion)
5. Environmental compatibility (at production, transportation, processing and end use)
6. Safety (toxicity, explosion and fire hazard)
7. Economy

On the basis of these criteria there is little uncertainty that electricity will be an important energy carrier in the future. Except for the storability criterion, electricity is superior to any other energy carrier in a non-fuel based system.

When it comes to fuel based energy systems, hydrogen has over the decades emerged as a promising candidate. Three studies are selected to summarise the reasons for this attention:

1. An analysis and comparison of conventional and alternative fuels to hydrogen based on the criteria, or merit factors, given above are given by Veziroglu and Barbir [2],[3]. The conclusion of this study was that hydrogen has several advantageous features and the highest overall merit factor. Besides being the best fuel for transportation, hydrogen was found to be the most versatile, efficient and environmentally compatible fuel.
2. A similar conclusion is given by Selvam [4]. Here specific attention was paid to the pros and cons of alcohol fuels, particularly methanol.
3. A study performed by the National Renewable Energy Laboratory for the U.S. Department of Energy [5] that emphasized the complementary properties of electricity and hydrogen, concluded that hydrogen is anticipated to join electricity as the foundation for a globally sustainable energy system using renewable energy.

The current annual hydrogen production is about 50 billions m^3 STP (Standard Temperature and Pressure) or 45 millions tons. It is widely used in the industry. Due to the problem of hydrogen storage and transportation large consumers of hydrogen (e.g. ammonia and oil refinement plants, etc.) prefer to have their own facilities for hydrogen production, instead of buying it from the suppliers. The amount of hydrogen sold commercially constitutes only a small fraction, ~5%, of the total hydrogen production [6]. Hydrogen contains more chemical energy per weight than any hydrocarbon or alternative synthetic fuel [7-9], but it is also the lightest existing substance and, therefore, problematic to store effectively in small containers.

Hydrogen has a very low boiling point (21 K at 1 bar) in addition to a low critical temperature (33 K), and its state in ambient conditions is as a low-density gas. One kilogram of hydrogen gas at room temperature and atmospheric pressure has a volume of 11.2 m^3 (to provide a 100 km run of a fuel cell car, it is necessary to have at least 33.6 m^3 of hydrogen gas on board [6]).

Even if realization of a “hydrogen society” can be several decades ahead, there are niches already today where hydrogen as an energy carrier is favourable. Due to its high energy density hydrogen has been an essential fuel in space programs for decades [5]. Recently the possibilities for hydrogen fuelled vehicles, (were hydrogen is utilized through a fuel cell) are investigated by the car manufactures. This could solve some of the problems connected to air pollution in big cities. Further, a compact hydrogen storage unit combined with a fuel cell could replace the battery and increase the stand by time of cell phones and laptop computers.

Another niche marked investigated is hydrogen stand alone power systems (HSAPS). HSAPS is defined as an autonomous system, which supplies energy without being connected to the electricity grid with hydrogen as an energy carrier. In a HSAPS the load is basically served by energy generated from renewable energy sources. A battery serves as short term energy storage, and buffer between the user and the energy source. During longer periods of excess energy, hydrogen is produced through electrolysis of water. The produced hydrogen can be stored in a metal hydride, and utilized in a fuel cell to produce electricity. Two billion people live without grid connection and live in thinly populated areas in developing countries, and the extension of the grid to these areas is for economical reasons and in some cases, also for political reasons not feasible. Therefore it exist a marked for HSAPS, as an alternative to expensive grid expansion, in remote and inaccessible areas or as replacement for conventional SAPS utilizing batteries and diesel generators.

The key technologies if hydrogen and electricity together would form a complete energy carrier system, are technologies for hydrogen production, storage, transportation and utilisation.

1.2 HYDROGEN STORAGE

The requirements for hydrogen storage systems are different for different applications. Low total weight is essential for mobile applications, but is not so important for the stationary ones, e.g. filling stations. Small total volumes are critical for small vehicles and portable devices but are less important for the stationary applications.

A fuel cell car needs to store at least 5 kg of hydrogen (600 MJ chemical energy) to match the range of gasoline-powered vehicles, with peak hydrogen consumption of 1-3 g/s to provide necessary acceleration [10]. Hydrogen storage systems for mobile applications should also be efficient with respect to performance and cost: A vehicular hydrogen storage system should also work at near-ambient temperature with high reversible hydrogen storage capacity and fast kinetics, particularly during recharging. It has to have mechanical stability towards intrusions in collisions and inflammable when penetrated. Some key challenges regarding hydrogen storage for mobile applications are given below [11]:

- Weight and Volume. The weight and volume density of hydrogen storage systems are presently too low, resulting in inadequate vehicle range compared to conventional petroleum fueled vehicles. Materials and components are needed that allow compact, lightweight, hydrogen storage systems while enabling greater than 300-mile range in all light-duty vehicle platforms.

- Efficiency. Energy efficiency is a challenge for all hydrogen storage approaches. The energy required to absorb and desorb hydrogen is an issue for reversible solid-state storage materials. Life-cycle energy efficiency is a challenge for chemical hydride storage in which the by-product is regenerated off-board. In addition, the energy associated with compression and liquefaction must be considered for compressed and liquid hydrogen technologies.

- Durability. Durability of hydrogen storage systems is inadequate. Materials and components are needed that allow hydrogen storage systems with a lifetime of 1500 cycles.

- Refueling Time. Refueling times are too long. There is a need to develop hydrogen storage systems with refueling times of less than three minutes, over the lifetime of the system.

- Cost. The cost of on-board hydrogen storage systems is too high, particularly in comparison with conventional storage systems for petroleum fuels. Low-cost materials and components for hydrogen storage systems are needed, as well as low-cost, high-volume manufacturing methods.

Hydrogen can be stored in several different ways, and all of them have their pros and cons, as discussed below.

1.2.1 Compressed hydrogen

Hydrogen gas can be compressed and stored in storage tanks that can hold it at the required pressure. The tanks can either be made from steel, aluminium or copper alloys that may be encased in fiberglass. The steel tanks are most often used for stationary applications where weight is not a hindrance as the steel tanks tend to be heavy. High pressure tanks also appear in some test cars. But safety and space remain significant concerns. The main research task within the field of compressed gas storage is to develop new safe low weight composite cylinders suitable for high pressures. However, it is inevitable that a considerable amount of energy is used to compress the hydrogen. If the hydrogen is compressed to 100, 300 or 700 bar will approximately 12, 18 and 24% of the stored hydrogen's energy be used to compression if a compressor with 85% efficiency is used.

1.2.2 Liquid hydrogen

Hydrogen can be stored as a liquid (LH_2) at 21.2 K at ambient pressure in cryogenic tanks. Liquid hydrogen has long been the fuel of choice for rocket applications[12]. The cooling and compressing process requires energy, resulting in a net loss of about 30% of the energy stored in the liquid hydrogen [11]. The storage containers lose energy due to boil-off of hydrogen, caused by diffusion of heat into the storage unit from the surroundings. The automotive company BMW has been researching the use of liquid hydrogen as a fuel for automobiles. They are currently working with test models that store hydrogen as a liquid in super-cooled tanks. The main research and development tasks are to:i) Develop more efficient liquefaction processes. ii) Lower the cost and improve the performance of the insulated containers. iii) Develop system that automatically captures the boil off and re liquefies the hydrogen.

1.2.3 Hydrogen stored in hydrogen rich liquids

Since hydrogen is a liquid only at low temperatures, another possible storage option could be to store hydrogen in a hydrogen rich liquid. The hydrogen rich liquid should be in liquid form at ambient temperatures be cheap and easy to produce, it should not be toxic, and possible to reform on board in mobile applications. One possible liquid is Methanol. Methanol is a liquid at room temperature and has a boiling point at 338 K. It is also possible to reform methanol into CO_2 and H_2 on board [12]. However, this is not an environmental friendly energy carrier due to the reforming by product CO_2.

1.2.4 H_2 storage in solids

The different alternatives for hydrogen storage within solid structures have attracted considerable focus within the recent years. The maturity of the field of solid H_2 storage has not reached the same level as for e.g. compressed and liquid hydrogen storage solutions. Storage of hydrogen in solid material has the potential to become a safe and efficient way to store energy, both for stationary and mobile applications. One can roughly divide the solid storage solution into four categories; i) high surface area materials such as nanostructures of carbon, ii) H2O- reactive chemical hydrides, iii)thermal chemical hydrides and iv)rechargeable hydrides. A summary of the main materials within these groups is presented in [13]. There are still many R&D tasks that need to be solved for these materials before they can be introduced into the commercial marked. The main advantage for choosing solid materials for hydrogen storage is high volume energy density and low pressures.

1.3 THESIS BACKGROUND AND OBJECTIVES

This thesis is part of the KMB project "Hydrogen storage in solid materials, from synthesis to system". This project was a co-operation between Institute of Energy Technology (IFE), University of Oslo (UIO) and The Foundation for Scientific and Industrial Research at the Norwegian Institute of Technology (SINTEF) with the main objective to further develop and build new competence in the area of storage of hydrogen in solids. The project sub-goals were to:

1) Develop new hydrogen storage materials based on micro-porous inorganic-organic hybrid materials, 2) Develop competence on encapsulation of materials in hydrogen storage units and system integration for near-market applications, and (3) Build up a network between R&D institutions and industry.

A joint venture betweent UIO and SINTEF performed the main work on development of new hydrogen storage materials. Sub goal two was given as the topic for the preseent thesis, and an additional objective for the thesis work was to be a link between the metal hydride storage group and system group at IFE. The following objectives were defined within the frames of sub goal two:

- Develop and verify an expression describing the kinetics of the gas solid reaction, suitable for use in heat and mass transfer modelling.
- Develop and verify heat and mass transfer models for metal hydride storage units.
- Test and evaluate metal hydride storage units.
- Study the interaction between a metal hydride storage unit and a fuel cell through simulations and experimental work.
- Build and thermally integrate a metal hydride storage unit with a water-cooled Proton Exchange Membrane (PEM) fuel cell and system testing.

To reach the objectives listed above the working strategy was to use and characterize a well-known material suitable for hydrogen storage applications. The chosen alloy was later tested in various storage units. The experimental results from the different storage units were used to verify heat and mass transfer models. The component interaction between an electrolyser, a metal hydride storage unit and a fuel cell was studied through system simulations. The experimentally verified models and the simulation results were used as the basis for the designing and integrating a metal hydride storage unit with a proton exchange membrane (PEM) fuel cell (FC). A computer program making it possible to study the interaction between the fuel cell and metal hydride storage unit was developed.

1.4 OUTLINE OF THESIS AND STRUCTURE OF WORK

The scope of work for this PhD thesis ranges from an in-depth study of the reaction kinetics in metal hydride (MH) materials, to the thermal behaviour of MH-systems (storage units) and, to integration simulation and operation of hydrogen subsystem into stand-alone renewable energy hydrogen power systems. The structure of the thesis is presented schematically in Figure 1.2

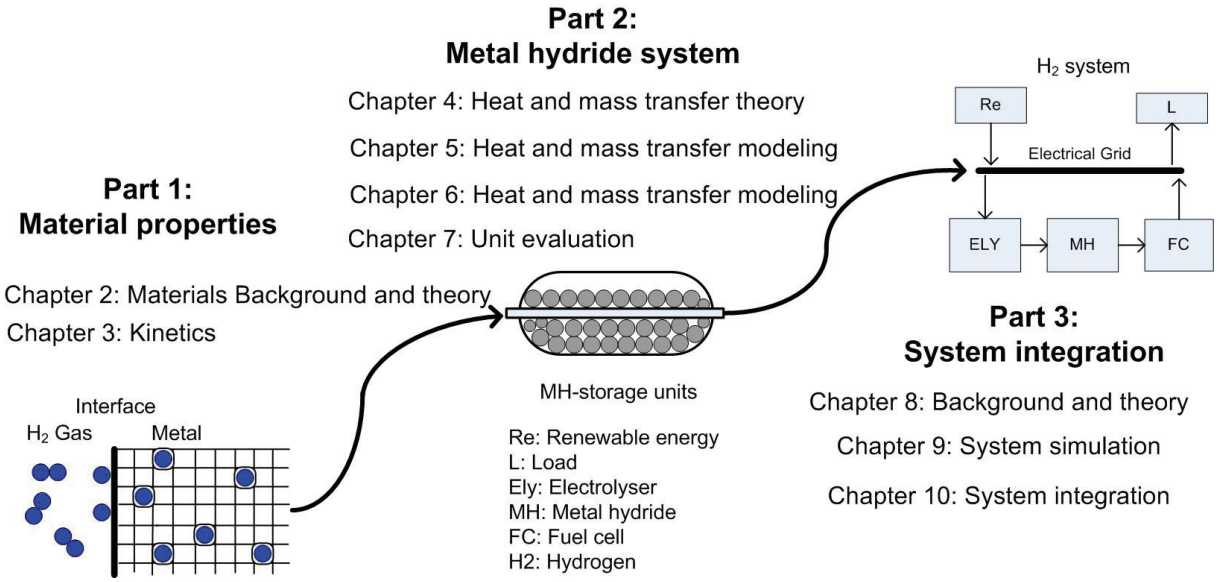

Figure 1.2 Structure of thesis

It can be seen from Figure 1.2 that the thesis is divided into three different parts. Part number one deals with characterization of the material itself. In this section the kinetic and thermodynamic behaviour of small samples of metal hydride powder has been investigated through testing, simulation and modelling. The major objective for this section was to develop and verify experimentally an expression for the gas-solid reactions kinetic suitable for usage in heat and mass transfer modelling.

The second and main part of this thesis deals with metal hydride systems, meaning larger metal hydride storage units loaded with 0.85-2.5 kg with metal hydride powder. The major aim for this part was to get hands on experience with larger metal hydride storage units. The charging and discharging characteristics of four different metal hydride storage units containing the same type of AB_5 alloy, but with different heat exchangers were experimentally investigated. The experimental results from the different units were analysed and compared with each other. Three different heat and mass transfer models were developed and experimentally verified through the performed experiments. The simplest model, a zero dimensional model, assumes uniform temperature, concentration and pressure in the metal hydride storage unit and is only valid if heat is very effectively distributed within the unit. The next model is more complex and is a one-dimensional heat and mass transfer model, assuming thermal equilibrium between the gas and solid. The last model is a two dimensional heat and mass transfer model assuming thermal non equilibrium between the gas and solid.

In the third part a hydrogen system is investigated both numerically and experimentally. The zero dimensional model (developed and experimentally verified in the second part) is implemented in a system simulation. The simulated system contains a fuel cell, a metal hydride storage unit and an electrolyser. The interaction between the components and the possibility to use the excess heat for domestic heating are investigated in the simulations. In the experimental part a metal hydride storage unit containing 18 kg of an AB_5 type of metal hydride powder is designed, constructed and filled with powder. This unit is thermally connected to a 1.2 kW proton exchange membrane (PEM) fuel cell. The operation characteristic of the metal hydride storage unit and fuel cell is found through experiments. The interplay of these two components is studied experimentally for different strategies regarding the thermal interaction during start up.

References

[1] British Petroleum Statistical Review of World Energy June 2007 (http://www.bp.com/multipleimagesection.do?categoryId=9017892&contentId=7033503) (25/07-2007).

[2] Veziroglu T, N, Barbir F. Initiation of hydrogen energy system in developing countries. International Journal of Hydrogen Energy 1992; 17(7): 527-538.

[3] Veziroglu T, N, Barbir F. Hydrogen - the Wonder Fuel. International Journal of Hydrogen Energy 1992; 17(6): 391-404.

[4] Selvam P. Alcohol fuels-the question of their introduction: A comparison with conventional vehicular fuels and hydrogen. International Journal of Hydrogen Energy 1992; 17(3): 237-242.

[5] NREL (1995) Hydrogen: The fuel for the future. National Renewable Energy Laboratory, US. Department of Energy, Washington. http://www.interstatetraveler.us/Reference-Bibliography/USDOE%20Hydrogen%20Fuel%20of%20the%20Future.pdf (02/08-2007).

[6] Schlapbach L. Hydrogen as a fuel and its storage for mobility and transport. MRS Bulletin 2002; 27(9): 675-676.

[7] Hydrogen Energy Equivalents.- H-ION SOLAR, Inc.- http://www.hionsolar.com/n-heq1.html.

[8] Properties of Fuels.- Alternative Fuels Data Center (AFDC); US Department of Energy, Office of Transportation Technologies. http://www.eere.energy.gov/afdc/pdfs/afv_info.pdf.

[9] Hamburg D, Yu, Dubovkin N, F. Hydrogen: Properties, Production, Storage, Transportation, Applications. Reference Book (in Russian). edn. Moscow:: "Khimia" Publ, 1989.

[10] Pettersson J, Hjortsberg, O. Hydrogen storage alternatives - a technological and economic assessment. - Volvo Teknisk Utveckling AB. KFB - Kommunikationsforsknings-beredningen, Stockholm. KFBs DNR 1998-0047, December 1999. - 38 pp.

[11] U.S Department of Energy (DOE) Hydrogen Fuel cells & Infrastructure Technologies Program http://www1.eere.energy.gov/hydrogenandfuelcells/storage/hydrogen_storage.html. 2007.

[12] Larminie J, Dicks A. Fuel cell systems explained. edn. Chichester, West Sussex: J. Wiley, 2003.

[13] International Energy Agency (IEA) Hydrogen Production and Storage-R&D Priorities and Gaps http://www.iea.org/textbase/papers/2006/hydrogen.pdf.

Part 1: Equilibrium and Kinetic Behaviour of Metal Hydride Powder

2 METAL HYDRIDES: BACKGROUND AND THEORY

Nomenclature

C	Hydrogen to metal atomic ratio	[-]
ΔH	Enthalpy	[kJ/mol]
P	Pressure	[bar]
R	Universal gas constant 8.314	[J/mol·K]]
ΔS	Entropy	[J/mol]
T	Temperature	[K]
T_C	Critical temperature	[K]
t	Time	[s]
ρ_H^*	Gravimetric hydrogen density	[%]
σ_H^*	Volumetric hydrogen density	[g/cm^3]
β	Beta phase	[-]
α	Alpha phase	[-]

Subscript

eq	Equilibrium
g	Gas
MH	Metal hydride

2.1 INTRODUCTION

The British chemist T.Graham [1] reported in 1866 a discovery of a new type of chemical compounds; he found that palladium was able to absorb large amounts of hydrogen gas forming what was to be known as a metal hydride (MH). A metal hydride is generally defined as a compound formed by hydrogen with a metal. After the discovery of the palladium hydride, further research on synthesis and characterization of different binary MH was done in the following years. Although most of the elements from the Periodic Table were found to form hydrides, a vast majority of them are not are not able to absorb and desorb hydrogen readily and reversibly at moderate temperatures and pressures. Nearly 100 years after the discovery of the binary MH, hydrogen interaction with intermetallic compounds containing two different metals was studied. ZrNi was investigated in 1958 by Libowitz [2] who showed that hydrogen uptake and release by this compound proceeds easily and is reversible, thus opening possibilities for applications of metal hydrides in hydrogen storage. Further studies have shown that there is a vast group of intermetallic hydrides formed by the compounds A_n B_m which exhibit extremely fast hydrogenation-dehydrogenation rates during charge and discharge by gaseous hydrogen. Such reversible H uptake and release proceeds at very convenient conditions, at ambient temperatures, 293-373 K, and at low pressures of 0.1-10 bar H_2. Intermetallic compounds used for hydrogen storage are usually classified into several groups according to their stoichiometry and types of structure such as AB_5, AB_3, AB_2, AB and A_2B. These are all interstitial hydrides, where the hydrogen atoms are located inside the cavities (interstitials) formed between the metal atoms. Some examples of the different groups are shown in Table 1. Here A stands for an active hydride forming element, including rare-earths metals, magnesium, calcium, zirconium and titanium, and B represents transition metals such as nickel, cobalt, iron, manganese and chromium.

Table 1: material properties for different types of intermetallic hydrides and liquid and gaseous hydrogen (ρ_H^* = gravimetric hydrogen density, σ_H^* = volumetric hydrogen density).

Type	Composition	P*eq* [bar]	Temperature [K]	$-\Delta H_H$ [kJ/mol]	ρ_H^* [wt %]	σ_H^* [g/cm^3]	Ref
AB_5	$LaNi_5H_{6.4}$	2.4	294	15.9	1.5	0.1	[3]
AB_3	$CeNi_3H_3$	0.09	323	21.4	0.9	0.03	[4]
AB_2	$ZrV_2H_{4.7}$[a]	$2.7\cdot10^{-6}$	414	80.3	2.4	0.13	[5]
AB	$TiFeH_{1.9}$[b]	3.2	303	14.0	1.8	0.1	[6]
A_2B	Mg_2NiH_4	3.3	572	32.3	3.6	0.1	[7]
	Compressed H_2	700	298	-	-	0.04	
	Liquid H_2	1.0	20	-	-	0.07	

a) No plateau, the data are taken at $ZrV_2H_{0.6}$
b) Presented for the plateau $TiFeH_{0.5}$➔TiFeH

The United States Department of Energy (DOE) has presented a series of design targets/goals for hydrogen storage system development[8]:

- Onboard hydrogen storage systems demonstrating specific energy of 2.0 kWh/kg (6 weight percent hydrogen) and energy density of 50 g H_2/litre at a cost of $4/kWh by 2010.

- Specific energy of 3.0 kWh/kg (9 weight percent hydrogen) 81 g H_2/litre, and $2.00/kWh by 2015.

Technologies that meet these design goals for hydrogen storage would permit the development of fuel cell powered vehicles that would meet consumer needs for vehicle performance, range, cost, and utility.

A comparison between the gravimetric and volumetric densities of various storage options is shown in Figure 2.1.

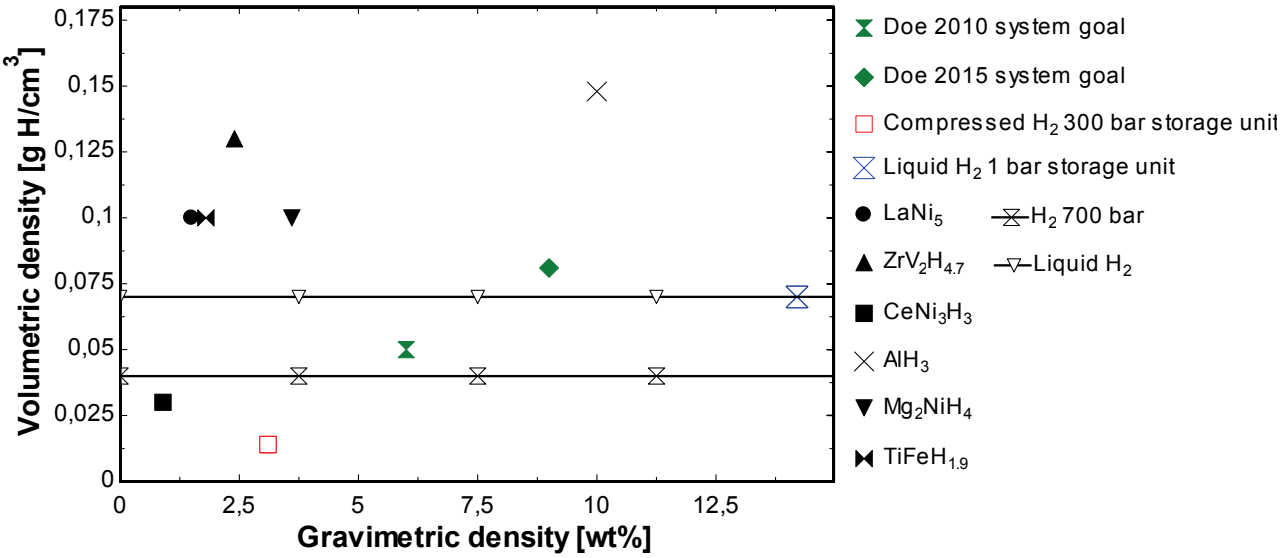

Figure 2.1 The gravimetric versus volumetric densities presented in Table 1 are plotted together with the DOE goals for hydrogen storage systems [8]. No gravimetric density has been defined for the liquid and compressed hydrogen since these are highly system dependent. Currently research are performed to find hydrides with higher gravimetric weight percent like aluminium hydride [9]. The compressed and liquid hydrogen storage containers was capable of storing 3.1 and 8.5 kg of hydrogen [10].

All the different storage alternatives presented in Figure 2.1 have their pros and cons. It can be seen that the majority of the metal hydrides cannot achieve high-enough weight percentages to fulfil the DOE goals. Ideally, the physical storage alternatives, *i.e.* storing hydrogen as a liquid or as high-pressure compressed gas, give reasonably high gravimetric densities. However, they do not fulfil the goals with regards to volumetric densities. In addition, storing hydrogen as a liquid requires an energy consuming liquefaction process (using the equivalent of 30 % of hydrogen's total energy contents), and better insulated tanks have to be developed to decrease the hydrogen losses due to boil of the hydrogen during long-time storage. Storing hydrogen as compressed gas, a considerable amount of energy is used for compression of the hydrogen to the desired pressure (using the equivalent of ca 14 % of the total energy content in hydrogen to compress it to 200 bar). In additions, it is safety questions then gases are stored at such high pressures. Finally, aluminium hydride is presently considered as practically irreversible and need extremely high pressures to be re-charged

again. Further improvements in all fields of hydrogen storage are needed in the future for solving the storage problem and fulfilling the requirements.

2.2 THERMODYNAMICS OF METAL HYDROGEN INTERACTIONS

Depending on the strength and type of the hydrogen-metal (H-M) bond, metals can be exothermic absorbers of hydrogen and almost all practical H-M systems are exothermic. Hydrogen gas in thermal equilibrium with hydrogen dissolved in a metal can then be expressed by the reaction:

$$M + \frac{1}{2} \cdot X \cdot H_2 \Leftrightarrow MH_X \,, \tag{1.1}$$

where M is the metal, H is hydrogen and x is the molar fraction of hydrogen absorbed in the metal. This reaction has an enthalpy change ΔH and an entropy change ΔS. The equilibrium pressure P is closely related to the absolute temperature T by the Van`t Hoff equation:

$$\ln P = \frac{\Delta H}{R \cdot T} - \frac{\Delta S}{R} \,, \tag{1.2}$$

where R is the universal gas constant and ΔH and ΔS are the enthalpy and entropy changes of the hydride formation. The H-M interaction is best understood through the use of phase diagrams. The most used diagrams are the Pressure Concentration Temperature (PCT) diagrams and the Van`t Hoff plots as shown in Figure 2.2.

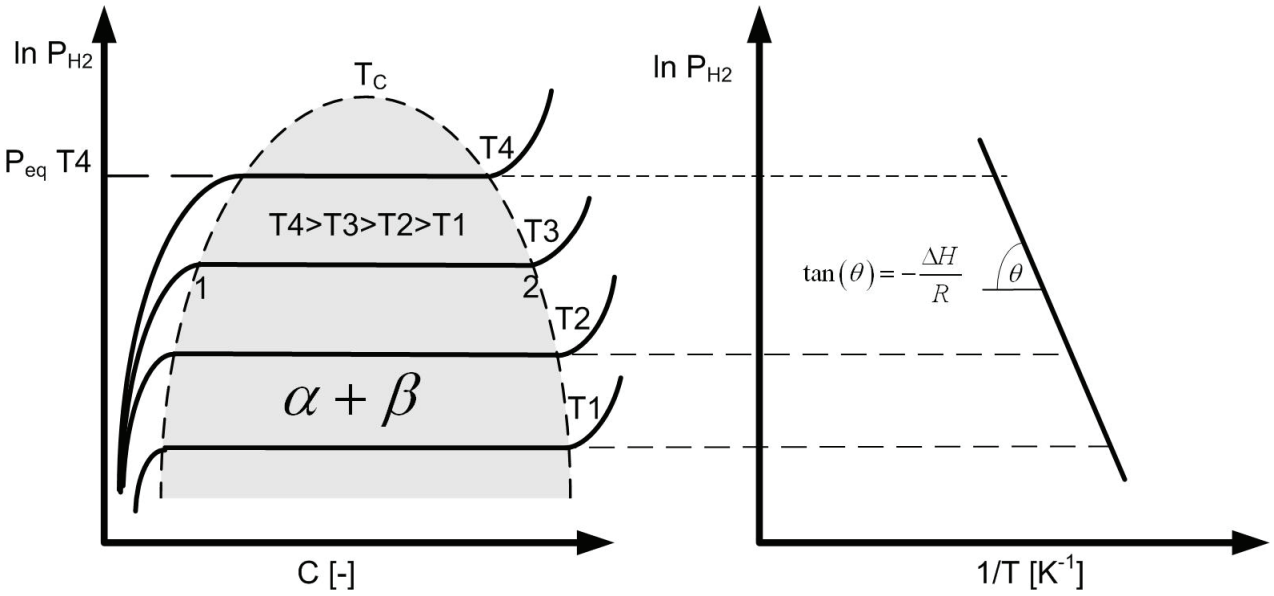

Figure 2.2 An idealized Pressure Composition Temperature (PCT) representation of isotherms for the solid solution phase (α) and hydride phase (β). The enthalpy ΔH of the hydride formation is obtained from the slope of a Van`t Hoff plot of ln(P_{eq}) versus 1/T.

Moving along one isotherm in Figure 2.2, hydrogen start to dissolve into the host-metal lattice at low concentrations as the surrounding gaseous hydrogen pressure increases. At point 1, a hydride is formed locally by the occupation of particular interstitial lattice sites (only for interstitial hydrides, not valid for *e.g.* alanates etc). In the α phase, the hydrogen atoms are

randomly distributed inside the metal. Under idealized equilibrium conditions, the hydrogen gas pressure remains constant as hydrogen is absorbed and the α phase is transformed into β phase. In the β phase, the hydrogen atoms lie in an organized structure inside the metal hydride. At point 2 the α phase is completely transformed into the β phase. Passing point 2, increased pressure is required to maintain further filling, because the most energetic preferable places in the lattice are already filled with hydrogen atoms. The slope and length of the equilibrium plateau is of particular importance for hydrogen storage application. A flat plateau enables the reversible absorption and desorption of hydrogen from a metal, simply by raising or lowering the surrounding hydrogen pressure above or below the plateau pressure. When raising the pressure, hydrogen is absorbed forming the β hydride phase. Lowering the pressure transforms the hydride into the α phase, and hydrogen is desorbed.

Typical examples of the hydride-forming compounds are Mg_2Ni, TiFe and $LaNi_5$. The availability of hydrogen stored in a metal matrix strongly depends on the stability of the hydride. Stability of the metal and intermetallic hydrides can be evaluated from the vant' Hoff plots ln*P* vs 1/T where P is the equilibrium pressure presented in Figure 2.3.

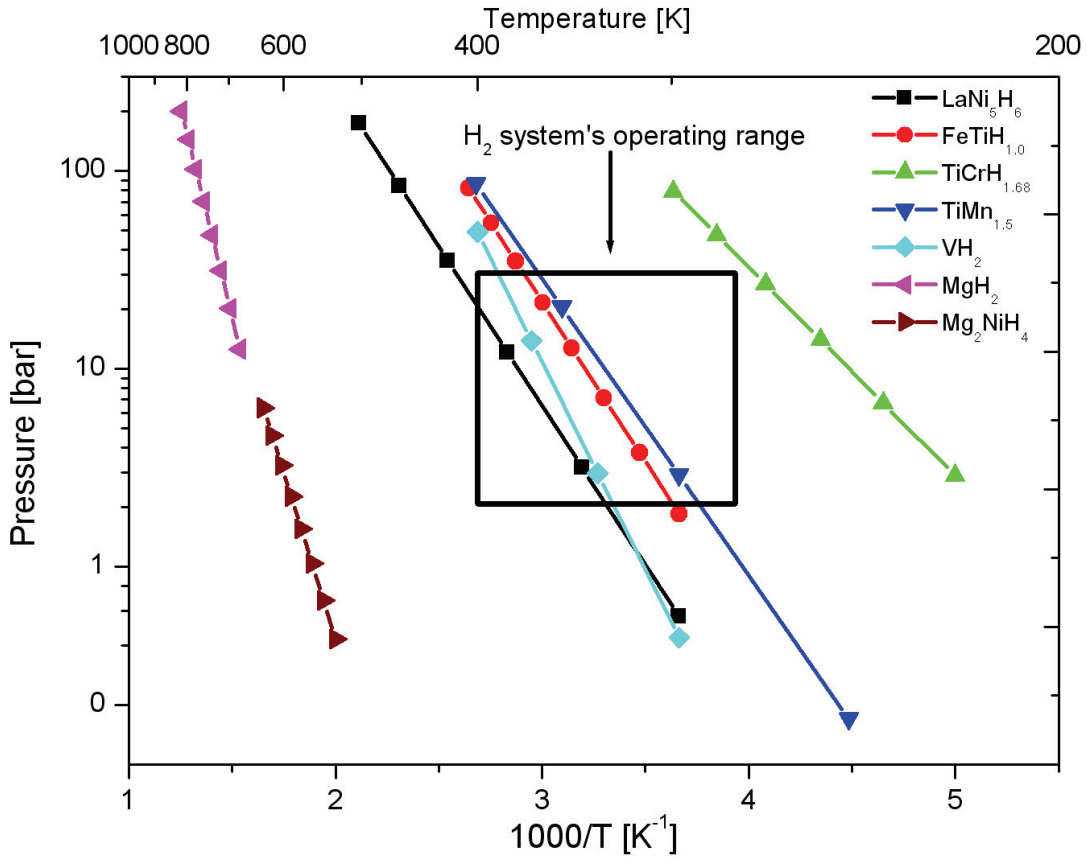

Figure 2.3. Vant' Hoff plots ln*P* vs 1/T for different metal-H systems [6,11-15]. The square represent typical hydrogen systems' operating pressure and temperatures spanning from 273-400 K and 2-30 bar.

From a practical point of view, in addition to the stability, there are several criteria that need to be fulfilled for a metal hydride to become an attractive hydrogen storage alternative [15]

1. High reversible hydrogen storage capacity, gravimetric and volumetric;
2. Convenient operating pressure and temperature ranges;
3. Fast reaction kinetic rates during hydrogen absorption and desorption processes;
4. Low degradation under the repeated cycling;
5. High availability of the component materials, and prospective for low cost;
6. Low sensitivity to the impurities in gaseous H_2, for example, to water vapour and to oxygen;
7. Safety aspects.

2.3 KINETICS OF METAL HYDRIDES

Hydrogen-metal reactions can be regarded as a special type of heterogeneous gas-metal reactions. There are specific features that make the kinetics of hydride formation different from other gas-solid reactions. The main two unique properties of M-H systems are in extremely high diffusivity of hydrogen dissolved in the metal lattice. In addition, many M-H systems will start to fracture at the very early stages of the reaction.

The reaction rate in a metal hydride is governed by a number of factors. Absorption and desorption of hydrogen may be divided into several independent steps as proposed by Martin et al. [16] and listed below .

Hydrogen absorption

1. Physisorption of hydrogen molecules on the surface of the metal.
2. Chemisorption and dissociation of hydrogen molecules.
3. Surface penetration of the atomic hydrogen into the bulk and formation of α-solid solution.
4. Diffusion of hydrogen atoms through the layer of α-solid solution, involving interstitial and vacancy mechanisms.
5. Hydride formation at the interface of the metal.

Hydrogen desorption

1. Hydride decomposition at the hydride/α-solid solution interface.
2. Diffusion of hydrogen atoms through the α-solid solution.
3. Penetration of hydrogen atoms from bulk to the surface.
4. Recombination of chemisorbed hydrogen atoms into the H_2 molecules and their physisorption on the surface.
5. Desorption from the surface into the gaseous phase.

Interpretation of kinetic data obtained on powder beds, in terms of intrinsic kinetics or type of mechanism, should be considered with great care. Many studies performed by different investigators led to different conclusions regarding the type of kinetics and controlling mechanisms. It has been pointed out [17] that extrinsic parameters such as heat transfer or mass transfer may dominate such powder kinetics and alter their overall behaviour. For each of all the steps above, functions based on physical assumptions, can be given with a high number of parameters associated with them, as has been done i.e. by Martin et al. [16]. To make a mathematical model of the gas - solid reaction it is often necessary to simplify by assuming a perfect geometry for the particles, uniform particle distribution and only one rate limiting step. A schematic illustration of the hydriding / dehydriding reactions are given in Figure 2.4.

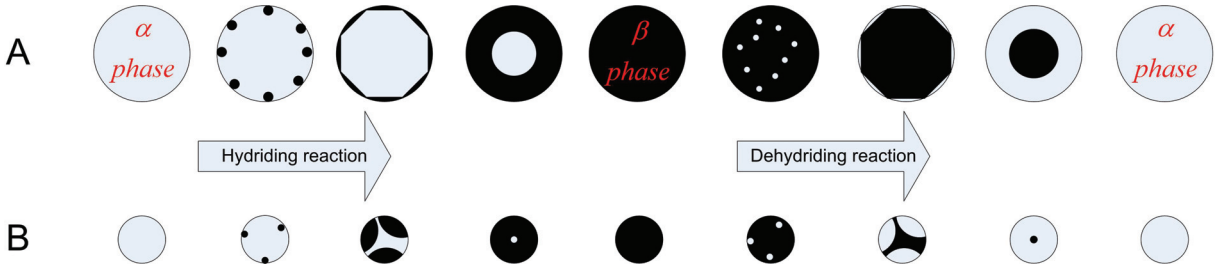

Figure 2.4 The hydriding /dehydriding reaction for large particles A and smaller particles B [18].

For large particles (path A in Figure 2.4), multiple nucleation sites at the surface will merge and form a closed layer that prevent fast diffusion of hydrogen to the core of the particle, slowing down the kinetics of the $\alpha - \beta$ phase transition, [18]. If the particles are small (path B in figure Figure 2.4), fast diffusion of hydrogen through the α phase remains possible for a larger fraction of the $\alpha - \beta$ phase transition [18]. For desorption in large particles (path A Figure 2.4), hydrogen has to diffuse through a thicker layer of the β phase, while hydrogen easer can reach the surface the surface for smaller particles.

The particle size and distribution affect the kinetic reaction path, as indicates in Figure 2.4. The particles are seldom uniformly sized with spherical shape in a real situation. In addition, the rate-limiting step can change with the hydrogen contents in the particles. All these factors can cause inaccuracies in a kinetic model.

Some authors [19-21] have used an empirical expression as shown in (1.3) to describe the gas solid reaction.

(1.3) $$\frac{\partial C}{\partial t} = f(C) \cdot f(T) \cdot f(P_g, P_{eq})$$

Here the reaction rate is a function of hydrogen concentration (C), system temperature (T) and hydrogen gas pressure at any given time and equilibrium pressure P_g, P_{eq}.

The form and the methodology used to derive the kinetic rate constants vary from research group to research group. Due to the differences in experimental set up, some laboratories have special equipment making it possible to hold either the reaction rate or the gaseous pressure constant during experiments. However, such equipment is expensive and requires a sophisticated set up to control the process and log the experimental data. Therefore the need for a methodology to perform experiments and treat experimental data obtained with a standard experimental set up was identified. The developed methodology presented in chapter three makes it possible to derive the kinetic rate constants from experiments performed with a Siverts-type of apparatus. A Sieverts-type apparatus is very common in laboratories dealing with characterization of metal hydrides and gives the developed methodology a wide range of possible users.

2.4 EXPERIMENTAL METHODS

In the process of developing a heat and mass transfer model, expressions for the gas solid reaction rate and the given alloys PCT curves are absolutely necessary.

Several correlations for the gas solid reaction rate are available in the literature. Even though the differences between the reaction rates for alloys in the AB_5 family are small, we decided not to base our modelling on literature data, and performed our own kinetic measurement. A schematic of the Siverts-type of apparatus used to perform the kinetic measurements and the alloys characteristic PCT curves are shown in Figure 2.5.

In the volumetric Sieverts method the sample to be investigated is placed into a closed reactor of a known volume. Hydrogen is then introduced into a connected gas collector system of known volume equipped with a pressure transducer. The measured hydrogen pressure determines the molar quantity of hydrogen gas in the collector. Then the valve between the collector and the reactor is opened, the amount of hydrogen absorbed or desorbed can be calculated from the changes in the measured pressure.

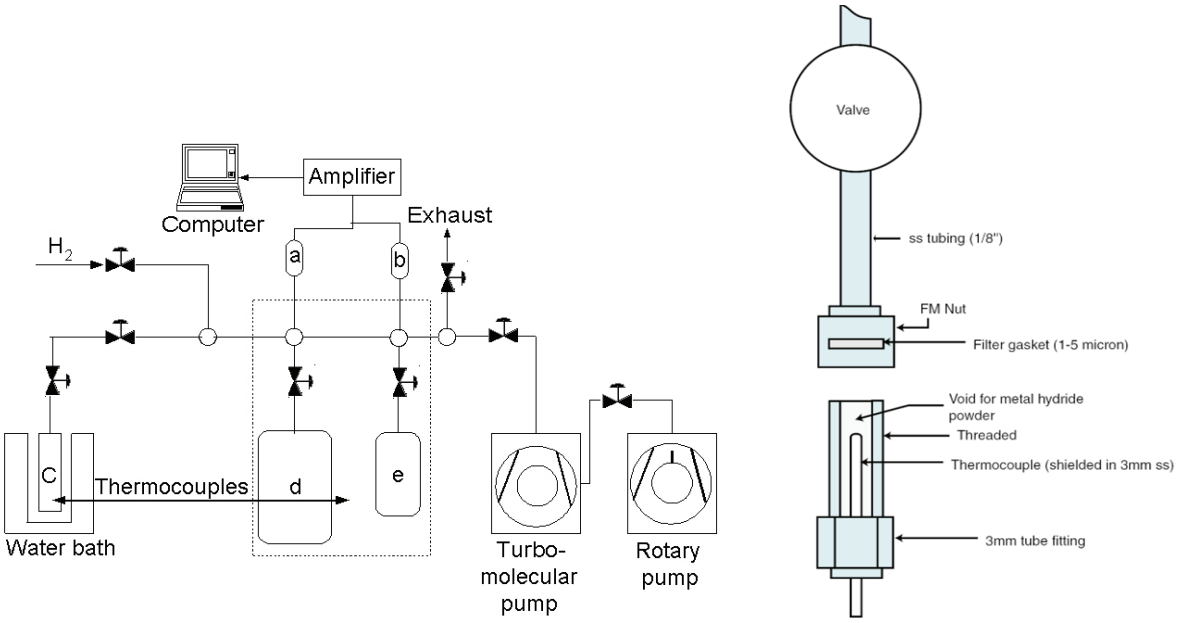

A B

Figure 2.5 A Scheme of the experimental Sieverts' type apparatus: a) pressure transducer of 1.0 bar; b) pressure transducer of 25.0 bar; c) sample reaction cell; d) 300cc buffer volume; e) 50cc buffer volume; f) water bath. B sample reactor with thermocouple for kinetic measurements. The metal hydride powder is inserted into the void and the FM nut closes the reactor. The valves are for keeping the reactors tight during mounting and un-mounting to the PCT set up.

The deviations from the ideal gas law are accounted for and the amount of hydrogen absorbed or desorbed by the metal hydride powder is calculated. We also assumed that the equilibrium state was reached when the change in hydrogen pressure was less than 10 mPa pr min. Kinetic information is obtained with the same experimental set up as described above. Hydrogen gas of 99.999% grade purity was used in the PCT and kinetic measurements performed in this study. There are several reasons for the kinetic measurements to give inaccurate results. These are discussed in chapter 3.

The schematic of the reactor used to perform the kinetic measurement is shown in Figure 2.5 B. This reactor had the possibility to add larger amount of thermal ballast and to monitor the sample temperature.

Two types of kinetic experiments are performed; the first one is called “stepwise”. Here the alloys reaction rate is measured. Then the alloy is stepped from equilibrium pressure to the next equilibrium pressure at the same isotherm (the same way as in the PCT measurements). The second type of measurement are called “full hydrating and dehydrating experiments”, here the alloy is fully charged and discharged in one step. The risk for deviation from isothermal conditions is larger for these types of experiments due to the larger amount of released heat during the experiment.

A scanning electron microscope (SEM) was used to record images of the powder particles before and after hydrogenation. In the present work, a Hitachi s-4300se field emission SEM was used to record the images shown in chapter 4. The pictures were used to derive the particle distribution and shape.

The dimensions of the unit cell, symmetry and atomic structure of the metal sublattice can be investigated with X-ray diffraction. However, the positions of light atoms such as hydrogen cannot be determined in a matrix of more significantly scattering metal atoms since X-ray scattering take place primarily by interaction with the electrons, defined by the atomic number of the element. It is possible to determine the structure with higher accuracy with a synchrotron X-ray compared to a conventional laboratory X-ray. The problem of peak overlaps is reduced to a minimum due to the high resolution permitting the maximal amount of unambiguous intensity data to be obtained from diffraction pattern.

2.5 PRELIMINARY EXPERIMENTS

Absorption and desorption experiments with the same amount of metal hydride powder and same charging and discharging pressures with and without thermal balast were performed. This was done to investigate the effect of the added nickel powder on the charging and discharging rates some of the results are presented in Figure 2.6.

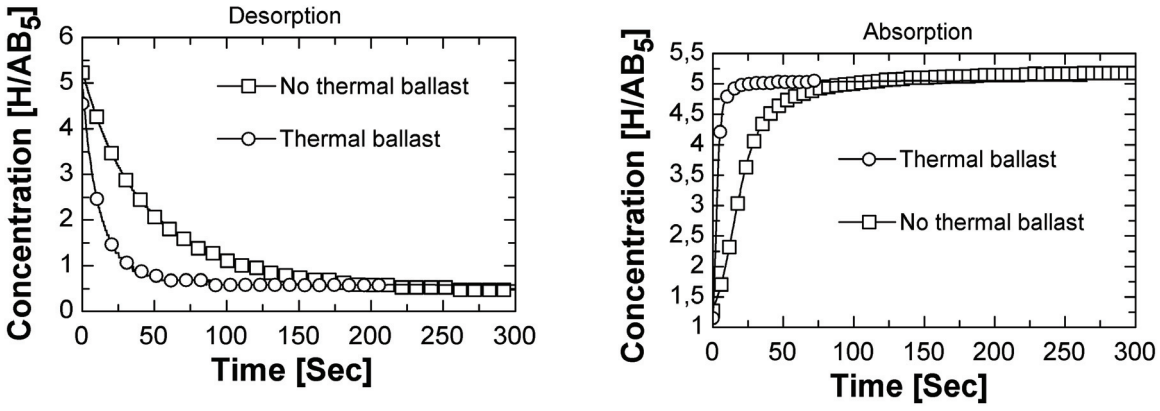

Figure 2.6 Calculated hydrogen concentration versus time for absorption and desorption experiments at 298 K with and without thermal ballast (some data points are removed to increase the readability).

The experiments shown in Figure 2.6 were performed using the 50 cubic centimetres buffer volume shown in Figure 2.1A. The starting pressure was 17 bar for both the absorption experiments and 1.8 bar for the desorption experiments. It can be seen that the reaction rate is considerably faster for both absorption and desorption with thermal ballast.

Since the reaction is faster with the thermal ballast, than without the ballast, is the additional mass transfer resistance from the added nickel powder small. However, even if thermal ballast is added and the amount of metal hydride powder is reduced it is still a risk for deviations from isothermal conditions. The measured sample temperatures is plotted versus time and shown in Figure 2.7, for a stepwise and full desorption at 298 K.

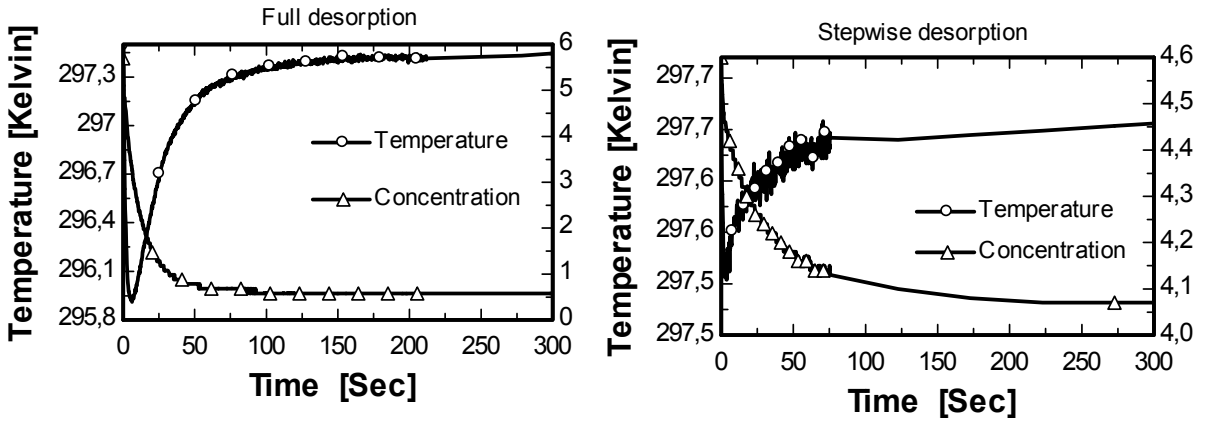

Figure 2.7. Measured temperature profile plotted together with the calculated hydrogen concentration during a stepwise (left side) and full desorption (right side) experiment at 298 K (some data points are removed to increase the readability)

There is a considerable temperature drop in the metal hydride powder during full desorption, as can be seen from Figure 2.7 (left-side graph). This indicates that the assumption of isothermal condition is not totally correct for the full absorption and desorption expression. Incorrect kinetic parameters can be found if a kinetic analysis based on data taken from full absorption and desorption experiments are performed. Even with the stepwise experiments it is some deviations from isothermal condition, as shown in Figure 2.7 (right-side graph). The measured temperature profile has the same principle shape for both the full and stepwise experiments. The maximum deviation from isothermal conditions occurs during the first seconds of the experiments, making the isothermal assumption invalid. The sample then returns to its initial temperature and the isothermal assumption is again valid.

Thermal ballast reduces the reaction time for both full absorption and desorption. The deviation from isothermal conditions is larger for full absorption and desorption experiments than for the stepwise experiments. During the stepwise absorption and desorption experiments the deviations from isothermal conditions are small. These preliminary results were considered when the experimental part of the work was planned in detail in order to yield thermodynamic and kinetic data describing metal-hydrogen interactions on the material and system levels. Some of these data will be presented later in Chapter 3 of this thesis.

References

[1] Graham T. On the Absorption and Dialytic Separation of Gases by Colloid Septa .1. Action of a Septum of Caoutchouc (Reprinted from the London, Edinburgh, and Dublin Philosophical Magazine and Journal of Science, Vol 32, Pg 401, 1866). Journal of Membrane Science 1995; 100(1): 27-31.

[2] Libowitz G, G, Hayes H, F, Gibb T, R, P. The System Zirconium-Nickel and Hydrogen. Journal of Physical Chemistry 1958; 62(1): 76-79.

[3] Van Mal H, H, Buschow K, H, J, Miedema A, R. Hydrogen Absorption in $LaNi_5$ and Related Compounds - Experimental Observations and Their Explanation. Journal of the Less-Common Metals 1974; 35(1): 65-76.

[4] Vanessen R, H, Buschow K, H, J. Hydrogen Sorption Characteristics of Ce-3d and Y-3d Intermetallic Compounds. Journal of the Less-Common Metals 1980; 70(2): 189-198.

[5] Pebler A, Gulbrans E, A. Equilibrium Studies on Systems $ZrCr_2H_2$ ZrV_2H_2 and $ZrMo_2H_2$ between 0 Degrees and 900 Degrees C. Transactions of the Metallurgical Society of Aime 1967; 239.

[6] Reilly J, J, Wiswall R, H. Formation and Properties of Iron Titanium Hydride. Inorganic Chemistry 1974; 13(1): 218-222.

[7] Reilly J, J, Wiswall R, H. Reaction of Hydrogen with Alloys of Magnesium and Copper. Inorganic Chemistry 1967; 6(12).

[8] Department of Energy (DOE) http://www1.eere.energy.gov/hydrogenandfuelcells/mission.html (07/08-07).

[9] Yartys V, A, Denys R, Mæhlen J, P, Frommen C, Fichtner M, Bulychev B, M, Emerich H. Double-Bridge Bonding of Aluminium and Hydrogen in the Crystal styctyre of γ-AlH_3. Inorganic Chemistry 2007; 46: 1051-1055.

[10] Larminie J, Dicks A. Fuel Cell Systems Explained (2nd Edition). edn. John Wiley & Sons., 2003.

[11] Bogdanovic' B, Bohmhammel K, Christ B, Reiser A, Schlichte K, Vehlen R, Wolf U. Thermodynamic investigation of the magnesium-hydrogen system. Journal of Alloys and Compounds 1999; 282: 84-92.

[12] Johnson J, R, Reilly J, J. Reaction of hydrogen with the low-temperature form (C15) of $TiCr_2$. Inorganic Chemistry ; Vol/Issue: 17:11 1978: Pages: 3103-3108.

[13] Reilly J, J, Wiswall R, H The Higher Hydrides of Vanadium and Niobium. Inorganic Chemistry 1970; 9(7): 1678-1682.

[14] Wiswall R, H, Reilly J, J. Inverse Hydrogen Isotope Effects in Some Metal Hydride Systems. Inorganic Chemistry 1971; 11(7): 1691-1696.

[15] Sandrock G. A panoramic overview of hydrogen storage alloys from a gas reaction point of view. Journal of Alloys and Compounds 1999; 295: 877-888.

[16] Martin M, Gommel C, Borkhart C, Fromm E. Absorption and desorption kinetics of hydrogen storage alloys. Journal of Alloys and Compounds 1996; 238(1-2): 193-201.

[17] Wang X, L, Suda S. Consistent determination of the intrinsic kinetic kinetic properties between hydrogen and hydriding alloys. Journal of Alloys and Compounds 1995; 231: 660-665.

[18] Bérubé V, Radtke G, Dresselhaus M, Chen G. Size effects on the hydrogen storage properties of nanostructured metal hydrides: A review. International Journal of Energy Research 2007; 31(6-7): 637-663.

[19] Cai H, Y, Millet P, Dantzer P. Intermetallic hydrides .1. Investigation of the rate of phase transformation. Journal of Alloys and Compounds 1995; 231(1-2): 427-433.

[20] Wang X, L, Suda S. A Dehydriding Kinetic-Study of $LaNi_{4.7}Al_{0.3}$ Hydride by a Step-Wise Method. Journal of the Less-Common Metals 1990; 159(1-2): 83-90.

[21] Wang X, L, Suda S. Study of the Hydriding Kinetics of $LaNi_{4.7}Al_{0.3}$-H System by a Step-Wise Method. Journal of the Less-Common Metals 1990; 159(1-2): 109-119.

3 INFLUENCE OF INTRINSIC HYDROGENATION/DEHYDROGENATION KINETICS ON THE DYNAMIC BEHAVIOUR OF METAL HYDRIDES: A SEMI EMPIRICAL MODEL AND ITS VERIFICATION

T. Førde[a], J.P. Maehlen[a], V.A. Yartys[a,*], M.V. Lototsky[a] and H. Uchida[b]

a) Institute for Energy Technology, P.O. Box 40, Kjeller, NO-2027, Norway

b) Department of Applied Science, Tokai University, 1117 Kita-Kaname, Hiratsuka-City, Kanagawa 259-1292, JAPAN

Published in International Journal of Hydrogen Energy

3.1 ABSTRACT

Metal hydrides can store hydrogen at low pressures and with high volumetric capacity. For the possible application as storage medium in hydrogen stand-alone power systems, large metal hydride hydrogen storage units are usually required. A reliable and verified kinetic correlation is an important tool in the designing process of a larger storage unit. This paper describes kinetic investigation of an AB_5 type alloy and its corresponding hydride, with the purpose of finding a semi-empirical correlation suitable for use in heat and mass transfer modelling and engineering design of metal hydride storage units.

Keywords: Hydrogen storage materials, gas-solid reactions, metal hydrides, modelling, kinetics

*Corresponding author: Fax: +47 63 81 29 05; E-mail: volodymyr.yartys@ife.no

3.2 INTRODUCTION

Metal hydrides are applied for reversible solid-state hydrogen storage at low pressures and with high volumetric capacity. One possible application for metal hydrides is as storage medium in hydrogen stand-alone power systems. The metal hydride storage system in such energy systems will usually contain several kg of the metal hydride powder.

Due to the relatively low heat conductivity of the hydrogenated and powdered material, heat transfer is in many cases the rate-limiting step in larger storage systems. However, a reliable and verified kinetic expression is an important tool in the designing process of a larger storage unit. For these reasons, the kinetic processes of hydrogen absorption/desorption in metal hydrides have been of considerable and growing interest during the last years.

Several expressions for the absorption and dehydriding reactions in metal hydrides are available in the literature. From an engineering/modelling point of view the expression have

to be a function of one or several of the modelling parameters, including hydrogen pressure, concentration and temperature at a given time. One of the major problems in finding a generally valid correlation is the fact that the rate constant can change with the phase of the metal hydride, due to the fact that the reaction between hydrogen gas and a metal consists of several partial reactions proceeding on the surface and in the bulk material. The role of these partial reactions has been considered earlier, for example, by Bloch and Mintz [1].

Uchida [2] discusses several factors that affect the intrinsic kinetic behavior of metal hydrides. These include modification of the surface properties (1,2) and modifications of the bulk properties (3); 1) The effect of air exposure on the reactivity, pressure dependency and activation energy on a pure $LaNi_5$ sample; 2) The effect of pre-treatment by alkaline solutions on the reaction rate and composition profile; 3) The effect of partial substitution of Ni with Al, Co and Mn on the surface kinetics after air exposure. The paper [2] clearly shows that there are many factors affecting the intrinsic kinetic behavior of metal hydrides, a fact that motivates the need for a simple way of finding an empirical correlation, able to describe the experimental results.

The aim of this study was to describe a method for treating experimental kinetic data obtained in a Sieverts like volumetric set up with the purpose of finding an semi- empirical expression valid for small pressure changes, suitable for use in heat and mass transfer modelling, and for engineering design of metal hydride storage units. The reaction rate should be expressed as a function of parameters which can be calculated at every particular moment in a model.

3.3 THEORETICAL AND EXPERIMENTAL DESCRIPTION

3.3.1 Theoretical background

Johnson, Mehl, and Avrami [3], developed the theory of isothermal transformation in metals and alloys based on a model of nucleation and growth. In this theory, a time dependent relation of the volume fraction of the phase transformed, α , can be written as:

(3.1) $$\alpha = 1 - \exp\left[(Kt)^n\right]$$

Here n is an integer or half integer, which depends on the mechanism and the dimensionality of growth, illustrated in Figure 3.1.

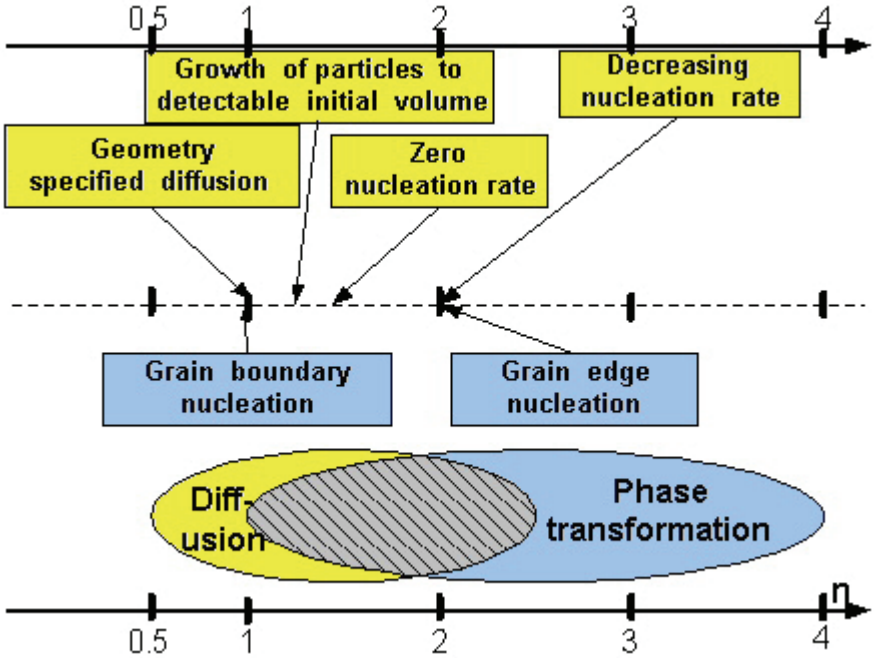

Figure 3.1 Pre-exponential factor n in (3.1), depending on the rate-limiting step. The rates of H_2 absorption/desorption are controlled by diffusion or by phase transformation. Boxes with different background colures, yellow and blue are used to differentiate between the two mechanisms. The reference data are presented in [3].

More details are given in [3]; K is defined as the effective overall reaction rate coefficient, and t is time. The Avrami equation has been used by several authors [4, 5], in the attempt to model and understand the hydrogen-metal gas reactions.

A kinetic investigation limited to finding the value of n, however, does not supply adequate information for precise determination of the rate-limiting step.

Another, alternative approach is the shrinking core model; for a comprehensive review consult Mintz and Zeiri [6]. Using this method, a simple evaluation of the reaction front velocity can be found from the overall rate measurement; however the sample-geometry and size distribution has to be taken into account. Martin et al. [7] used another technique to analyse experimental data; the overall reaction was divided into the partial reactions. The equations for the different partial reactions are fitted to experimental data, the goodness of the fit indicates which of the different processes is the rate limiting one.

A vast variety of empirical expressions exist in the literature suitable for heat and mass transfer analysis; some of these are presented in Table 3.1.

Table 3.1 Kinetic expressions for the formation and decomposition of the metal hydrides available in literature.

Kinetic law	E_a	Comment	Application	Ref
Absorption $LaNi_5$				
$F = 1 - \exp(Kt)$	27 (kJ/mol)	Assumed rate limiting step is phase transformation at $\alpha - \beta$ interface n=1	Used for analysing kinetic data	[8]
$\frac{dF}{dt} = n \cdot K\left[P_g - P_{eq}\right] \cdot \left[1 - F(t)\right] \cdot t^{n-1}$	(-)	n in the range (0.8-1.4), experiments performed in the hydrogen to metal range (1-3), at constant discharge rates.	Used for analysing kinetic data	[9]
$dF/dt = \frac{1}{\frac{1}{K(P - P_{eq}) \cdot 3 \cdot (1-F) \cdot \left[-\ln(1-F)\right]^{2/3}} + \frac{4\pi RD(P - P_{eq})}{(1-F)^{-1/3} - 1}}$	(-)	Model is a combination of nucleation and growth and shrinking core	Used for analysing kinetic data	[10]
$\dot{m} = Ca \cdot \exp\left(-\frac{E_a}{RT}\right) \cdot \ln\left(\frac{P_g}{P_{eq}}\right) \cdot (\rho_{ss} - \rho_s)$	21 (kJ/mol)	-	Used in modelling	[11]
Desorption $LaNi_5$				
$F = 1 - \exp(Kt)$	37 (kJ/mol)	Assumed rate limiting step phase transformation at $\alpha - \beta$ interface n=1	Used for analysing kinetic data	[8]
$dF/dt = K(P_{eq} - P) \cdot (1-F)^2$	(-)	Second order reaction	Used for analysing kinetic data	[10]
$\dot{m} = C_d \cdot \exp\left(-\frac{E_a}{RT}\right) \cdot \frac{P_{eq} - P_g}{P_{eq}} \rho_s$	16 (kJ/mol)	-	Used in modelling	[11]

F is reacted fraction (-), P pressure, Ca rate constant, Ea activation energy, density, m is rate of hydrogen mass absorbed or desorbed, t time and n Johnson-Mehl-Avrami morphological parameter.

Extensive studies performed by investigators of metal hydrides, have led to different conclusions regarding the type of kinetics and controlling mechanisms involved. These discrepancies may be due to variations in the experimental set ups used and introduction of the related errors. Wang and Suda [12] have identified 5 different reasons for experimental errors, which include:

1. Deviation from isothermal conditions.
2. Unbalanced system, i.e. mismatch between system volume and sample mass.
3. Effect of preparation method on surface state of the alloy particles.
4. Size of particles; Suzuki et al. [13] reported a considerable change in desorption rate due to a reduction in median particle size from 18 to 10 μm.
5. Experimental conditions, for example the effect of different evacuation periods on the hydrogenation rate and on the rate-controlling step, as illustrated by Uchida et al. [14].

In addition, the pressure should, if possible, be kept constant to isolate one of the driving forces in the reaction. To avoid the effect of deviation from isothermal conditions, the stepwise experiments have been reported in [9, 15]. In the latter work an Avrami type of expression has been performed and used to analyze the experimental data obtained for a $LaNi_5$ intermetallic compound. We used the conclusions from this theoretical analysis as a basis for proper organization of our experiments.

3.4 EXPERIMENTAL DETAILS

The experimental set up and reactor are shown in Figure 3.2.

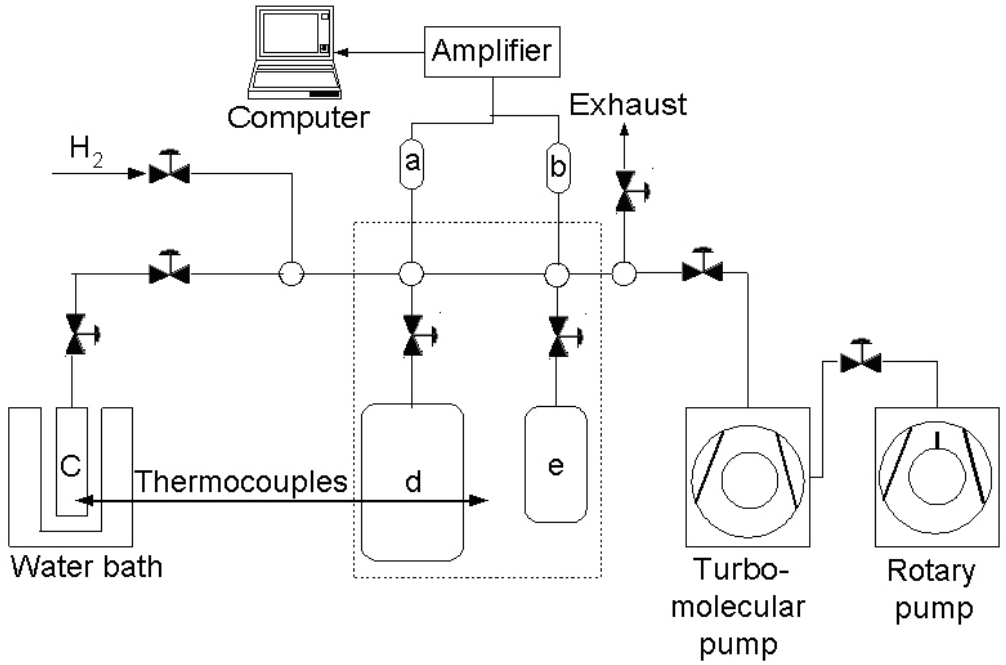

Figure 3.2 Scheme of the experimental Sieverts' type apparatus: a) pressure transducer of 1.0 bar; b) pressure transducer of 25.0 bar; c) sample reaction cell; d) 300cc buffer volume; e) 50cc buffer volume; f) water bath.

A thermocouple is inserted into the sample reactor, the temperature and hydrogen pressure were monitored every 20 milliseconds. The rate of H_2 desorption/absorption was measured volumetrically by monitoring the increase/decrease of H_2 pressure, the experimental facility is described in detail in [16] .

The supplier LABTECH Int. Co. Ltd. Alloys Research and Manufacturing provided a mischmetal-modified AB_5-type alloy as an activated powder; the delivered powder was studied by SEM microscopy. The alloy consists of particles with a non-regular shape varying in size from 2…5 to 50…60 micron, while the major fraction is approximately 15 micron. Some cracks can be observed in the coarse particles. (The EDS data collected in the course of the SEM studies allowed to estimate the component composition of the alloy corresponding to the formula $La_{0.83}Ce_{0.10}Pr_{0.04}Nd_{0.03}Ni_{4.40}Al_{0.60}$.) To minimize the effect of changes in sample temperature during the measurements, a small sample of 0.16 g alloy was mixed with 0.98 g of nickel powder with 99.999% purity; the latter was used as a thermal ballast. The thermal ballast increases the thermal conductivity and heat capacity of the system. Hydrogen absorption by the nickel powder is negligible at hydrogen pressure and temperature

conditions, applied in the present work. The small sample size combined with the relative large system volume ensures collection of reliable data. Before starting the measurements, the sample was heated under vacuum to 523 K for 2 hours, and then cycled several times in hydrogen to reach reproducible hydrogen storage capacity and half time of the reaction. The hydrogen used during the experiments was of 99.9999 purity. Two types of experiments were performed, a complete and a stepwise absorption/desorption. The experimental procedures of the stepwise and complete desorption methods employed in this work are shown in Figure 3.3.

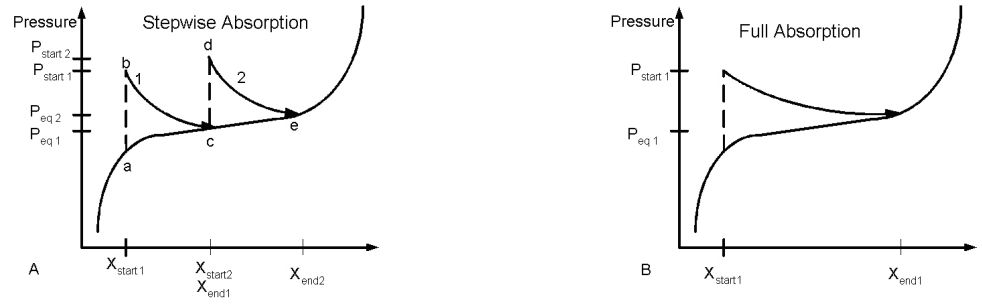

Figure 3.3 Schemes of the two types of experiments, A) stepwise absorption and B) full absorption. The hydrogenation reaction proceeds from P_{start} to $P_{equilibrium}$ or from X_{start} to X_{end} in each run. For the stepwise experiment, the experiments go through the route a-b-c-d-e, the X_{end} concentration becomes the starting point in the next run.

The full absorption and desorption experiments were performed with and without thermal ballast; the stepwise absorption and desorption experiment were performed only with thermal ballast. Full absorption and desorption were performed in the concentration range from 0.6 to 5.5 of hydrogen to metal atomic ratios. During the stepwise and full absorption/desorption experiments the system is shifted from its equilibrium condition and the transition towards a new equilibrium is monitored.

3.4.1 Treatment of the experimental data

Due to the asymptotic behaviour of the experimental data we use (3.2) to fit it. The reaction rate was found by differentiation of the fitted data.

(3.2) $$y(t) = \frac{A_1 t^B + A_2}{t^B + A_3}$$

y can be either pressure or concentration and *t* is time. This equation fulfils the asymptotic behaviour of the measured pressure and calculated concentration as $t \to \infty$ for absorption and desorption. A_1, A_2, A_3, B are fitting parameters ($A_1/A_2/A_3>0$, and $B>1$). This expression suits better for fitting the kinetic data than a polynomial one, due to the absence of oscillations. Figure 3.4 shows an example of how well the smoothing expression fits the experimental data.

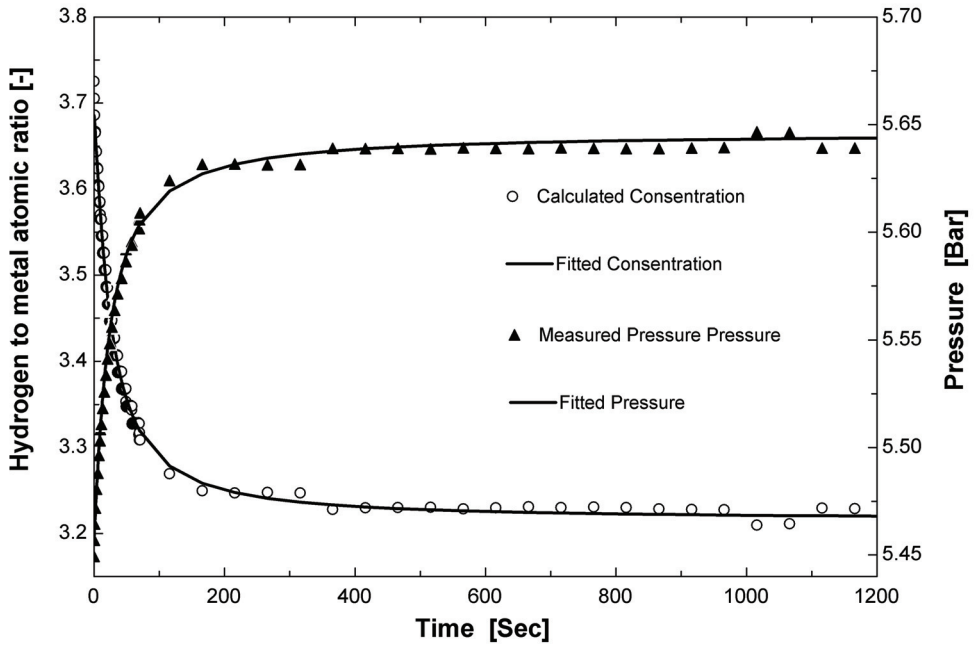

Figure 3.4 Measured pressure and calculated concentration plotted together with fitted data for one desorption experiment.

The equilibrium pressure, used as a parameter in the kinetic expression, is found using linear interpolation between the experimentally measured data points in the pressure-composition-temperature (PCT) diagram.

3.4.2 Derivation of kinetic expression

The dimensionless reacted fraction X is determined for absorption and desorption, from:

(3.3) $$X = \frac{C - C_1}{C_2 - C_1}$$

(3.4) $$X = \frac{C_2 - C}{C_2 - C_1}$$

C is the actual hydrogen concentration, C_1 and C_2 are the concentration limits of the initial and final states of the reaction. Differentiation of a general equation for a gas solid reaction $F(X) = Kt$, where t is time and K is a rate constant, leads to.

(3.5) $$\frac{d}{dX}\left[F(x)\right] \cdot \frac{dx}{dt} = K$$

The function F(X) was approximated by the Avrami-Erofeev equation and is shown (3.6).

(3.6) $$F(x) = \left[-\ln(1-x)\right]^{1/n}$$

Finally, (3.5) can be combined with (3.6) giving (3.7).

$$\frac{\left[-\ln\left(1-x\right)\right]^{\frac{1}{n}-1}}{n\left(1-x\right)}\cdot\frac{dx}{dt}=K \tag{3.7}$$

Strictly speaking, (3.7) was derived as a description of phase transformation processes, which mechanisms involve nucleation and growth of a new phase in a solid. However, as it has been shown in [17, 18], it can adequately describe both phase transformations and diffusion-controlled reactions. The rate constant K can be split into a pressure dependent and temperature dependent terms $K(P)$ and $K(T)$ (3.8).

$$K=K\left(P\right)\cdot K\left(T\right)=K\left(P\right)\cdot K_0\exp\left(-\frac{E_a}{RT}\right) \tag{3.8}$$

$K(T)=K_0\exp\left(-\frac{E_a}{RT}\right)$ is the pressure independent term, E_a is the activation energy, R is a gas constant, K_0 is the pre-exponential factor. Several forms for the pressure dependent term $K(P)$ have been suggested in the literature, dependent on the rate limiting step of the reaction. For diffusion as the rate limiting step, $K(P)$ is related to the square root of P [18]:

$$\begin{aligned} K\left(P\right)&=1-\left(\frac{P_{eq}}{P}\right)^{1/2} \quad \text{absorption}\\ K\left(P\right)&=1-\left(\frac{P}{P_{eq}}\right)^{1/2} \quad \text{desorption}\end{aligned} \tag{3.9}$$

For adsorption as the rate-limiting step Martin et al. [7] argued that physisorption of the H_2 molecules is linearly dependent on the hydrogen pressure. In contrast to that, the following chemisorption step, which includes a dissociation of the H_2 molecules, is related to the difference between the applied gas and equilibrium pressure:

$$\begin{aligned} K\left(P\right)&=\left(P-P_{eq}\right) \quad \text{absorption}\\ K\left(P\right)&=\left(P_{eq}-P\right) \quad \text{desorption}\end{aligned} \tag{3.10}$$

For phase transformation as the rate-limiting step, $K(P)$, is related to the logarithm of the applied and equilibrium gas pressure ratio [19].

$$\begin{aligned} K\left(P\right)&=\ln\left(P/P_{eq}\right) \quad \text{absorption}\\ K\left(P\right)&=\ln\left(P_{eq}/P\right) \quad \text{desorption}\end{aligned} \tag{3.11}$$

Finally, the pressure dependence of the reaction rate can be taken into account using the semi-empirical pressure normalisation method described in [20] and [21]:

(3.12)
$$K(P) = \frac{P - P_{eq}}{P_{eq}} \quad \text{absorption}$$
$$K(P) = \frac{P_{eq} - P}{P_{eq}} \quad \text{desorption}$$

3.5 RESULTS AND DISCUSSION

The data used to derive the constants in the kinetic expression are taken from the pressure-composition-temperature (PCT) diagram and are presented in Figure 3.5 together with the corresponding Van't Hoff plot.

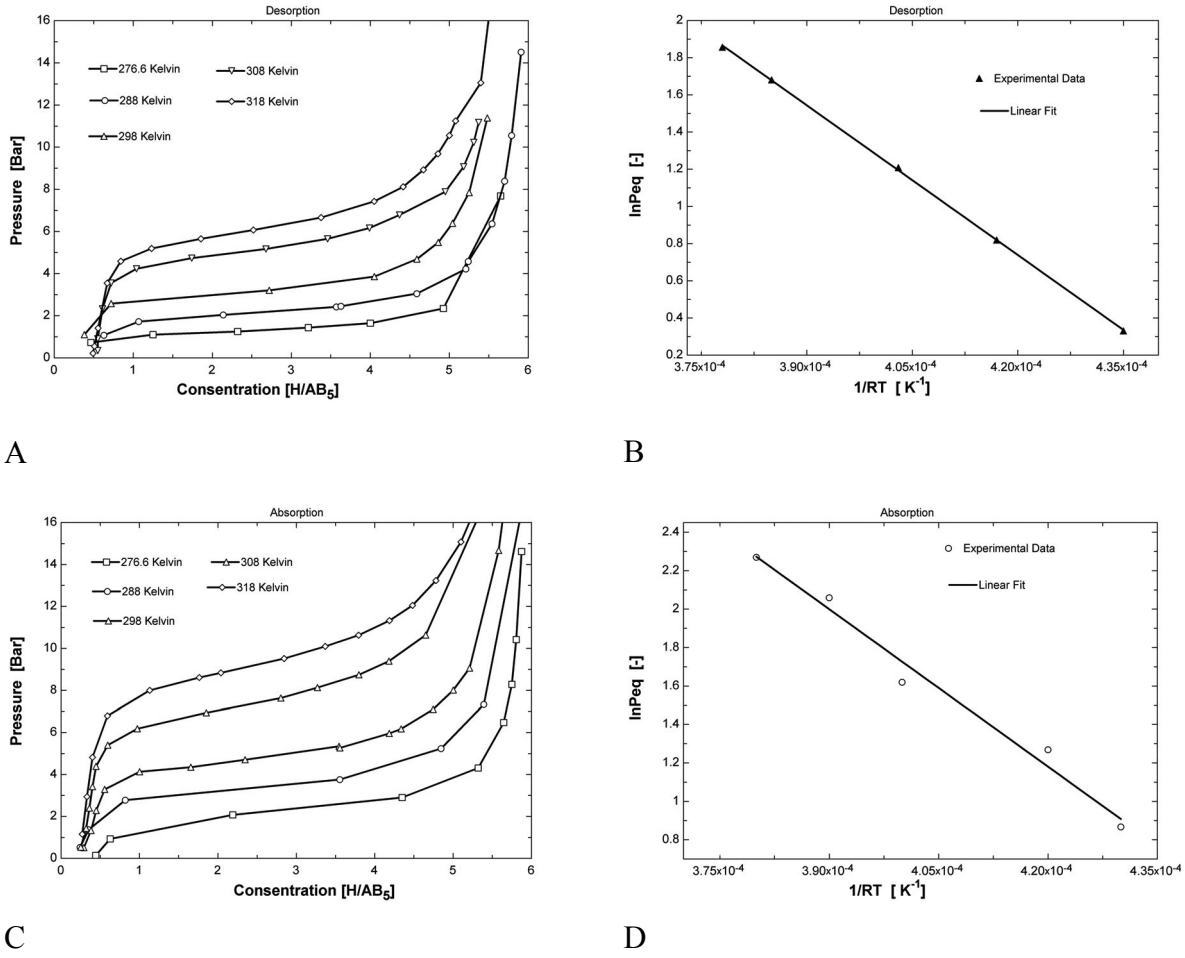

Figure 3.5 Isotherms of hydrogen absorption and desorption at several temperatures, together with corresponding Van't Hoff plot.

From Figure 3.5 the enthalpies of absorption and desorption are calculated to $\Delta H_{absorption} = -27$ kJ/mol H_2 and $\Delta H_{desorption} = 26$ kJ/mol H_2, respectively. For comparison, two different experiments were performed, full desorption and absorption with and without thermal ballast. As expected, the reaction proceeds much faster with thermal ballast, especially the time for 90% completed reaction is markedly reduced. The maximum deviation from isothermal conditions for a stepwise experiment is measured to 0.2 K. The change in

temperature and deviation from isothermal condition are considerably larger for the full absorption experimens than for the stepwise ones, deviating with as much as 2.3 K.

3.5.1 Analysis of experimental data

In order to identify the fitting parameters that will allow (3.7) to fit all the experimental data, two major criteria have to be fulfilled.

Criterium 1: Plotting $K_n = \frac{\left[-\ln(1-x)\right]^{\frac{1}{n}-1}}{n(1-x)}$ versus $K(P)$ for the different pressure dependencies presented in (3.9)-(3.12) and for selected values of n (n=0.5, 1, 1.5, 2, 2.5, 3, 4); the plots should yield a straight line $K_n = A_T \cdot K(P)$ for all the experiments at the same isotherm. Criterium 2: The temperature dependent term $K(T) = K0 \cdot \exp\left(-\frac{E_a}{RT}\right)$ found from step one in the analysis should have Arhenius behaviour. The pressure dependency and *n* value giving Pearson correlation coefficients closest to one for both criteria are selected.

The temperature dependent term is plotted in an Arhenius plot, shown in Figure 3.6 for n=1.5 and n=2, with the pressure dependency presented in (3.11).

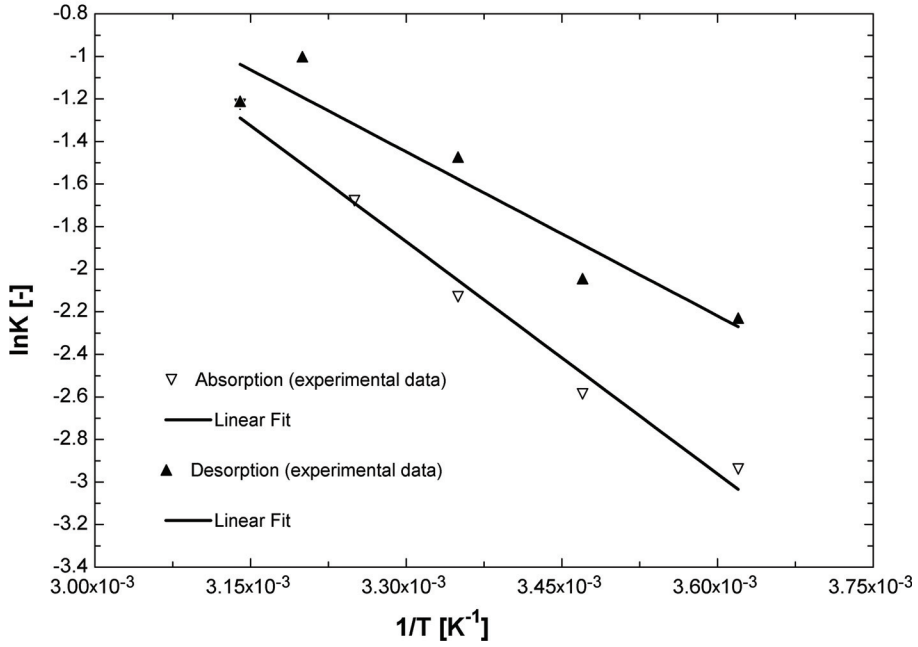

Figure 3.6 Arhenius plots of the pressure independent terms for the stepwise desorption and absorption experiments, with n=1.5 for desorption and 2 for absorption and the pressure dependence [19] taken from Equation 11.

These values for the pre-exponential factor *n* and pressure dependency gives the best Pearson correlation coefficients in the analysis described above.

Full absorption and desorption experiments at (273, 298 and 323 K) without thermal ballast were carried out in addition to the full absorption experiments shown in Figure 3.7.

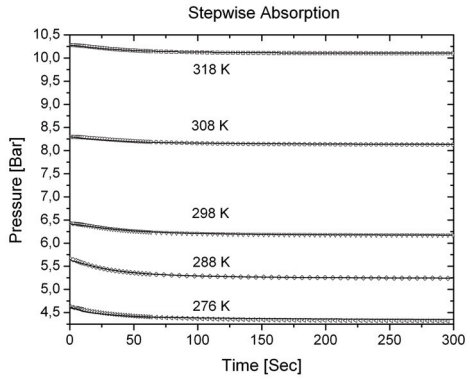

A

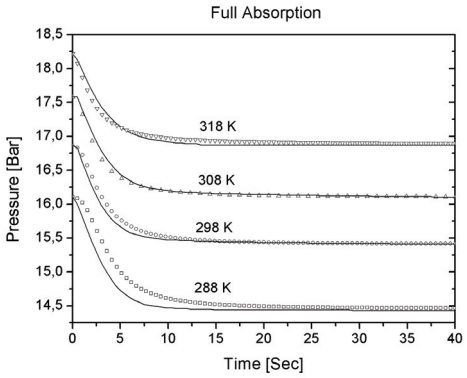

B

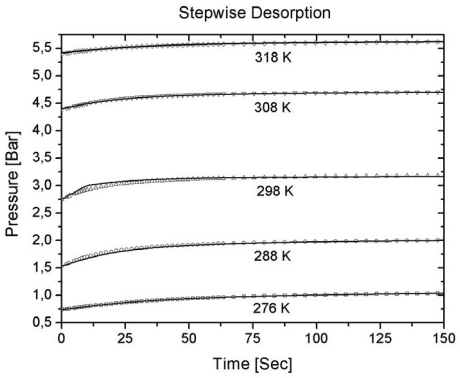

C

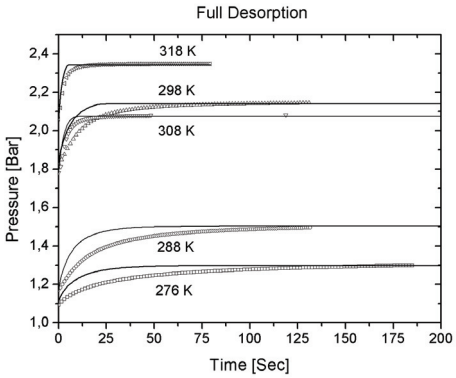

D

Figure 3.7 Calculated (line) and experimental (dots) dependencies for typical absorption and desorption experiments. The stepwise experiments were done within the plateau area. The full absorption and desorption experiments spans from the two regions.

(3.2) was used to smoothen the data for the full absorption and desorption experiments with and without thermal ballast with high accuracy. The results of these experiments are presented in Table 3.2, together with the results from the stepwise measurements.

Table 3.2 Kinetic parameters found from different hydrogen absorption and desorption experiments.

	Desorption	*Absorption*
Stepwise	n=1.5	n=2.0
E_a (kJ/mol)	25±6	26±6
KO (s^{-1})	731±10	798±10
Pressure dependence	$K(P)=\ln\left(P_{eq}/P\right)$	$K(P)=\ln\left(P/P_{eq}\right)$
Full hydrogenation with out thermal ballast	n=2.0	n=4.0
E_a (kJ/mol)	24±2	20.5±8
KO (s^{-1})	271±2.8	254.5±26
Pressure dependence	$K(P)=\ln\left(P_{eq}/P\right)$	$K(P)=1-\left(\frac{P_{eq}}{P}\right)^{1/2}$
Full hydrogenation with thermal ballast	n=1.5	n=1.5
E_a (kJ/mol)	37±4	27±5
KO (s^{-1})	26±4	22±7
Pressure dependence	$K(P)=\ln\left(P_{eq}/P\right)$	$K(P)=\ln\left(P/P_{eq}\right)$

The Pearson correlation coefficient for criteria 1 and 2 are rather high (R^2>0.85) for the experiments with and without thermal ballast. However, the experiments with thermal ballasts had slightly better correlations.

3.5.2 Modelling

To check the validity of the proposed correlations for the absorption and desorption rates, the gas pressure in the reactor is approximated with a zero dimensional model of the experimental reactor and compared with experimental results. The model assumes an isothermal reaction and that the ideal gas law applies. The rate of changes in the dimensionless variable X, defined by (3.3) and (3.4), is modelled by (3.7), $K(P)$ and $K(T)$ are derived from the analysis of the stepwise data. The change in the actual hydrogen to metal concentration $\frac{dC_s}{dt}=\frac{dx}{dt}\cdot(C_1-C_0)$ is found from the derivatives of (3.3) and (3.4). The number of moles of H_2 gas in the reactor is found from the relationship between the change in number of gas molecules per time and the rate of change in hydrogen to metal molecules per time $\frac{d(Mol\_H_2)}{dt}=0.5\cdot Mol\_Metal\cdot\frac{dC_S}{dt}$. Finally, to take into consideration the different temperatures in the experimental set up, the assumptions of uniform gas pressure and conservation of mass were made. Some representative modelling results of the measured and modelled gas pressures at different temperatures for stepwise and full absorption/desorption experiments are shown in Figure 3.7. The simple model describes the stepwise experiments with high accuracy. However, some deviations from isothermal conditions exist in the full desorption and absorption experiments.

3.6 DISCUSSION

The value n, used in (3.6) varies in the narrow range between 1 and 2 for all the experiments. The exception is only for full absorption without thermal ballast, thus, the full absorption and desorption experiments cannot be considered as appropriate experiments due to deviation from isothermal behaviour. Values of n between 1 and 2 are in accordance with values found in the literature and presented in Table 3.1. Both nucleation and growth or diffusion mechanism are indicated as rate limiting steps in Figure 3.1 for n values in this range. The pressure relations found in the analysis of the experimental data are the same, except for the full absorption without thermal ballast. However, the different pressure relations presented in (3.9)-(3.12) are only affecting the analysis of the experimental data to a some extent, with exception for the one given in (3.10), which gives markedly lower correlation coefficients. The difficulties in determining the rate-limiting step based on pressure dependences and n values are clearly illustrated with these results. The activation energies found in the different experiments are consistent with the literature values presented in Table 3.1. However, the values found for absorption and desorption in the stepwise experiments are closer to each other and more reliable then the ones found from the full absorption and desorption experiments. The modelled results presented in Figure 3.7 show that the expression successfully simulates the experimental data in case when the deviation from isothermal conditions is negligible as for the stepwise experiments. A more significant difference between the modelled and measured results was observed in the full absorption and desorption experiments. The reason for this difference could be deviation from isothermal conditions. The expression proposed in present paper is rather simple and the rate-limiting step could change during absorption or desorption. Thus, a more complex model taking into account the changes in rate limiting step as a function of hydrogen concentration (for example, a combination of a shrinking core and Avrami expressions) will be developed in future.

3.7 CONCLUSIONS

A method and an analytic approach allowing an adequate description of the experimental kinetic data, performed in a volumetric experimental set up are proposed and verified. The developed kinetic expression reproduces the experimental data with high accuracy when thermal effects can be negligible and pressure variations are small.

This expression is precise and simple enough to use in a heat and mass transfer analysis and optimisation of the larger scale hydrogen storage units. The experimental procedure and analytic data treatment methodology described in this paper yield activation energies and Avrami pre-exponential factors close to the published in literature.

Acknowledgements

This work received a support from Norsk Hydro ASA, Statkraft and the Norwegian Research Council.

References

1. Bloch, J. and M.H. Mintz, *Kinetics and mechanisms of metal hydrides formation - A review.* Journal of Alloys and Compounds, 1997. **253**: p. 529-541.

2. Uchida, H., *Surface processes of H_2 on rare earth based hydrogen storage alloys with various surface modifications.* International Journal of Hydrogen Energy, 1999. **24**: p. 861-869.

3. Christian, J.W., *The theory of transformations in metals and alloys*. 3rd ed. 2002, Amsterdam: Pergamon.

4. Millet, P. and P. Dantzer, *Impedance of metal hydride electrodes. Rate of phase transformation limited by nucleation and growth mechanisms.* Electrochemistry Communications, 1999. **1**(5): p. 163-166.

5. Rudman, P.S., *Hydriding and Dehydriding Kinetics.* Journal of the Less-Common Metals, 1983. **89**(1): p. 93-110.

6. Mintz, M.H. and Y. Zeiri, *Hydriding Kinetics of Powders.* Journal of Alloys and Compounds, 1995. **216**(2): p. 159-175.

7. Martin, M., et al., *Absorption and desorption kinetics of hydrogen storage alloys.* Journal of Alloys and Compounds, 1996. **238**(1-2): p. 193-201.

8. Koh, J.T., et al., *A Comparison of the Hydriding and Dehydriding Kinetics of $LaNi_5$ Hydride.* Journal of the Less-Common Metals, 1989. **153**(1): p. 89-100.

9. Cai, H.Y., P. Millet, and P. Dantzer, *Intermetallic hydrides .1. Investigation of the rate of phase transformation.* Journal of Alloys and Compounds, 1995. **231**(1-2): p. 427-433.

10. Inomata, A., H. Aoki, and T. Miura, *Measurement and modelling of hydriding and dehydriding kinetics.* Journal of Alloys and Compounds, 1998. **278**(1-2): p. 103-109.

11. Nasrallah, S.B. and A. Jemni, *Heat and mass transfer models in metal-hydrogen reactor.* International Journal of Hydrogen Energy, 1997. **22**(1): p. 67-76.

12. Wang, X.L. and S. Suda, *Consistent determination of the intrinsic kinetic properties between hydrogen and hydriding alloys.* Journal of Alloys and Compounds, 1995. **231**(1-2): p. 660-665.

13. Suzuki, Y., T. Haraki, and H. Uchida, *Effect of $LaNi_5H_6$ hydride particles size on desorption kinetics.* Journal of Alloys and Compounds, 2002. **330**: p. 488-491.

14. Uchida, H., S. Seki, and S. Seta, *Effect of surface contamination on the hydriding behaviors of $LaNi_{4.5}Al_{0.5}$, $LaNi_{2.5}Co_{2.5}$ and $LaNi_{4.5}Mn_{0.5}$.* Journal of Alloys and Compounds, 1995. **231**(1-2): p. 403-410.

15. Wang, X.L. and S. Suda, *A dehydriding kinetic-study of $LaNi_{4.7}Al_{0.3}$ hydride by a step-wise method.* Journal of the Less-Common Metals, 1990. **159**(1-2): p. 83-90.

16. Sato, M., *Studies of hydrogen absorption and desorption processes in advanced intermetallic hydrides*. Unipub. 2005, [Oslo]: Ph.D Thesis from Department of Chemistry Faculty of Mathematics and Natural Sciences University of Oslo : Unipub.

17. Karty, A., J. Grunzweig-Genossar, and P.S. Rudman, *Hydriding and Dehydriding Kinetics of Mg in a Mg-Mg_2Cu Eutectic Alloy - Pressure Sweep Method.* Journal of Applied Physics, 1979. **50**(11): p. 7200-7209.

18. Rudman, P.S., *Hydrogen-Diffusion-Rate-Limited Hydriding and Dehydriding Kinetics.* Journal of Applied Physics, 1979. **50**(11): p. 7195-7199.

19. Bloch, J., *The kinetics of a moving metal hydride layer.* Journal of Alloys and Compounds, 2000. **312**(1-2): p. 135-153.

20. Ron, M., *The normalized pressure dependence method for the evaluation of kinetic rates of metal hydride formation/decomposition.* Journal of Alloys and Compounds, 1999. **283**(1-2): p. 178-191.

21. Skripnyuk, V.M. and M. Ron, *Hydrogen desorption kinetics in intermetallic compounds C2, $C5_1$ and $C5_2$ with Laves phase structure.* International Journal of Hydrogen Energy, 2003. **28**(3): p. 303-309.

Part 2: Modelling and Experimental Work with Storage Units

4 METAL HYDRIDE STORAGE UNITS: BACKGROUND, THEORY AND EXPERIMENTAL SET UP

Nomenclature

A	Molar mass fraction between initial alloy and hydrogen gas	[-]
$A_{\beta\sigma}$	Area of the $\beta-\sigma$ interface	[m^2]
$A_{\beta e}$	Area of the entrances and exits of the β-phase	[m^2]
a_p	Solid/gas heat transfer surface	[m^2/m^3]
C	Hydrogen-to-metal atomic ratio	[-]
C_s	Stefan Boltzmann constant (=5.76)	[$W/m^2 \cdot K^4$]
c_p	Specific heat capacity	[J/kg·K]
d_p	Particle diameter	[m]
F	Body force per unit volume	[N/m^3]
Gr	Grashof number	[-]
h	Heat transfer coefficient	[$W/m^2 \cdot K$]
ΔH	Heat of reaction	[J/mol]
k	Thermal conductivity	[W/m·K]
K_D	Permeability	[m^2]
Kn	Knudsen number	[-]
M	Molar mass	[g/mol]
Nu	Nusselt number	[-]
P	Pressure	[bar] or [Pa]
P^β	Total pressure in the β-phase	[Pa]
Pe	Peclet number	[-]
Pr	Prandtl number	[-]
$\dot{Q}$	Heat duty	[W]
$\dot{q}$	Heat source or sink	[W/m^3]
R	Universal gas constant (=8.314)	[J/mol·K]
r_p	Particle radius	[m]
r	Radius	[m]
Re	Reynolds number	[-]
s	Distance between plates	[m]
S_p	Percentage swelling of alloy	[%]
T	Temperature	[K]
t	Time	[s]
UA	Heat duty per unit driving force	[W/K]
X	Dimensionless concentration	[-]
V	Volume	[m^3]
v	Superficial volume averaged velocity	[m/s]
v^β	Gas velocity	[m/s]
$\tilde{v}_g$	Gas volume	[m^3]
Z	Viscous work term	[$1/s^2$]
μ	Dynamic viscosity	[kg/m·s]
Λ	Molecular mean free path	[m]
ε	Porosity	[-]

∂	Particle roughness	[m]
γ	Accommodation coefficient	[-]
ϕ	Surface coverage	[-]
θ	Angle	radians
ρ	Density	[kg/m^3]
ρ^{β}	Density in the β-phase	[kg/m^3]
$\dot{\Pi}$	H_2 reaction rate (absorption>0>desorption)	[mol/s·m^3] or [kg/s·m^3]
β-phase	The gas phase	[-]
σ	Solid phase	[-]
ζ	Expansion coefficient	[1/K]
ϑ	Ratio of average channelling length to particle diameter	[-]
ψ	Shape factor	[-]

Subscript	
abs	Absorption
Cond	Conduction
des	Desorption
f	Fluid
eff	Effective
eq	Equilibrium
g	Gas
initial	Initial
H	Hydrogen
max	Maximum
MH	Metal hydride
p	Particle
r	Radial
Rad	Radiation
reac	Reaction
sb	Solid to bulk
shell	The shell of the metal hydride reactor
s	Solid
w	Water
ws	Wall to solid
wp	Wall to particle
θ	Angular

4.1 INTRODUCTION

Hydrogen storage in the metal hydrides (MH) makes it possible to create very compact, safe and technologically flexible hydrogen storage units, which are promising in a number of applications.

Several companies all over the world e.g. USA, Japan, Europe, China, are engaged in hydrogen storage in MH. A brief summary concerning companies and institutions engaged in the application of MH is presented in Table 4.1.

Table 4.1 Companies and institutions engaged in metal hydride applications

Company / institution (country)	Main activities	Ref.
Ergenics, Inc. (USA)	Hydride Alloys MH-Heat Pumps MH-Heat Storage	[1]
Hydrogen Components, Inc. (USA)	MH-H storage units MH-H-compressors	[2]
ECD Ovonics (USA)	Ni-MH batteries MH alloys and H storage systems	[3]
The Japan Steel Works, Ltd. (Japan)	Hydride alloys MH-H storage units Ni-MH batteries Hydrogen fuel cells MH-Heat storage, conversion and transportation MH-Actuators	[4]
Japan Metals & Chemicals Co., Ltd. (Japan)	Hydride alloys MH-H storage units MH-heat pumps	[5]
HERA Hydrogen Storage Systems, GmbH (Canada – Germany)	MH-H storage units Hydride Alloys	[6]
LABTECH Int. Co. Ltd. (Bulgaria)	MH-H storage units Hydride Alloys	[7]
Institute of Mechanical Engineering Problems (Ukraine)	MH-H storage units MH-H compressors MH-based evacuation/gas supply systems for vacuum-plasma technologies	[8]

Mainly, commercial MH storage units are intended for laboratory applications providing safe and compact storage of high-purity hydrogen (capacity ranging from 30–40 Nl to a few Nm^3, with 1–10 bar supply pressure).

Development of a metal hydride hydrogen storage unit involves the solution of two main problems. The first includes the appropriate selection of hydrogen storage material, starting from the consumer's specification: required hydrogen storage capacity, pressure/temperature ratings, and other operating conditions (H_2 purity, required cycle lifetime, etc.). The second problem concerns the appropriate design of the metal hydride container. This solution is connected, in turn, to the solution of a number of engineering problems. One of them is to increase the total volume and weight efficiencies of the H storage unit. The containers are conventionally made of stainless steel, as the material is stable in hydrogen atmosphere in a wide pressure/temperature range. Some applications use aluminium, allowing increased mass storage efficiency. Recent applications using, composite high-pressure hydrogen storage cylinders (thin-wall aluminium liner wrapped by a carbon-fibre-reinforced plastic) are of

special interest [9]. Usage of aluminium as a main design material of a MH container seems promising, since it has lower density and higher thermal conductivity than stainless steel conventionally used. However, the main problems with aluminium are the limitation of the maximum allowed temperature, due to aging effects, and hydrogen corrosion of aluminium.

Developing mathematical models describing the heat and mass in metal hydride reactors will improve the understanding of the behaviour of metal hydride storage units, through for example parametric testing. Such models are developed and experimentally verified in the present work. It is not feasible to base the verification of a model entirely on literature data; therefore several metal hydride storage units were built and experimentally tested. The work carried out related to designing and testing of the various units provided valuable hands-on experience with several practical issues, like leak testing, filling and emptying, measurements and finally on the design of metal hydride storage units. This practical work also provided the possibility to compare the performance of metal hydride storage units having different geometries and heat management. The tested units were filled with the same metal hydride alloy. The charging and discharging times of the different units were compared as functions of hydrogen gas pressure and cooling/heating water temperatures.

Experimental investigation of MH containers have been presented in the open literature as listed in Table 4.2

Table 4.2 overview and details of published metal hydride reactors.

Ref.	Material	Amount of alloy [kg]	H_2 capasity/ dimensions	Container Material	Results	Application
[10]	$MmNi_{4.64}Al_{036}$	94.6	10 Nm^3 L=900 mm o.d=254 mm	Stainless steel	Verified heat and mass transfer model	-
[11]	$Lm_{1.06}Ni_{4.96}Al_{0.04}$ Lm=La55%,Ce2.5% Pr7.7%, ND34.1%		316 Nl L=1500 mm D=87.5 mm	Stainless Steel	Experimental results and heat transfer properties	Fuel cell 500 W
[12]	$Ti0_{.42}Zr_{0.58}Cr_{0.78}$ $Fe0_{.57}Ni0_{.2}Ni_{0.2}$ $Mn_{0.39}Cu_{0.03}$	11.3	Height=105 mm Length=210 mm Width=326 mm	Aluminium	Verified heat and mass transfer model	-
[9]	Potential material Wt% > 3	5	250 Nl	Aluminium carbon fibres	High weight % potential (combination high pressure and hydride powder)	Transport (Paper study)

The most typical layout involves a cylindrical container, 40-60 mm in diameter for smaller hydrogen storage capacities (up to 500 Nl H_2), and 100-250 mm diameter for larger capacities (up to 10 Nm^3). The upper size limit of a single large-scale MH container is restricted by heat transfer limitations slowing down the recharge dynamics. The container can be provided with heat transfer elements, including internal heat exchangers, and/or a porous metal matrix containing MH powder in the void space in order to improve the heat transfer performance.

The aim of this part of the thesis is to improve the understanding of the behaviour of metal hydride storage units through experiments and simulations of different metal hydride storage units.

4.2 THEORETICAL BACKGROUND

To fully understand the heat and mass transfer in the metal hydride reactor it is necessary to formulate the governing equations for the conservation of mass, momentum and heat. These equations are described in detailed in the following paragraphs.

4.2.1 Momentum equation

The Navier-Stokes equation

Motion of fluid must comply with several fundamental laws of nature. In particular, at each point in the fluid, conservation of mass and species as well as Newton's second law of motion must be satisfied. For a differential control volume in a fluid, Newtons 2nd law state that the sum of all forces acting on the control volume must equal the net rate at which momentum leaves the control volume (outflow-inflow). Two kinds of forces may act on the fluid, body forces, which are proportional to the volume, and surface forces, which are proportional to the area.

The Navier-Stokes equation describing flow in a 2-dimensional cylindrical geometry for an incompressible fluid with constant fluid properties flowing through a porous medium is given by Equation (4.1) [13].

$$\rho^{\beta}\left(\frac{\partial v_r^{\beta}}{\partial t}+v_r\frac{\partial v_r^{\beta}}{\partial r}+\frac{v_\theta^{\beta}}{r}\frac{\partial v_r^{\beta}}{\partial \theta}-\frac{\left(v_\theta^{\beta}\right)^2}{r}\right)=$$
$$-\frac{\partial P^{\beta}}{\partial r}+\mu\left[\frac{1}{r}\frac{\partial}{\partial r}\left(r\frac{\partial v_r^{\beta}}{\partial r}\right)-\frac{v_r^{\beta}}{r^2}+\frac{1}{r^2}\frac{\partial^2 v_r^{\beta}}{\partial \theta^2}-\frac{2}{r^2}\frac{\partial^2 v_r^{\beta}}{\partial \theta^2}-\frac{2}{r^2}\frac{\partial v_\theta^{\beta}}{\partial \theta}\right]+F_r \qquad (4.1)$$
$$\rho^{\beta}\left(\frac{\partial v_\theta^{\beta}}{\partial t}+v_r^{\beta}\frac{\partial v_\theta^{\beta}}{\partial r}+\frac{v_\theta^{\beta}}{r}\frac{\partial v_\theta^{\beta}}{\partial \theta}+\frac{v_r^{\beta}v_\theta^{\beta}}{r}\right)=$$
$$-\frac{1}{r}\frac{\partial P^{\beta}}{\partial \theta}+\mu\left[\frac{1}{r}\frac{\partial}{\partial r}\left(r\frac{\partial v_\theta^{\beta}}{\partial r}\right)-\frac{v_\theta^{\beta}}{r^2}+\frac{1}{r^2}\frac{\partial^2 v_\theta^{\beta}}{\partial \theta^2}+\frac{2}{r^2}\frac{\partial v_r^{\beta}}{\partial \theta}\right]+F_\theta$$

The first equation is the conservation of momentum in the radial direction, and the second represents momentum conservation in the θ-direction. The left hand side of Equation (4.1) expresses the inertial force, which is the product of the mass and acceleration of the fluid element. The two first terms on the right hand side are surface forces. Surface forces are forces caused by the pressure gradient within the fluid (the first term on the right side) and friction forces caused by the fluid's viscosity and velocity gradients within the fluid. The last term on the right side is body forces that act directly on the fluids' mass. Gravitational, centrifugal, magnetic and/or electric fields may contribute to the body force.

The Navier-Stokes equation (Equation (4.1)) describes the flow in the gas phase of the porous medium. Additionally, the requirements given by Equations (4.2)-(4.4) must be fulfilled.

$$\frac{1}{r}\frac{\partial\left(\rho r v_r^{\beta}\right)}{\partial r}+\frac{1}{r}\frac{\partial\left(\rho v_\theta^{\beta}\right)}{\partial \theta}=0 \qquad \textit{Continuity (no absorption / desorption)} \qquad (4.2)$$

(4.3) $$v^{\beta} = 0 \qquad at\ A_{\beta\sigma} \qquad No\ slip\ condition$$

(4.4) $$v^{\beta} = f\left(r,\theta,t\right) \qquad at\ A_{\beta e} \qquad Inlet/outlet\ conditions$$

The Stokes equation

In the case of small particle Reynolds numbers, i.e. $\mathrm{Re}_p = \frac{\rho \cdot v \cdot d_p}{\mu \cdot \varepsilon} << 1$, also known as creeping flow or Stokes flow, the fluid inertia force is smaller than the viscous force and can be neglected. Equation (4.1) simplifies into Equation (4.5), known as the Stokes equation. The cases presented in Chapter 5 and Chapter 6 all have $\mathrm{Re_p} << 1$.

(4.5)

$$0 = -\frac{\partial P^{\beta}}{\partial r} + \mu\left[\frac{1}{r}\frac{\partial}{\partial r}\left(r\frac{\partial v_r^{\beta}}{\partial r}\right) - \frac{v_r^{\beta}}{r^2} + \frac{1}{r^2}\frac{\partial^2 v_r^{\beta}}{\partial\theta^2} - \frac{2}{r^2}\frac{\partial^2 v_r^{\beta}}{\partial\theta^2} - \frac{2}{r^2}\frac{\partial v_{\theta}^{\beta}}{\partial\theta}\right] + F_r \qquad In\ the\ \beta\ phase$$

$$0 = -\frac{1}{r}\frac{\partial P^{\beta}}{\partial\theta} + \mu\left[\frac{1}{r}\frac{\partial}{\partial r}\left(r\frac{\partial v_{\theta}^{\beta}}{\partial r}\right) - \frac{v_{\theta}^{\beta}}{r^2} + \frac{1}{r^2}\frac{\partial^2 v_{\theta}^{\beta}}{\partial\theta^2} + \frac{2}{r^2}\frac{\partial v_r^{\beta}}{\partial\theta}\right] + F_{\theta} \qquad In\ the\ \beta\ phase$$

The boundary conditions are given by Equation (4.2) – (4.4)

The Stokes equation with its appropriate boundary conditions describes the velocity field in the porous medium void space.

The Darcy equation

In 1856, Henry Darcy investigated the flow of water in vertical homogeneous sand filters in connection with the fountains of the city of Dijon (France) [14]. The one-dimensional evidence of the famous Darcy formula shown in Equation (4.6) was formulated based on these observations [15].

If the method of volume averaging is applied to Equation (4.5), the Darcy equation and the volume averaged continuity equation shown in Equation (4.6) can be derived. The method of volume averaging is a technique that can be used to rigorously derive continuum equations for multiphase systems [16]. This means that equations which are valid within a particular phase can be spatially smoothed to produce equations that are valid everywhere.

(4.6)

$$v_r = -\frac{K_{D,r}}{\mu}\frac{\partial P}{\partial r}$$

$$v_{\theta} = -\frac{K_{D,\theta}}{\mu}\frac{1}{r}\frac{\partial P}{\partial\theta}$$

$$\frac{1}{r}\frac{\partial\left(rv_r\right)}{\partial r} + \frac{1}{r}\frac{\partial v_{\theta}}{\partial\theta} = 0 \qquad Continuity\ (no\ absorption/desorption)$$

In Equation (4.6) body forces such as gravimetric forces and buoyancy forces caused by thermal gradients within the bed are neglected. This is a reasonable assumption since

hydrogen gas has low density at ambient temperatures and low pressures, i.e. small amount of hydrogen mass, and the low permeability of the porous bed resulting in negligible velocities caused by density gradients.

This equation (Equation (4.6) forms the basis for the analysis of a wide range of physical phenomena which often requires extensions to include effects of inertia, compressibility and coupling with heat and mass transfer.

The change of scale that can be accomplished by the method of volume averaging is illustrated in Figure 4.1 and is thoroughly discussed by Whitaker in [16].

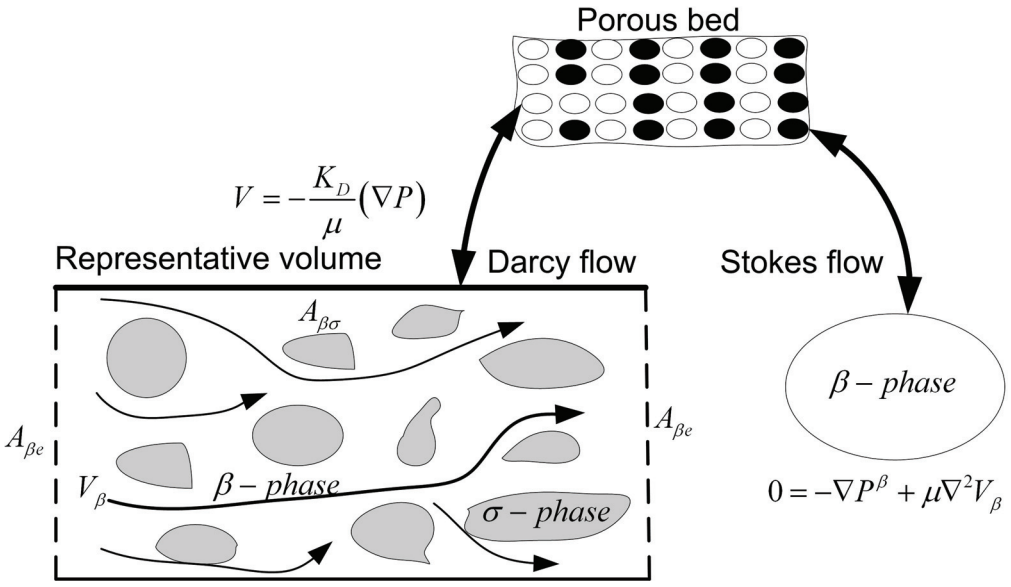

Figure 4.1 Change of scale

In Figure 4.1 it is indicated that the Stokes equation is valid in the $\beta - phase$ (the gas phase) that occupies the pores, and that the Darcy equation is valid everywhere in the porous medium. To obtain Equation (4.6) from Equation (4.5), one must first form the local volume average of Stokes equation. This leads to an averaged equation that contains spatial deviations of the pressure and velocity for which one must develop a closure relation. In the case of Darcy's law, the closure problem controls the form of the macroscopic equation and it provides a mean of predicting the permeability tensor K_D.

4.2.2 Energy conservation

First law of thermodynamics

The first law of thermodynamics, shown in Equation (4.7), is a relation that brings together three concepts in thermodynamics: Work transfer, heat transfer and energy.

$$E_2 - E_1 = \int_1^2 d\dot{Q} - \int_1^2 dW \tag{4.7}$$

It can be stated as: The change of energy in a control volume must be equal to the amount of energy transferred across the control volume boundaries. The system's energy is comprised of

its internal, kinetic and potential energy. The change in kinetic energy is neglected here due to the low density and small velocity gradients of the hydrogen gas for the system considered. The change in potential energy is also neglected, due to the low gas density and small vertical elevation difference inside the metal hydride storage unit. The maximum change in system mass is ca. 1.5% of the total system mass during a charging or discharging experiment. The change in the hydrogen gas internal energy is equal to the change in temperature multiplied by the gas heat capacity [17] if hydrogen is assumed to be an ideal gas. The assumption of ideal gas behaviour is reasonable since the metal hydride reactors considered operate at pressures and temperature ranges 1-15 bar and 273-323 K.

Heat can be transferred into or out of the system by convection, conduction and radiation. Due to the low system temperature (below 323 K) and small particles (grain size <10 mm) heat transfer by radiation is small compared to conduction and convection and may therefore be neglected [18].

Energy may also be transferred to and from the system/control volume by work interaction involving body and surface forces. The work done by the body forces is neglected in the analysis performed in this thesis, since the only working body force is gravity and buoyancy forces.

The Energy equation

The governing equation describing the temperature field is the energy equation, shown in Equation (4.8), which describes the conservation of energy for an incompressible fluid [19].

$$\rho \cdot c_p \left(\frac{\partial T}{\partial t} + v_r \cdot \frac{\partial T}{\partial r} + v_\theta \cdot \frac{\partial T}{\partial \theta} \right) = \frac{1}{r} \frac{\partial}{\partial r} \cdot \left(k_g \cdot r \cdot \frac{\partial T}{\partial r} \right) + \frac{1}{r} \frac{\partial}{\partial \theta} \cdot \left(k \cdot \frac{1}{r} \cdot \frac{\partial T}{\partial \theta} \right) + \mu \cdot \phi + \dot{q} \tag{4.8}$$

The first term on the left hand side is the rate of gain of energy per unit volume. The second and third terms on the left side are the rate of energy input per unit volume due to advection. The first and second terms on the right side are the rate of energy input per unit volume due to conduction. The third term on the right side is the rate of work done on fluid per unit volume by viscous forces (also shown in Equation (4.9)), and the last term on the right side is the rate of heat generation per unit volume.

$$\mu \cdot \phi = 2 \cdot \mu \cdot \left\{ \left(\frac{\partial v_r}{\partial r} \right)^2 + \left[\frac{1}{r} \left(\frac{v_\theta}{\partial \theta} + v_r \right) \right]^2 + \left[\frac{1}{r} \frac{\partial v_r}{\partial \theta} + r \frac{\partial}{\partial r} \left(\frac{v_\theta}{r} \right) \right] \right\}^2 \tag{4.9}$$

Simulations presented in Chapters 5 and 6 in this thesis indicate that both the gas velocity and the velocity gradients will be small inside the reactor. Hence the work done by viscous forces is small and is therefore neglected in this thesis.

Separate phase energy equations

Since there is significant heat generation occurring in the solid phase, a temperature difference between the solid and gas phase may result. It is assumed that each phase is continuous and represented with appropriate effective thermal conductivities. Energy can be exchanged between the two phases by convective heat and mass transfer.

Equation (4.10) describes energy conservation for the gas phase and Equation (4.11) is the corresponding solid phase energy equation.

$$\varepsilon \cdot \left(\rho \cdot c_p\right)_g \cdot \left(\frac{\partial T_g}{\partial t} + v_r \cdot \frac{\partial T_g}{\partial r} + v_\theta \cdot \frac{\partial T_g}{\partial \theta}\right) = \frac{1}{r}\frac{\partial}{\partial r} \cdot \left(k_g \cdot r \cdot \frac{\partial T_g}{\partial r}\right) + \frac{1}{r}\frac{\partial}{\partial \theta} \cdot \left(k_g \cdot \frac{1}{r} \cdot \frac{\partial T_g}{\partial \theta}\right) - h_{sf} \cdot a_p \left(T_g - T_{MH}\right) \tag{4.10}$$

$$\left(1-\varepsilon\right) \cdot \left(\rho \cdot c_p \frac{\partial T}{\partial t}\right)_{MH} = \frac{1}{r}\frac{\partial}{\partial r} \cdot \left(k_{eff,MH} \cdot r \cdot \frac{\partial T_{MH}}{\partial r}\right) + \frac{1}{r}\frac{\partial}{\partial \theta} \cdot \left(k_{eff,MH} \cdot \frac{1}{r} \cdot \frac{\partial T_{MH}}{\partial \theta}\right) + \dot{q} + h_{sf} \cdot a_p \left(T_g - T_{MH}\right) \tag{4.11}$$

The solid phase energy conservation equation could be even more complex if thermal gradients inside the particles were taken into account. However, the analyses in this thesis assume the particles to have uniform temperature.

One phase energy equation

The magnitude of the last term in Equations (4.10) and (4.11) determines whether thermal equilibrium is a valid assumption. The temperature difference between the solid and gas phases can be roughly estimated from $\left|\Delta T_{g-MH}\right| = \frac{\dot{\Pi} \cdot \Delta H}{h_{sf} \cdot a_p}$. If the heat exchange between the two phases is poor separate equations for each phase is necessary in order to determine the temperature distribution. The magnitude of the gas/solid heat transfer coefficient h_{sf} is difficult to measure, as h_{sf} for a heated single particle in an otherwise uniform temperature field is expected to be significantly different than that for particles in packed beds [19]. Some correlations for gas/solid heat transfer coefficients are given by Equation (4.19)-(4.22). All correlation except the Kunii correlation approaches the conduction limit Nu=2 as Re_p approaches 0. This limit represents heat transfer by conduction from a sphere to a surrounding stagnant fluid.

The thermal mass of hydrogen in a control volume is small compared to the thermal mass of metal hydride due to the low hydrogen density. This means that only a small amount of energy is needed to change the hydrogen temperature in each control volume.

The assumption of thermal equilibrium between the two phases is valid for situations where the temperature difference between the two phases is small, and for this situation Equations (4.10) and (4.11) simplifies into Equation (4.12).

$$\rho \cdot c_p \cdot \left(\frac{\partial T}{\partial t} + v_r \cdot \frac{\partial T}{\partial r} + v_\theta \cdot \frac{\partial T}{\partial \theta}\right) = \frac{1}{r}\frac{\partial}{\partial r} \cdot \left(k_{eff} \cdot r \cdot \frac{\partial T}{\partial r}\right) + \frac{1}{r}\frac{\partial}{\partial \theta} \cdot \left(k_{eff} \cdot \frac{1}{r} \cdot \frac{\partial T}{\partial \theta}\right) + \dot{q} \tag{4.12}$$

Here, T is the volume averaged temperature for both phases and the term $\left(\rho \cdot c_p\right)$ is calculated from Equation (4.13).

$$\rho \cdot c_p = \varepsilon \left(\rho_g \cdot c_{p,g}\right) + \left(1-\varepsilon\right) \cdot \left(\rho_{MH} \cdot c_{p,MH}\right) \tag{4.13}$$

Zero dimensional energy equation

Equation (4.12) can be simplified even further into Equation (4.14) if thermal gradients in the porous bed are small. This can occur if heat is distributed very effectively inside the reactor with e.g. an internal heat exchanger.

(4.14) $$\rho \cdot c_p \cdot V = m \cdot c_p \cdot \frac{\partial T}{\partial t} = \dot{q} + \dot{Q}_W + \dot{Q}_{H_2} + \dot{Q}_{shell}$$

The left hand side of Equation (4.14) represents the change in thermal energy in the metal hydride bed and on the right hand side are the energy fluxes due to the hydrogen gas/solid chemical reaction, heat added from external sources (Q_w), the heat of the hydrogen flow into the reactor (Q_{H2})and heat exchanged with the reactor shell (Q_{shell}). The temperature of the reactor shell can be calculated from an energy balance equation such as Equation (4.15).

(4.15) $$m_{shell} \cdot c_{P,shell} \frac{\partial T_{shell}}{\partial t} = \dot{Q}_{shell} + \dot{Q}_{surrounding}$$

The reactor shell can not be assumed to have the same temperature as the reactor bed due to its high thermal mass and poor heat transfer between the reactor bed and shell.

Gas and solid mass balance

The hydrogen gas mass balance is calculated from Equation (4.16)

(4.16) $$\varepsilon \cdot \frac{\partial \rho_g}{\partial t} + v_r \cdot \frac{\partial \rho_g}{\partial r} + v_\theta \cdot \frac{\partial \rho_g}{\partial \theta} = -\dot{\Pi}$$

The solid mass balance is calculated from Equation (4.17).

(4.17) $$\frac{\partial C}{\partial t} = \dot{C}$$

4.3 HEAT TRANSFER PARAMETERS

A mathematical model depends on reliable input parameters, since any errors in the model input parameters may propagate and produce inaccurate results. The parameters used in the mathematical model described above are discussed in the following.

4.3.1 Heat transfer, thermal conductivity, particle and size distribution

The metal hydride material properties such as kinetics and Pressure Concentration Temperature (PCT) relations are discussed in Chapter 1-2 of this thesis; specific properties were also experimentally verified. The different models of heat transfer in a porous stagnant bed were discussed by Kunni and Yagi [20], and are listed below.

1. Heat transfer through solid by heat conduction.
2. Heat conduction through the contact surfaces of the solid particles.
3. Radiation heat transfer between surfaces.
4. Heat transfer by conduction through fluid film near the contact surface.
5. Heat transfer by convection (solid/gas/ solid).

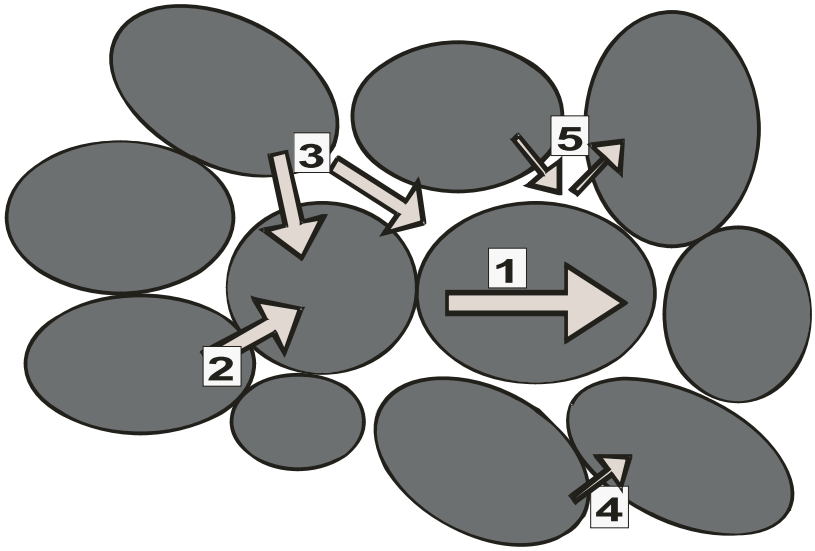

Figure 4.2 heat transfer paths in a porous bed.

The effective thermal conductivity of a porous bed is made up of a combination of the above listed mechanisms.

In addition to the material structure and composition, the effective thermal conductivity of the porous bed is influenced by the interaction between the different heat transfer mechanisms. For values of $(Gr \cdot Pr)<100$ the convective heat transfer in pores can be neglected [18] **,** and at temperatures above ca 473 K, thermal radiation may contributes to the granular material effective thermal conductivity [18].

Measurement of the thermal conductivity requires good control of the heat fluxes and temperature gradients in the experimental set up. The experimental methods can be divided into steady state and transient methods. The transient methods can in general be used to measure on smaller samples than the steady state methods. The steady state methods require no information of other material properties, whereas the transient methods require knowledge of the sample specific heat capacity and density. The majority of the published data on thermal conductivity for metal hydrides are based upon measurement on bulk powder samples, and not solid alloys. From these experiments it is only possible to extract the effective thermal conductivity, and some selected published data are presented in Table 4.3.

Table 4.3 Measured effective thermal conductivity

Ref.	Material	Temperature [K]	Pressure [bar]	Gas	Effective thermal conductivity [W/(m·K)]	Measurement technique
[21,22]	$Mg\text{-}MgH_2$	523-653	1-5	H_2	2-8	Transient
[23]	$LaNi_{4.7}Al_{0.3}H_x$	133-193	10^{-6}-60	H_2, He, N_2, Ar	0-1	Transient
[24-26]	$TiMm_{1.5}$		0.2-50		0.25-1	Steady state

The only way to extract the thermal conductivity of the solid metal hydride alloy from effective thermal conductivity measurements is to calculate backwards based on data and correlations for the effective thermal conductivity. Some of the correlations take into

consideration the shape of the solid particles, the orientation and distribution of the particles and the contact resistance between the particles.

The effective thermal conductivity of the metal hydride bed varies with pressure, temperature and the gas used in the fluid phase. However, as shown by Hahne and Kallweit [23] the largest change in effective thermal conductivity occurs in the pressure range from zero to one bar, independently of the type of gas and number of times the sample has been cycled. This large change in effective thermal conductivity at lower pressure is caused by the Knudsen effect, i.e. at Knudsen numbers (defined as the ratio of the average pore diameter to the mean free path of the gas molecules) smaller than unity the flow may be treated as a homogenous continuum [27]. The gas conductivity will decrease when the Knudsen numbers becomes large [19] which again will decrease the effective thermal conductivity. The gas mean free path can be calculated from Equation (4.18) [28].

(4.18)
$$\Lambda = \frac{16}{5} \cdot \sqrt{\frac{R \cdot T}{2\pi \cdot M}} \cdot \frac{\eta}{p}$$

Calculated Knudsen numbers for various pore diameters are shown in Figure 4.3, where the mean free path is calculated from Equation (4.18) and assuming hydrogen gas at temperature 293 K.

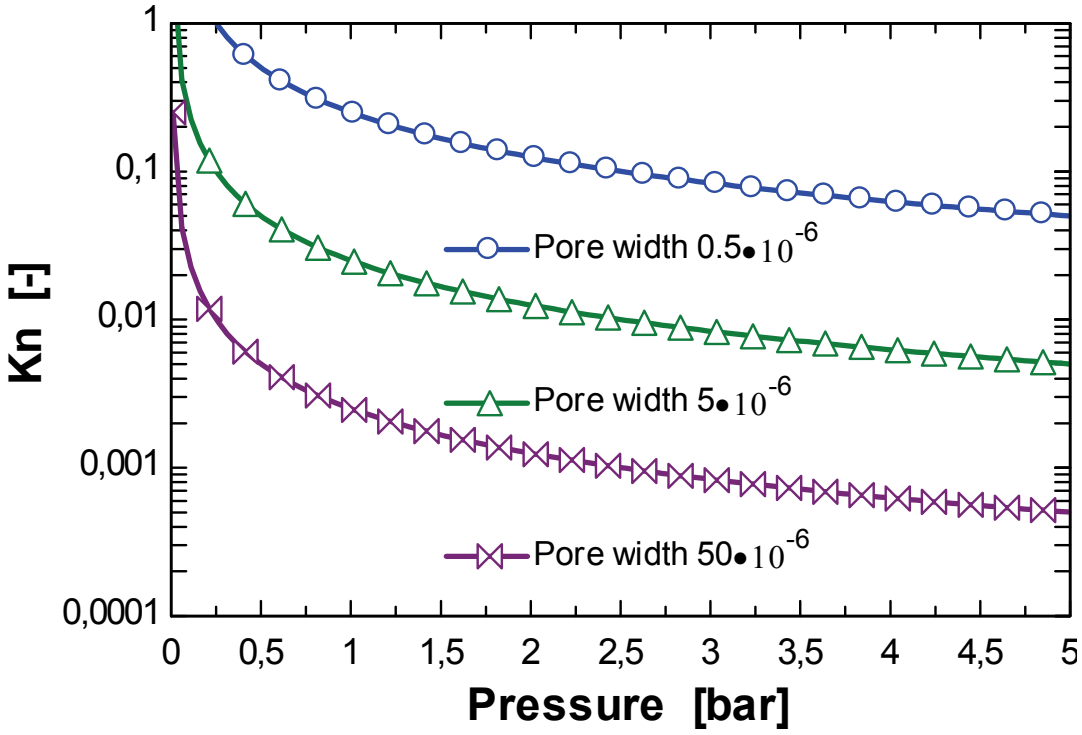

Figure 4.3 Knudsen number versus pressure

It can be seen from Figure 4.3 that the Knudsen number is less than 1 for gas pressures above ca 1 bar for pore diameters larger than ca 0.5 μm. Hence for average pore diameter larger than 0.5 μm can the gas be treated as a continuum.

Several models and correlations have been proposed for the prediction of the effective thermal conductivity for a porous medium. In general, literature correlations predict the effective thermal conductivity as a function of the thermal conductivities of each phase and the

porosity. A selection of published correlations for the effective thermal conductivity is given in Table 4.4.

Table 4.4 Overview of effective thermal conductivity correlations in porous media

Ref.	Comments	
[27]	Parallel arrangement of solid and gas	$k_{eff,\parallel} = \varepsilon \cdot k_f + (1-\varepsilon) \cdot k_s$
[27]	Serial arrangement of solid and gas	$k_{eff,\perp} = \dfrac{1}{\dfrac{1-\varepsilon}{k_s} + \dfrac{\varepsilon}{k_f}}$
[27]	Combination of series and parallel of solid and gas	$k_{eff} = \dfrac{1}{\dfrac{1-V_f}{k_{eff,\perp}} + \dfrac{V_f}{k_{eff,\parallel}}} \quad V_f$ V_f is volumetric fraction of parallel arrangement
[27]	Geometric mean	$k_{eff} = k_f^{\varepsilon} \cdot k_s^{(1-\varepsilon)}$
[29]	Zehner and Schlünder	$k_{eff} = k_f \cdot \left(1 - (1-\varepsilon)^{1/2} + \dfrac{2 \cdot (1-\varepsilon)^{1/2}}{1 - K \cdot B} \cdot \left(\dfrac{(1-K) \cdot B}{(1-K \cdot B)^2} \cdot \ln\left(\dfrac{1}{K \cdot B} \right) - \dfrac{B+1}{2} - \dfrac{B-1}{1-K \cdot B} \right) \right)$ $K = \dfrac{k_f}{k_s} \qquad B = 1.25 \cdot \left(\dfrac{1-\varepsilon}{\varepsilon} \right)^{10/9}$
[27]	Batchler and O' Brian	$k_{eff} = k_f \cdot \left(4 \cdot \ln\left(\dfrac{k_s}{k_f} \right) - 11 \right)$
[30]	Woodside and Messmer	$k_{eff} = \dfrac{a \cdot k_s \cdot k_f}{k_s (1-d) + d \cdot k_f} + c \cdot k_f \qquad c = \varepsilon - 0.03 \;\; a = 1 - c \;\; d = \dfrac{1-\varepsilon}{a}$
[31]	Kunii and Smith	$k_{eff} = \varepsilon \cdot k_f + \dfrac{\beta (1-\varepsilon)}{\theta + \gamma \cdot \dfrac{k_f}{k_s}} \qquad \theta = \dfrac{\frac{1}{2} \cdot \left(\dfrac{\kappa - 1}{\kappa} \right)^2 \cdot \sin^2 \theta_0}{\ln\left(\kappa - (\kappa - 1) \cdot \cos\theta_0 \right) \cdot \left(\dfrac{\kappa - 1}{\kappa} \right) \cdot (1 - \cos\theta_0)} - \dfrac{2}{3} \cdot \dfrac{1}{\kappa}$ $\sin^2 \theta_0 = \dfrac{1}{n} \qquad \beta = 0.9 - 1 \qquad \gamma = \dfrac{2}{3} \qquad \kappa = \dfrac{k_s}{k_f}$ n is the number of contact points on a semi-spherical surface of one solid particle

The minimum value of the effective thermal conductivity is obtained from the serial model where the solid and the fluid phases are assumed to be in layers normal to the direction of the heat flow. The maximum value of the effective thermal conductivity is for the parallel distribution model where the solid and fluid phases are assumed to be in layers parallel to the heat flow direction. The combination model presented in Table 4.4 is a combination of these two models. In the geometric mean model the effective thermal conductivity is given by the weighted geometric mean of each of phases thermal conductivities.

Zehner and Schlünder [29] presented a model based on a one-dimensional heat flow model for conduction through a packed bed of spherical particles where they assumed point contact for particles in the direction of heat flow. Batchler and O'Brian [27] based their correlation on

a solution of the Laplace equation in solid and fluid domains. Woodside and Messmer [30] suggested a model which was a combination of series and parallel distributions. They used an electrical conductivity analogy of an aggregate of conductive particles saturated with conducting electrolyte to derive a modified resistor model equation to predict the effective thermal conductivity. The derived expression for c was based on experimental data. Kunii and Smith [31] developed an expression for the effective thermal conductivity based on the heat transfer mechanisms shown in Figure 4.2. However, in the expression shown in Table 4.4 and plotted Figure 4.4 the terms for heat transfer through the contact surfaces (point 2 in Figure 4.4) and the radiation heat transfer term (point 3 in Figure 4.4) were neglected.

The thermal conductivity of solid $LaNi_5$ was found to have a value of 30 W/(m·K) by Pons and Dantzer [32]. The calculated bed effective thermal conductivity based on the correlations presented in Table 4.4, using a solid phase conductivity spanning from 18 to 42 W/(m·K), a porosity of 0.5, and hydrogen gas at 1 bar and 298 K is shown in Figure 4.4.

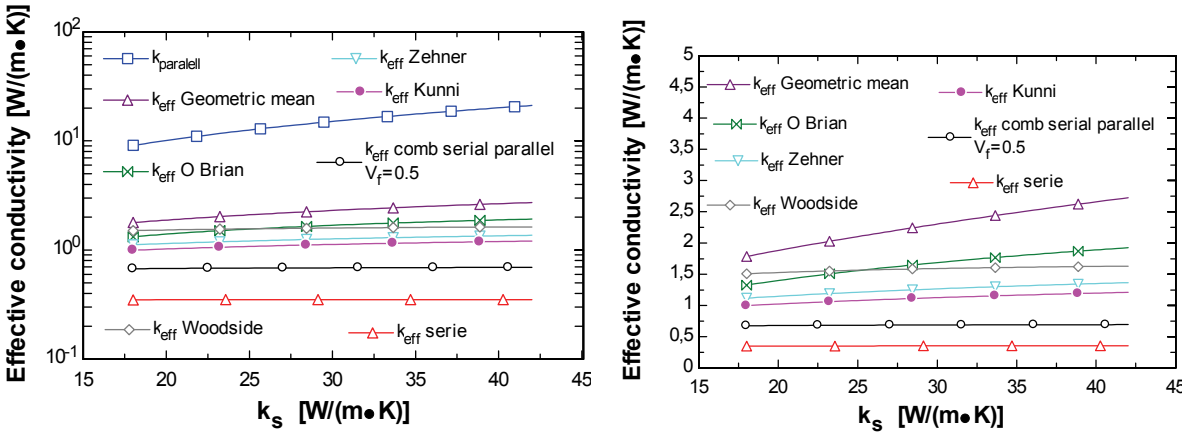

Figure 4.4 Effective thermal conductivity as function of different solid conductivities, assuming a porosity of 0.5 and hydrogen gas at 1 bar and 298 K. (A) is plotted with logarithmic ordinate axis and (B) using linear coordinates.

It is observed from Figure 4.4 that the serial and parallel configurations give the minimum and maximum values for the effective thermal conductivity. It is also seen that variations in the solid phase thermal conductivity affects the calculated effective thermal conductivity only to a small extent. The calculations were repeated using porosities of 0.4 and 0.6, and the effect of the estimated effective thermal conductivity was observed to be small, except for the serial and geometric mean correlations. However, it has to be taken into account that some of the theoretical models are based on assumptions of perfectly shaped (spherical) particles, with no variations through the porous bed. In a realistic metal hydride bed the particles will have irregular shape, and the bed packing density and porosity may vary within the bed. The particles under investigation in this study were studied with SEM microscope and are shown in Figure 4.5.

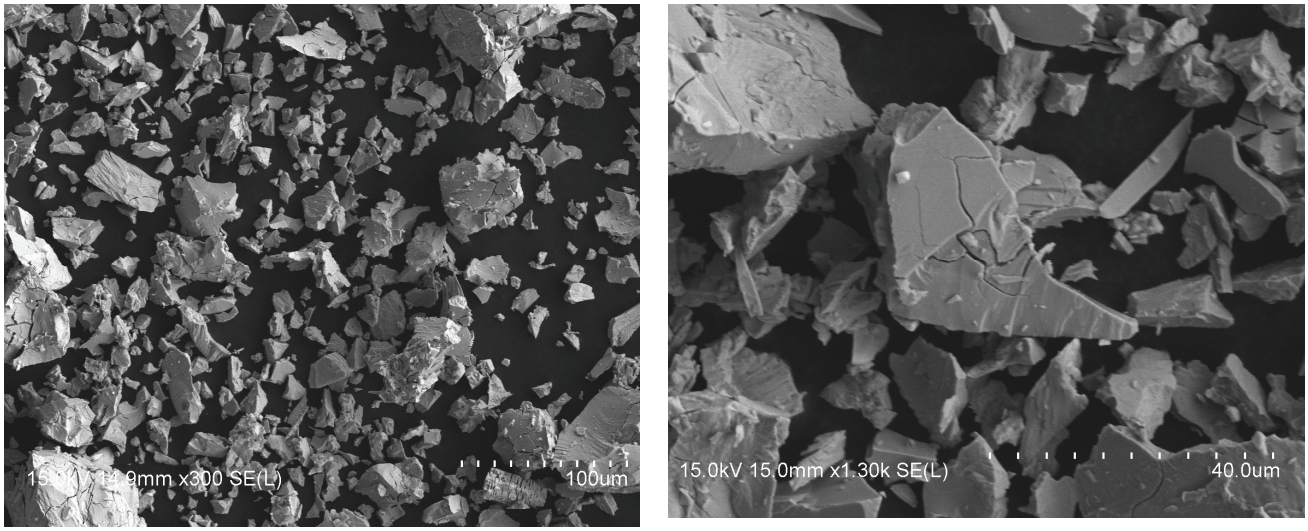

Figure 4.5 SEM images of the $Mm_{1-x}La_xNi_5$ (as received from supplier).

It can be seen that the larger particles had some cracks. The alloy consisted of rather fine particles of non-regular shape varying in size from ca 2 to 60 μm. A histogram of grain size distribution is shown in Figure 4.6.

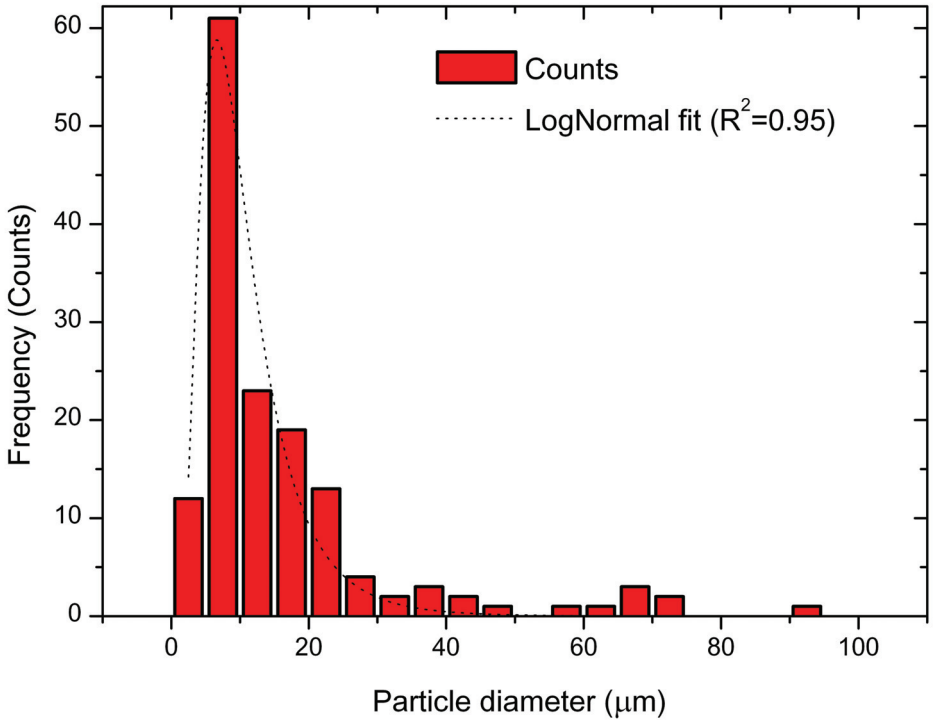

Figure 4.6 Particle size distribution of $Mm_{1-x}La_xNi_5$ (as received from supplier).

A log-normal fit [33] of the data gave a mean particle diameter of 9.3±0.6 μm. It can be seen from Figure 4.6 that the shape of the curve fitted log-normal particle distribution function has a narrow peak yielding a small value for the standard deviation.

During cycling the particles would crack and the average particle distribution moved towards smaller particles.

4.3.2 Particle surface area, and solid/gas heat transfer coefficient

The volumetric (specific) surface area (a_p) used in Equations (4.10) and (4.11) is the gas/solid contact surface area per unit volume of the matrix. For uniformly sized spherical particles this area can be estimated to $a_p = \frac{4\pi r_p^2}{4/3\,\pi r_p^3}\cdot(1-\varepsilon) = \frac{6}{d_p}(1-\varepsilon)$. The heat transfer coefficient (h_p) in Equation (4.10) and (4.11) is an important parameter if the gas and solid phases are in thermal non-equilibrium. This parameter is difficult to measure especially at small Re_p [19]; however, some correlations are available in the literature, as shown by Equations (4.19)-(4.21).

(4.19) $$Nu_p = h_{sf}\frac{d_p}{k_g} = 2.0 + 0.75\cdot \mathrm{Pr}^{1/3}\cdot \mathrm{Re}_p^{3/5}$$ Dang, [34]

(4.20) $$Nu_p = h_{sf}\frac{d_p}{k_g} = 2.0 + 0.6\cdot \mathrm{Pr}^{1/3}\cdot \mathrm{Re}_p^{1/2}$$ Ranz [35]

(4.21) $$Nu = 2 + 1.1\mathrm{Pr}^{1/3} + \mathrm{Re}_p^{0.6}$$ Wakao and Kaguei [36]

The Reynolds numbers used in the correlations are calculated based on the real gas velocity and particle diameter, i.e. $\mathrm{Re}_p = \frac{v\cdot d_p\cdot \rho_g}{\varepsilon\cdot\mu}$. Another correlation was proposed by Kunni and Smith [37]:

(4.22) $$Nu_p = h_{sf}\frac{d_p}{k_g} = \frac{\psi}{6(1-\varepsilon)\vartheta}Pe_p$$ Kunni and Smith [37]

Here ψ is a shape factor equal to unity for spherical particles [37] and ϑ is the ratio of average channelling length to particle diameter, a value estimated to 10 [38]. For the particle sizes covered in the present study Equations (4.19)-(4.21) all yield gas/solid heat transfer coefficients larger than 1000 W/m^2·K even for $Re_p \rightarrow 0$, while Equation (4.22) yields heat transfer coefficients in the range (0-200 W/(m·K)) for particle diameters spanning from 1-100 μm and real gas velocities between 0 and 5 m/s.

4.3.3 Permeability coefficient and porosity

Porosity is defined as the volume fraction occupied by the void. For uniformly sized spheres, the smallest possible porosity of ε=0.259 is obtained for the close-packed arrangement. It can be shown that the porosity of the bed is independent of the sphere diameter [39]. Examples of a loose and a tight packing is shown in Figure 4.7.

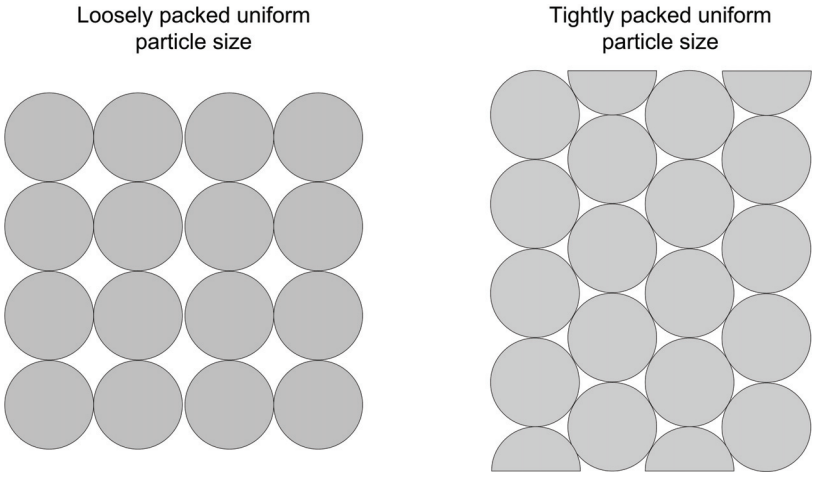

Figure 4.7 Loosely (ε=0.476) and tightly (ε=0.259) packed bed with uniformly spherical sized particle [40].

Typical bed porosities for non-uniformly sized and irregularly shaped particles are given in Table 4.5 [27].

Table 4.5 Examples of average bulk porosities [27].

Material	Porosity
Sandstone	0.08 – 0.38
Silica powder	0.37 – 0.49
Soil	0.43 – 0.54
Sand (loose beds)	0.37 – 0.5
Cigarette filters	0.17 – 0.49

In general the packing near bounding surfaces are looser than in the bulk resulting in increased local porosity [27]. However, these changes in local porosity are normally confined to distances from the wall in the order of d_p and can be neglected if the radius of the reactor is much larger than the particle diameter [27].

The permeability coefficient K_D in the Darcy equation (Equation (4.6)) is a measure of the systems ability to transport a fluid. Some, typical bed permeability coefficients are given in Table 4.6

Table 4.6 Bulk permeabilities for selected porous beds [27]

Material	Permeability K_D [m^2]
Sandstone (oil sand)	$5.0 \cdot 10^{-16} - 3.0 \cdot 10^{-12}$
Silica powder	$1.3 \cdot 10^{-14} - 5.1 \cdot 10^{-14}$
Soil	$2.9 \cdot 10^{-13} - 1.4 \cdot 10^{-11}$
Sand (loose beds)	$2.0 \cdot 10^{-11} - 1.8 \cdot 10^{-10}$
Cigarette filters	$1.1 \cdot 10^{-9}$

K_D can be determined through experimental measurements or estimated using empirical correlations. Examples of empirical correlations are given by Equations (4.23) and (4.24), where both correlations assume Darcy type flow conditions. The Kozeny-Carman correlation, Equation (4.23) assumes no electrochemical reactions between the particles, and that the particles are relatively compact.

(4.23) $$K_D = \frac{\varepsilon^3}{180 \cdot (1-\varepsilon)^2} \cdot d_p^2$$

For a packed bed of spherical particles with a narrow range of distribution in size, Rumpf and Gupte [41] showed that Equation (4.24) corresponded well with experimental data in the porosity range $0.35 \leq \varepsilon \leq 0.67$.

(4.24) $$K_D = \frac{\varepsilon^{5.5}}{5.6} d_p^2$$

4.3.4 Heat transfer coefficients

A commonly used method in the development of an overall heat transfer coefficient (h) to the porous bed is to split it into i) a contact conductance between the wall and the surface of the bed and ii) a bed bulk penetration conductance. The possible effect of these two heat transfer mechanism on the temperature field is illustrated in Figure 4.8.

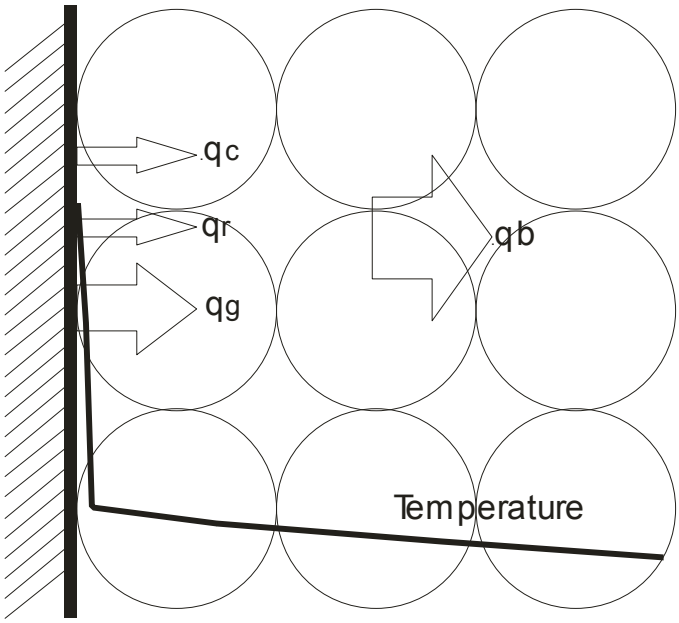

Figure 4.8 The temperature distribution and heat fluxes in a packed bed.

The wall-to-solid contact resistance is responsible for the temperature drop close to the wall in Figure 4.8 , while the bulk penetration resistance will cause a bulk temperature gradient. For most cases, at least if the heat penetration distance is larger than a critical distance, the bulk penetration resistance will be larger than the wall heat transfer resistance.

If a serial scheme is used the overall heat transfer coefficient can be calculated with Equation (4.25) [42].

(4.25)
$$\frac{1}{h} = \frac{1}{h_{ws}} + \frac{1}{h_{sb}}$$

Wall heat transfer coefficient, h_{ws}

The properties of the porous bed close to a bounding wall is changing within in the distance of one particle diameter, where the porosity can be higher or lower than the bulk porosity depending on the shape of the particles [27]. The wall-to-bed surface heat transfer resistance is strongly dependent on the thermal conductivity of the gas phase, thermal radiation and contact area conduction. These phenomena may be considered to be independent of each other, and the wall-to-bed surface heat transfer coefficient can thus be estimated by a summation [42] as shown by Equation (4.26).

(4.26)
$$h_{ws} = h_{cond} + h_{rad} + h_g$$

h_{ws} is the total wall to bed surface heat transfer coefficient, h_g is the heat transfer coefficient due to molecular gas conduction, estimated from Equation (4.27) [42].

(4.27)
$$h_{cond} = \frac{2 \cdot k_g}{r} \cdot \left[(Kn+1) \cdot \ln\left(1 + \frac{1}{Kn}\right) - 1 \right]$$
$$Kn = \frac{2 \cdot \Lambda}{r} \cdot \frac{2-\gamma}{\gamma}$$

Kn is a modified Knudsen number, Λ is the mean free path of the gas molecules calculated with Equation (4.18), r_p is the particle radius and γ is the accommodation coefficient which is around 0.8-1 for normal gases at moderate temperatures[43]. h_{cond} is the contact area conduction heat transfer coefficient. The contribution of the contact area conduction to the wall-to-bed surface heat transfer coefficient is strongly dependent of the material, the geometry of the granules and the structure of the particle surface. h_{cond} is negligible for poorly conducting granules. Muchowski [44] measured values of h_{cond} between 30 and 55 W/m^2·K for bronze spheres of 0.1-1.0 mm diameter.

h_{rad} is the radiation contribution to the heat transfer coefficient from the wall to the bed and can be estimated using (4.28) [42].

(4.28)
$$h_{rad} = 0.04 \cdot C_s \cdot \varepsilon \cdot \left(\frac{T}{100}\right)^3 \quad , where \quad C_s = 5.76 \left[\frac{W}{m^2 \cdot K^4}\right]$$

Another method of estimating the wall-to-bed surface heat transfer coefficient is to use Equation (4.29) presented by Schlünder [43].

(4.29)
$$h_{ws} = \phi \cdot h_{wp} + (1-\phi) \frac{2 \cdot k_g / d_p}{\sqrt{2} + (2 \cdot Kn + 2 \cdot \delta) / d_p} + h_{rad} + h_{cond}$$

ϕ is the surface coverage (typical values are 0.4-1) and δ is the particle roughness (typical values are from 0-100 μm) and h_{wp} is the heat transfer coefficient for a single particle, calculated from Equation (4.30).

(4.30) $$h_{wp} = \frac{4 \cdot k_g}{d_p}\left[\left(1+\frac{2 \cdot Kn + 2 \cdot \delta}{d_p}\right)\cdot \ln\left(1+\frac{d_p}{2 \cdot \Lambda + 2 \cdot \delta}\right) - 1\right]$$

Tsutomu [12] suggested Equation (4.31) for the wall heat transfer coefficient.

(4.31) $$\frac{h_{ws} \cdot d_p}{k_g} = \frac{2}{k_g / k_{eff,V} - k_f / k_{eff,MH}}$$

$k_{eff,v}$ is the effective thermal conductivity in the vicinity of the metal hydride bed. It is calculated from Kunii's correlation given in Table 4.4 using the porosity near the wall.

Bulk heat transfer coefficient, h_{sb}

It can be seen from Equation (4.25) that the overall heat transfer coefficient (h) also depends on the effective bulk heat transfer coefficient for the stagnant packed bed (h_{sb}). The bulk heat transfer coefficient can be calculated by applying Fourier's theory of heat conduction and depends on the boundary conditions [45], and consists of a superposition of two asymptotic solutions (a short term ($h_{sb}(t)$) and a long term solution ($h_{sb,\infty}$)) as indicated in Equation (4.32).

(4.32) $$h_{sb} = \sqrt{h_{sb}^2(t) + h_{sb,\infty}^2}$$

The long and short term solutions of the heat conduction equation are given by Equations (4.33) and (4.34) if constant temperature is used as a boundary condition, and by Equations (4.35) and (4.36) if constant heat flux is used as a boundary conditions.

(4.33) $$h_{sb} = \sqrt{\frac{1}{\pi}\cdot\frac{k_{eff}\left(\rho \cdot c_p\right)_{eff}}{t}}$$

(4.34) $$h_{sb,\infty} = \frac{3 \cdot k_{eff}}{s}$$

(4.35) $$h_{sb} = \frac{\sqrt{\pi}}{2}\cdot\sqrt{\frac{k_{eff}\cdot\left(\rho \cdot c_p\right)_{eff}}{t}}$$

(4.36) $$h_{sb,\infty} = \frac{\pi^2 \cdot k_{eff}}{4 \cdot s}$$

Equations (4.33)-(4.36) were derived from the solution of the heat conduction equation between two plates [42].

Tsutomu [12] used a steady-state model for the bed surface to bulk heat transfer coefficient $h_{sb,}$ Equation (4.37).

(4.37) $$\frac{1}{h_{sb}} = \frac{s}{2 \cdot k_{eff}}$$

The bed bulk heat transfer coefficient also becomes very large for very high effective thermal conductivities. In these cases the overall heat transfer coefficient will approach the value of the wall to bed surface heat transfer coefficient (h_{ws}).

The value of the bulk heat transfer coefficient becomes large in some special situations as described by [28]: i) as time approaches zero (then the bed is at the initial temperature), ii) when the heat capacity of the bed approaches infinity (due to a strong heat sink or source in the bed), iii) if the bed is perfectly stirred.

For case of ii and iii h_{sb} is multiplied with a function f(ph) to yield a more correct overall heat transfer coefficient (h), and suggestions for the function f(ph) are given in [42] for four different cases.

Wall to bulk heat transfer coefficient, h

The correlations presented above yield different values for the wall-to-bed heat transfer coefficient. However, for all correlations the wall-to-bed surface heat transfer coefficient (h_{ws}) was at least 100 times larger than the bed surface-to-bulk heat transfer coefficient (h_{sb}). The largest values for the wall-to-bed surface heat transfer coefficient was achieved with Kuniis correlation followed by the Equation (4.27), The Schlünder [28] correlation (Equation (4.29)) gave the smallest value for the wall-to-bed surface heat transfer coefficient. In Equation (4.27) and (4.29) the gas conduction part (h_{cond}) is the most important contributor in the wall-to-solid heat transfer coefficient (h_{ws}).

Figure 4.9 shows the overall heat transfer coefficient (wall-to-bulk h) calculated using Equation(4.25). Equation (4.26) was used to calculate the wall-to-bed surface heat transfer coefficient (h_{ws}) while the bed surface-to-bulk heat transfer coefficient (h_{sb}) was calculated with Equation (4.32) and Equation (4.37). The plate distance was set to 46 mm, the gas pressure was 1 bar, the temperature was 298 K, the packing density was 4000 kg/m^3 and the effective conductivity used was 1.5 W/m·K.

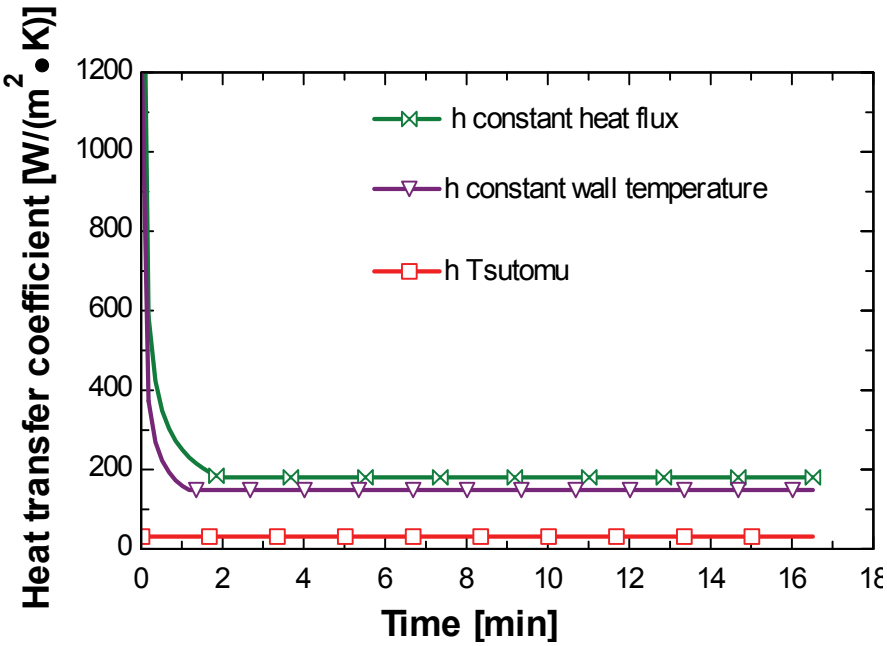

Figure 4.9 Calculated overall heat transfer coefficient from using Equation (4.26) for the wall to bed surface heat transfer coefficient and Equations (4.32) and (4.37) for the bulk heat transfer coefficient.

It can be seen from Figure 4.9 that the heat transfer coefficient based on transient solutions yield higher values in the beginning, and approaches an asymptotic value at large time. The overall heat transfer coefficient calculated with the Tsutomu correlation gives lower values. However, none of the plotted correlations take into account the chemical reaction in the metal hydride bed, which will contribute to a larger overall heat transfer coefficient.

4.3.5 Heat capacity and swelling

The solid density of the metal hydride is known to change due to swelling of the particles at higher hydrogen-to-metal atomic ratios. A $LaNi_5$ alloy was reported to swell as much as 18.9% during hydrogenation [46], and this process is assumed to be reversible. The solid density is affected by this swelling and may be estimated from Equation (4.38) if the swelling is assumed to be a linear function of H/AB_5 concentration.

(4.38)
$$\rho_{MH} = \frac{(A+C)}{\left(1+\frac{S_p \cdot C}{100 \cdot C_{Max}}\right)} \cdot \frac{\rho_{MH\ initial}}{A}$$

The assumption of a linear variation in the solid density is not strictly correct, since there is much less expansion at low hydrogen-to-metal concentrations (α phase), but this is a realistic simplification.

The change in a $LaNi_5$ alloy specific heat capacity at different states of hydrogenation was measured by Dantzer [47] and Ohlendorf [48]. Their results are shown in Figure 4.10.

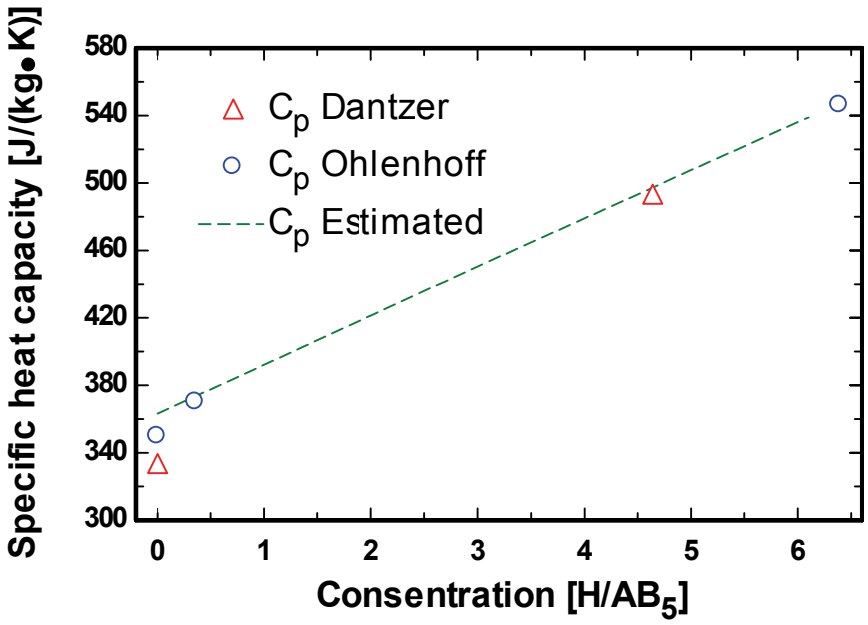

Figure 4.10 shows measured literature values (Dantzer [47] and Ohlendorf [48]) and estimated specific heat capacity (Equation (4.39)) of a $LaNi_5$ alloy as a function of state of hydrogenation

The change in specific heat capacity due to hydrogenation is estimated with the additive Neuman kop rule (Equation (4.39)) [49].

(4.39)
$$c_p = \frac{\sum M_i \cdot c_{p,i}}{\sum M_i}$$

M_i and $c_{p,i}$ are the masses and specific heat capacities of the components in the alloy. To determine the specific heat capacity of hydrogen inside the metal, literature data [47,48] were fitted to the calculated specific heat capacity using $c_{p,H}$ as the unknown parameter. A good fit was achieved using $c_{p,H}$ 13 J/mol·K (13000 J/kg·K); this value being slightly lower compared to the specific heat capacity of gaseous hydrogen ($c_{p,H2}$=14332 J/kg·K). In a misch metal modified AB_5 type alloy the same value for the heat capacity of absorbed hydrogen will be used and the misch metal alloy will be added in the heat capacity calculation.

4.4 EXPERIMENTAL SET UP

The experimental set up used to test the hydrogen storage units is shown in Figure 4.11.

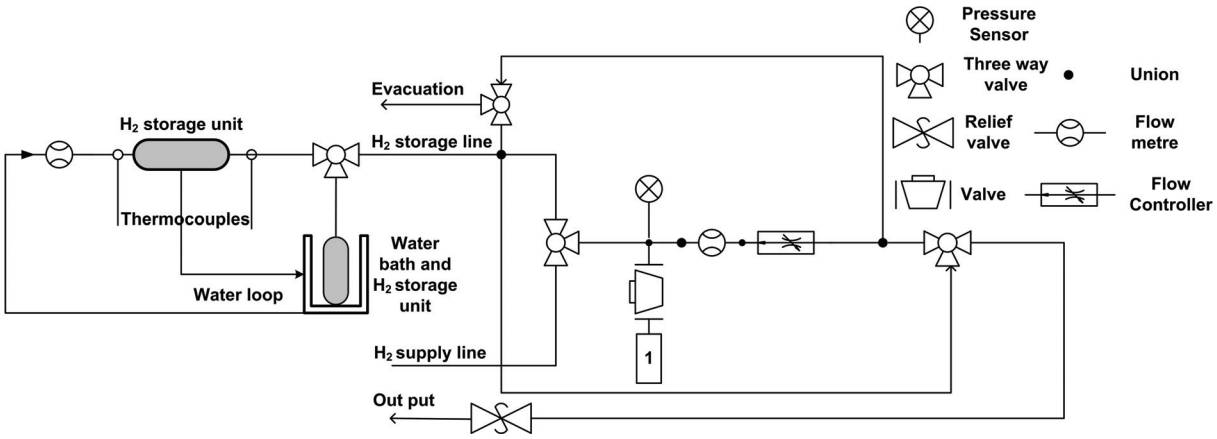

Figure 4.11 Schematic diagram of the set up for testing of the hydrogen storage units. (1) is a buffer volume.

The absorption and desorption flow rates were controlled/monitored with a flow controller and a flow metre. The hydrogen gas pressure was measured with a pressure gauge. The desired charging pressure could be set with a pressure regulator during absorption, while a relief valve was used to control the discharge pressure. This made it possible to measure absorbing/desorbing hydrogen flow rates and the corresponding gas pressure. It was also possible to charge and discharge the units having a constant flow rate by using flow controllers.

Vacuum conditions could be applied using a rotary vacuum pump connected to the evacuation line. A constant water flow rate of heating/cooling water was supplied with a 30 litre water bath, having a thermal regulation system and an adjustable pump for external circulation of water.

Three of the tested units had internal heat exchangers, the fourth unit had heat exchange through the reactor shell. The tested units having internal heat exchangers were connected as shown in Figure 4.11. In this set up it was possible to measure the water flow rate and temperature at the inlet and outlet of the metal hydride storage unit. The unit with no internal heat exchanger was simply immersed into the water bath for better thermal management, as indicated in Figure 4.11

Prior to experiment start-up the different units were leak tested and volume calibrated using argon gas, and cycled several times with reversible storage capacity and reproducible charging and discharging rates. The hydrogen used during all the experiments was of 99.9999% purity.

4.5 TEST GEOMETRIES

To improve the understanding of the dynamic processes in a metal hydride storage reactor and to collect experimental data for the verification of the mathematical models, several metal

hydride storage units were tested. The reactors ability to transfer heat in and out of the metal hydride bed is important due to the low effective thermal conductivity of metal hydride granulates. Considerable amount of heat is produced or consumed in the gas/solid reaction. Therefore the design of the heat exchangers is important. The ideal heat exchanger should have zero mass and occupy no volume, but have an infinitely large heat transfer surface. These criteria are of course impossible to fulfil. Therefore it becomes necessary to map the heat exchangers requirements regarding ability to transfer heat relative to its weight and volume in order to approach the optimum design.

Four different metal hydride reactors having different heat exchanger geometries were tested in the experimental set up shown in Figure 4.11. The simplest reactor was a cylindrical reactor (Unit#A) made of stainless steel with no internal heat exchanger, but heat transfer through the external walls. This reactor had three internal thermocouples positioned at different radial positions and two thermocouples welded to the outer wall of the reactor. It was submerged in a water bath. More detailed information of this unit is presented in Chapter 5.

The reactors presented in Chapter 6 had an internal heat exchanger which could be replaced. Two types of heat exchangers were tested: A brush type heat exchanger (Unit#C) and a tube type heat exchanger (Unit#D). The reactor shell for (Unit#C) and (Unit#D) was made from aluminium. Both reactors had four internal thermocouples positioned at different radial positions, and two external thermocouples glued to the outside reactor wall.

Finally, a reactor having an internal heat exchanger consisting of a tube with radial fins (Unit#B) was tested. The shell and heat exchanger of Unit#B were made of aluminium. This reactor had four external thermocouples glued to the outer wall. (Unit#B) is presented in more detail in Chapter 7.An overview of the different units is given in Table 4.7.

Table 4.7 Tested metal hydride reactors.

Reactor	Mass of metal hydride powder [kg]	Heat transfer area [m^2]	Heat exchanger type	Heat exchanger geometry
Unit#A	0.85	0.017	External	Cylindrical
Unit#B	2.2	0.093	Internal	Finned
Unit#C	2.3	0.21	Internal	Brush
Unit#D	2.5	0.014	Internal	Tube

All units were filled with the same type of AB_5 alloy, which was characterised in chapter 3. A more detailed description of the different units is given below.

4.5.1 Unit#A

The unit presented in chapter 5 was the simplest unit in terms of heat exchanger geometry. It had no internal heat exchanger and was simply immersed into a water bath for thermal management. The unit was made from a standard Swagelock cylinder [50] with a steel shell, as shown in Figure 4.12.

Figure 4.12. Unit#A tested in Chapter 5.

LABTECH Int. Co. Ltd. Alloys Research and Manufacturing [7] provided the mischmetal-modified alloy as an activated powder. 850 g of the alloy was loaded into the test reactor. The reactor consisted of an internal filter element with a length of 190 mm and an outer diameter of 10.55 mm, through which the hydrogen entered and left the reactor. The reactor had an outer and inner diameter of 50.8 and 46.08 mm, respectively, and the inner length of the reactor was 200 mm. The total heat transfer surface, defined as the surface area between the reactor wall and metal hydride powder, was 0.017 m^2.

Three 1/8-inch thermocouples having a 5 s response time were inserted at different radial positions (9.7, 13.3 and 17.2 mm from the cone centre), and 90 mm from the bottom of the reactor. A fourth thermocouple was soldered to the outer wall to monitor the wall temperature during the experiments.

4.5.2 Unit#B

This unit was included in the comparison of the different storage units presented in chapter 7. The development and creation of the unit was done in collaboration with Raufoss Automotive Fuel Systems and IFE. The unit had an internal heat exchanger consisting of a circular tube with external annular fins. An illustration of the unit is shown in Figure 4.13

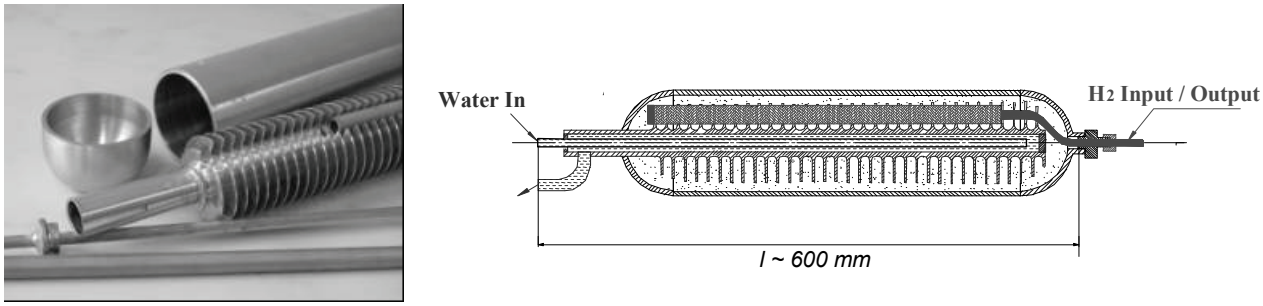

Figure 4.13 Schematic of the Raufoss Automotive Fuel System unit investigated in Chapter 7.

Both the reactor shell and heat exchanger were made of aluminium, and the unit was filled with 2.2 kg of metal hydride powder. The unit had an inner length of 560 mm, an internal diameter of 50 mm, and a wall thickness of 2.5 mm. The heat exchanger consisted of 33 annular fins with a thickness of 1 mm.

4.5.3 Unit#C and Unit#D

In Chapter 6 one reactor containing ca 2.4 kg of metal hydride powder is analysed. This reactor was designed by IFE and built by Prototech and was used in a project for the European Space Agency (ESA). This unit was designed to accommodate different heat exchanger geometries, and two types of heat exchangers were tested, as shown in Figure 4.13.

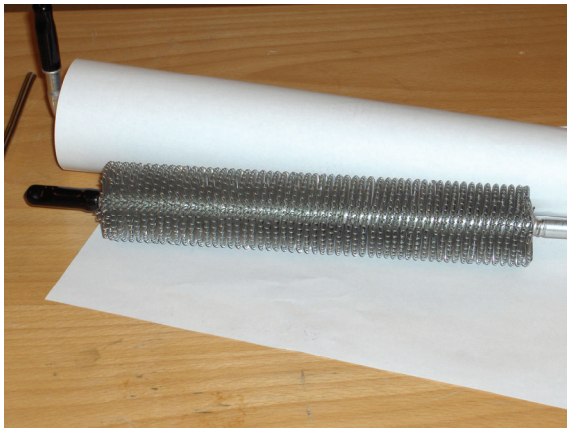

(A) Brush type heat exchanger, Unit#C

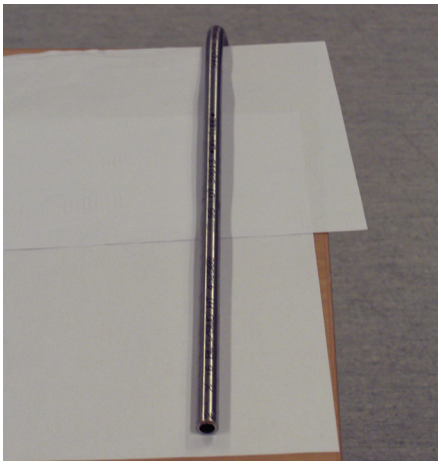

(B) Tube type heat exchanger, Unit#D

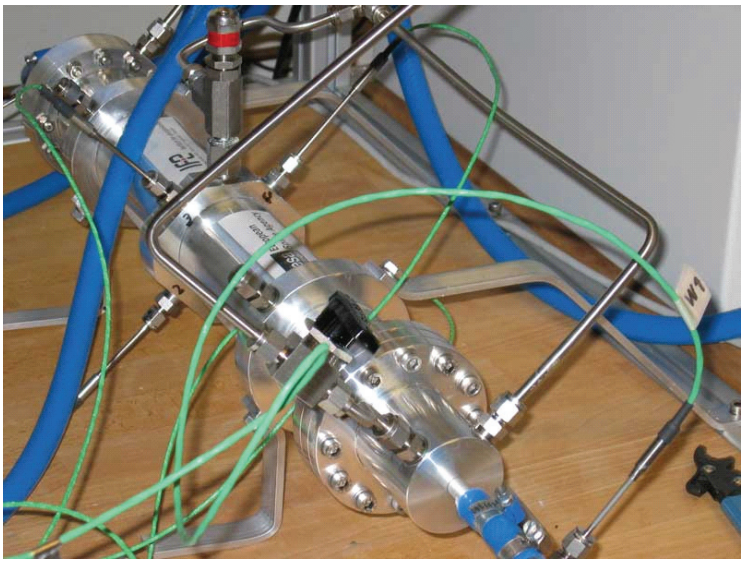

(C) the experimental set up

Figure 4.14 The reactor tested in Chapter 6, and its heat exchanger configurations.

Figure 4.14(C) shows the reactor considered in Chapter 6. The tested internal heat exchangers differed considerably in layout. The heat exchanger shown in Figure 4.14(A) (Unit#C) was a brush type heat exchanger where the average heat conduction paths were very short. The heat

exchanger shown in Figure 4.14(B) (Unit#D) was a plain tube type heat exchanger and had a much longer average heat conduction path. Four thermocouples were inserted as shown in Figure 4.14(C) and the distances of the thermocouples from the axis of the heat exchangers were 4.75, 9.19, 13.63 and 18.06 mm. More details of these units are given in Table 4.8.

Table 4.8 Details of the two different units tested in Chapter 6.

Total inner volume available for metal hydride powder	700 cm^3	Inner length of cylinder	46 cm
Outer diameter of aluminium heat-exchanger tube (water tube)	0.95 cm	Inner diameter of aluminium outer shell	6.10 cm
Thickness of Teflon heat-insulating layer	0.80 cm	Thickness of outer heat insulation layer	1.5 cm
Mass of metal hydride powder heat exchanger configuration Unit#D	2.4 kg	Mass of metal hydride powder heat exchanger configuration Unit#C	2.2 kg
Surface area of heat exchanger configuration Unit#D	140 cm^2	Surface area of heat exchanger configuration Unit#C	2100 cm^2
Pitch of fins configuration Unit#C	0.1 cm	Diameter of fins configuration Unit#C	0.07 cm
Diameter of filter elements	0.6 cm	Height of fins configuration Unit#C	1.72 cm

4.6 PRELIMINARY RESULTS

The reactors behave differently during charging and discharging, Figure 4.15 shows the measured hydrogen concentration versus time for all reactors presented above, plus the kinetic reactor presented in Chapter 3. They were charged at 9.5±0.2 bar charging pressure and using 298 K cooling water.

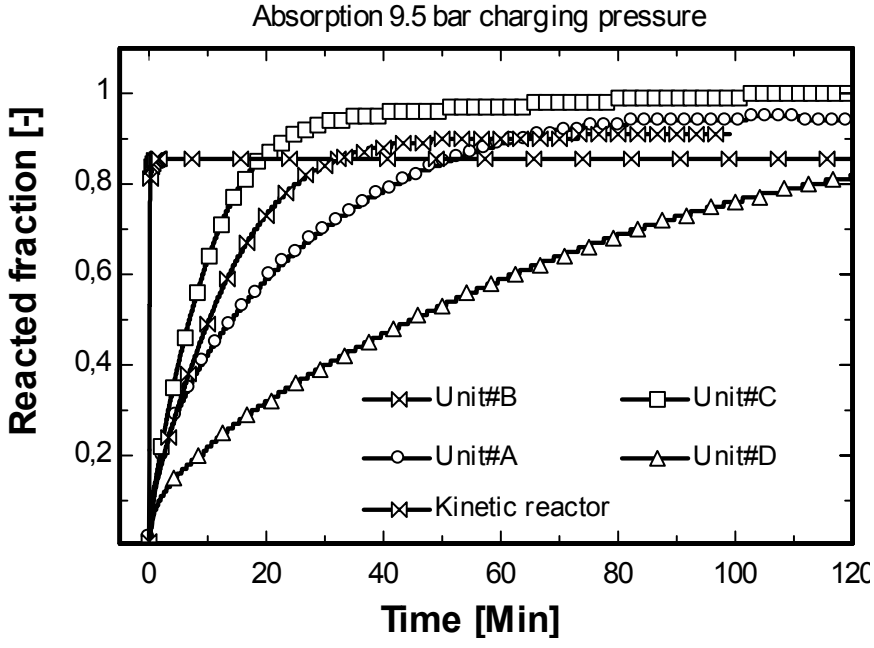

Figure 4.15 Charging of the different reactors with a 9.5 bar charging pressure and 298 K cooling water

We observe from Figure 4.15 that the kinetic reactor is by far the fastest reactor, having close to isothermal conditions. The concentration profiles of the other reactors have more dampened profiles and are charged at slower rates. The behaviour of the individual reactors will be treated in more details in the following chapters.

References

[1] Ergenics, Inc. 373 Margaret King Ave. Ringwood, Nj 07456, USA; http://www.ergenics.com/ (02/11-07).

[2] Hydrogen Components, Inc.12420 North Dumount Way, Littleton, CO 80125, USA: http://www.hydrogencomponents.com/ (01/11-07).

[3] ECD Ovonics. 2956 Waterview Drive Rochester Hills, Michigan 48309 http://www.ovonic.com/ (01/11-07).

[4] The Japan Steel Works, Ltd. Hydrogen Energy Center. Hibiya Mitsui Bldg., 1-2 Yurakucho 1- Chome, Chioda-ku,Tokyo 100-006, Japan; http://www.jsw.co.jp/en/index.html (01/11-07).

[5] Japan Metals & Chemical Co., Ltd. Hydrogen Energy Center. Hibiya Mitsui Bldg., 1-2, Yurakucho 1 Chome, Chuo-ku, Tokyo 103-8531, Japan; http://www.jmc.co.jp/jmc.nsf/doc/english_index (01/11-07).

[6] Hera Hydrogen Storage Systems, 577 Le Brenton Longueuil,Quêbec, Canada; Hoefner Strasse 45, 90431,Nuremberg, Germany; http://herahydrogen.com/ (01/11-07).

[7] LABTECH Int. Co. Ltd. Alloys Research and Manufacturing. Mladost-1, bl.25/A, Sofia-1784, BULGARIA; http://labtech.solo.bg/ (01/11-07).

[8] A.N. Pogorny Institute of Mechanical Engineering Problems of National Academy of Sciences of Ukraine. 2/10 Pozharsky str., Kharkow 61046, Ukraine; http://www.ipmach.kharkov.ua/English/enind.htm (07/11-07).

[9] Takeichi N, Senoh H, Yokota T, Tsuruta H, Hamada K, Takeshita H, T, Tanaka H, Kiyobayashi T, Takano T, Kuriyama N. "Hybrid hydrogen storage vessel", a novel high-pressure hydrogen storage vessel combined with hydrogen storage material. Int J Hydrogen Energy 2003; 28(10): 1121-1129.

[10] Nishimura K, Inazumi C, Oguro K, Uehara I, Itoh Y, Fujitani S, Yonezu I. Simulation and evaluation of a hydrogen storage system using hydrogen storage alloy for a chemical CO2 fixation and utilization system. Int J Hydrogen Energy 2000; 25(11): 1087-1093.

[11] Levensque S, Ciureau M, Roberge R, Motyka T. Hydrogen storage for fuel cell systems with stationary applications - I. Transient measurement technique for packed bed evaluation. Int J Hydrogen Energy 2000; 25(11): 1095-1105.

[12] Oi T, Maki K, Sakaki Y, S. Heat transfer characteristics of the metal hydride vessel based on the plate-fin type heat exchanger. J Power Sources 2004; 125(1): 52-61.

[13] Whitaker S. The Forcheimer Equation: A Theoretical Development. Transport in Porous Media 1996; 25(1): 27-61.

[14] Bear J. Hydraulics of Groundwater. edn. McGraw-Hill.

Online version available at:

http://www.knovel.com/knovel2/Toc.jsp?BookID=1359&VerticalID=0,

[15] Darcy H. Les Fontaines Publiques de la Ville de Dijon (Dalmont, Paris) 1856.

[16] Whitaker S. The method of volume averaging. edn. Dordrecht: Kluwer, 1999.

[17] Kutz M. Mechanical Engineers' Handbook - Energy and Power (3rd Edition). edn. http://www.knovel.com/knovel2/Toc.jsp?BookID=1532&VerticalID=0 (05/10-07),

[18] Tavman I, H. Effective thermal conductivity of granular porous materials. International Communications in Heat and Mass Transfer 1996; 23(2): 169-176.

[19] Rohsenow W, M, Hartnett J, P, Cho Y, I. Handbook of Heat Transfer (3rd Edition). McGraw-Hill. Online version available at: http://www.knovel.com/knovel2/Toc.jsp?BookID=1626&VerticalID=0 (01/11-07).

[20] Sakae Y, Kunii D. Studies on Effective Thermal Conductivities in Packed Beds. AIChE Journal 1957; 3(3): 373-381.

[21] Kapischke J, Hapke J. Measurement of the effective thermal conductivity of a Mg-MgH_2 packed bed with oscillating heating. Experimental Thermal and Fluid Science 1998; 17(4): 347-355.

[22] Kapischke J, Hapke J. Measurement of the Effective Thermal Conductivity of a Metal Hydride Bed with Chemical-Reaction. Experimental Thermal and Fluid Science 1994; 9(3): 337-344.

[23] Hahne E, Kallweit J. Thermal conductivity of metal hydride materials for storage of hydrogen: Experimental investigation. Int J Hydrogen Energy 1998; 23(2): 107-114.

[24] Suda S, Kobayashi N. Experimental Measurment of Thermal Conductivity. Journal of the less-common metals 1980; 74: 127-136.

[25] Suda S, Kobayashi N, Yoshida K. Thermal Conductivity in metal hydride beds. Int J Hydrogen Energy 1981; 6: 521-528.

[26] Suda S, Komazaki Y, Kobayashi N. Effective thermal conductivity of metal hydride beds. Journal of the Less-Common Metals 1983; 89: 317-324.

[27] Kaviany, M. Principles of heat transfer in porous media. edn. New York: Springer, 1991.

[28] Schlünder E, U. Heat Transfer to Packed and Stirred Beds from the Surface of Immersed Bodies. Chemical Engineering and Processing 1984; 18(1): 31-53.

[29] Zehner P, Schlünder E, U. Thermal conductivity of Packings at Moderate Temperatures Chemie Ingenieur Technik 1970; 42: 933-944.

[30] Woodside W, Messner JH. Thermal Conductivity of Porous Media. 1. Unconsolidated Sands. J Appl Phys 1961; 42(4).

[31] Kunii D, Smith J, M. Heat Transfer Characteristics of Porous Rocks. AIChE J 1960; 6(1): 71-78.

[32] Pons M, Dantzer P. Determination of Thermal-Conductivity and Wall Heat-Transfer Coefficient of Hydrogen Storage Materials. Int J Hydrogen Energy 1994; 19(7): 611-616.

[33] Gottstein G. Physical foundations of materials science. edn. Berlin: Springer, 2004.

[34] Dang V, U, Delcambre B. Experimental study and modelization of a long term, underground, rock bed thermal storage system, coupled with air solar collectors Revue Phys Appl 1987; 22(7): 487-503

[35] Ranz W, E. Friction and transfer coefficients for single particle and packed beds, Chem. Chem Eng Progress 1952; 48(247): 247-253.

[36] Wakao N, Kaguei S. Heat and mass transfer in packed beds. edn. New York: Gordon and Breach Science Pub., 1982.

[37] Kunii D, Suzuki M. Particle-to-Fluid Heat and Mass Transfer in Packed Beds of Fine Particles. Int J Heat Mass Transfer 1967; 10(7): 845-852.

[38] Nakagawa T, Inomoata A, Aoki H, Miura T. Numerical analysis of heat and mass transfer characteristics in the metal hydride bed. Int J Hydrogen Energy 2000; 25(4): 339-350.

[39] Scheidegger A, E. The physics of flow through porous media. edn. Toronto: University of Toronto Press, 1957.

[40] Cell aggregation and sphere packing http://www.tiem.utk.edu/~gross/bioed/webmodules/spherepacking.htm (07/1007).

[41] Rumpf H, C,H, Gupte A, R. Zur Theorie der Zugfestigkeit von Agglomeraten bei Kraftübertragung an Kontaktpunkten. Chemie Ingenieur Technik 1970; 42(8): 538-540.

[42] Hewitt G, F. Heat exchanger design handbook 1998 Part 1: Heat exchanger theory; Part 2 : Fluid mechanics and heat transfer. edn. New York: Begell House,Inc, 1998.

[43] Schlünder E, U. Heat-Transfer from Heated Walls to Packed-Beds of Metal Particles at Various Pressures. Int J Heat Mass Transfer 1974; 17(9): 1087-1091.

[44] Muchowski E. Wärmeübergang wom Boden vibrierter Gefässe an Kugelschüttungen bei Atmospärendruck und im Vakuum edn. Ph.D Thesis from University of Karlsrhue, 1977.

[45] Carslaw H, S, Jaeger J, C. Conduction of heat in solids. 2nd edn. Oxford: 1959.

[46] Yartys V, A, Burnasheva V, V, Semenenko K, N, Fadeeva N, V, Solovev S, P. Crystal-Chemistry of $RT_5H(D)X$, $RT_2H(D)X$ and $RT_3H(D)X$ Hydrides Based on Intermetallic Compounds of $CaCu_5$, $MgCu_2$, $MgZn_2$ and $PuNi_3$ Structure Types. Int J Hydrogen Energy 1982; 7(12): 957-965.

[47] Dantzer P, Orgaz E. Thermodynamics of Hydride Chemical Heat-Pump .2. How to Select a Pair of Alloys. Int J Hydrogen Energy 1986; 11(12): 797-806.

[48] Ohlendorf D, Flotow H, E. Heat-Capacities and Thermodynamic Functions of $LaNi_5$, $Lani_5H_{0.36}$ and $Lani_5H_{6.39}$ from 5 to 300 K. Journal of the Less-Common Metals 1980; 73(1): 25-32.

[49] Liyan Q, White M, A. The Constituent Additivity Method to Estimate Heat Capacities of Complex Inorganic Solids. J Chem Educ 2001; 78 (8): 1076-1079.

[50] Swagelock Fluid System Technologies http://www.swagelok.com/search/find_partnumbers_results.aspx?PS=304L-HDF4-300&PG=0&RPR=5 (02/11-07).

5 HEAT TRANSFER CHARACTERISATION OF A METAL HYDRIDE STORAGE CONTAINER DURING HYDROGEN CHARGE AND DISCHARGE

T. Førde[1] E. Næss[2] and V.A. Yartys[1]

1) Institute for Energy Technology (IFE), Kjeller. Norway

2) Norwegian University of Science and Technology, Trondheim, Norway

5.1 ABSTRACT

A numerical model for the transient hydrogen charge/discharge rates and thermal behaviour of metal hydride reactors was developed and verified against experiments using a cylindrical reactor filled with AB_5 type metal hydride. The experimental set up used a reactor submerged in an isothermal water bath, and had a storage capacity of 130 Nl hydrogen. Hydrogen gas was introduced/extracted through a porous tube located along the centreline of the reactor, and heat was transferred through the external surface of the reactor. The numerical model assumes local thermal equilibrium between the gas and solid phases, and incorporates the pressure and temperature-dependent hydrogen reaction rates, as well as heat transfer in the porous metal hydride bed. The model was verified through experimental data. The models sensitivity to perturbation in its parameters is also investigated. It was found that activation energy, effective conductivity and heat of reaction were the most important parameters. Experiments at different water bath temperatures and charge/discharge hydrogen pressures, were performed. These experiments indicated a relation ship between charging/discharging time and applied gas pressures. In addition the reactors ability to deliver a constant hydrogen flow with different water bath temperature experimentally was investigated.

Nomenclature

A	Molar weight fraction between initial alloy and hydrogen gas	[-]
c_p	Specific heat capacity	[J/kg·K]
C	Hydrogen to metal atomic ratio (H/M)	[-]
C_1	H/M Ratio lower limit	[-]
C_2	H/M Ratio upper limit	[-]
D_p	Particle diameter	[m]
E_a	Activation energy	[J/mol]
ΔH	Heat of reaction	[J/mol]
K_D	Permeability	[m^2]
k_{eff}	Effective thermal conductivity	[W/m·K]
$\dot{m}$	H_2 reaction rate	[mol/s·m^3] or [kg/s·m^3]
m	Mass	[kg]
M	Molar mass	[kg]
P	Pressure	[Pa]
Pe	Peclet number	[-]
R	Universal gas constant 8.314	[J/mol·K]
r	Radius (used in modelling equations)	[m]
r_1	Filter radius	[m]
r_2	Reactor wall outer radius	[m]
r_3	Reactor wall inner radius	[m]
S	Percentage swelling of alloy	[%]
T	Temperature	[K]
V_g	Superficial gas velocity	[m/s]
$\dot{Q}$	Heat transfer rate	[W]
X	Scaled concentration (related to contents of C)	[-]
Z	Rate constant	[1/s]
ε	Porosity	[-]
Γ	Reacted fraction	[-]
ρ	Density	[kg/m^3]
μ	Dynamic viscosity	[kg/m·s]
η	Avrami fitting parameter	[−]
α	Heat transfer coefficient	[W/m^2·K]

Subscript

alloy	Alloy
eq	Equilibrium
g	Gas
H	Hydrogen
initial	Initial
La	Lanthanum
Ni	Nickel
MH	Metal hydride
Mass	Total mass
Mm	Mich metal
max	Maximum
Wall	Reactor wall
w	Water
wb	Wall to bulk

5.2 INTRODUCTION

Hydrogen as an energy carrier is an alternative to fossil fuels. The advantage of using hydrogen is its high calorific value as a fuel and its possibility to be produced from renewable energy sources. However, storage of hydrogen is a major problem, which has to be solved before the hydrogen economy can have a breakthrough. Hydrogen can be stored as a gas, as a liquid or in a metal hydride; there are pros and cons for all the different solutions. However, for some applications such as stationary hydrogen stand-alone power systems (HSAPS), metal hydrides are promising candidates as hydrogen storage medium. The process of hydrogen storage in metal hydrides is associated with heat release during hydrogen absorption and heat consumption during desorption. Due to the poor effective thermal conductivity of metal hydride granulate beds, combined with high rates of heat adsorption/desorption, the process of removing/adding and distributing heat in a storage vessel during charging/discharging may become limiting for the hydrogen charge/discharge rates. Several numerical models describing the heat and mass transfer processes are available in the literature. The group of Jemni and Nasrallah has published a number of articles [1-5] describing heat and mass transfer in a reactor with heat transfer at the outer surface, where hydrogen leaves and enters at the top of the reactor. They used their model to study the validity of the simplifying assumptions used by various authors (like the assumption of thermal equilibrium between gas and solid) and the effect of different physical modelling input parameters (such as thermal conductivity). Mat, Kaplan and Aldas [6-8] extended the analysis to three dimensions for a cylindrical geometry and verified their model using literature data. Recently two new reactors for comparison and model verification were built [9]. The assumption of thermal equilibrium between gas and solid and the importance of heat convection was analysed by Nakagawa et al [10] for a cylindrical reactor where hydrogen was introduced at the top of the reactor. They also considered the influence of variable physical properties such as heat capacity as a function of reacted fraction. Their results indicated that both the assumption of thermal equilibrium and neglecting the convection term in the energy equation influenced the total amount of hydrogen desorbed from the reactor. Kuznetsov [11] presented analytic criteria for the validity of some of the most commonly applied assumptions, together with an analytic solution of an idealized heat and mass transfer situation.

The aim of this work was to establish and experimentally validate a one-dimensional heat and mass transfer model. The model assumes thermal equilibrium between the hydrogen gas and metal hydride. The model was validated using a cylindrical hydrogen storage container where hydrogen was distributed from the centre and heat was transferred through the reactor walls.

5.3 MATHEMATICAL MODEL

The equations governing the heat transfer, mass transfer and chemical reaction within the hydrogen storage bed are presented hereafter. The model describes a cylindrical storage container, shown in Figure 5.3. The container is filled with an AB_5 type metal hydride in the form of a powder, and hydrogen is filled or discharged through a central tube (filter tube) positioned in the middle of the storage unit. Due to the symmetry of the storage unit, heat transfer and hydrogen transport will mainly be in the radial direction, simplifying the numerical model to a one-dimensional transient model case.

Thermal equilibrium between the storage bed and hydrogen gas are assumed; hence, only one common energy equation for both the gas and solid phase is necessary, as given by Equation (5.1). Angular symmetry around the filter element is assumed and axial variations are neglected in the presented model.

(5.1) $$\rho \cdot c_p \cdot \frac{\partial T}{\partial t} - \frac{1}{r} \cdot \left(r \cdot k_{eff} \cdot \frac{\partial T}{\partial r} \right) + \rho_g \cdot c_{p,g} \cdot V_g \cdot \frac{\partial T}{\partial r} = \dot{m} \cdot \left| \Delta H \right|$$

Here $\dot{m}$ is the gas-solid reaction rate and is defined as $\dot{m}_{abs} > 0 > \dot{m}_{des}$ and $\left(\rho \cdot c_p \right)$ is a volume-averaged term, calculated from Equation (5.2).

(5.2) $$\rho \cdot c_p = \varepsilon \left(\rho_g \cdot c_{p,g} \right) + (1 - \varepsilon) \cdot \left(\rho_{MH} \cdot c_{p,MH} \right)$$

The gas density ρ_g is calculated using the ideal gas law and tabulated values for the heat capacity at standard condition are used. The metal hydride density is calculated with (5.6) and the metal hydride heat capacity is calculated with Equation (5.5).

The hydrogen gas mass balance is calculated from Equations (5.3)

(5.3) $$\varepsilon \cdot \frac{\partial \rho_g}{\partial t} + V_g \cdot \frac{\partial \rho_g}{\partial r} = -\dot{m}$$

$\dot{m}$ is the gas solid reaction rate calculated from Equation (5.10). The solid mass balance is calculated with Equation (5.4).

(5.4) $$\frac{\partial C}{\partial t} = \dot{C}$$

5.4 MODELLING PARAMETERS

The porosity (ε) is calculated from a simple macroscopic consideration, i.e. $\varepsilon = \frac{Gas\ Volume}{Total\ Volume} = 1 - \frac{\rho_{packing}}{\rho_{MH}}$. The packing density (bulk density $\rho_{packing}$) was measured to $\rho_{packing} \approx 3900 \ \frac{\text{kg}}{\text{m}^3}$ using a volumetric method and with unhydrogenated powder. The crystallographic density of solid $LaNi_5$ is $\rho_{MH} = 8310 \frac{kg}{m^3}$. Using these values the porosity was calculated to be $\varepsilon \approx 0.47$, which is comparable to values used by other authors [1-3,5,6,8,9].The porosity is assumed to be constant in the present model even though local values as high as 0.7 may occur in the region in the near vicinity of the container and central

tube walls (typically a region extending about half a particle diameter from the solid wall [12]). The value of ΔH for absorption and desorption were taken from Førde et al [13].

The specific heat capacity of the metal hydride $\left(c_{p,MH}\right)$ is influenced by the amount of adsorbed hydrogen, and may be expressed in terms of the hydrogen-to-metal atomic ratio $\left(C\right)$[14,15]. In the present work the specific heat capacity was expressed by the Neuman kop (additive) rule, Equation (5.5):

(5.5) $$c_{p,MH} = \frac{5 \cdot M_{Ni} \cdot c_{p,Ni} + M_{La} \cdot c_{p,La} + M_{Mm} \cdot C_{p,Mm}}{M_{alloy} + \Gamma \cdot C_{\max} \cdot M_H} + \frac{\Gamma \cdot C_{\max} \cdot M_H \cdot c_{p,H}}{M_{alloy} + \Gamma \cdot C_{\max} \cdot M_H}$$

Here, $\Gamma = \frac{C}{C_{\max}}$ is the reacted fraction and $C_{\max}$ is the maximum H/AB_5 molar ratio. To determine the heat capacity of hydrogen inside the metal, literature data [14,15] were fitted to the calculated specific heat capacity using $c_{p,H}$ as the unknown parameter. A good fit was achieved using $c_{p,H} = 13000\left[\frac{J}{kg \cdot K}\right]$; this value being slightly lower compared to the specific heat capacity of gaseous hydrogen at standard temperature and pressure($c_{p,H_2} \approx 14332 \frac{J}{kg \cdot K}$).

The solid density of hydrogenated metal hydride (ρ_{MH}) was estimated using a linear relationship, as shown is Equation (5.6). We do not know the exact volume expansion of our alloy however the metal hydride was assumed to increase its volume (swell (S)) with 18.9%, which are the same as the measured expansion for an $LaNi_5$ alloy [16].

(5.6) $$\rho_{MH} = \frac{\left(A + C\right)}{\left(1 + \frac{S \cdot C}{100 \cdot C_{Max}}\right)} \cdot \frac{\rho_{MH\ initial}}{A}$$

The assumption of a linear variation of the solid density is not strictly correct, since there is much less expansion at low hydrogen to metal concentrations (α phase), but this is a realistic simplification.

Several models are available for the effective thermal conductivity in porous media. Important parameters are the porosity, the size and shape of the particles, the gas pressure, and the gas and solid material thermal conductivities. Hane and Kallweit [17] measured the effective thermal conductivity of $LaNi_{4.7}Al_{0.3}$ and found that for pressures below 1 bar the effective thermal conductivity was highly pressure dependent and that the pressure dependency of the effective thermal conductivity decreased for pressures above 1 bar at 293.15 K. They also measured that the influence of particle decay during cycling only affected the effective thermal conductivity in the lower gas pressure regions (below ca. 0.01 bar). Hane and Kallweit [17] also measured the effective conductivity at different hydrogen-to-metal concentrations and found that for equilibrium pressures above 1 bar, the effective thermal conductivity was little influenced by the hydrogen-to-metal concentrations. Deng et al [18]

developed a model for the effective thermal conductivity in a metal hydride bed and showed through a parametric analysis that the effect of various porosities (in the range $0.3 < \varepsilon < 0.6$) and temperatures ($300 < T < 400$ K) on the effective thermal conductivity was small as long as the solid thermal conductivity was less than $50\frac{W}{m \cdot K}$. For solid thermal conductivities below $50\frac{W}{m \cdot K}$ the effective thermal conductivity was estimated to be between 0.5 and 2.0 $\left[\frac{W}{m \cdot K}\right]$.

In order to estimate the energy transfer due to advection in Equation (5.1) a velocity field with its corresponding pressure field must be established. The hydrogen pressure is also an important parameter in the calculation of the reaction rate of hydrogen absorption and desorption. The Darcy flow model is valid in circumstances where the order of magnitude of the pore Reynolds number (Equation (5.7)) is much smaller than unity [19]:

(5.7) $$\mathrm{Re}_p = \frac{V_g \cdot D_p \cdot \rho_g}{\mu \cdot \varepsilon}$$

For the experiments reported in the present paper the highest measured flow rate out of the reactor was about 50 Nl/min, corresponding to a local pore Reynolds number of ca. 0.018, indicating that Darcy's flow model (Equation(5.8)) is valid.

(5.8) $$V_g = -\frac{K_D}{\mu_g} \cdot \frac{\partial P_g}{\partial r}$$

The permeability (K_D) of the porous medium is calculated using the Carman Coecensky Equation (5.9) taken from [19], μ is the dynamic viscosity at standard condition and P is the gaseous pressure.

(5.9) $$K_D = \frac{D_P^2 \cdot \varepsilon}{180 \cdot (1-\varepsilon)^2}$$

The rate of the solid/gas reaction ($\dot{m}$) are part of the source term occurring in the mass balance equations (Equations (5.1) and (5.3)) and in the energy equation (Equation (5.2)) and is estimated using Equation (5.10) [13] .

(5.10)
$$\frac{\left[-\ln(1-X)\right]^{\frac{1}{n}-1}}{n(1-X)} \cdot \frac{dX}{dt} = Z \cdot \exp\left(-\frac{E_a}{R \cdot T}\right) \cdot \ln\left(\frac{P_g}{P_{eq}}\right) \qquad \textit{Absorption}$$

$$\frac{\left[-\ln(1-X)\right]^{\frac{1}{n}-1}}{n(1-X)} \cdot \frac{dX}{dt} = -Z \cdot \exp\left(-\frac{E_a}{R \cdot T}\right) \cdot \ln\left(\frac{P_{eq}}{P_g}\right) \qquad \textit{Desorption}$$

The dimensionless coefficient X is calculated from Equation (5.11) and varies between 0 and 1. n is a fitting parameter and Z is a rate constant.

(5.11)
$$X = \frac{C - C_1}{C_2 - C_1} \qquad Absorption$$
$$X = \frac{C_2 - C}{C_2 - C_1} \qquad Desorption$$

In Equation (5.11) C represents the actual particle hydrogen concentration, and C_1 and C_2 are the concentration limits of the initial and final states of the reaction.

Another important parameter in Equation (5.10) is the equilibrium pressure P_{eq}, which is a function of both temperature and solid hydrogen concentration.

The equilibrium pressure was measured experimentally using a Sivert type of experimental set up described by Sato [20]. and is modelled using the model presented by Lototsky at al. [21]. The experimentally found pressure concentration isotherms was fitted to a model developed by Lototsky at al. [21]. The Lotosky model contains 6 fitting parameters and reproduces the experimental data with good accuracy covering the entire concentration and temperature ranges. A comparison between measured and simulated equilibrium pressures are shown in Figure 5.1.

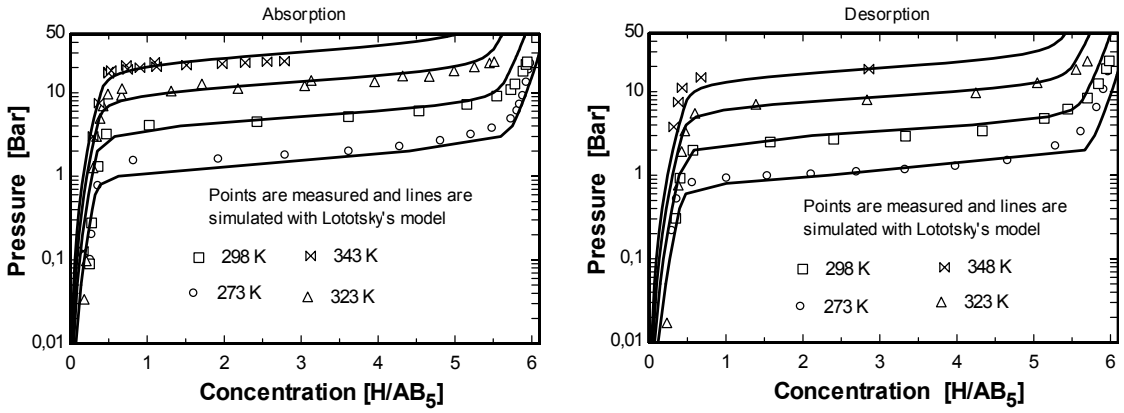

A B

Figure 5.1 Measured and simulated pressure and concentration isotherms for absorption A and desorption B.

5.5 INITIAL AND BOUNDARY CONDITIONS

In order to solve Equations (1.1) and (1.6)-(1.8), a proper set of boundary conditions must be defined. For the present conditions, the applicable boundary conditions are given by Equations (5.12) -(5.14):

(5.12) $$P_g(r,0) = P(0) \qquad T(r,0) = T(0) \qquad C_{MH}(r,0) = C_{MH}(0)$$

(5.13) $$\frac{\partial T(r_1,t)}{\partial r} = 0 \qquad T(r_2,t) = T_{wall}$$

(5.14) $$P_g(r_1,t) = P_g \qquad \frac{\partial P_g(r_3,t)}{\partial r} = 0$$

The hydride bed is assumed to initially have a uniform temperature T(0), hydrogen-to-metal atomic concentration C(0) and gas pressure P(0). Heat is transferred to or from the reactor wall by convection heat transfer between the reactor wall and the surroundings. Two options are available for the reactor wall boundary condition: Either the wall heat flux is estimated from the external wall heat transfer coefficient and surrounding fluid temperature, or a Dirichlet condition where the wall temperature on the surface is prescribed. In the present study, a prescribed wall temperature is used, as this was measured experimentally.

A Neuman type of boundary condition was used for the gas pressure at the filter element. The outer container wall was assumed to be impervious for the hydrogen gas.

The set of equations were solved using the Finite-Element computer code Comsol Multiphysic 3.2a [22]. Correct computational element resolution was assured by successively refining the computational mesh until the simulated results were unaffected by further refinements.

5.6 EXPERIMENTAL SET UP

Testing of the metal hydride storage container was performed using an experimental set up as shown in Figure 5.2.

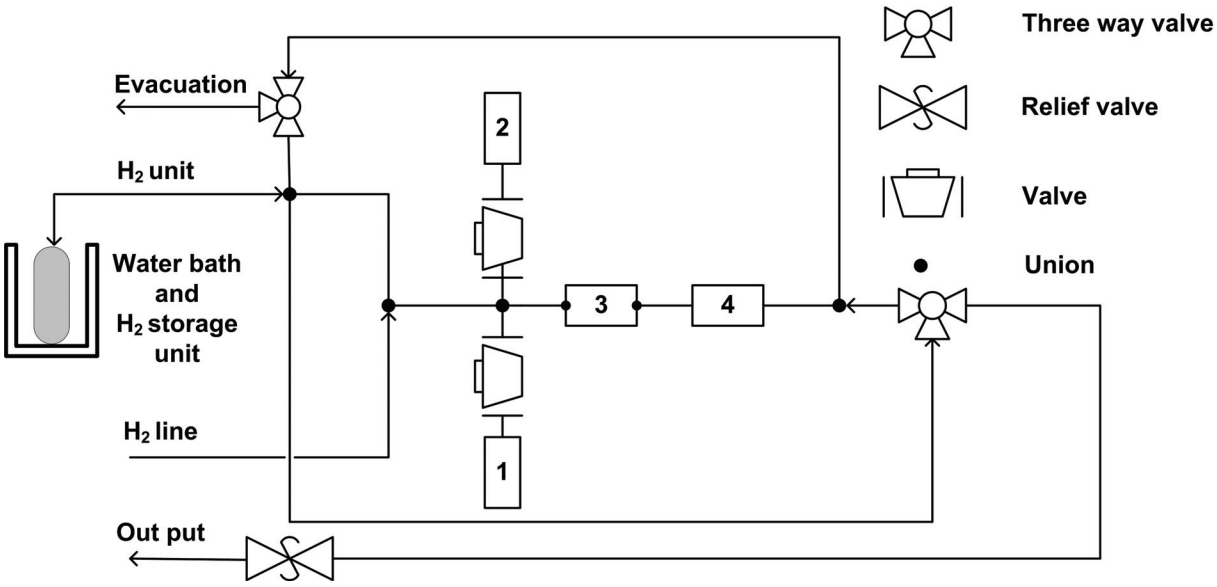

Figure 5.2 Schematic diagram of the set up for the testing hydrogen storage units: 1 Buffer volume, 2 pressure sensor (0-25 bar absolute), 3 hydrogen flow meter (0-30 l/min), 4 flow controller.

The set up consisted of a storage container, a water bath, a H_2 flow meter (3), thermocouples, a gas pressure sensor (2), an evacuation line connected to a vacuum pump and an exhaust line. The test bench was connected to a gas distribution system containing both argon and hydrogen. This set up made it possible to measure both the hydrogen flow rate and the tank pressure. In addition, a flow controller (4) was installed, enabling charging and discharging at constant hydrogen flow rates. The desired charging/ discharging pressures were fixed using a needle valve during discharging and by using a pressure regulator valve during charging. Hydrogen with a maximum pressure of 10 bar was supplied during charging of the unit. In addition, vacuum conditions were provided by a rotary vacuum pump equipped with an in-

line vacuum sensor. The cylindrical Hydrogen storage reactor is shown in Figure 5.3 was connected to the test bench described above.

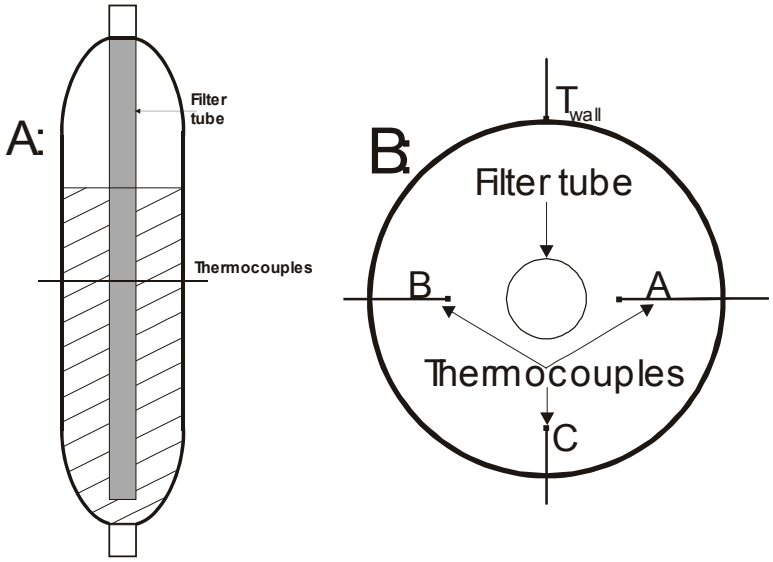

Figure 5.3 Schematic of the metal hydride test reactor with thermocouples positioned at various radial positions, thermocouple A is closest to the centre of the reactor and thermocouple C is closest to the reactor wall.

The reactor shell had outer and inner diameters of 50.8 and 46.1 mm, respectively, yielding a total external heat transfer surface of 0.16 m^2 (i.e. a specific heat transfer surface of 0.19 m^2/kg metal hydride). The internal length of the reactor was 200 mm. Hydrogen entered and left the reactor through a filter element positioned in the centre of the reactor. The filter element was made from stainless steel, had a length of 190 mm and an outer diameter of 10.5 mm. The test reactor was immersed into a water bath, where water is circulated in a short external circuit and back into the water bath, creating well-stirred conditions. Three 3.2 mm diameter thermocouples with 5 seconds response time were inserted into the reactor at different radial positions (9.7, 13.3 and 17.2 mm from the centre) at an axial position 90 mm from the bottom of the reactor. In addition a thermocouple was welded to the outside reactor wall at the same axial position as the other thermocouples. The reactor was filled with 850 g of a mischmetal-modified alloy AB_5 type of alloy ($La_{0.83}Ce_{0.1}Pr_{0.04}Nd_{0.03}Ni_{4.40}Al_{0.60}$). The alloy was supplied by LABTECH [23] in an activated form. Before any experiments were performed, the metal hydride powder was heated to 433 K under vacuum conditions for ca 3 hours for activation. The capacity was checked through volumetric charging of the reactor and cycled several times achieving reproduce able values of reversible capacity and reaction time. The hydrogen used during all the experiments was of 99.9999 % purity.

5.7 EXPERIMENTAL AND MODELLING RESULTS

5.7.1 Experimental results

The main purpose of the experiments was to characterise the metal hydride storage unit's thermal behaviour, including the reactors ability to deliver hydrogen at various pressures, temperatures and flow rates. Two different types of experiments were performed: charging and discharging at constant pressure and discharging with a constant flow rate. The constant desorption flow rate experiments were performed to simulate an application where the reactor

should supply hydrogen to e.g. a fuel cell operating at a close to constant load, hence a constant hydrogen flow rate was supplied from the metal hydride unit. In these experiments the gas pressure and metal hydride temperature decreased slowly until the reactor no longer was capable of delivering the prescribed flow. Desorption experiments were performed using constant water bath temperatures of 293, 303 and 313 K. The reactor was capable of delivering 80% of its total capacity of approximately 130Nl at a constant flow rate of $1.9 \frac{Nl}{\min \cdot kg} H_2$ with a 1.1 bar end pressure and 293 K water bath temperature. A flow of 1.9 litres per kg per minutes correspond to absorption or desorption rate of 0.001439 H/AB_5 per seconds. More than 95% of the total reactor capacity could be delivered at the same flow rate and end pressure but with a water bath temperature raised to 303 K. The reactor's ability to deliver hydrogen was not changed when the water bath temperature was increased to 313 K. However, at higher end pressures the reactor's ability to deliver hydrogen was more sensitive to the water bath temperature, due to the rapid fall in equilibrium pressure at lower hydrogen concentrations. The performed experiments indicated that a stack of three reactors at the conditions described above can deliver ca. 4.8 Nl/min for at least 60 minutes, corresponding to the amount of hydrogen required to deliver ca 400-W electrical power from a PEM fuel cell, based on operation experience from a reel 500 W fuel cell.

However, during the charging and discharging experiments at constant pressure the response in both pressure and temperature are much faster than for the constant flow rate experiments. During charging and discharging the pressure raised or decreased to the given charging or discharging pressure within a period of 180 s for all the performed experiments. The measured temperatures experienced a rapid transient period the first 180 s of the experiment as shown in Figure 5.5 and Figure 5.6. The maximum or minimum for the different thermocouples occurred first for the thermocouple closest to the reactor wall and last for the thermocouple closest to the centre of the reactor. The thermocouple closest to the reactor centre always experienced the largest fluctuation in temperature. This is due to the reactor's low thermal conductivity, and high heat of reaction.

In order to investigate the effect of different charging and discharging pressures on the reactor behaviour and charging times, several experiments were performed. These experiments indicated that both the reaction rate and the amount of hydrogen gas absorbed/desorbed depended strongly on the charging/discharging pressures. In the early stage of the reaction, both the temperature and hydrogen concentration changed rapidly until the equilibrium pressure reached the hydrogen gas pressure. After approximately three minutes the reactor reached its maximum temperature (charging) or minimum temperature (discharging) and the reaction rate decreased. At this time the reactor temperature started to decrease (charging) or increase, (discharging). This change in temperature caused a corresponding change in the equilibrium pressure, hence more hydrogen could be absorbed (charging mode) or desorbed (discharging mode). Finally, the temperature in the reactor approached the water bath temperature, and the metal hydride equilibrium pressure approached the charging/discharging pressure. This indicated that the process was reaction rate controlled until the reactor's maximum or minimum temperature was reached and heat transfer controlled for the rest of the charging or discharging reaction.

The effect of various charging and discharging rates on the time required for the reactor to absorb or desorb 50% if its full capacity was investigated by performing experiments at water bath temperatures of 293, 303 and 313 K and with different charge/discharge pressures, some results are shown in Figure 5.4. Prior to each experiment the reactor temperature was uniform

and equal to the water bath temperature. During the absorption and desorption experiments the initial gas pressure was kept at 0.5 and 10 bar respectively for all the performed experiments.

Figure 5.4A and C, shows the relationship between the charging/ discharging pressure and the time required to absorb or desorb 50% of its full capacity at constant water bath temperature.

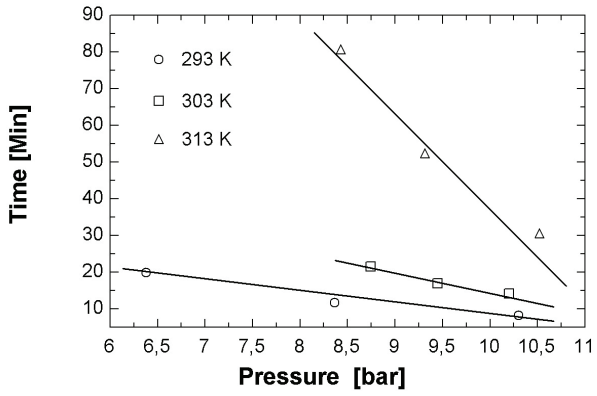

A: Absorption

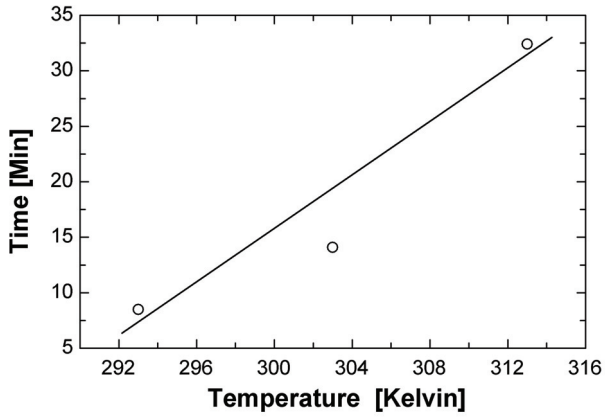

B: Absorption

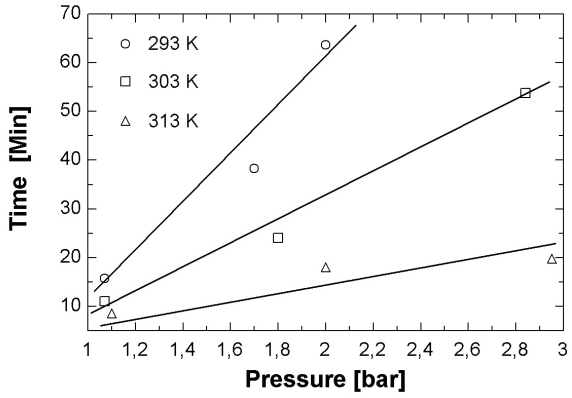

C: Desorption

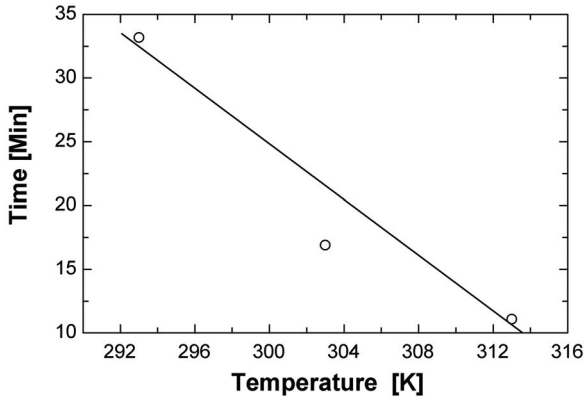

D: Desorption

Figure 5.4 Shows the time for 50% reacted fraction for absorption and desorption as a function of different charging/discharging pressures (A, C) and as a function of different temperatures (B, D) then the charging and discharging pressures are kept constant.

It can be seen from Figure 5.4 A and C, the reaction time decreases with increased charging pressure for absorption and with lower discharge pressure for desorption. This change in reaction time can be explained from the shape of the metal hydrides pressure-concentration-temperature (PCT) curves. It is observed from Figure 5.1 that the metal hydride is able to absorb more hydrogen at higher pressures at constant temperature. The decrease in reaction time during desorpion can be explained with the same argument i.e that the metal hydride is able to desorb more of its total capacity at the same temperature if the gas pressure is decreased. The influence of the water bath temperature on the charging time is shown in Figure 5.4 B and D for charging/discharging, respectively. The discharging pressure used in

Figure 5.4 D was 1.4 bar and the charging pressure used in Figure 5.4B was 10.1 bar. It can bee seen that the reaction time decreases with lower temperatures for absorption and increases for desorption. These changes in reaction time are related to the metal hydrides PCT characteristic.The metal hydride is able to absorb more hydrogen at the same charging pressure if the temperature is decreased and is able to desorb more hydrogen at the same discharge pressure if the temperature is increased.

To further analyse and improve the understanding of the experimental results an energy balance was performed using Equation (5.15). The experimental reactor was considered as four different radial control volumes, each having the inserted thermocouples in the centre of the control volume. The measured temperatures were assumed being representative for each control volume temperature. The temperature of the control volume closest to the reactor wall was taken as the average of the wall thermocouple and thermocouple C shown in Figure 5.2. The metal hydride mass in each control volume was estimated based on the total metal hydride mass and the sizes of the different control volumes; these masses were denoted m_1, m_2, m_3 and m_4.

(5.15) $$\sum_{i=1}^{4} m_i \cdot c_{p,i} \cdot \frac{\partial T_i}{\partial t} + m_{reactor} \cdot c_{p,wall} \cdot \frac{\partial T_{wall}}{\partial t} - \dot{Q}_{H_2} - \dot{Q}_{reaction} = \dot{Q}_w$$

Heat is removed or supplied to the reactor by the hydrogen gas $\dot{Q}_{H_2}$, heat is also produced or consumed in the solid metal reaction $\left(\dot{Q}_{reaction}\right)$ and heat is also transferred into or out of the reactor to the surrounding. All the heat fluxes except the heat exchange between the reactor wall and water bath $\left(\dot{Q}_w\right)$ were estimated based on measured values. These heat fluxes are used in Equation (5.15) to calculate the heat flux between the water bath and metal hydride reactor.

The calculations indicate that $\left|\dot{Q}_w\right| \geq \left|\dot{Q}_{reaction}\right| \geq \left|\dot{Q}_{H_2}\right| \geq \left|\dot{Q}_{mass}\right|$, where $\dot{Q}_{mass}$ is the energy used to change the temperature of the metal hydride bed and the reactor shell.

The estimated wall heat duty ($\dot{Q}_w$), and the estimated heat flux $\dot{Q}_w$ was used to estimate the reactors inner wall temperature T_{wall}. This value was used together with the mass averaged metal hydride bed temperature $\left(\overline{T}_{MH}\right)$ to estimate the wall to metal hydride heat transfer coefficient $\alpha_{wb} = \frac{\dot{Q}_w}{T_{wall} - \overline{T}_{MH}}$. The reactor wall to hydride bed heat transfer coefficient dropped rapidly towards an asymptotic value of 300-400 $W/\left(m^2 \cdot K\right)$ over a period of about 10-15 minutes for all experiments. The metal hydride bed heat transfer coefficient was calculated using mass averaged temperatures, yielding slightly higher coefficients than predicted using the literature correlation of [12], where a steady state coefficient of ca. 200 $W/m^2 \cdot K$ was calculated, based on an effective bed thermal conductivity of $1.5 W/\left(m \cdot K\right)$. The observed difference between measured and calculated heat transfer coefficients can be accounted for by the hydrogenation/ dehydrogenation reactions taking place in the bed material, which is not accounted for in the correlation. Chemical reactions act like a heat

source/ heat sink and will increase the value of the apparent heat transfer coefficient, as pointed out by Schlünder [24].

5.7.2 Numerical results and their discussion

The numerical model presented above was compared to selected experimental results in order to verify the model. The set of modelling parameters used in the calculations are given in Table 5.1. The results of an absorption experiment where the unit was filled at a charging pressure of 7 bar, a water bath temperature of 293 K and an initial gas pressure of 0.5 bar in the system (before starting the absorption) are shown in Figure 5.5.

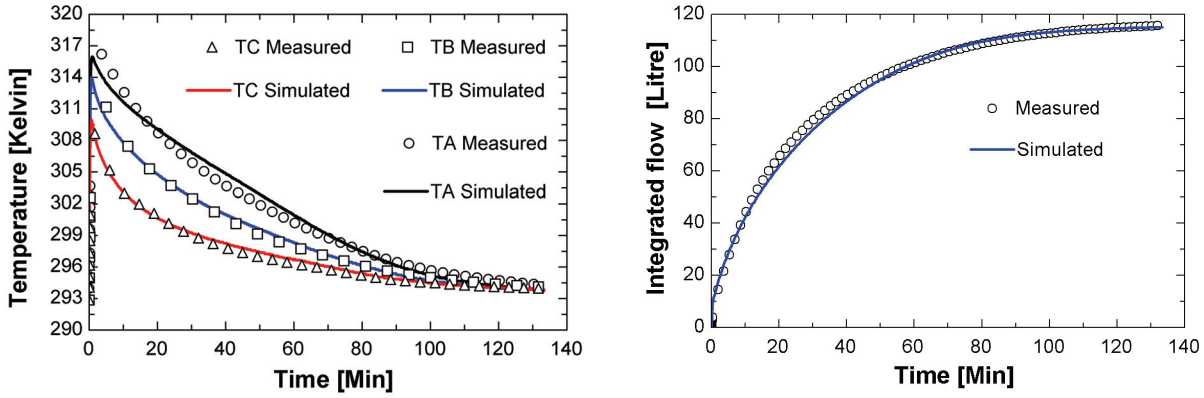

A B

Figure 5.5 Measured and simulated temperatures during absorption with 293 K in the water bath and a pressure of 7 bar, and the measured and simulated flow out of the reactor. TA correspond to thermocouple A, TB to thermocouple B, TC to thermocouple C in Figure 5.3, and B shows the measured and simulated flow.

From Figure 5.5 it is observed that the measured and calculated temperature profiles are in good agreement. The measured and calculated hydrogen flows also correspond well to each other establishing confidence in the numerical model. A radial temperature profile is also observed, the temperature is monotonically increasing towards the centre of the reactor. This is as expected, since there is a finite and limiting effective thermal conductivity of the granular metal hydride bed.

Similarly, a desorption experiment was performed where hydrogen was desorbed through a relief valve set to a downstream pressure of 2.5 bar, and a water bath temperature of 303K. Both the experimental results and results from the numerical calculations are shown in Figure 5.6.

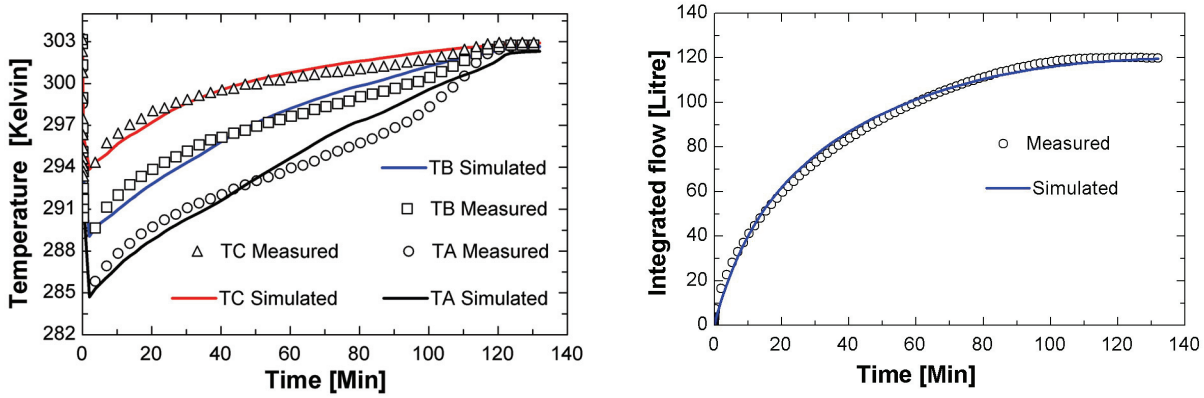

A B

Figure 5.6 Measured and simulated temperatures during desorption with 303 K in the water bath and a constant desorption pressure of 2 bar. TA correspond to thermocouple A, TB to thermocouple B, TC to thermocouple C in Figure 5.3, and B shows the measured and simulated flow.

The numerical predictions agree well with the experimental results. The temperature variations are smallest closest to the reactor wall and largest in the centre of the reactor, due to the finite thermal conductivity of the metal hydride powder. The total amount of hydrogen flow out of the reactor is predicted with good accuracy for the entire experiment duration.

For both absorption and desorption situations the temperature changes were smallest close to the water bath. The reaction rate and equilibrium pressure is linked to the temperature and therefore the reaction rate is higher close to the heat transfer surface. An overview of the value of the most important modelling parameters is given in Table 5.1.

Table 5.1 Modelling parameters used in present work.

Absorption		Desorption	
Parameters	Values	Parameters	Values
$c^{1}_{p,MH}$ [J/kg·K]	350	$c^{2}_{p,MH}$ [J/kg·K]	540
Z^{A} [1/s]	271	$^{A}Z^{D}$ [1/s]	254
E^{A}_{a} [kJ/mol]	25	E^{D}_{a} [kJ/mol]	26
ΔH^{A} [kJ/mol]	-27	ΔH^{D} [kJ/mol]	26
C_1 [-]	0.1	C_2 [-]	6
$\rho^{1}1$ [kg/m^3]	8310	Swelling [%]	18.9
k_{eff} [W/m^2·K]	1.5	K_D [m^2]	$1.38 \cdot 10^{-11}$
ε [-]	0.5	D_p [μm]	10

1 initial alloy 2 completely hydrated
A Absorption D Desorption

The sensitivity of the various modelling parameters on the calculated reactor behaviour was investigated by systematically varying each parameter in the model.

In the numerical simulation the reactor was charged with a 9 bar gas pressure, the initial gas pressure in the reactor was 1 bar with corresponding hydrogen to metal atomic ratio of 0.09. The initial temperature and boundary wall temperature $T(r_2,t)$ was kept at 293 K.

The Peclet number defined as the ratio of the amount of heat transferred with advection divided with the amount of heat transferred through conduction number was calculated. The Peclet numbers maximum value was reached in the beginning of the simulations and never exceeded a value of 10-3. From this it is concluded that heat transferred by advection is less important than heat transported by conduction.

The wall to bed heat transfer coefficient (α_{wb}) based on a mass averaged temperature was calculated from the simulation. The wall to bed heat transfer coefficient found through the simulations yielded similar result as the one found from the experimental energy balances.

The set of parameters given in Table 5.1 were used as basic parameters, and each of the parameters were sequentially perturbed with a scaling coefficient K_{scaling}. These perturbations effect of the time used to charge the reactor with 85% of its total capacity was then calculated. The results are given in Table 5.2

Table 5.2 Sensitivity analysis the table shows the percentages change in times it takes to charge the reactor with 85% of its total capacity, with different perturbations in model parameters. $K_{scaling}$ is defined as $\frac{parameter\ value}{reference\ parameter\ value}$ where the reference parameter value is given in Table 5.1.

K_{scaling}	Z	E_a	$c_{p,MH}$	S	k_{eff}	ΔH
1.4	-3.4	1850	0.4	-2.1	-22.7	26.2
1.2	-2.1	144.7	0.4	-2.1	-12.0	13.3
1.1	-1.3	28.3	-0.1	0.0	-6.4	6.9
0.9	0.4	-8.6	-1.4	-0.1	5.6	-7.3
0.8	3.0	-8.6	-1.7	0.0	17.6	-15.0
0.6	8.9	-8.6	-1.7	0.0	45.9	-27.9

To further analyse the data presented in Table 5.2, some of the parameters (Z, Ea, ΔH and k_{eff}) were normalized to their largest absolute value yielding relative values varying between plus and minus hundred percent. These new values are plotted versus the perturbation factor $K_{scaling}$ in Figure 5.7. We have chosen not to present the influence of the swelling factor S and heat capacity $c_{p,MH}$ since perturbation of these parameter only to a small extend changes the charging time. It can be seen from Figure 5.7 that perturbations of Z, k_{eff} and ΔH yield a linear change in the charging time; however, perturbations in Ea yield asymptotic behaviour in charging time.

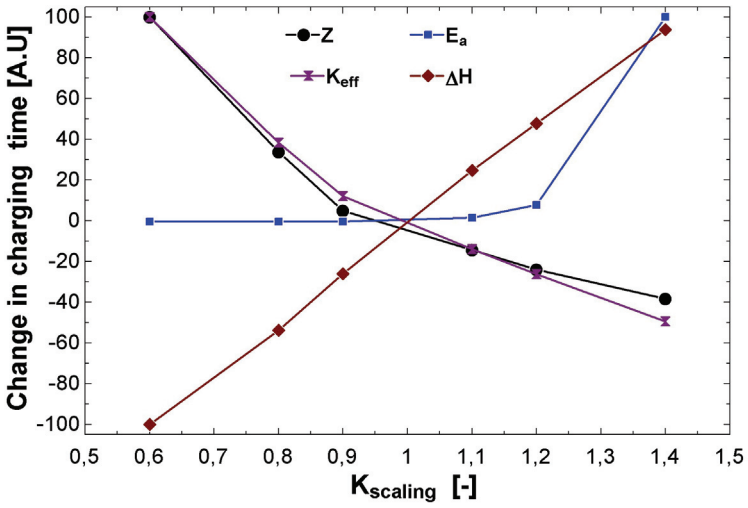

Figure 5.7 Normalised change in times it takes to charge the reactor with 85% of its total capacity. $K_{scaling}$ is defined as the fraction between the parameters value and the reference value. The reference parameter value is given in Table 5.2.

The simulation shows that an increase in the activation energy with 40 % increases the charging time with more than 100 %, on the other hand a decrease in the activation energy will not cause the same decrease in charging time due to the fact that the reaction is already fast. An increase in the thermal conductivity of 40% decreases the charging time with 23 %, approximately the similar result is achieved by decreasing the heat of reaction with 40%. However, a decrease in the effective conductivity of 40% will cause a larger increase in the effective charging time, due to the fact that the effective conductivity already is small. It can further be seen that a change in heat capacity rate constant and swelling cases minor changes in the charging and discharging time. A decrease or increase in the rate constant will not affect the reaction rate since its value already is large for the hydrogenation of the studied AB_5 type alloy. The heat capacity and swelling factor are more passive parameters not directly connected neither to the heat transport nor to the reaction rate. Therefore these two parameters are less important for the charging and discharging time than the activation energy, thermal conductivity and heat of reaction.

5.8 Conclusions

A cylindrical reactor filled with the AB5 type ($La_{0.83}Ce_{0.1}Pr_{0.04}Nd_{0.03}Ni_{4.40}Al_{0.60}$) alloy was investigated with respect to the rates of hydrogen charging and discharging. The unit was able to deliver more than 80 % of its capacity towards a 1.1 bar gas pressure with a constant flow rate of 0.001439 H/AB_5 per sec if the water bath temperature was held above 293 K. The charge and discharge times for this reactor were dependent on both charging and discharging pressure and surrounding water bath temperature in the temperature range from 293-313 K. A one-dimensional transient heat and mass transfer model was developed, reproducing the reaction rates and temperature fields in the reactor with good accuracy. A sensitivity analysis indicating that the activation energy, effective thermal conductivity and heat of the reaction were the most sensitive parameters for this system. All simulations showed that the reaction was fastest in the beginning if a charge/discharge cycle, and close to the external heat transfer surface. The performed experiments and simulations indicate that the charging and discharging process is reaction rate controlled in the first part of the experiment while the other part of the experiment is heat transfer controlled.

Acknowledgements

The authors will thank Dr Jan Petter Mæhlen for the assistance of filling the reactor with metal hydride powder and assembling the thermocouples.

References

[1] Jemni A, Nasrallah B, S, Lamloumi J. Experimental and theoretical study of a metal-hydrogen reactor. Int J Hydrogen Energy 1999; 24(7): 631-644.

[2] Jemni A, Nasrallah B, S. Study of 2-Dimensional Heat-Transfer and Mass-Transfer During Absorption in a Metal-Hydrogen Reactor. Int J Hydrogen Energy 1995; 20(1): 43-52.

[3] Jemni A, Nasrallah B, S. Study of 2-Dimensional Heat and Mass-Transfer During Desorption in a Metal-Hydrogen Reactor. Int J Hydrogen Energy 1995; 20(11): 881-891.

[4] Jemni A, Nasrallah B, S, Lamloumi J. Study of Heat and Mass-Transfer in a Metal Hydrogen Reactor. Zeitschrift Fur Physikalische Chemie-International Journal of Research in Physical Chemistry & Chemical Physics 1994; 183: 197-203.

[5] Nasrallah B, S, Jemni A. Heat and mass transfer models in metal-hydrogen reactor. Int J Hydrogen Energy 1997; 22(1): 67-76.

[6] Aldas K, Mat M, D, Kaplan Y. A three-dimensional mathematical model for absorption in a metal hydride bed. Int J Hydrogen Energy 2002; 27(10): 1049-1056.

[7] Mat M, D, Kaplan Y. Numerical study of hydrogen absorption in an $LmNi_5$ hydride reactor. Int J Hydrogen Energy 2001; 26(9): 957-963.

[8] Mat M, D, Kaplan Y, Aldas K. Investigation of three-dimensional heat and mass transfer in a metal hydride reactor. International Journal of Energy Research 2002; 26(11): 973-986.

[9] Demircan A, Demiralp M, Kaplan Y, Mat M, D, Veziroglu T, N. Experimental and theoretical analysis of hydrogen absorption in $LaNi_5$ H_2 reactors. Int J Hydrogen Energy 2005; 30(13-14): 1437-1446.

[10] Nakagawa T, Inomata A, Aoki H, Miura T. Numerical analysis of heat and mass transfer characteristics in the metal hydride bed. Int J Hydrogen Energy 2000; 25(4): 339-350.

[11] Kuznetsov A, V, Vafai K. Analytical Comparison and Criteria for Heat and Mass-Transfer Models in Metal Hydride Packed-Beds. Int J Heat Mass Transfer 1995; 38(15): 2873-2884.

[12] Hewitt G, F. Heat exchanger design handbook 1998 Part 1: Heat exchanger theory; Part 2 : Fluid mechanics and heat transfer. edn. New York: Begell House, Inc, 1998.

[13] Førde T, Maehlen J, P, Yartys V, A, Lototsky M, V, Uchida H. Influence of intrinsic hydrogenation/dehydrogenation kinetics on the dynamic behaviour of metal hydrides: A semi-empirical model and its verification. Int J Hydrogen Energy 2007; 32(8): 1041-1049.

[14] Dantzer P, Orgaz E. Thermodynamics of Hydride Chemical Heat-Pump .2. How to Select a Pair of Alloys. Int J Hydrogen Energy 1986; 11(12): 797-806.

[15] Ohlendorf D, Flotow H, E. Heat-Capacities and Thermodynamic Functions of $LaNi_5$, $Lani_5H_{0.36}$ and $LaNi_5H_{6.39}$ from 5 to 300 K. Journal of the Less-Common Metals 1980; 73(1): 25-32.

[16] Yartys V, A, Burnasheva V, V, Semenenko K, N, Fadeeva N, V, Solovev S, P. Crystal-Chemistry of $RT_5H(D)X$, $RT_2H(D)X$ and $RT_3H(D)X$ Hydrides Based on Intermetallic Compounds of $CaCu_5$, $MgCu_2$, $MgZn_2$ and $PuNi_3$ Structure Types. Int J Hydrogen Energy 1982; 7(12): 957-965.

[17] Hahne E, Kallweit J. Thermal conductivity of metal hydride materials for storage of hydrogen: Experimental investigation. Int J Hydrogen Energy 1998; 23(2): 107-114.

[18] Sun D, W, Deng S, J. A Theoretical-Model Predicting the Effective Thermal-Conductivity in Powdered Metal Hydride Beds. Int J Hydrogen Energy 1990; 15(5): 331-336.

[19] Kaviany M. Principles of heat transfer in porous media. edn. New York: Springer, 1991.

[20] Sato M. Studies of hydrogen absorption and desorption processes in advanced intermetallic hydrides. Ph.D Thesis from Department of Chemistry Faculty of Mathematics and Natural Sciences University of Oslo [Oslo], 2005.

[21] Lototsky M, V, Yartys V, A, Marinin V, S, Lototsky N, M. Modelling of phase equilibria in metal-hydrogen systems. J Alloys Compd 2003; 356: 27-31.

[22] Comsol multiphysics. www.comsol.se., 03.06-2007.

[23] LABTECH Int. Co. Ltd. Alloys Research and Manufacturing. Mladost-1, bl.25/A, Sofia-1784, BULGARIA; . http://labtech.solo.bg/, 03.07-2007.

[24] Schlünder E,U. Heat Transfer to Packed and Stirred Beds from the Surface of Immersed Bodies. Chemical Engineering and Processing 1984; 18(1): 31-53.

6 CHARGING AND DISCHARGING TIMES OF HYDROGEN FOR A METAL HYDRIDE STORAGE TANK

T. Førde[1], V.A. Yartys[1], J.P. Mæhlen[1], E. Næss[2] and A. Vik[3]

1) Institute for Energy Technology (IFE), Kjeller. Norway

2) Norwegian University of Science and Technology, Trondheim Norway

3) CMR Prototech AS, Bergen Norway

6.1 ABSTRACT

This paper presents experimental results together with heat and mass transfer models of a metal hydride unit with a reversible storage capacity of 340 Nl of hydrogen. Charge and discharge experiments were performed at four different temperatures and with different pressures and flow rates. The experiments were carried out with two types of heat exchangers: One brush type and one tubular type. Two transient heat and mass transfer models were developed, a zero dimensional model for the configuration with the brush type heat exchanger and a more complex two-dimensional model for the tubular type heat exchanger.

Nomenclature

a_p	Particle surface area	[m^2]
A	Molar mass fraction between initial alloy and hydrogen gas	[-]
c	Hydrogen to metal atomic ratio	[-]
C_1	Hydrogen to metal atomic ratio lower limit	[-]
C_2	Hydrogen to metal atomic ratio upper limit	[-]
c_p	Specific heat capacity	[J/kg·K]
d_p	Particle diameter	[m]
E_a	Activation energy	[J/mol]
h	Convective heat transfer coefficient	[W/m^2·K]
$\dot{F}$	Total amount of hydrogen absorbed or desorbed in the reactor	[mol/s]
ΔH	Heat of reaction	[J/mol]
K	Thermal conductivity	[W/m·K]
K_0	Rate constant	[1/s]
K_D	Permeability	[m^2]
m	Mass	kg or mol
$\dot{m}_{H_2,g}$	Hydrogen flow rate in and out of the reactor	[kg/s]
M	Molar Mass	[g/mol]
n	Molar quantity	[mol]
NTU	Number of transfer units	[-]
NU	Nusselt number	[-]
P	Pressure	[bar]
Pr	Prandtl number	[-]
$\dot{Q}$	Heat duty	W
$\dot{Q}'''$	Heat duty per unit volume	W/m^3
R	Universal gas constant	[J/mol·K]
r	Radius	[m]
r_1	Water tube inner radius	[m]
r_2	Water tube outer radius	[m]
r_3	Filter elements radius	[m]
r_4	Reactor wall inner radius	[m]
r_5	Reactor wall outer radius	[m]
Re	Reynolds number	[-]
T	Temperature	[K]
t	Time	[s]
UA	Heat duty per unit driving force	[W/K]
V	Velocity	[m/s]
X	Dimensionless concentration	[-]
μ	Dynamic viscosity	[kg/m·s]
ε	Porosity	[–]
ρ	Density	[kg/m^3]
$\dot{\Pi}$	H_2 reaction rate	[mol/s·m^3] or [kg/s·m^3]
Θ	Heat exchanger effectiveness	[-]
Γ	Reacted fraction	[-]
$\tilde{v}_g$	Gas volume	[m^3]

Subscript

Al	Aluminium
eq	Equilibrium
eff	Effective
g	Gas
H	Hydrogen
in	In
MH	Metal hydride
mass	Mass
max	Maximum
r	Radial
n	Pre exponential Avrami coefficient
w	Water
sf	Solid to fluid
θ	Angular
wall	Wall

6.2 INTRODUCTION

Currently fossil fuels such as oil, coal and natural gas are the main sources of energy. Not only will these sources be depleted in the future, but the environmental aspect of burning fossil fuel is also a source of growing concern. Although renewable energy is available all around the world, both seasonal variations and availability turns energy storage into a critical issue. Some metals have the ability to absorb hydrogen gas where hydrogen molecules first dissociate on the metal surface and then diffuse as atomic hydrogen into the metal lattice occupying interstitial sites. At higher hydrogen concentrations the induced stresses by the interstitial hydrogen atoms makes a phase transformation to an ordered hydride phase energetically favourable. This phase transition depends on temperature, pressure and hydrogen concentration and is reversible for a number of metal-hydrogen systems. The process of hydrogen storage in metal hydrides is associated with heat release during hydrogen absorption (charging mode) and heat consumption during hydrogen desorption (discharging mode). The poor thermal conductivity of metal hydride granulates in combination with demands of high absorption and desorption hydrogen flow rates makes thermal control of the metal hydride storage unit a critical issue. Due to the large heat flows associated with the ab- and desorption processes it is necessary to implement a heat exchanger inside the storage container, and the heat exchanger surface has to be optimized for the application and operating conditions considered.

Several numerical models describing the heat and mass transfer in metal hydride storage containers are available. The group of Jemni and Nasrallah has published a number of articles [1-4]. They found that assumption of thermal equilibrium was only valid in the hydriding case. They also found that the heat and mass transfer processes was two dimensional in their modelling case. They modelled the heat and mass transfer processes in a cylindrical reactor having heat transfer through the container wall and having hydrogen leaving and entering the reactor at the top.

The group of Mat, Kaplan and Aldas followed up this work with a series of papers ([5] [6] [7]) extending the analysis to three dimensions for cylindrical geometries. These numerical models were verified by comparison to literature data. Recently, this group has designed two new experimental reactors for comparison and model verification [8]. The assumption of thermal equilibrium between the gas and solid in a metal hydride bed was analyzed numerically by Nakagawa et al. [9] for a cylindrical reactor with hydrogen entering and leaving the reactor at the top. They also considered the influence of variable physical properties such as granulate specific heat capacity as a function of reacted fraction. Their results indicated that both the assumption of thermal equilibrium and neglecting the convection effects influenced the total amount of hydrogen desorbed from the reactor. Kuznetsov and Vafai [10] presented analytic criteria for the validity limits of some of the most commonly applied modeling assumptions, and an analytical solution of a simplified heat and mass transfer model. There are not many published zero dimensional metal hydride models in the literature. However, Gambini [11,12] presented a simplified zero dimensional model assuming no temperature gradients in the metal hydride (i.e. a ‘stirred reactor’ type model) which was used to study the transient behaviour of two coupled metal hydride reactors.

The aim of this work was to characterize the performance of a metal hydride storage unit having different heat exchanger configurations at different charging / discharging pressures

and temperatures. The experimentally tested units were used to verify a model describing the heat and mass transport within the reactors. Two different heat and mass transfer models were developed to improve the understanding of the physical processes within the reactor; a complex two dimensional model and a simpler zero dimensional model. The zero dimensional model will be implemented into Hydrogems library (www.hydrogems.no). Hydrogems is a collection of different models suitable for simulations of stand alone power systems.

6.3 EXPERIMENTAL SET UP

An experimental test bench specially developed for characterising hydrogen storage units was used for the investigation of metal hydride containers having different internal heat exchanger configurations. A schematic of the test bench is shown in Figure 6.1. It contains a H_2 flow meter, temperature measurement points, pressure sensor and an evacuation line. The test bench is connected to a gas-distribution system containing both argon and hydrogen. A flow controller makes it possible to keep constant flow rate during hydrogen charging and discharging. The gas pressure is adjusted with a needle valve during hydrogen discharging and by a pressure regulator valve during charging. Hydrogen at a maximum pressure of 10 bar can be supplied during charging of the unit. Additionally, secondary vacuum conditions are provided by a rotary vacuum pump equipped with an in-line vacuum sensor.

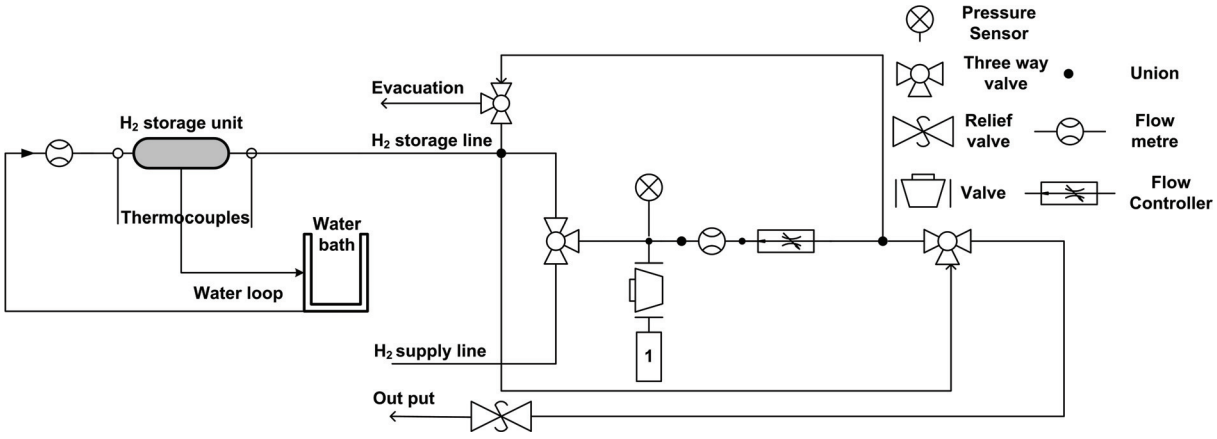

Figure 6.1 Schematic of the test bench for the testing of hydrogen storage units containing pressure sensor (0-25 bar absolute), flow meter (0-30 Nl/min), buffer volume (1) and flow controller.

6.3.1 The test reactor

The test reactor developed by IFE and CMR Prototech in a project founded by the European Space Agency [13], has a cylindrical geometry with an internal volume of ca 700 cm^3; water is circulated through a pipe positioned axially in the centre of the reactor. The reactor shell is made from aluminium with an 8 mm Teflon layer on the inside wall. The reactor is insulated with 12 mm rubber type insulation on the outer wall. Hydrogen enters and leaves the container through four filter elements positioned symmetrically around the centre of the reactor.

Two heat exchanger configurations were used in this work, as presented in Figure 6.2. Heat exchanger Tubular-type-configuration (Figure 6.2a) is simply a steel tube for water circulation positioned along the central axis of the storage unit. Heat exchanger Brush-type-configuration (Figure 6.2b) consists of an inner aluminium tube where water circulates, also positioned along the central axis of the storage unit, with thin aluminium wires (fins) wrapped around. The fin pitch is very small and provides a short effective heat transfer distance. However, the fins are clamped on to the central tube with a wire creating an appreciable heat transfer contact resistance. The central tubes in both heat exchanger configurations have the same diameters.

More details of the tested reactors are given in Table 6.1. Temperature profiles inside the reactor during charging and discharging were recorded using four thermocouples, positioned as indicated by the thick solid lines in Figure 6.2.

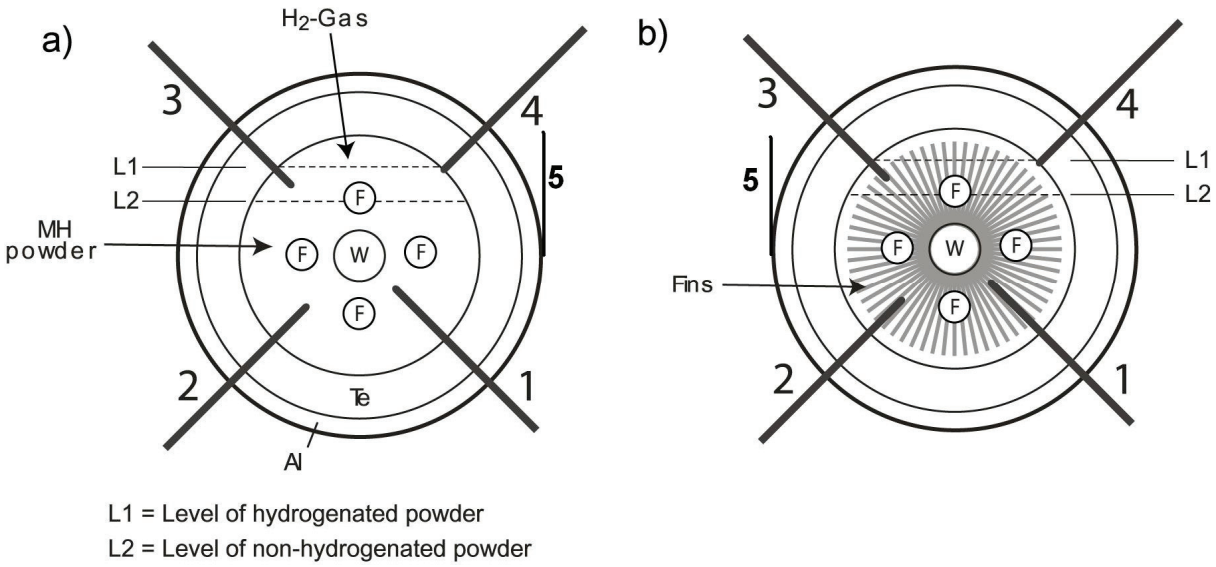

Figure 6.2 Location of thermocouple junctions. a) - heat exchanger Tubular-type-configuration and b) - heat exchanger Brush-type-configuration , the thermocouple tip distances from the centre of the container are: 1 – 4.75 mm, 2 – 9.19 mm, 3 – 13.63 mm, 4 – 18.06 mm. , and one thermo couple is welded to the outside of the reactor 5.

Table 6.1 Dimensions of the different reactors

Total internal volume available for metal hydride powder	700 cm^3	Internal cylinder length	460 mm
Central tube O.D.	9.5 mm	Inside diameter of aluminum shell	61 mm
Teflon heat-insulating layer thickness	8.0 mm	Outer insulation layer thickness	12 mm
Reactor shell material	Aluminium	Reactor mass	5.7 kg
Reactor with tube type heat exchanger (Tubular type)			
Metal hydride powder mass	2.454 kg	Heat exchanger surface area	140 cm^2
Reactor with brush type heat exchanger (Brush type)			
Metal hydride powder mass	2.236 kg	Heat exchanger surface area	2100 cm^2
Fin pitch	1 mm	Fin diameter	0.7 mm
Filter element diameter	6 mm	Fin length	17.2 mm

The reactor was filled (and refilled after change of heat exchanger configuration) with an AB_5 type of metal hydride powder (as received by the supplier [14]). To achieve uniform packing of the metal hydride, an in-house developed procedure was used during loading of the powders, followed by thorough vibration of the cylinder after loading. Before starting the experiments the reactor was heated to 370 K at vacuum conditions for 2 hours. The reactor was charged and discharged several times to ensure that the capacity was reversible. The hydrogen used during all the experiments had a purity of 99.999%. The test reactor was connected to the test bench as indicated in Figure 6.1. The heating/cooling water was supplied using a water bath with external circulation and an adjustable water pump. The water flow rate and temperature change through the metal hydride container were constantly recorded.

The kinetic properties of the AB_5 metal hydride powder was previously investigated by Førde et al [15]. It was found that the gas/solid reaction rate was very fast and could be adequately described using the expression given in Equation (6.1)

$$\frac{\left[-\ln\left(1-X\right)\right]^{\frac{1}{n}-1}}{n\left(1-X\right)}\cdot\frac{\partial X}{\partial t}=K_0\exp\left(-\frac{E_a}{RT}\right)\cdot\ln\left(\frac{P_g}{P_{eq}}\right)\qquad \textit{Absorption}$$

(6.1)

$$\frac{\left[-\ln\left(1-X\right)\right]^{\frac{1}{n}-1}}{n\left(1-X\right)}\cdot\frac{\partial X}{\partial t}=-K_0\exp\left(-\frac{E_a}{RT}\right)\cdot\ln\left(\frac{P_{eq}}{P_g}\right)\qquad \textit{Desorption}$$

Here n is a fitting parameter and K_0 is a rate constant. The dimensionless coefficient X, varying between 0 and 1,is calculated using Equation (6.2):

(6.2)

$$X = \frac{C - C_1}{C_2 - C_1} \qquad Absorption$$

$$X = \frac{C_2 - C}{C_2 - C_1} \qquad Desorption$$

In Equation (6.2) C is the actual particle hydrogen concentration, whereas C_1 and C_2 are the concentration limits of the initial and final states of the reaction. Another important parameter in Equation (6.2) is the equilibrium pressure P_{eq}, which is a function of both temperature and absorbed hydrogen concentration. The equilibrium pressure was measured experimentally using the experimental set up described in [16] and was described using a model developed by Lototsky et al. [17]. The results are presented in Figure 6.3 showing that the model reproduces the experimental data with good accuracy for the entire experimental concentration and temperature ranges.

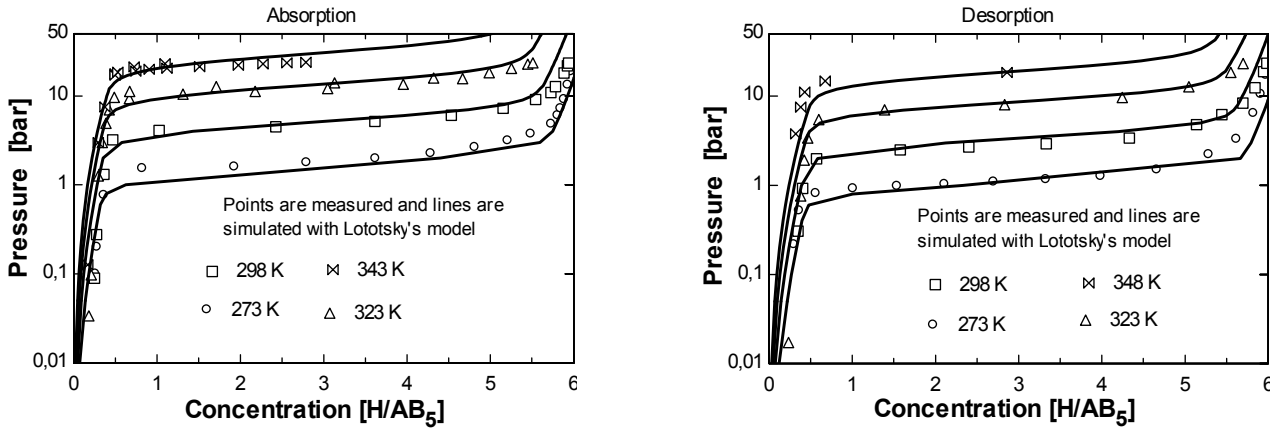

Figure 6.3 Pressure–composition isotherms for the AB_5-type metal hydride system. Calculated curves using the Lototsky-model [17] are shown as lines and experimental data are shown as discrete points.

6.4 RESULTS AND DISCUSSION

6.4.1 Hydrogen charging discharging experiments

A set of experiments using different cooling/heating water temperatures and charging/ discharging pressures were performed in order to characterize the metal hydride unit. Before each absorption experiment, the initial hydrogen gas pressure in the reactor was set to 0.5 bar. The influence of the different charging/discharging pressures and cooling/heating water temperatures on the time it took to reach 50% of the unit's H_2 storage capacity are presented in Figure 6.4 for Tubular-type heat exchanger (configuration 1) and in Figure 6.5 for Brush-type heat exchanger (configuration 2).

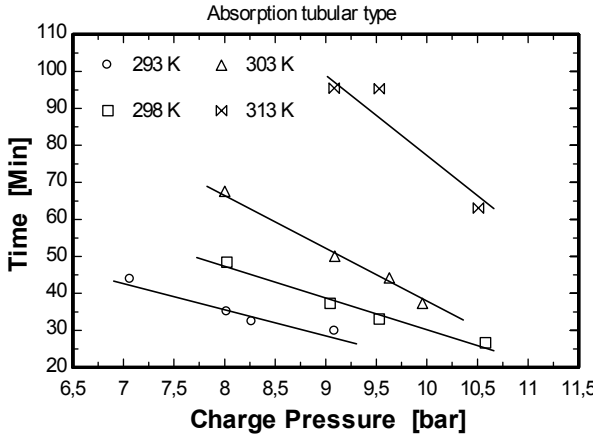

A

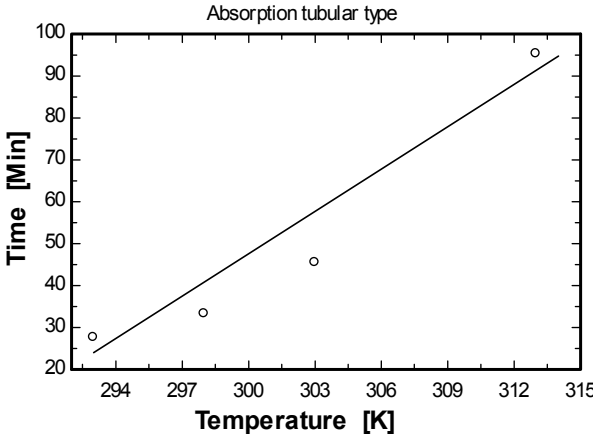

B

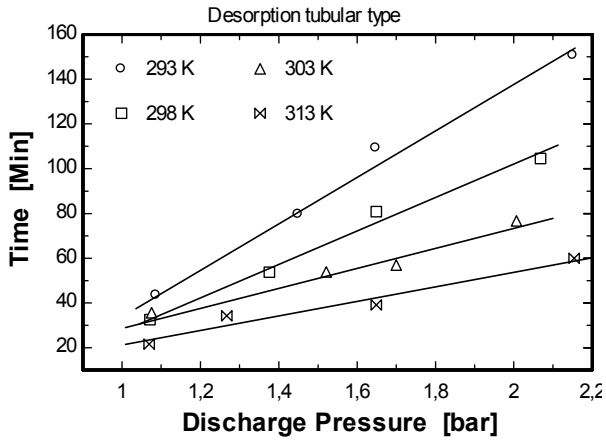

C

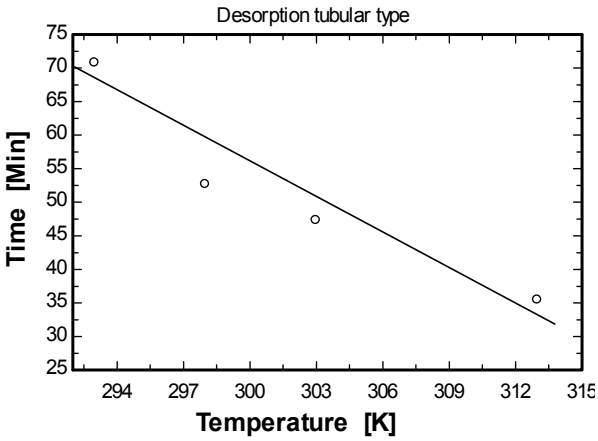

D

Figure 6.4 Absorption/Discharge times to reach 50% of storage capacity for Tubular-type-configuration as function of pressure and water inlet temperature (figures A and C) and as function of water inlet temperature at constant pressure (figures B and D).

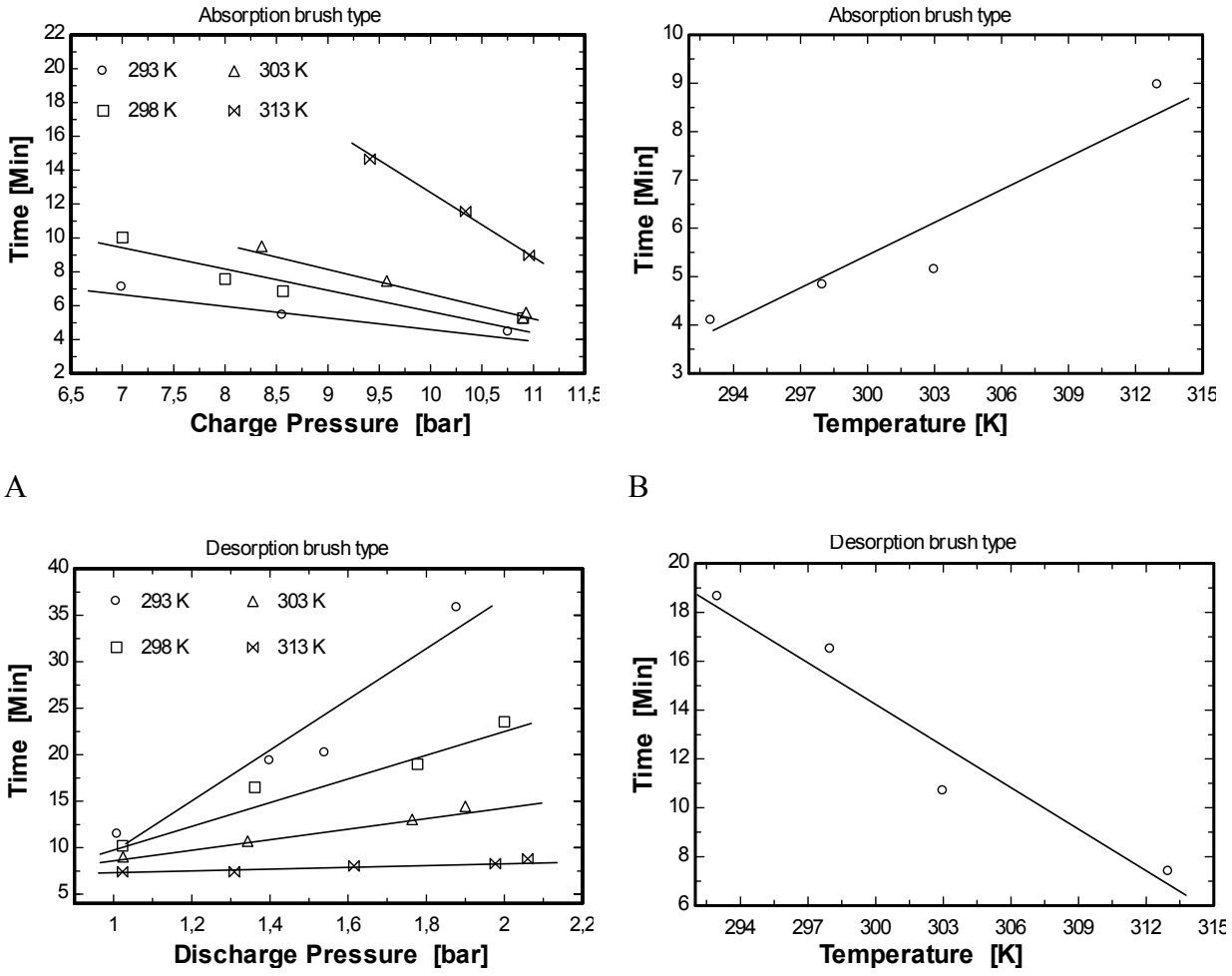

Figure 6.5 Absorption/Discharge times to reach 50% of storage capacity for Brush-type heat exchanger (configuration 2) as function of pressure and water inlet temperature (figures A and C) and as function of water inlet temperature at constant pressure (figures B and D).

The graphs in Figure 6.4A and Figure 6.5A show that there is an almost linear dependency between the charging pressure and half-time, i.e. time required to reach 50% of maximum storage capacity (provided that the charging gas pressures are above the equilibrium plateau pressure of the hydride system). The discharge half-time similarly exhibits a linear dependency with the discharge pressure (Figure 6.4C and Figure 6.5C). The influence of the water inlet temperature on the charging time at constant charging pressure shown in Figure 6.4B and Figure 6.5B, also indicate a linear dependency. Similar results were found for the desorption experiments (see Figure 6.5D and Figure 6.4D) at constant discharge pressure and constant water flow rate. From Figure 6.5 and Figure 6.4 it is observed that the Brush-type-configuration reaches the point of 50 % reacted fraction at less than 20% of the time used for the same reactor with Tubular-type-configuration under the same experimental conditions (pressure, water temperature and rate). Also for higher charging and discharging fractions like 75 and 90 % of the reactors capacity, similar linear-like dependences between charging and discharging time and gas pressure and water temperature were observed.

In order to improve the understanding of the performances of the reactor an energy balance was carried out. The energy balance took into account the amount of energy used to change the temperature of the metal hydride powder and reactor shell $\dot{Q}_{mass}$, the amount of energy produced in the reaction $\dot{Q}_{reaction}$, energy transported into and out of the reactor with the hydrogen gas $\dot{Q}_{H_2}$ and the amount of energy transported into or out of the reactor with the heating cooling water $\dot{Q}_w$. All the heat fluxes were estimated based on the measured temperatures and flow rates of the hydrogen gas and heating/cooling water. The performed energy balance is well defined for both absorption and desorption experiments indicating that the heat losses to the surrounding are negligible. The results from the energy balance calculations showed that $|\dot{Q}_w| \geq |\dot{Q}_{reaction}| \geq |\dot{Q}_{H_2}| \geq |\dot{Q}_{mass}|$ for both heat exchanger configurations. For the Brush-type-configuration, all the measured temperatures inside the metal hydride reactor were close to the average temperature for both the absorption and desorption experiments. The maximum deviation was for thermocouple #4 (see Figure 6.2) which experienced a maximum deviation of 1.5 K from the average temperature during the absorption process. During charging/discharging towards a set pressure, the temperatures in the reactor quickly changed until the gas pressure reached the equilibrium pressure, and the remaining charging/discharging process was strongly influenced by the heat transport. Discharging at a constant flow rate resulted in a moderate temperature drop of the metal hydride for the beginning of the experiment until the temperature difference between the metal hydride bed and heating water was large enough to transfer the energy consumed in the gas/solid reaction. The behaviour of the Tubular-type-configuration was similar to the Brush-type-configuration. However the measured temperatures deviated more due to the larger heat transfer distances.

In order to check the influence of the water flow rate, absorption and desorption experiments having the same pressure but with varying water flow rates were performed. These experiments indicated that the half-time for both charging and discharging for the different heat exchanger configurations were independent of the water flow rate in the interval of (0.5-6) kg/min (Reynolds numbers of 1800-23000). Oi et al [18] reported similar behaviour, i.e. the performance of their reactor was practically independent of the water flow rate.

The overall heat duty per unit driving force ($UA_{w\text{-}MH}$) was calculated from Equation (6.7). For the Brush-type-configuration, $UA_{w\text{-}MH}$ was found to be in the range 25-50 W/K for all absorption and desorption experiments for water flow rates above 1 litre/min. For lower water flow rates $UA_{w\text{-}MH}$ decreased, reaching a value of 5 W/K for a water flow rate of 0.2 litre/min. For the Tubular-type-configuration $UA_{w\text{-}MH}$ was found to be in the range 4-9 W/K for all experiment with water flow rates above 1 litre/min. Similarly, when the water flow rate was reduced to 0.3 litre/min $UA_{w\text{-}MH}$ decreased significantly, resulting in numbers between 1 and 2 W/K. These changes in $UA_{w\text{-}MH}$ directly affect the performance of the reactor. The Brush-type-configuration had the highest reduction in $UA_{w\text{-}MH}$ and the largest change in charging/discharging time. The half-time more than doubled for this reactor when the water flow rate was reduced to less than 0.3 l/min. The Tubular-type-configuration experienced significantly less changes in $UA_{w\text{-}MH}$, and had only a 10% increase in charging and discharging half-times when the water flow rate was reduced to 0.3 litre/min.

The reactors ability to provide a constant hydrogen discharge flow rate at different heating water temperatures and at constant water flow rates and discharge pressures is shown in Figure 6.6 for the two configurations considered.

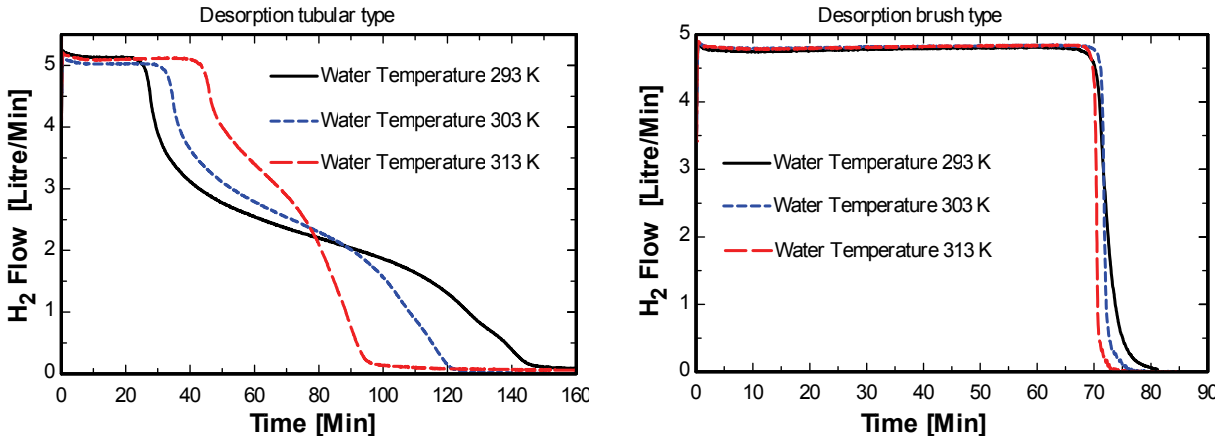

A B

Figure 6.6 Desorption hydrogen flow rates as a function of water inlet temperatures and time for A - Tubular-type-configuration and B –. Brush-type-configuration The water flow rate was 1 liter/min, and the hydrogen pressure was set to 1.1 bar.

The graphs presented in Figure 6.6 shows that the brush type heat exchanger (Brush-type-configuration) is capable of delivering more than 90% of the stored hydrogen at a constant flow rate of 4.8 liter/min (0.085 H/AB_5 per minute) for water temperatures as low as 293 K. The situation is dramatically different for the plain tube heat exchanger (Tubular-type-configuration), where only 40% of the available hydrogen is delivered at 293 K and 60% at 313 K.

6.5 NUMERICAL PREDICTIONS

Numerical models for the prediction of heat and mass transfer in the two considered reactor configurations were developed in order to emulate the reactor behaviour. In the Brush-type-configuration the average distance between the pin fins is very short providing efficient heat distribution. This was confirmed by the almost uniform internal temperature distribution measured for this unit - no internal temperatures deviated more than 2 K from the average temperature. A zero dimensional model (i.e. a 'stirred reactor'-type model with no internal gradients) was therefore adequate for predicting the behaviour of this configuration. However, for the Tubular-type-configuration, a significant radial temperature distribution was observed, caused by the low thermal conductivity of the metal hydride in combination with a long heat transfer conduction path. Thus, a more complex model was needed to describe the behaviour of this storage unit. The numerical models developed for the two different configurations are described in the following paragraphs, where, also, comparisons with experimental results are presented.

6.5.1 Brush type heat exchanger mathematical model

In a system simulation the amount of energy consumed or produced in the form of heat in the metal hydride is an important parameter. Thermal energy is produced or consumed due to the

chemical gas-solid reactions. Heat can enter or leave the reactor through the cooling/heating water, or through the hydrogen gas flow in and out of the reactor. Also, some energy is transferred to the surroundings by convective heat transfer. In the reactors considered, thermal energy is accumulated in the metal hydride powder, the hydrogen gas and in the aluminium casing. Hence, the reactor shells heat capacities are important damping factors for the transient behaviour of the whole systems.

In the model of the Brush-type configuration, we are assuming thermal equilibrium between the metal hydride powder and the hydrogen gas. It should be noted that Nakagawa [9]has shown that reactor behaviour can be influenced by this assumption. On the other hand, the complexity of Nakagawa model is much higher than for our model. The reactor aluminium shells total heat capacity $c_{p,Al}$ is more than 2.5 times larger than the metal hydride powder total heat capacity $c_{p,MH}$, and cannot be omitted in the model. In addition, the reactor shell and metal hydride powder is separated with an 8 mm isolating Teflon layer, thus one cannot use the assumption that these two parts are in thermal equilibrium. The equations governing the transient temperature development of the metal hydride powder and reactor shell are presented below, where Equation (6.3) represents the applicable energy equation for the interior part of the metal hydride reactor assuming a uniform metal hydride temperature, and Equation (6.4) represents the energy equation for the aluminium shell.

(6.3) $$\left(m_{MH}\cdot c_{p,MH}+m_g\cdot c_{p,g}\right)\cdot\frac{\partial T_{MH}}{\partial t}=\dot{Q}_{reaction}+\dot{Q}_w+\dot{Q}_{H_2}+\dot{Q}_{Al}$$

(6.4) $$m_{Al}\cdot c_{P,Al}\frac{\partial T_{Al}}{\partial t}-\dot{Q}_{Al}$$

Here, m_{MH}, m_g and m_{Al} are the masses of the metal hydride powder, the gaseous hydrogen and the aluminium reactor shell, $c_{p,MH}$, $c_{p,g}$ and $c_{p,Al}$ are the specific heat capacities of the metal hydride powder, the gaseous hydrogen and the reactors aluminium shell. The different heat fluxes in and out of the reactor $\dot{Q}_{reaction}+\dot{Q}_w+\dot{Q}_{H_2}+\dot{Q}_{Al}$ are calculated using Equations (6.5),(6.6) ,(6.9) and (6.10). The specific heat capacity of the metal hydride, $c_{p,MH}$, changes with the hydrogen-to-metal atomic ratio [19,20], and is modelled using the Neumann-Kopp rule, Equation (6.20). Similarly, the metal hydride density is influenced by the hydrogen-to-metal atomic ratio, and is calculated using Equation (6.19). The amount of energy consumed or released due to the hydrogen gas-solid reaction $\dot{Q}_{reaction}$ is calculated using Equation (6.5) below:

(6.5) $$\dot{Q}_{reaction}=\dot{F}\cdot\Delta H$$

Here, ΔH is the heat of reaction and $\dot{F}$ is the total amount of hydrogen absorbed or desorbed in the metal hydride reactor, $\dot{F}$ is defined negative for desorption and positive for absorption. $\dot{Q}_w$ is the heat removed or supplied to the metal hydride unit through the heating/cooling water circuit, found by solving Equations (6.6) and (6.7) below simultaneously:

(6.6) $$\dot{Q}_W=\dot{m}_w\cdot c_{p,W}\cdot\Theta\cdot\left(T_{w,in}-T_{MH}\right)$$

(6.7) $$\dot{Q}_W = \dot{m}_w \cdot c_{p,W} \left(T_{w,in} - T_{w,out} \right)$$

For the current case with a system with uniform metal hydride temperature, it is defined as $\Theta = 1 - \exp(-NTU)$ [21] where NTU is number of transfer units $NTU = \frac{UA_{w-MH}}{\dot{m}_{water} \cdot c_{p,w}}$ where UA_{w-MH} is the heat duty per unit driving force between the heat exchanger and the metal hydride bed and is found by solving Equation (6.8) using experimental data obtained from absorption and desorption experiments.

(6.8) $$\dot{Q}_W = UA_{W-MH} \cdot \frac{T_{w,out} - T_{w,in}}{\ln\left(\frac{T_{MH} - T_{w,out}}{T_{MH} - T_{w,in}} \right)}$$

The heat removed or supplied to the reactor from the hydrogen gas $\dot{Q}_{H_2}$ is calculated using Equation (6.9):

(6.9) $$\begin{aligned} \dot{Q}_{H_2} &= \dot{m}_{H_2,g} \cdot c_{p,H_2} \cdot \left(T_{surrounding} - T_{MH} \right) \quad Absorption \\ \dot{Q}_{H_2} &= \dot{m}_{H_2,g} \cdot c_{p,H_2} \cdot T_{MH} \quad Desorption \end{aligned}$$

The hydrogen flow rate into and out of the reactor $\dot{m}_{H_2,gas}$ is defined to be positive for charging and negative for discharging of the unit and $T_{surrounding}$ is the room temperature. Finally, heat is also flowing through the insulating Teflon layer to the aluminium reactor shell, as described by Equation (6.10)**:**

(6.10) $$\dot{Q}_{Al} = UA_{MH-Al} \cdot \left(T_{Al} - T_{MH} \right)$$

Here T_{Al} is the temperature of the reactor shell and UA_{MH-Al} is the heat transfer number from the metal hydride bed to the reactor shell, typically between 5-7 W/K.

The mass balance for the solid and gas phase is defined in Equation (6.11) for the solid phase and in Equation (6.12) for the gas phase:

(6.11) $$\frac{\partial C}{\partial t} = \dot{C}$$

$\dot{C}$ in Equation (6.11) is the hydrogen to metal atomic ratio absorption or desorption rate and is obtained from Equation (6.1).

(6.12) $$\frac{\partial P_{gas}}{\partial t} = \frac{\partial n_{H_2}}{\partial t} \cdot \frac{R \cdot T_{MH}}{\tilde{v}_g} + \frac{n_{H_2} \cdot R}{\tilde{v}_g} \cdot \frac{\partial T_{MH}}{\partial t}$$

The term $\frac{\partial n_{H_2}}{\partial t}$ in Equation (6.12) is the change in the number of moles of hydrogen gas and depends on the amount of hydrogen leaving or entering the reactor, and the amount of

hydrogen absorbed in or desorbed from the solid metal hydride powder, while $\tilde{v}$ is the volume of the gaseous hydrogen. This model was compared to experimental data, and the results are presented in section 1.5.3.

6.5.2 Boundary conditions

For all experiments the water inlet temperature and water flow rate was used as boundary conditions for the thermal model. Further, the tank gas pressure was used as a boundary condition for absorption type simulation and the hydrogen flow rate out of the reactor was used as boundary conditions for the mass balance and reaction rate equations.

The set of equations described above were solved using the Engineering Equation Solver (EES) (see http://www.fchart.com), with the boundary conditions given by Equations (6.13)-(6.15):

(6.13) $$T(t=0)=T_{w,in}(t=0) \qquad P(t=0)=P_g(t=0) \qquad P_{eq}(t=0)=P_{eq,estimated}(t=0)$$

(6.14) $$\text{A)} \quad P_g(t)=P_g(0) \qquad \text{or} \quad \text{B)} \quad \dot{P}_g(t)=\dot{P}_{system}(t)$$

(6.15) $$T_{w,in}(t)=T_w(measured) \qquad \dot{m}_w(t)=\dot{m}_w(measured)$$

Two types of boundary conditions were used for calculating the hydrogen flow in and out of the reactor (Equation (6.14)). In a typical tank system situation, the reactor will be charged using an electrolyser, supplying hydrogen at a given pressure. Hence, the boundary condition of Equation (6.14) A was used for hydrogen absorption simulations. Further, the storage unit will typically be supplying a fuel cell, and the amount of hydrogen required by the fuel cell will depend on the system electricity demand. Therefore, the boundary condition of Equation (6.14) B was used for desorption simulations.

6.5.3 Results

Measured temperature profiles and hydrogen flow rates from the Brush-type-configuration charging and discharging experiments were compared to simulations using the model described above. As discussed above, since the metal hydride radial temperatures were nearly uniform an average bed temperature value was used. Typical time-series plots of the main data from an absorption (charging) and desorption (discharging) experiment are shown in Figure 6.7 and Figure 6.8.

In the charging case the unit was filled at a charging pressure of 8.3 bar. The cooling water inlet temperature was set to 298 K with a water flow rate of 1 litre/min. The reactor temperature was uniform before the experiment started, and the initial gas pressure was 0.5 bar while the initial hydrogen-to-metal concentration was established from the isothermal Pressure-Composition relations described using the Lototsky model [17].

In the discharge experiment the unit was desorbed towards an end pressure of 1.5 bar, with a heating water inlet temperature of 293K and a water flow rate of 1 litre/min. The temperature in the reactor was uniform before the experiment started and the initial gas pressure was 9.6 bar. The initial hydrogen-to-metal concentration was again found using the Lototsky model.

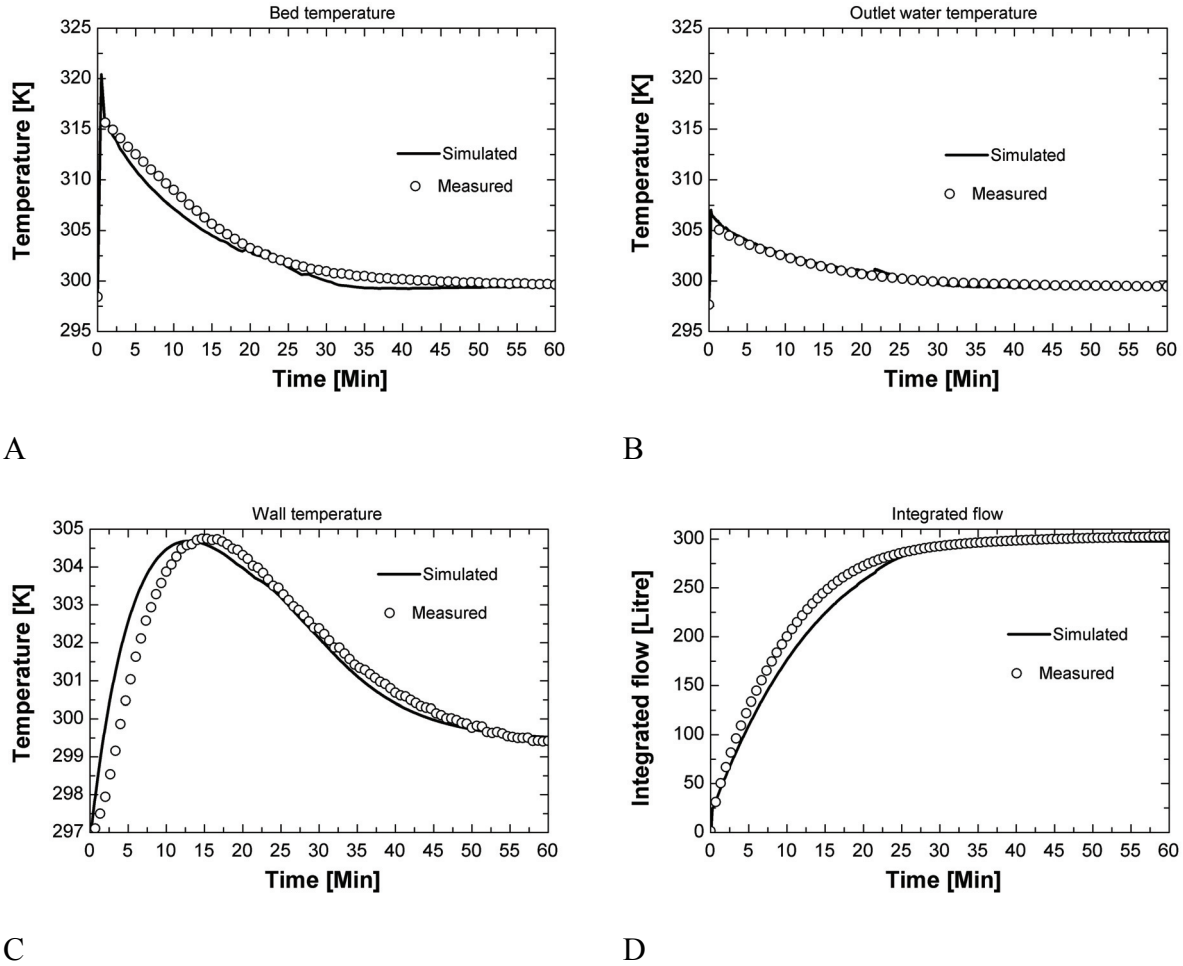

Figure 6.7 Measured and simulated time series for a typical absorption experiment for the Brush-type-configuration. A - average measured and simulated metal hydride bed temperature, B - measured and simulated water outlet temperature, C - measured and simulated outer wall temperature, and D - simulated and measured integrated hydrogen flow rate.

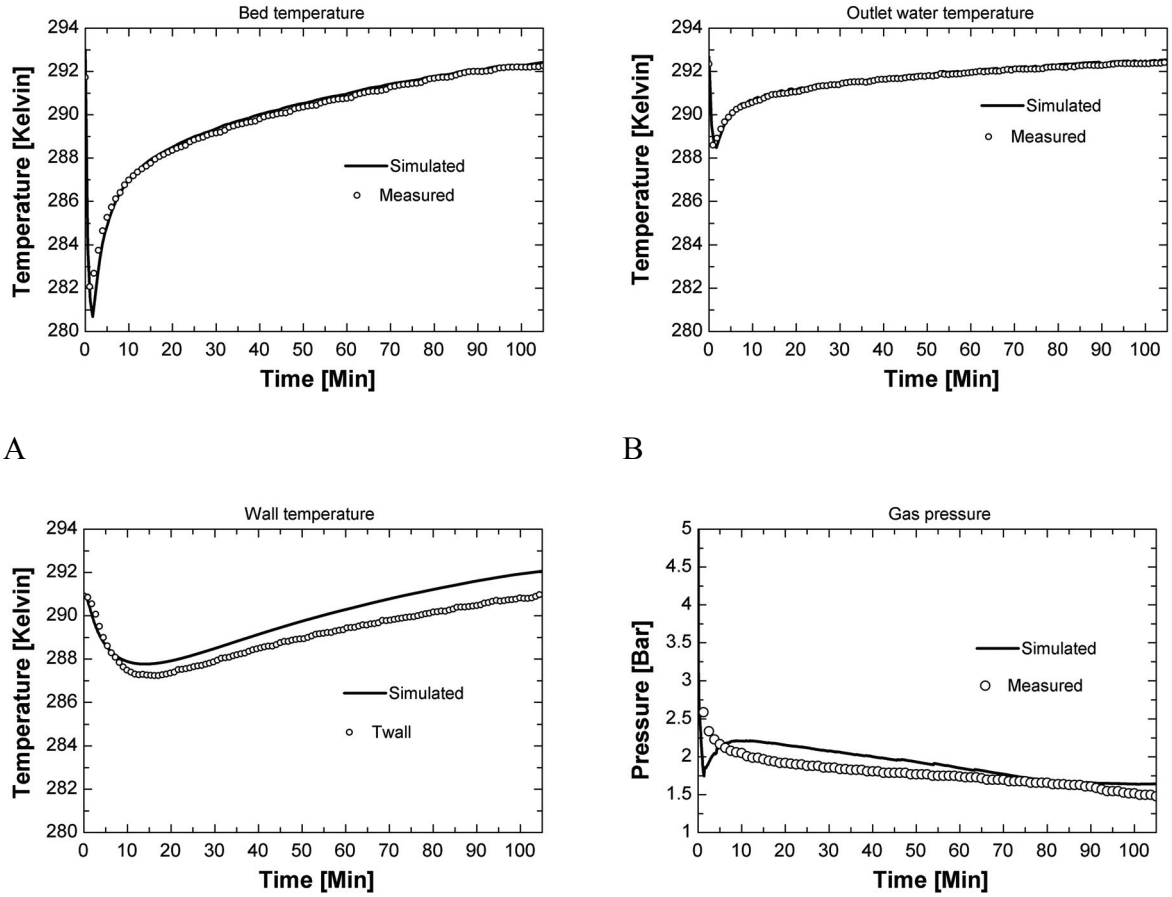

Figure 6.8 Measured and simulated time series for a typical desorption experiment for the Brush-type-configuration. A - average measured and simulated metal hydride bed temperature, B - measured and simulated water outlet temperature, C - measured and simulated outer wall temperature, and D - simulated and measured reactor pressure.

This ‘zero dimensional’ (or ‘stirred reactor’) model is capable of simulating both hydrogen charging and discharging experiments. Both the simulated bed temperature and outlet cooling water reaches their maximum (absorption) and minimum (desorption) values within the first minutes. The simulated wall temperature responds slower than the bed temperature and reaches its maximum and minimum values later. Teflon acts like a thermal resistance between the wall and metal hydride bed. The wall maximum and minimum values are also much smaller than the beds maximum values as it can be seen in Figure 6.7 and Figure 6.8.

In the charging experiment a constant charging pressure is chosen as a boundary condition since this will be the typical boundary condition in a system simulation. It can be seen from Figure 6.7 that the model is capable to predict the temperature development and flow rate out of the tank with high accuracy.

In the desorption experiment a constant hydrogen flow out of the reactor is chosen as an boundary condition. For the discarging experiments are the simulated and measured gas tank pressure compared in Figure 6.8D. It can be seen that the simulated gas pressure undershoots in the beginning of the experiments and overshot in the end of the experiment. This is due to

the simplicity of the model and the corresponding undershoots and overshot in the simulated bed temperature.

6.5.4 Tube type heat exchanger mathematical model

The 'zero dimensional' model described above is only suitable to describe metal hydride containers with very short heat transfer distances, i.e. uniform bed temperatures. In order to model the behaviour of the Tubular-type-configuration a more complex heat and mass transfer model is required. If thermal non-equilibrium between the gas and solid phase is assumed, two energy equations are required, one for the gas phase (Equation(6.16)) and one for the solid phase (Equation (6.17)):

(6.16)

$$\left(\varepsilon\cdot\rho\cdot c_p\right)_g\cdot\left(\frac{\partial T_g}{\partial t}+v_r\cdot\frac{\partial T_g}{\partial r}+v_\theta\cdot\frac{\partial T_g}{\partial\theta}\right)=\frac{1}{r}\frac{\partial}{\partial r}\cdot\left(k_g\cdot r\cdot\frac{\partial T_g}{\partial r}\right)+\frac{1}{r}\frac{\partial}{\partial\theta}\cdot\left(k_g\cdot\frac{1}{r}\cdot\frac{\partial T_g}{\partial\theta}\right)-h_{sf}\cdot a_p\left(T_g-T_{MH}\right)+\dot{Q}'''_{H_2,MH}$$

(6.17)

$$\left(1-\varepsilon\right)\cdot\left(\rho\cdot c_p\frac{\partial T}{\partial t}\right)_{MH}=\frac{1}{r}\frac{\partial}{\partial r}\cdot\left(k_{eff,MH}\cdot r\cdot\frac{\partial T_{MH}}{\partial r}\right)+\frac{1}{r}\frac{\partial}{\partial\theta}\cdot\left(k_{eff,MH}\cdot\frac{1}{r}\cdot\frac{\partial T_{MH}}{\partial\theta}\right)+\dot{\Pi}\cdot\Delta H+h_{sf}\cdot a_p\left(T_g-T_{MH}\right)+\dot{Q}'''_{H_2,g}$$

Here, the term $\dot{Q}'''_{H_2,MH}$ represent the heat transfer due to the hydrogen flux in and out of the metal hydride alloy and is defined as $\dot{\Pi}\cdot c_{p,H_2}\left(T_g-T_{MH}\right)$ for absorption and 0 for desorption. A similar term $\dot{Q}'''_{H_2,g}$ is used in the gaseous energy equation and is defined as 0 for absorption and $\dot{\Pi}\cdot c_{p,H_2}\left(T_g-T_{MH}\right)$ for desorption. $\dot{\Pi}$ is the rate of the solid-gas reaction calculated with Equation (6.1) and defined as positive definite for absorption and negative definite for desorption (i.e $\dot{\Pi}_{abs}>0>\dot{\Pi}_{des}$).

In solving the energy equations, the following assumptions were made: The porosity (ε) is assumed to be constant, the gas density (ρ_g) is calculated from the ideal gas law, the solid density, ρ_{MH}, changes during absorption and desorption due to the swelling and shrinking of the particles, and is calculated using Equation (6.19).

The hydrogen gas balance is calculated using Equation (6.18):

(6.18)

$$\varepsilon\cdot\frac{\partial\rho_g}{\partial t}+v_r\frac{\partial\rho_g}{\partial r}+v_\theta\cdot\frac{\partial\rho_g}{\partial\theta}=-\dot{\Pi}$$

The solid mass balance is calculated from Equation (6.11).

An energy equation similar to the solid phase equation (Equation (6.17)) is used to establish the temperature profile in the Teflon layer and aluminium shell. For this use the source term and porosity are zero, and material properties for the respective materials (Teflon and aluminium) are used. In addition, the contact resistance between the aluminium and Teflon materials are assumed to be zero.

6.5.5 Modelling parameters

The solid density of hydrogenated metal hydride ρ_{MH} was estimated using a linear relationship as shown in Equation (6.19). The swelling, S, of the metal hydride particles during hydrogenation were estimated to 18.9 % [22]. The swelling was assumed to be a reversible process.

(6.19)
$$\rho_{MH} = \frac{A + C}{1 + \frac{S \cdot C}{100 \cdot C_{Max}}} \cdot \frac{\rho_{MH,initial}}{A}$$

The implied assumption of a linear variation in the solid density with absorbed hydrogen is not totally correct since there is a much less expansion at low hydrogen to metal concentrations (α phase) but this is an acceptable simplification. The gas and solid thermal conductivities (k_g and k_{MH}) are also important parameters in the mathematical model. The gas conductivity is assumed constant independent of pressure and temperature, which is a reasonable assumption. However, there are several models for the effective thermal conductivity in porous media. Important parameters for the effective conductivity are porosity, particle size and shape, gas pressure and the thermal conductivities of the gas and the solid material. Hane and Kallweit [23] measured the effective conductivity of a $LaNi_{4.7}Al_{0.3}$ compound and found that the influence of increased pressure on the effective thermal conductivity decreased dramatically for pressures above 1 bar at 293.15 K. They also measured that the effect of particle decay during cycling only affected the effective thermal conductivity in the lower pressure regions (gas pressures below 0.01 bar). Hane and Kallweit further measured the effective thermal conductivity at different hydrogen-to-metal concentrations and found that for equilibrium pressures above 1 bar the influence of the hydrogen-to-metal concentrations was small. Deng et al. [24] measured the effective thermal conductivity for a Lanthanum-rich Mischmetal alloy and compared the experimental data with theoretical values. They showed through a parametric analysis that the effect of porosity (in the range 0.3-0.6) and temperature (in the range 300-400) K on the effective thermal conductivity was small as long the solid conductivity was less than 50 W/m·K. Pons and Dantzer [25] estimated the solid conductivity of an $LaNi_5$ alloy to 30±10 W/m·K.

The effective thermal conductivity used in the solid energy Equation (6.17) is based on literature values for the effective bulk thermal conductivity from which the gas phase conductivity is subtracted, i.e. $K_{eff,MH} = K_{eff} - \varepsilon \cdot k_g = 1.5$.

The specific capacity (c_p) is an important parameter because it influences the systems thermal response. In the present model the specific heat capacities of the aluminium shell and the hydrogen gas were assumed constant. The specific heat capacity of the metal hydride, however, has been reported by several investigators to be influenced by the hydrogen-to-metal atomic ratio [19,26]. As for the Brush-type configuration, in the present model this influence is modelled using the additive Neumann-Kopp rule:

(6.20)
$$c_{p,MH} = \frac{5 \cdot M_{Ni} \cdot c_{p,Ni} + M_{La} \cdot c_{p,La} + M_{mm} \cdot C_{p,mm}}{M_{alloy} + \Gamma \cdot C_{\max} \cdot M_H} + \frac{\Gamma \cdot C_{\max} \cdot M_H \cdot \cdot c_{p,H}}{M_{alloy} + \Gamma \cdot C_{\max} \cdot M_H}$$

Here, $\Gamma = \frac{C}{C_{\max}}$ is the reacted fraction and C_{max} is the maximum A/AB_5 molar ratio. To find the heat capacity of hydrogen inside the metal, literature data [19,26] were fitted to the calculated heat capacity with $c_{p,H}$ as the unknown parameter. A good fit was achieved $c_{p,H}$= 13000 J/kg·K for that is quite close to the capacity of gaseous hydrogen (14332 J/kg·K).

The specific surface area of the solid phase is estimated from $a_p = \frac{6(1-\varepsilon)}{d_p}$ where d_p is the particle diameter which can vary from 10-100 μm in a metal hydride bed. The velocity used in Equation (6.16) and (6.18) is calculated with the Darcy's Equation (6.21):

(6.21)
$$V_r = -\frac{K_D}{\mu_g} \cdot \frac{\partial P_g}{\partial r}$$
$$V_\theta = -\frac{K_D}{\mu_g} \cdot \frac{1}{r} \frac{\partial P_g}{\partial \theta}$$

Here, K_D is the permeability of the porous medium, calculated from the Carman Coecensky equation [27], $K_D = \frac{D_p^2 \cdot \varepsilon}{180 \cdot (1-\varepsilon)^2}$ yielding values in the range of (10^{-10}-10^{-12}) for particles with diameters (D_p) between 10-100 μm and porosity of 0.5. The Darcy flow model (Equation (6.20)) is valid in circumstances where the order of magnitude of the pore Reynolds number is smaller than unity [27]. With a maximum measured flow rate of 50 Normal litres/min in/out of the reactor, the maximum local pore Reynolds number at a position closest to the inlet/outlet of the reactor was estimated to Re_{max}=0.018, which is well within the validity region of Equation (6.20). Several correlations in the literature exist for predicting the solid-to-gas heat transfer coefficient. Unfortunately, as the Reynolds number numbers approaches zero the uncertainty in the correlations becomes much higher, presumably due to experimental uncertainties. Common for several of the dimensionless heat transfer correlations published in literature, such as Wakao and Kaguei [28] and by Whitaker [29], are that the Nusselt number is a function of both the Reynolds and Prandtl numbers, and approaches the asymptotic value

of Nu=2 when the Reynolds number approaches zero. The proposed correlation by Wakao and Kaguei Equation (6.22), is used in the simulation.

(6.22) $$Nu = \frac{h_{sf} D_p}{k_g} = 2 + 1.1\,\mathrm{Re}^{0.6} \cdot \mathrm{Pr}^{1/3}$$

6.5.6 Boundary conditions

The equations were solved using the commercial Finite Element Method (FEM) package Comsol Multiphysics v.3.2a (www.comsol.se) using the initial and boundary conditions given in Equations (6.23)-(6.27) below. Due to the reactor symmetry around the central water tube shown in Figure 6.2, only half of the reactors cross section was modelled.

During the simulations the computational elements were gradually refined until the simulation results remained unaffected by the number of computational elements.

(6.23) $$T(r,\theta,0) = T(0) \qquad P_g(r,\theta,0) = P_g(0) \qquad P_{eq}(r,\theta,0) = P_g(0)$$

(6.24) $$\frac{\partial P_g}{\partial r}(r_4,\theta,t) = 0 \qquad \frac{\partial P_g}{\partial r}(r_1,\theta,t) = 0 \qquad P_g(r_3,\theta,t) = P_g$$

(6.25) $$T(r_5,\theta,t) = T(r_5) \qquad \frac{\partial T}{\partial r}(0,\theta,t) = 0 \qquad -k\frac{\partial T(r_1,\theta,t)}{\partial r} = h\left(T_w - T(r_1,\theta,t)\right)$$

(6.26) $$-k_s \frac{\partial T(r_4,\theta,t)}{\partial r} = h\left(T_{MH}(r,\theta,t) - T(r_4,\theta,t)\right)\cdot(1-\varepsilon_{wall})$$

(6.27) $$-k_g \frac{\partial T(r_4,\theta,t)}{\partial r} = h\left(T_g(r,\theta,t) - T_w(r_4,\theta,t)\right)\cdot\varepsilon_{wall}$$

The entire computational domain and the metal hydride bed were assumed to initially have a uniform temperature, hydrogen-to-metal atomic concentration and gas pressure T_0, C_0, P_0 as indicated by Equation (6.23). The reactor walls were assumed to be impervious, and no flux boundaries were used at the interface between the gaseous hydrogen and the isolating Teflon layer, the water tube, and for the symmetry line dividing the reactor in half. A constant pressure boundary condition was used at the filter elements during charging and discharging of the reactor as indicated in Equation (6.24).

The measured temperature at the outer wall (thermocouple number 5 in Figure 6.2) is used as the boundary condition at the outer wall as indicated in Equation (6.25). We are neglecting the contact resistance between the aluminium reactor wall and the isolating Teflon. Heat is transferred into or out of the interior of the reactor at the Teflon wall and at the water pipe tubing. The heat flux into or out of the reactor at these surfaces are estimated with equations (6.26) and (6.27). However, at the symmetry line dividing the reactor in half, isolation is used

as a boundary condition. Finally, the heat flux into the water side wall of the water tube, $\dot{Q}_w$, is calculated with the convective heat flux conditions described in Equation (6.25). The gas temperature was assumed to be continuous across the internal surface between the gaseous expansion/safety volume and porous reactor volume. The velocity field in the gas volume above the metal hydride was established using the Darcy equation, Equation (6.20). However, the permeability coefficient (K_D) was set to a very high value (1000 times higher than the value in the porous bed) and the porosity was set to unity, reducing it to a potential flow problem.

6.5.7 Results

In order to improve the understanding of the thermal behavior of the Tubular-type-configuration reactor, the two-dimensional heat and mass transfer model as described above was implemented into Comsol 3.2a and solved numerically. Several simulations were performed and compared with experimental data.

In the absorption experiment (Figure 6.10) was the reactor charged using P_{H2} = 8.7 bar, the cooling water inlet temperature was 302.7 K and the water flow rate was 1.3 litre/min. The initial gas pressure was 0.5 bar and the corresponding hydrogen-to-metal concentration was found using the Lototsky [30] equilibrium model.

In the desorption experiment (Figure 6.11) was the initial gas pressure 9.5 bar, the initial temperature was 293 K, the heating water flow rate was 1.3-litre/ min and had an inlet temperature of 293K. The reactor desorbed towards a constant gas pressure of 2 bar and the initial hydrogen concentration (C) was estimated with the Lotosky PCT model.

A snapshot of the simulation for the absorption simulation is presented in Figure 6.9 below.

It can be seen from Figure 6.9 A that the temperature drop through the water pipe positioned in the centre of the reactor is small, and that the lowest temperatures occurred close to the water pipe. The insulating Teflon positioned close to the wall prevented the distribution of heat into the reactor shell quite effectively. The temperature within the reactor shell was noticeable lower than the temperatures within the reactor bed. Figure 6.9 B shows the simulated hydrogen to metal (H/AB_5) concentration profile for the same absorption simulation. It can be seen that the highest concentrations occur close to the cooling water pipe. This is logical since this area has the lowest temperature and needs higher hydrogen concentration to bring the equilibrium pressure towards the hydrogen gas pressure.

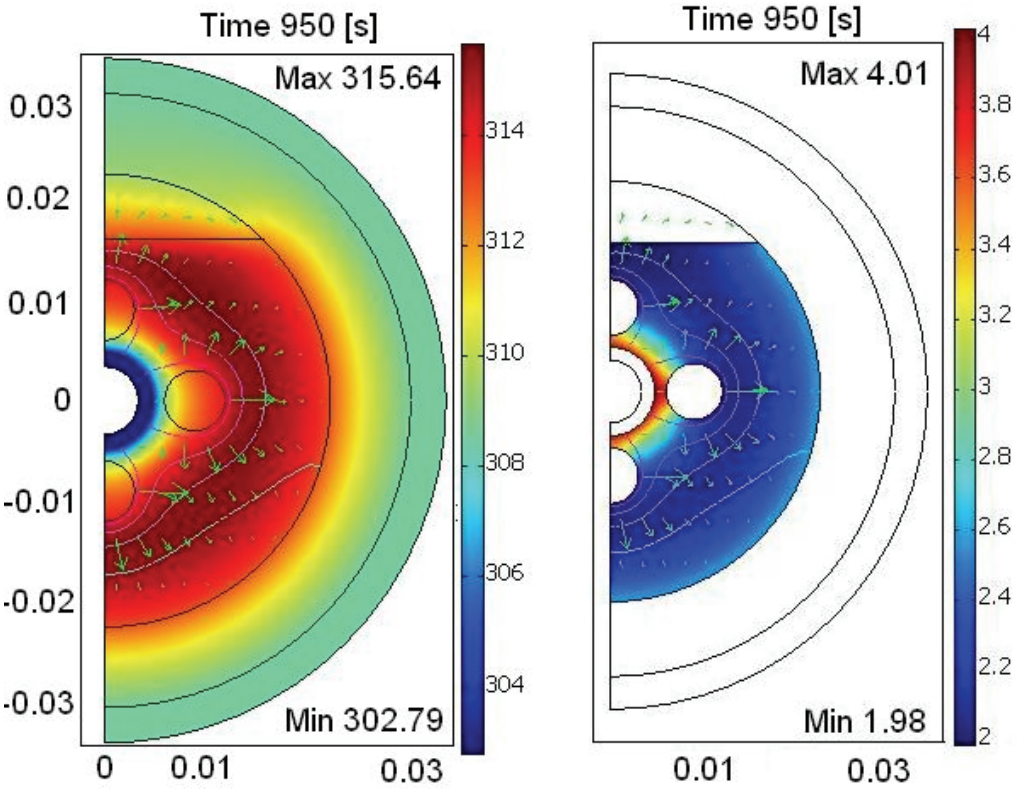

A B

Figure 6.9 Snapshot of the absorption experiment simulation at time 950 s, A shows the hydrogen gas, reactor Teflon layer, reactor shell temperature profile. B shows the reactor hydrogen to metal (H/AB_5) concentration profile.

Three different lines are plotted in Figure 6.10 and Figure 6.11 the dotted lines represent the experimental data, for the experiment described above. The line denoted Hsf A (solid drawn) and Hsf B (dashed line) are calculated with the equations described above. The convective gas solid heat transfer coefficient h_{sf} are estimated with the Wakao and Kaguei correlation (Equation (6.22)) with an particle diameter of 15 μm , for the lines denoted $H_{sf,A}$ in Figure 6.10 and Figure 6.11. While for the lines denoted $H_{sf,B}$ in Figure 6.10 and Figure 6.11 the product $h_{sf} \cdot a_p$ is set equal to an constant value of $3.3 \cdot 10^4$. $h_{sf} \cdot a_p = 3.3 \cdot 10^4$, yield gas solid heat transfer coefficients between 0.1-1 $W/m^2 \cdot K$ with spherical particles with diameters from 10-100 μm.

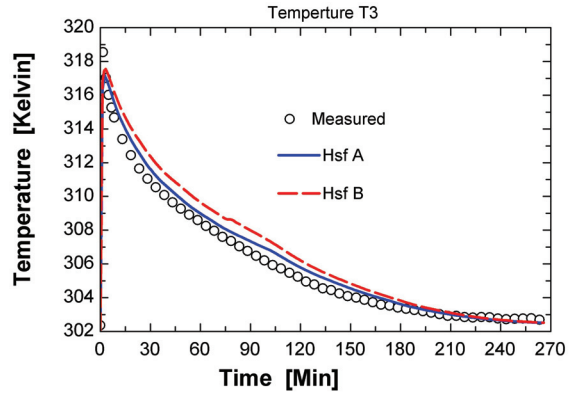

A

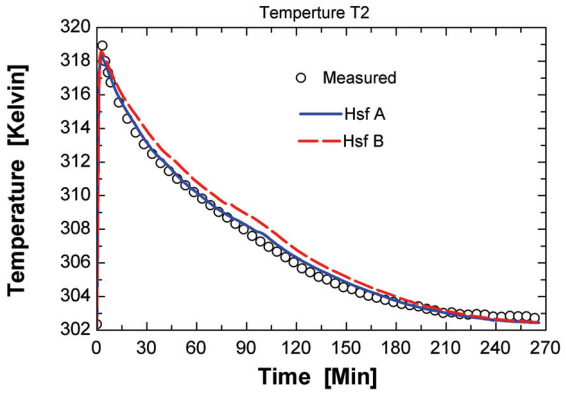

B

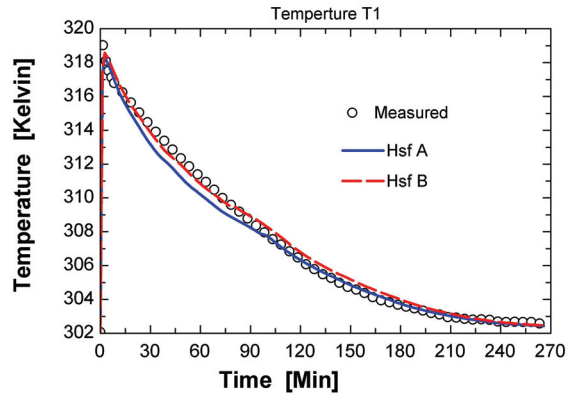

C

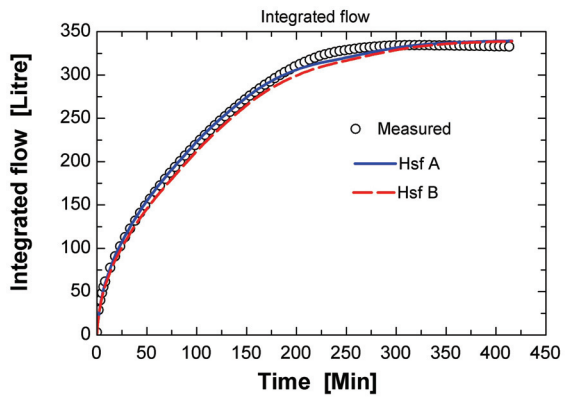

D

Figure 6.10 Typical adsorption experiments for the Tubular-type-configuration, including simulations of the solid temperature T_{MH}, A, B and C – temperature-time histories for different radial positions (see Figure 1.2), D - measured and simulated total amount of hydrogen into the reactor.

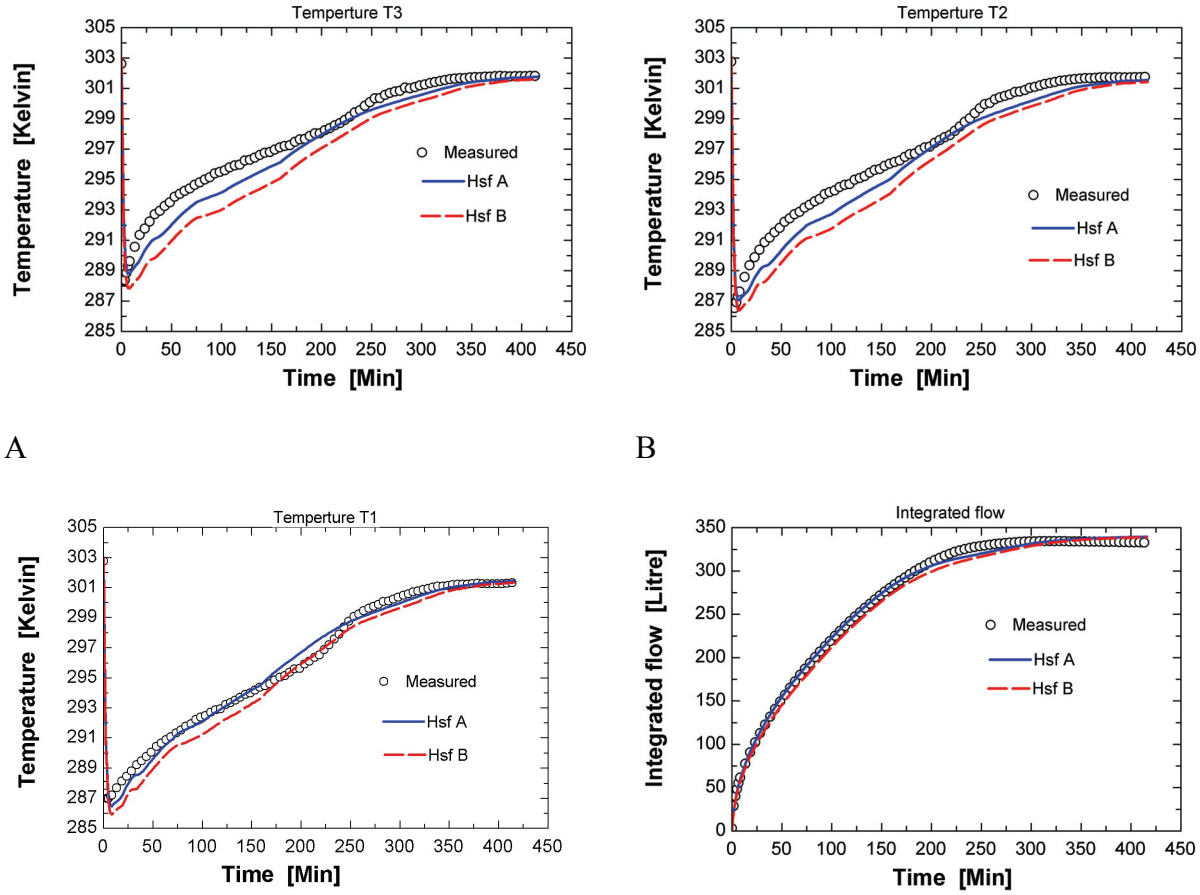

Figure 6.11 Typical desorption experiment for the tubular-type-configuration, including simulations of the solid temperature T_{MH}. A, B and C – temperature-time histories for different radial positions (see Figure 1.2), D - measured and simulated total amount of hydrogen out of the reactor.

The temperature changes very rapidly during the first few minutes of the experiments due to the fast kinetic reaction causing almost the same maximum or minimum temperature in the entire metal hydride bed.

The highest and lowest temperature was measured at thermocouple position 2 (Figure 6.10A and Figure 6.11 A). This is because thermocouple 1 is closer to the heating cooling water and thermocouple 3 is affected by the thermal ballast stored within the reactor wall and insulating Teflon layer.

The metal hydride equilibrium pressure also changes rapidly during the experiments first few minutes due to changes in temperature and H/AB_5 concentration. The equilibrium pressure continues to change until it approaches the charging or discharging gas pressure.

In the first 3 minutes the difference between the equilibrium and gas pressure is the main driving force in the gas-solid reaction. Then the difference between the equilibrium pressure and the gas pressure reduces to less than about |0.3| bar and the bed temperature decreases (absorption) or increases (desorption) due to heat transfer to or from the cooling/heating

water. The main driving force is now changed from pressure difference to heat transfer. This indicates that the reactor's performance is controlled by the material properties of in the beginning of the reaction and by the heat transfer in the rest of the experiment.

The effect of the two different reaction regimes (pressure difference and heat conduction) can be observed in Figure 6.11D where the derivative of the total amount of hydrogen released makes a deflection after ca 3 minutes, representing a change from the pressure driven to the heat transfer controlled regime. The hydrogen gas velocity has a maximum value during the first seconds of the experiments, with values as high as 2.5 cm/s close to the filter element, but drops rapidly towards values below 0.2 cm/s in the interior of the reactor, yielding low particle Reynolds numbers (in the range less than 100).

The hydrogen gas is entering or leaving the reactor through the filter elements shown in Figure 6.2. The amount of hydrogen entering or leaving the reactor is not evenly distributed between the filter elements, 40% of the total flow is passing through the filter positioned in the middle of the reactor, while 28% and 32% of the total flow passes through the top and bottom filter in the absorption experiment denoted $H_{sf,A}$. However, simulations indicate that the charge or discharge time is not changed even if hydrogen is only allowed to enter or leave the reactor through one filter element. This indicates that gaseous mass transport is not the rate limiting factor for this reactor design.

The Peclet number (Pe) defined as the fraction between the gas phase heat flux and the solid phase heat flux is calculated for both $H_{sf,A}$ and $H_{sf,B}$. The simulated Pe numbers are less than 0.1 in the bulk of the bed for both simulations, indicating that most of the heat is transferred by conduction.

Several investigators have discussed the assumption of thermal equilibrium between the gas and solid phases. An important parameter for deciding whether the gas and solid phases are in thermal equilibrium is the magnitude of the product ($h_{sf} \cdot a_p$) and the heat production/ consumption rate $\dot{Q} = \dot{m}_H \cdot \Delta H$. The maximum difference between the gas and solid can roughly be estimated with $\left|T_{MH} - T_g\right| \approx \frac{\dot{Q}}{h_{sf} \cdot a_p}$. The heat rates are in the range of $\dot{Q}$=$1 \cdot 10^5$-$6 \cdot 10^5$ W/m^3 in the presented simulations. The highest heat production/consumption rates are produced in the beginning of the experiments, close to the heat exchanger and external wall surfaces.

The size of the specific surface area a_p is highly dependent on the porosity of the bed and the particle diameter. Assuming a porosity of 0.45 and particle diameter ranging between 10· and 100· μm gives a specific surface area in the range of ($3.3 \cdot 10^4$-$3.3 \cdot 10^5$) m^2/m^3.

If the gas-to-solid heat transfer coefficient is estimated from the correlation of Wakao and Kaguei [28](Equation (6.22)), the heat transfer coefficient approaches an asymptotic value between (3.58-35.8 $\cdot 10^3$) W/m^2·K, with particle diameters between 10-100 μm as Re approaches zero. These approximations indicates that the assumption of thermal equilibrium will be valid if the Wakao and Kaguei correlation for the gas solid convective heat transfer coefficient is used. It is confirmed through simulations that the temperature difference between the gas and solid will be>10^{-3} K if the Wakao and Kaguei correlation is used. Other values for the product of $h_{sf} \cdot a_p$ were also tested out numerically using a constant as the heat transfer number between the gas and solid. As long as the product was higher than 10^6, the hydrogen flow and simulated temperature profiles remained unaffected. Similar results were

presented by Lloyd [31]. This implies that for particles with diameters in the range (10-100) μm, the simulated amount of charged/discharged hydrogen and radial temperature profiles will be unaffected as long as the solid-to-gas heat transfer coefficients are larger than 100 $W/m^2 \cdot K$. Showing that the assumption of thermal equilibrium only are valid as long as the product of $h_{sf} \cdot a_p$ are lager then a lower value.

It can be seen from Figure 6.10 and Figure 6.11 that the solid temperature (T_{MH}) are generally a little bit higher (absorption) and lower (desorption) for $H_{sf,B}$ than for $H_{sf,A}$. The temperature difference between the gas (T_g) and solid (T_{MH}) if $H_{sf,B}$ is used can be as high as 10 K in the first part of the simulations. Since less heat is transferred between the gas and solid in these two cases. How these two gas solid heat transfer coefficients also influences the time it takes to charge or discharge the reactors can be seen in Figure 6.10D and Figure 6.11D. The charging or discharging time will be longer if the h_p corresponding to $H_{sf,B}$ is used. The influence of the variation in the gas solid heat transfer coefficient on the solid temperature T_{MH} and charging time is not larger due to the fact that only a small amount of the total heat fluxes are transported through the gas phase.

6.6 CONCLUSIONS

As long as the Reynolds number for the water flow in the heat exchanger is above 3700 the hydrogen charging and discharging times are independent of the water flow rate. The brush type heat exchanger configuration improves the performance of the reactor remarkably, and makes it capable of delivering more than 90% of its total storage capacity at a constant hydrogen flow rate of 0.085 H/AB_5 per minute independent of the temperature of the heating fluid. The same reactor with a tubular type heat exchanger configuration was incapable of delivering more then approximately 60% of the total hydrogen storage capacity with a hydrogen flow rate of 0.085 H/AB_5 per minute. The charge/discharge half-times were more than 6 times faster for the brush type heat exchanger configuration, clearly indicating that heat transfer is the rate limiting factor for the metal hydride reactor with tubular-type heat exchanger. A ‘stirred-reactor’ (‘zero dimensional’) model for the metal hydride reactor with brush type heat exchanger was developed and verified against experimental data. A two-dimensional heat and mass transfer model was established for the plain tube heat exchanger configuration, which was verified by comparison with experimental data. The validity of the assumption of thermal equilibrium between gas and solid phase was discussed and justified.

Acknowledgements

This work received a support from Norsk Hydro ASA, Statkraft and the Norwegian Research Council. A great thanks goes to Dr Roman V Denys for help with changing of heat exchangers and filling the tank with metal hydride powder. Sincere thanks goes to the first author’s parents Helga and Gunnar Førde and his girlfriend Elin Aschim for the financial support during the completion of this study.

References

[1] Jemni A, Nasrallah B, S. Study of 2-Dimensional Heat-Transfer and Mass-Transfer During Absorption in a Metal-Hydrogen Reactor. Int J Hydrogen Energy 1995; 20(1): 43-52.

[2] Jemni A, Nasrallah B, S. Study of 2-Dimensional Heat and Mass-Transfer During Desorption in a Metal-Hydrogen Reactor. Int J Hydrogen Energy 1995; 20(11): 881-891.

[3] Jemni A, Nasrallah B, S, Lamloumi J. Study of Heat and Mass-Transfer in a Metal Hydrogen Reactor. Zeitschrift Fur Physikalische Chemie-International Journal of Research in Physical Chemistry & Chemical Physics 1994; 183: 197-203.

[4] Nasrallah B, S, Jemni A. Heat and mass transfer models in metal-hydrogen reactor. Int J Hydrogen Energy 1997; 22(1): 67-76.

[5] Mat M, D, Kaplan Y. Numerical study of hydrogen absorption in an Lm-Ni-5 hydride reactor. Int J Hydrogen Energy 2001; 26(9): 957-963.

[6] Aldas K, Mat M, D, Kaplan Y. A three-dimensional mathematical model for absorption in a metal hydride bed. Int J Hydrogen Energy 2002; 27(10): 1049-1056.

[7] Mat M, D, Kaplan Y, Aldas K. Investigation of three-dimensional heat and mass transfer in a metal hydride reactor. International Journal of Energy Research 2002; 26(11): 973-986.

[8] Demircan A, Demiralp M, Kaplan Y, Mat M, D, Veziroglu T, N. Experimental and theoretical analysis of hydrogen absorption in LaNi5-H-2 reactors. Int J Hydrogen Energy 2005; 30(13-14): 1437-1446.

[9] Nakagawa T, Inomoata A, Aoki H, Miura T. Numerical analysis of heat and mass transfer characteristics in the metal hydride bed. Int J Hydrogen Energy 2000; 25: 339-350.

[10] Kuznetsov A, V, Vafai K. Analytical Comparison and Criteria for Heat and Mass-Transfer Models in Metal Hydride Packed-Beds. Int J Heat Mass Transfer 1995; 38(15): 2873-2884.

[11] Gambini M. Metal Hydride Energy-Systems Performance Evaluation .B. Performance Analysis Model of Dual Metal Hydride Energy-Systems. Int J Hydrogen Energy 1994; 19(1): 81-97.

[12] Gambini M. Metal Hydride Energy-Systems Performance Evaluation .A. Dynamic Analysis Model of Heat and Mass-Transfer. Int J Hydrogen Energy 1994; 19(1): 67-80.

[13] European Space Agency http://www.esa.int/esaCP/Norway.html (22/10-07).

[14] LABTECH Int. Co. Ltd. Alloys Research and Manufacturing. Mladost-1, bl.25/A, Sofia-1784, BULGARIA; http://labtech.solo.bg/.

[15] Førde T, Maehlen J, P, Yartys V, A, Lototsky M, V, Uchida H. Influence of intrinsic hydrogenation/dehydrogenation kinetics on the dynamic behaviour of metal hydrides: A semi-empirical model and its verification. Int J Hydrogen Energy 2007; 32(8): 1041-1049.

[16] Sato M. Studies of hydrogen absorption and desorption processes in advanced intermetallic hydrides. edn. [Oslo]: Ph.D Thesis from Department of Chemistry Faculty of Mathematics and Natural Sciences University of Oslo: Unipub, 2005.

[17] Lototsky M, V, Yartys V, A, Marinin V, S, Lototsky N, M. Modelling of phase equilibria in metal-hydrogen systems. J Alloys Compd 2003; 356: 27-31.

[18] Oi T, Maki K, Sakaki Y, S. Heat transfer characteristics of the metal hydride vessel based on the plate-fin type heat exchanger. J Power Sources 2004; 125(1): 52-61.

[19] Dantzer P, Orgaz E. Thermodynamics of Hydride Chemical Heat-Pump .2. How to Select a Pair of Alloys. Int J Hydrogen Energy 1986; 11(12): 797-806.

[20] Ohlendorf D, Flotow H, E. Heat-Capacities and Thermodynamic Functions of $LaNi_5$, $LaNi_5H_{0.36}$ and $LaNi_5H_6$.39 from 5 to 300 K. Journal of the Less-Common Metals 1980; 73(1): 25-32.

[21] Incropera F, P, Dewitt D, P. Introduction to heat transfer. edn. Hoboken, N.J.: Wiley, 2007.

[22] Yartys V, A, Burnasheva V, V, Semenenko K, N, Fadeeva N, V, Solovev S, P. Crystal-Chemistry of $RT_5H(D)X$, $RT_2H(D)X$ and $RT_3H(D)X$ Hydrides Based on Intermetallic Compounds of $CaCu_5$, $MgCu_2$, $MgZn_2$ and $PuNi_3$ Structure Types. Int J Hydrogen Energy 1982; 7(12): 957-965.

[23] Hahne E, Kallweit J. Thermal conductivity of metal hydride materials for storage of hydrogen: Experimental investigation. Int J Hydrogen Energy 1998; 23(2): 107-114.

[24] Sun D, W, Deng S, J. A Theoretical-Model Predicting the Effective Thermal-Conductivity in Powdered Metal Hydride Beds. Int J Hydrogen Energy 1990; 15(5): 331-336.

[25] Pons M, Dantzer P. Determination of Thermal-Conductivity and Wall Heat-Transfer Coefficient of Hydrogen Storage Materials. Int J Hydrogen Energy 1994; 19(7): 611-616.

[26] Ohlendorf D, Flotow H, E. Experimental Heat-Capacities of $LaNi_5$, Alpha-$LaNi_5H_{0.36}$, and Beta-$LaNi_5H_{6.39}$ from 5 to 300-Degrees-K - Thermodynamic Properties of the $LaNi_5$-H_2 System. J Chem Phys 1980; 73(6): 2937-2948.

[27] Kaviany M. Principles of heat transfer in porous media. 2nd edn. New York: Springer, 1995.

[28] Wakao N, Kaguei S. Heat and mass transfer in packed beds. edn. New York: Gordon and Breach Science Pub., 1982.

[29] Whitaker S. Fundamental principles of heat transfer. edn. New York: Pergamon Press, 1977.

[30] Lototsky M, V, Yartys V, A, Marinin.V, S, Lototsky N, M. Modelling of phase equilibria in metal-hydrogen systems. J Alloys Compd 2003; 356: 27-31.

[31] Lloyd G, M. Formulation and Numerical Solution of Non-Local Thermal Equilibrium Equations for Multiple Gas/Solid Porous Metal Hydride Reactors. J Heat Transfer 2001; 123(3): 520-526.

7 EXPERIMENTAL STUDIES AND THEORETICAL COMPARISON OF FOUR DIFFERENT METAL HYDRIDE STORAGE UNITS

T. Førde[1], V.A. Yartys[1] and E. Næss[2]

1) Institute for Energy Technology (IFE), Kjeller. Norway

2) Norwegian University of Science and Technology, Trondheim, Norway

7.1 ABSTRACT

Metal hydrides can store hydrogen at low pressures with high volumetric capacity. This makes them good candidates for hydrogen storage media. This paper compares the hydrogen charging and discharging times of four different metal hydride reactors with different geometry of the heat exchangers. The reactors are filled with (0.85-2.5) kg of AB_5 type metal hydride powder. A total energy balance for the different units is performed and is used to calculate the heat duty per unit driving force.

Nomenclature

A	Heat transfer area	[m^2]
C	Hydrogen to metal atomic ratio	[-]
ρ	Density	[kg/m^2]
c_p	Heat capacity	[J/kg·K]
$\dot{F}$	Flow rate	[mol/s] or [kg/s]
K_{eff}	Effective conductivity	[W/m·K]
h	Heat transfer coefficient	[W/m^2K]
ΔH	Heat of reaction	[J/mol]
M	Mass	[kg]
P	Pressure	[bar]
T	Temperature	[K]
T	Time	[s]
R	Radius	[m]
UA	Heat duty per unit driving force	[W/K]
$\dot{Q}$	Heat duty	[W]
$X_{Thermocuple}$	Thermocouple position	[m]
ε	Porosity	[-]

Subscript

bath	Bath
g	Gas
in	In
MH	Metal hydride
sb	Solid to bulk
surr	Surroundings
reaction	Reaction
reactor	Reactor
out	Out
w	Water
wb	Wall to bulk
ws	Wall to solid

7.2 INTRODUCTION

Metal hydrides can have many applications. These include hydrogen compressors, heat pumps and storage units. There are several challenges in using metal hydrides as hydrogen storage medium, since the reactors' performance does not depends only on the material properties. Due to the large amount of heat consumed or released in the gas solid reaction it is important to remove or add heat in an efficient way to optimise the reactor performance.

A metal hydride storage unit consists of a reactor shell, made of aluminium, composite material or stainless steal. The choice of reactor shell material depends on the requirements, regarding tank price, H_2 storage weight percent, working temperature and pressure. The reactor is filled with metal hydride powder and the gas is often distributed internally through a filter element. The metal hydride powder consists of fine particles, the particles will typically have a size distribution spanning from 10-40 μm after a few cycles. Many storage units have an internal heat exchanger used to distribute and remove heat in an efficient way. The design and choice of heat exchanger depends on the requirement to the reactors filling and discharging time, price and compactness. It is assumed in this paper that the heat transfer mechanism in a metal hydride bed is the same as in other porous beds, e.g. a catalyst bed. The heat duty per unit driving force UA is an important parameter characterising the reactors heat transfer properties. In this paper the heat duty per unit driving force are calculated from experimental data and are used to compare the different unit s' heat transfer characteristics.

Several metal hydride reactors have been proposed and described in the literature over the last years for usage in various applications. Comparison between experimental and simulated data is presented by Nishimura et al. [1] for a 10 Nm^3 scale hydrogen storage unit with internal tube type heat exchanger. Experimental data for a reactor with 4000 litre hydrogen storage capacity with a U-shaped tube heat exchanger is presented by Levensque et al. [2]. In this reactor the metal hydride powder is packed into Al foam and hot gas is circulated in the tube type heat exchanger. This unit is used to serve a 500 W proton exchange membrane fuel cell (PEM). A theoretical deduction of the overall heat transfer coefficient for a finned type heat exchanger based on the theory described by Kuni et al. [3-5], was presented by Oi et al. [6] together with experimental results for a metal hydride storage unit containing a plate-fin type heat exchanger.

The main objective of this paper is to experimentally compare and analyse the performance of four different metal hydride storage reactors filled with the same type of AB_5 alloy. Three of the tested reactors have an internal heat exchanger while in the last reactor heat transfer into and out of the reactor occurs through the outer surfaces.

7.3 THEORY

A normal assumption in the development of an overall heat transfer coefficient (U) from the heating or cooling surface to the porous bed is to use a serial scheme as indicated in Equation (7.1).

$$\frac{1}{U} = \frac{1}{A \cdot h_{\infty,'h/c}} + R_{cond} + \frac{1}{A \cdot h_{wb}} \tag{7.1}$$

Here A represent the active heat transfer area. The first term in Equation (7.1) represent the heat transfer coefficient from the heating or cooling medium. Some heat exchangers are designed so that heat has to be transferred by conduction with the belonging heat transfer resistance R_{cond}. The two heat transfer coefficients can be calculated based on literature correlations found in for example [7]. The last term in Equation (7.1) h_{wb} is the heat transfer coefficient between the heat exchanger wall and reactor bed. The wall to bed heat transfer coefficient (h_{wb}) can be split into a convection coefficient from the wall to the bed surface h_{ws} and from the bed surface to the bulk of the bed h_{sb} as indicated in Equation (7.2).

(7.2) $$\frac{1}{h_{wb}} = \frac{1}{h_{ws}} + \frac{1}{h_{sb}}$$

When heat is transferred from the walls to a packed bed of granules, a wall resistance appears (h_{ws}) that strongly depends on the transport properties of the gas phase. In addition, heat will be exchanged by radiation and contact area conduction [8]. These heat transfer phenomena can be considered to be independent of each other [8], and can be estimated with the correlations given by Schlünder [9]. The bulk penetration coefficient h_{sb} is derived from the exact solution of the energy equation without heat source or sinks. To take into account the chemical reactions within the metal hydride bed, h_{sb} can be multiplied with a function f(). Some examples of such functions are given in [8].

However, the heat duty per unit driving force UA can also be calculated from experimental data with Equation (7.3).

(7.3) $$\dot{Q}_w = UA \cdot \Delta T$$

Where Q_w is the heat flux into or out of the reactor, either calculated with Equation (7.6) or (7.7). ΔT is the temperature difference between the heating/cooling water and metal hydride bed calculated with Equation (7.4) or (7.5) .

(7.4) $$\Delta T = \frac{T_{w,out} - T_{w,in}}{\ln\left(\frac{T_{MH} - T_{w,out}}{T_{MH} - T_{w,in}}\right)}$$

(7.5) $$\Delta T = T_{w,bath} - T_{MH}$$

Here, $T_{w,out}$ is the measured temperature of the outlet water, $T_{w,in}$ is the measured temperature of the inlet water, T_{MH} is the mass averaged metal hydride temperature and $T_{w,bath}$ is the temperature of the water bath. If the reactors has an internal heat exchanger the temperature difference ΔT is calculated with the logarithmic mean temperature Equation (7.4) [7], otherwise the temperature difference is estimated with equation (7.5).

To further analyse and improve understanding of the reactors behaviour an energy balance is performed using Equation (7.6).

(7.6) $$\dot{Q}_m = \dot{Q}_{reaction} + \dot{Q}_g + \dot{Q}_w$$

Here $\dot{Q}_w$ is the heat flux flowing between the reactor and heating cooling fluid, $\dot{Q}_g$ is heat transferred into and out of the reactor with the hydrogen gas, $\dot{Q}_{reaction}$ is the energy produced or consumed in the chemical reaction between the gas and solid and $\dot{Q}_m$ is the energy used to change the temperature of the metal hydride powder and the reactor it self. The equations used to calculate and estimate these energy fluxes are given in equation (7.7) below.

$$
\begin{aligned}
\dot{Q}_m &= c_{p,\tau\,eactor} \cdot m_{reactor} \cdot \frac{\partial T_{reactor}}{\partial t} + c_{P,MH} \cdot m_{MH} \frac{\partial T_{MH}}{\partial t} \\
\dot{Q}_{reac} &= \dot{F}_g \cdot \Delta H \\
\dot{Q}_g &= c_{p,g} \cdot T_{MH} \cdot \dot{F}_g \qquad \textit{Desorption} \\
\dot{Q}_g &= c_{p,g} \cdot \left(T_{surr} - T_{MH}\right) \cdot \dot{F}_g \qquad \textit{Absorption} \\
\dot{Q}_w &= \dot{F}_w \cdot c_{P,w} \cdot \left(T_{w,in} - T_{w,out}\right)
\end{aligned}
\tag{7.7}
$$

Here $T_{reactor}$ is the temperature of the reactor shell and T_{MH} is the mass averaged temperature of the metal hydride powder, $m_{reactor}$ is the mass of the reactor shell, m_{MH} is the metal hydride powder mass, c_P is heat capacity, $\dot{F}_w$ is the flow rate of the circulating heating/cooling water, $T_{w,in}$ is the heating/cooling water inlet temperature and $T_{w,out}$ is the outlet temperature of the heating/cooling water. The hydrogen flow rate into and out of the reactor $\dot{F}_g$ is equal to the measured rate of hydrogen entering or leaving the reactor. The flows are negative in the energy balance if hydrogen is leaving the reactor and positive if hydrogen enters the reactor. In these simplified energy balance calculations the hydrogen gas is assumed to be in thermal equilibrium with the metal hydride powder.

7.4 EXPERIMENTAL SET UP

A principal sketch of the experimental set up used to characterise the different reactors is shown in Figure 7.1.

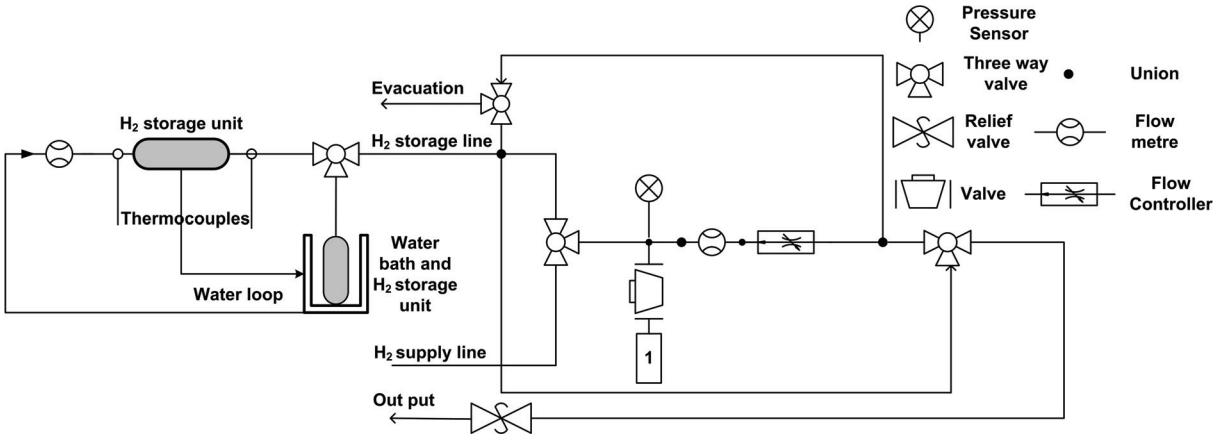

Figure 7.1 Schematic diagram of the set up for the testing hydrogen storage units: Containing 1 Buffer volume, pressure sensor (0-25 bar absolute), volume flow meter (0-30 l/min) and a flow controller

The absorption and desorption flow rates are controlled or monitored with a flow controller and a flow metre. The hydrogen gas pressure is measured with a pressure gauge. The desired

charging pressure can be set with a pressure regulator during absorption, while a relief valve is used to control the discharge pressure. Vacuum conditions can be applied using a rotary vacuum pump connected to the evacuation line. A constant water flow rate of heating/cooling water is supplied with a water bath. If the tested units have an internal heat exchanger, the temperatures of the inlet and outlet water are measured together with the circulating water flow rate. Unit#A in Figure 7.2 has no internal heat transfer device and this unit is simply immersed into the water bath during the absorption and desorption experiments.

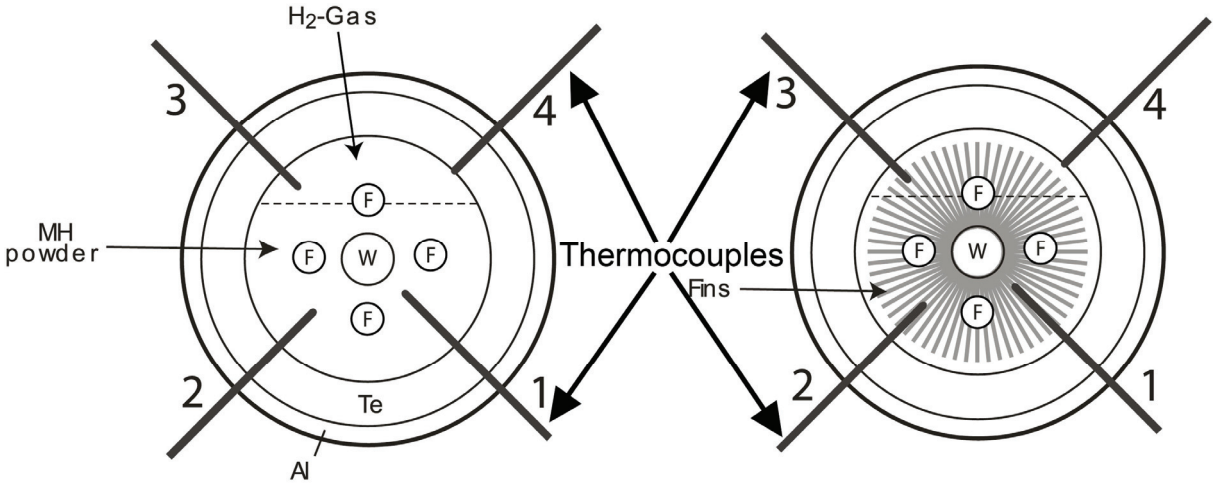

D) Unit#D F=Filter element W=Water tube C) Unit#C

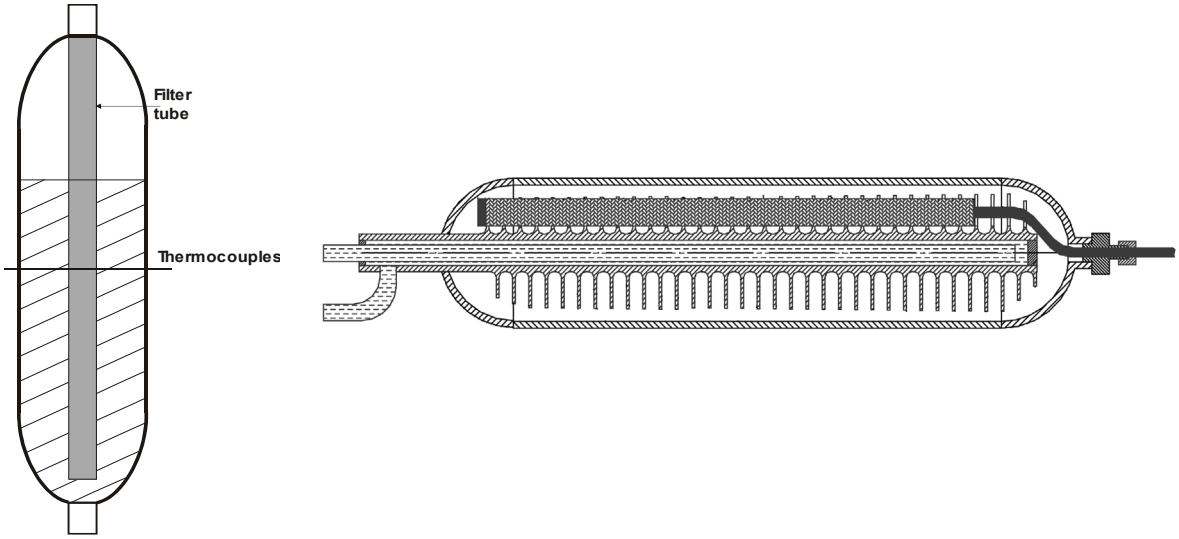

A) Unit#A) B) Unit#B

Figure 7.2 Schematic drawing of the tested reactors A) cylindrical without heat exchanger, B) with a plate finned heat exchanger, C) with a brush type heat exchanger, D) with a tube type heat exchanger.

Four different metal hydride reactors were tested. The cylindrical reactor (Unit#A) is made in stainless steal with external heat transfer surfaces. This reactor has three internal thermocouples positioned at different radial position and two thermocouples welded to the outer wall of the reactor. The plate finned reactor's (Unit#B) shell and heat exchanger are

made of aluminium. This reactor has four external thermocouples glued to the outer wall. Both the brush type reactor (Unit#C) and tube type reactor (Unit#D) are made of aluminium. Both reactors have four internal thermocouples positioned at different radial positions, and two external thermocouples glued to the outside reactor wall.

A 0.8 cm of isolating Teflon layer is inserted between the metal hydride bed and the reactor wall in Unit#C and D. In addition Unit#B, C, D are insulated with 1.2 cm rubber type insulating material. All the different metal hydride reactors were filled with the same type of AB_5 alloy ($La_{0.83}Ce_{0.10}Pr_{0.04}Nd_{0.03}Ni_{4.40}Al_{0.60}$) provided by a commercial supplier [10]. The reaction rate of this alloy is reported by Førde et al. [11]. This alloy's equilibrium pressures with hydrogen to metal atomic ratio of 3 at different temperatures are given in Table 7.1 for absorption and desorption. More detailed pressure, concentration and temperature curves are given in [11].

Table 7.1 The alloy used in the various units, equilibrium pressure at various temperatures and hydrogen to metal atomic ratio of three.

Temperature [K]	283	288	293	298	303	308	313	318
P_{eq} Desorption [bar]	1.8	2.2	2.7	3.3	4.0	4.8	5.8	6.8
P_{eq} Absorption [bar]	2.8	3.4	4.2	5.0	6.1	7.3	8.6	10.2

It can be seen from Table 7.1 that the alloys middle point equilibrium pressure varies strongly with temperature and that the absorption curves has a higher equilibrium pressure than the desorption curves at the same temperature, due to irreversibility in the absorption desorption cycle.

More details regarding the different reactors are given in Table 7.2. In addition to the reactors described above, experiments were also performed with a kinetic reactor described in detail in [11], this reactor operates close to isothermal condition during charging and discharging and is used as a reference.

Table 7.2 Details of the different reactors

Reactor	Mass of metal hydride powder [kg]	Heat exchanger type	Heat transfer area [m^2]	Maximum heat transfer distance [m]
Unit#A (Cylindrical)	0.85	External	0.017	0.017
Unit#B (Fin type)	2.2	Internal	0.093	0.005
Unit#C (Brush type)	2.3	Internal	0.21	0.001
Unit#D (Tube type)	2.5	Internal	0.014	0.018

The amount of powder filled in each reactor was weighted in advance and losses during filling were subtracted. Unit#A was submerged into a water bath and the heat transfer area was defined equal to the surface area of the metal hydride powder towards the heating/cooling water. This area was estimated based on the metal hydride density, shape of the reactor and amount of powder. The heat transfer area in Unit#B includes the fins and the water tube area and was estimated from the technical drawings. In Unit#C the heat transfer area of one fin was calculated based on fin length and diameter. The surface area was then multiplied with the number of fins. The heat transfer area belonging to the water tube was estimated from the length and diameter of the tube minus the base area of one fin multiplied with the total number of fins. The total heat transfer area for Unit#C was the sum of the fins surface area

and the water tubes surface area. The heat transfer area in Unit#D was calculated from the length and diameter of the water tube.

The maximum heat transfer distance is defined as the distance from the outer wall to the filter element for Unit#A. For Unit#B and Unit#C the maximum heat transfer distance is defined as half the distance between two fins. The maximum heat transfer distance in unit#D is set equal to the distance from the wall of the water tube to the inner wall of the reactor shell.

After loading, leak testing and activation, all the reactors were cycled several times with reversible capacity prior to the performed experiments. The hydrogen used during all the experiments was of 99.9999% purity. The experiments were performed in the following manner. The reactors temperature was uniform and the reactors gas pressure was stable before any experiment was started. The cooling/heating water's inlet temperature was kept stable during the entire experiments for the reactors with an internal heat exchanger. For these reactors was also the flow rate of the heating cooling water kept stable through the whole experiment. For Unit#C which was immersed into a water bath during the experiments are the water bath temperature was kept constant through the whole experiment. The units are assembled to the experimental set up as shown in Figure 7.1 and the desired discharge pressure is controlled with a needle valve, and the desired charging pressure was set with a pressure regulator and kept constant through the entire experiment.

7.5 RESULTS AND DISCUSSION

How good a metal hydride hydrogen storage unit performance, is normally evaluated based on its gravimetric and volumetric energy density and the charge and discharging time. The charging and discharging time is affected by several parameters: Firstly the intrinsic kinetics of the metal hydride powder, secondly the hydrogen mass transfer within the porous metal hydride bed, and thirdly how effective heat can be removed or supplied to the metal hydride bed. The intrinsic kinetics for the alloy used in the different reactors described above has been investigated by Førde et al. [11] and is found to be very fast. A small amount of metal hydride powder was completely charged at less than twenty seconds, showing that the intrinsic material properties are not rate limiting.

Furthermore, if the mass transport in the gaseous phase is the rate limiting step, large pressure gradients in the gaseous pressure could be expected within the metal hydride bed. In Unit#C and Unit#D four filter elements are distributing the hydrogen gas within the porous bed ensuring short mass transfer distances. The largest mass transfer distances occur in Unit#A (0.017 metre) and Unit#B (0.03 metre). Heat and mass transfer simulations indicate that the pressure drop never exceed 0.016 bar for Unit#A. Thus, as a rough approximation we can assume that the pressure drop in Unit#B will not exceed 0.032 bar. A decresase or increase in the gaseous pressure with 0.032 bar will neither affect the particles equilibrium concentration of hydrogen to any large extent, nor the hydrogen absorption or desorptioin rates of the MH particles. It is there fore reasonable to assume that the transport of hydrogen gas through the porous bed is not the rate limiting factor for the tested units.

The internal temperatures were measured for Unit#A, Unit#C and Unit#D during all the experiments. For Unit#B only temperatures of the outer reactor wall was measured. During both charging and discarging of the reactors the average bed temperature was found to either sink or decrease rapidly during the first 1-2 minutes and slowly move towards the heating or cooling water temperature. These temperatures affect the reactors equilibrium pressure and

the powder's ability to absorb or desorb hydrogen and therefore also the reactor's charging or discharging rates. We therefore we conclude that the reactors ability to remove or bring heat in to the metal hydride bed is the rate limiting process. Due to the metal hydride beds poor effective thermal conductivity.

As long as the rate limiting factor is the same in all the tested reactors it is possible to compare their performance even though the reactor size varies. Several experiments were performed and used to compare the behaviour of the different reactors. Figure 7.3 shows the time it takes to charge all the different reactors to 50 percent of the total capacity with different charging pressures and at various temperatures. All the experiments were performed in the experimental set up described above, and with identical initial conditions (uniform temperature and stable gas pressure).

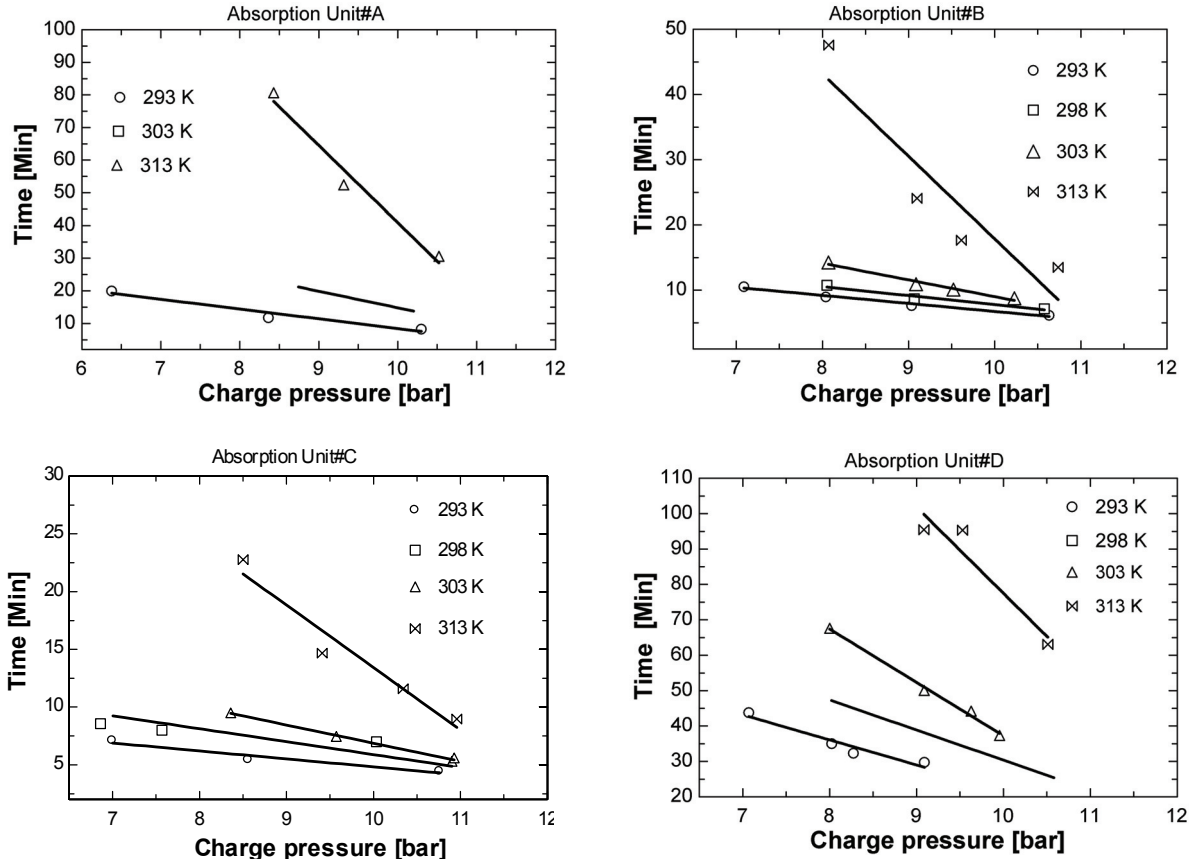

Figure 7.3 Time for 50 % charging for all the different reactors at various temperatures and pressures.

It can be seen from Figure 7.3 that there is a relationship between charging pressure and time to 50% charging and that the charging time increase with higher starting temperature. It is also clear that the Unit#C (brush type) reactor is the fastest reactor followed by the Unit#B (fined type) reactor. The cylindrical Unit#And the Unit#D (tube type) reactor is the slowest reactor. The Unit#C is 8 times faster than the Unit#D (tube type). These two reactors are identical except the heat exchanger. The same type of experiment was performed to compare the time it takes for the different reactors to discharge 50% of their total capacity towards

different discharge pressures with various temperatures of the heating water. The results are shown in Figure 7.4.

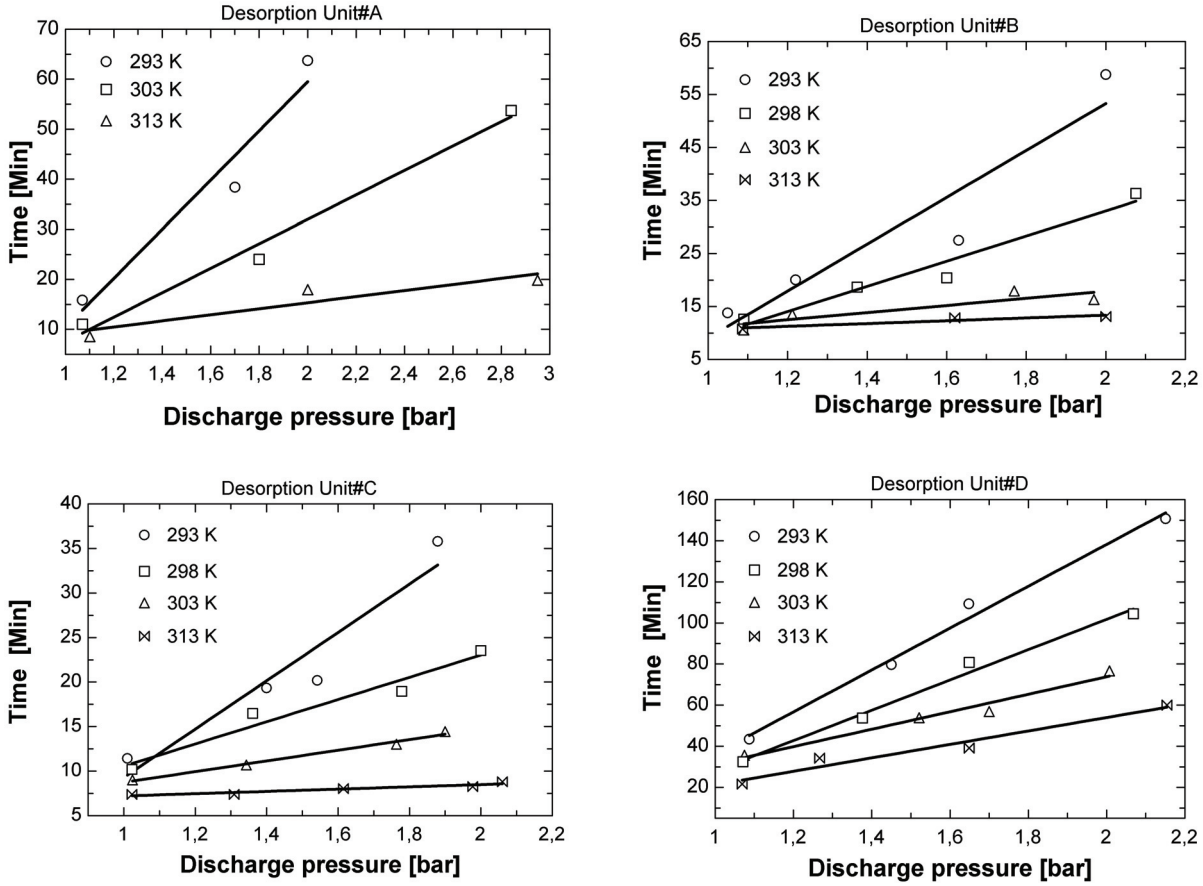

Figure 7.4 Time for 50% discharge for different reactors at various discharge pressures and temperatures.

It can be seen from Figure 7.4 that there is a relationship between discharge pressure and time to 50% discharging and that the discharge time decreases with higher starting temperature.This is due to the importance of the difference between gaseous pressure and equilibrium pressure as a driving force in the expression for the alloys reaction rate. Again the Unit#C is the fastest followed by Unit#B and Unit#C while Unit#D is the slowest. It can bee seen from Figure 7.3 that the fastest charging of the reactors occurs with the lowest cooling water temperature and highest charging gas pressure. It can also be seen from Figure 7.4 that the reactors will always discharge fastest with highest temperature on the heating water and working towards a low discharge pressure. The fastest charging experiment (10.5 charging pressure and 293 K cooling water) is slightly faster than the fastest discharge experiment (1.1 bar discharge pressure and 313 K heating water). This is most likely due to the material's thermodynamic properties, i.e. the hydrogen pressure, composition isothermal behaviour. The difference between charging/discharging pressure and plateau midpoints equilibrium pressure (given in Table 7.1) is 6.3 for the absorption case and 4.7 for the desorption case.

In a practical system, e.g. if the metal hydride reactor is used together with a fuel cell the reactor will more likely desorb with a constant hydrogen flow rate. Thus the different reactors' ability to deliver a constant hydrogen flow rate of 2.2 litre pr minute pr kg metal hydride powder towards a discharge pressure of 1.1 bar with 303 K heating water was

investigated. A flow of 2.2 liters pr minute pr kg metal hydride powder correspond to an absorption or desorption rate of 0.085 H/AB_5 pr min, and also correspond to the amount of hydrogen used if 500 W should be delivered from a PEM fuel cell from.

The trend for these constant flow experiments was the same as for charging and discharging time experiments, Unit#C and Unit#B was the best reactors-capable of delivering more than 95% of their total capacity at a constant flow rate. Unit#A was able to deliver ca 80 % of its total capacity and Unit#D is the least efficient reactor, only capable of delivering ca 48 % of its total capacity with the given discharge conditions.

To further analyse the various reactors the energy balance described in (7.6) is carried out. The energy balance is well defined for all the different reactors. The results from the energy balance indicate the following sizes of the different energy fluxes in absolute values $\left|\dot{Q}_{reaction}\right| \geq \left|\dot{Q}_w\right| > \left|\dot{Q}_g\right| > \left|\dot{Q}_m\right|$ for all the different units. Based on the performed energy balance and (7.3) the heat duty per unit driving force UA was calculated, some results for the various reactors are given in Table 7.3.

Table 7.3 Calculated heat duty per unit driving force UA.

Parameters	Unit#A Cylindrical	Unit#B Finned plate	Unit#C Brush	Unit#D Tube	Reactor E Kinetic
UA $\left[\frac{W}{K}\right]$	8 ± 3	20 ± 5	30 ± 6	4 ± 2	500 ± 50

Unit#C has the highest heat duty per unit driving force, followed by Unit#B, Unit#A and Unit#D. Unit#C should have some contact resistance because the brush type heat exchanger is strapped to the water tube with thin wires, however the heat transfer distance is very short yielding small bulk penetration resistances. The heat exchanger in the Unit#B consists of one piece of aluminium, however, the heat transfer distance is somewhat larger then Unit#C. We also observe that the heat duty per unit driving force has a characteristic shape with higher values in the beginning of the experiments and moves toward an asymptotic value.

The equations given by Schünder [9] are used to estimate the theoretical wall to bed surface convective heat transfer coefficient h_{ws}. The bed surface to bulk heat transfer coefficients h_{sb} is calculated using the correlations taken from [8] with constant temperature as a boundary condition and 50 mm heat transfer distance. These calculations indicate that the molecular gas conduction is the most important heat transfer mechanism close to the wall and that the wall to bed surface convective heat transfer coefficient h_{sb} is more than 100 times larger than the bed surface to bulk convective heat transfer coefficient. These estimations indicate that the wall contact resistance is negligible, and these theoretical results are in agreement with the experimental results published by Dantzer [12] .

To further understand the heat transfer characteristic of the different units, the wall to bed heat transfer coefficient were estimated based on experimental data for some of the reactors. In order to calculate the wall surface to bulk heat transfer coefficient, we need to estimate the wall temperature and the mass average metal hydride bulk temperature. This cannot be done for Unit#B, since this unit do not have internal measuring points. Neither is it possible to estimate the wall to bed heat transfer coefficient for Unit#C due to the uncertainty of the contact resistance between the brush type heat exchanger and the water tube. The temperature

of the inner wall-heating surface can be estimated for both Unit#A and D. To find the inner wall temperature in Unit#A unit we use the measured outer wall temperature and the estimated heat flux between the reactor and water bath, it is assumed that no energy is used to heat or cool the reactor wall. For Unit#D the inner wall temperature is estimated based on an average water temperature, the calculated water heat flux and an estimated convective water heat transfer coefficient. The calculated heat transfer coefficient from the wall to bed, for Unit#A and Unit#D has a characteristically shape with higher values in the beginning of the experiment and moves toward an asymptotic value in the end of the experiment. The calculated wall to bed heat transfer coefficient for the Unit#A is slightly larger than the calculated heat transfer coefficient for Unit#D. This could be due to geometrical differences or underestimation of the heat transfer surfaces or because the heat flux is over estimated. It is also good correspondence between the wall to bed heat transfer coefficient calculated from experimental data and theory. The heat transfer coefficients derived from experiment are consistently larger than the one estimated with the equation presented in [8] since these equation are neglecting the effect of chemical reactions within the bed. There is no clear difference between neither the heat duty per unit driving force UA nor the calculated wall to bed heat transfer coefficient, for the various absorption or desorption experiments. This is most likely due to the small difference in both absorption and desorption enthalpy and reaction rate.

If we combine the data presented in Figure 7.3 and Figure 7.4 with the data from Table 7.3 it is possible to plot the 50% charging and discharging time for certain given pressure as a function of heat duty per unit driving force as shown in Figure 7.5.

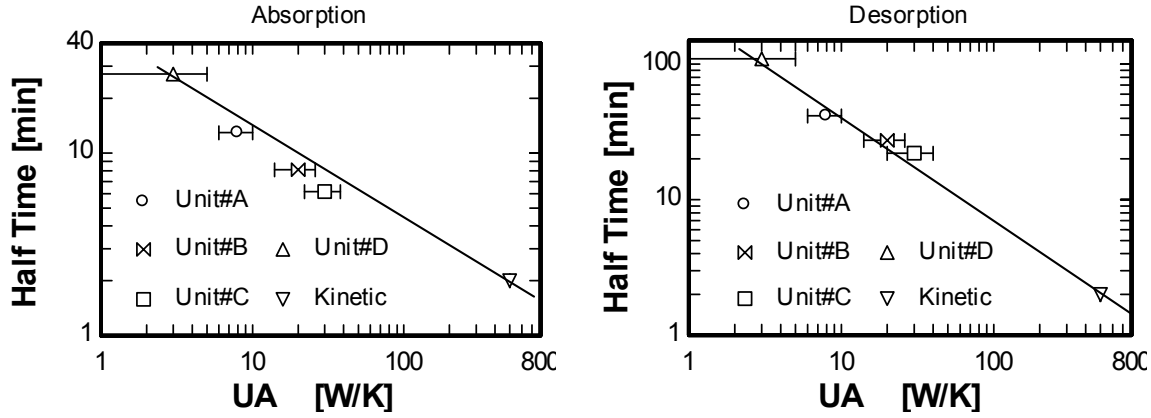

A B

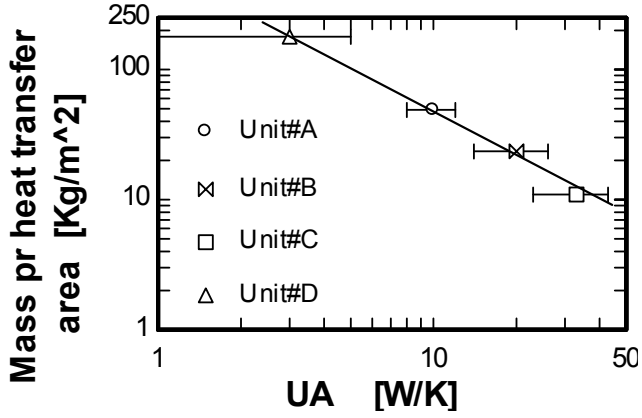

C

Figure 7.5 A and B Relationships between heat duty per unit driving force and charging and discharging half time. C Relationship between heat duty per unit driving force and mass pr heat transfer surface area.

The absorption data shown in Figure 7.5A are taken from experiments charged with 9.5 bar gas pressure and 303 K temperature of the cooling water. The data presented for the desorption case in Figure 7.5B are taken from desorption experiments with a 1.1 discharge pressure and 303 K heating water. It can be seen from Figure 7.5 that there is a relationship between the heat duty per unit driving force and the time it takes for the reactor to discharge 50% of their total capacity, if plotted in a logarithm diagram. Figure 7.5 C also shows that it is a relationship between the different units heat duty per unit driving force and heat transfer area pr kg of metal hydride powder. This relationship will most likely be more dependent on the geometry of the heat exchangers if the different units are scaled up.

7.6 CONCLUSIONS

The performance of four different metal hydride storage units is characterized and analysed. A relationship between charging/discharging pressure and charging/discharging time is found. The brush type heat exchanger is a good and economic alternative to use as a heat exchanger. The AB_5 type of metal hydrides powder used in the investigated reactors is capable of delivering more than 90% of their total capacity with a flow rate of 0.085 H/AB_5 pr min, with

303 K heating water towards a 1.1 discharge pressure if the heat duty per unit driving force is above 20 W/K**.** The product of the overall heat transfer number U and heat transfer surface affects the charging and discharging time and depend on the reactors heat transfer surfaces.

Acknowledgements

This work received a support from Norsk Hydro ASA, Statkraft and the Norwegian Research Council. A great thanks also goes to the first author's parents Helga and Gunnar Førde and his girlfriend Elin Aschim for the financial support during the completion of this study

References

[1] Nishimura K, Inazumi C, Oguro K, Uehara I, Itoh Y, Fujitani S, Yonezu I. Simulation and evaluation of a hydrogen storage system using hydrogen storage alloy for a chemical CO_2 fixation and utilization system. International Journal of Hydrogen Energy 2000; 25(11): 1087-1093.

[2] Levesque S, Ciureanu M, Roberge R, Motyka T. Hydrogen storage for fuel cell systems with stationary applications - I. Transient measurement technique for packed bed evaluation. International Journal of Hydrogen Energy 2000; 25(11): 1095-1105.

[3] Kunii D, Smith J, M. Heat Transfer Characteristics of Porous Rocks. Aiche Journal 1960; 6(1): 71-78.

[4] Kunii D, Smith J, M. Heat Transfer Characteristics of Porous Rocks .2. Thermal Conductivities of Unconsolidated Particles with Flowing Fluids. Aiche Journal 1961; 7(1): 29-34.

[5] Kunii D, Suzuki M. Particle-to-Fluid Heat and Mass Transfer in Packed Beds of Fine Particles. International Journal of Heat and Mass Transfer 1967; 10(7): 845.

[6] Oi T, Maki K, Sakaki Y, S. Heat transfer characteristics of the metal hydride vessel based on the plate-fin type heat exchanger. Journal of Power Sources 2004; 125(1): 52-61.

[7] Incropera F, P, Dewitt D, P. Introduction to heat transfer. edn. Hoboken, N.J.: Wiley, 2007.

[8] Hewitt G, F. Heat exchanger design handbook 1998 Part 1: Heat exchanger theory; Part 2 : Fluid mechanics and heat transfer. edn. New York: Begell House,Inc, 1998.

[9] Schlünder E, U. Heat Transfer to Packed and Stirred Beds from the Surface of Immersed Bodies. Chemical Engineering and Processing 1984; 18(1): 31-53.

[10] LABTECH Int. Co. Ltd. Alloys Research and Manufacturing. Mladost-1, bl.25/A, Sofia-1784, BULGARIA; http://labtech.solo.bg/. 03.06-2007.

[11] Førde T, Maehlen J, P, Yartys V, A, Lototsky M, V, Uchida H. Influence of intrinsic hydrogenation/dehydrogenation kinetics on the dynamic behaviour of metal hydrides: A semi-empirical model and its verification. International Journal of Hydrogen Energy 2007; 32(8): 1041-1049.

[12] Pons M, Dantzer P. Determination of thermal conductivity and wall heat transfer coefficient of hydrogen storage materials I International Journal of Hydrogen Energy 1994; 19(7): 611-616.

[13] International standard (ISO 5168) Measurement of fluid flow-Estimation of uncertainty of a flow-rate measurements. 1978.

Appendix A7.1: Uncertainty

Estimation and treatment of uncertainty

Background and theory

A result of a given measurement is, usually, only an estimate of the specific value of the quantity subject to the measurement. The results are therefore complete only when supplemented with quantitative uncertainty. Measurement errors are commonly divided into four different groups.

- Spurious errors
- Random errors
- Constant systematic errors
- Variable systematic errors

Spurious errors

These errors are related to human errors or instrument malfunction. Such errors should not be incorporated into any statistical analysis and the measurement should be discarded. A through analysis of the measurement chain, from measurement point to conversion of data, and documented measurement routines minimize the risk of having spurious errors.

Random errors

Random errors are referred to as precision or experimental errors. They are caused by numerous, small, independent influences, which prevent a measurement system from delivering the same measured value for repeated measurements with the same input values. The magnitude of the deviation from the mean value is quantified as a statistical uncertainty. The mean value of a population of repeated measurements is derived from (7.A.1). This is the best estimate for the true value of the measured parameter. In large populations the data points are assumed to vary by chance and get close to a normal distribution.

(7.A.1) $$\bar{A} = \frac{1}{n}\sum_{i=1}^{n} A_i$$

When the sample size is small, it is necessary to correct to correct the statistical results that are based on a normal distribution by means of the student –t probability.

Constant systematic errors

Systematic uncertainty is fixed and gives a constant output being either too high or too low compared to the true value. The uncertainty may be evaluated by an approximation to a standard deviation. This value is determined by experience, knowledge or pure judgment of the uncertainty involved. A basis for this evaluation may include:

- Specifications from the manufacturer of equipment

- Calibration to known values
- Experience from previous measurements
- General knowledge or experience with the equipment
- Other means

Variable systematic errors

Variable systematic errors are identified when the output of an instrument vary in the operating range of the instrument. Flow measurements are typical, where the error increase as the flow rate decreases towards the lower limit of the measurement range.

Propagation of errors

It is recommended by international standards [13] to disregards errors contributions, which are significantly smaller than the largest component. The result y of an experiment calculated from a set of measurements, has an uncertainty s_c in the calculated results Equation (7.A.2).

(7.A.2) $$y = f\left(x_1, x_2, x_3, ...x_n\right)$$

The uncertainty s_c can be estimated with Equation (7.A.3). If the parameters are dependent of each other's, an additional covariance term has to be added to (7.A.3).

(7.A.3) $$S_c^2 = \sum^{n}\left(\frac{\partial f}{\partial x_i}\right)^2 \cdot S^2\left(x_i\right)$$

where the partial derivate $\frac{\partial f}{\partial x_i}$ is the sensitivity of the calculated result with respect to the parameter x_i.

Uncertainty calculations

Unit#B, Unit#C and Unit#D

The signals from the thermocouples and flow meters were connected to a data logger, which converts the signals. All the temperature measurements were carried out by K type thermocouples calibrated in the working temperature interval to an accuracy of 0.7 Kelvin. Both the hydrogen and water flow measurements were carried out with commercial flow meters. The hydrogen flow meter had an accuracy of 0.5% and the water flow meter had an accuracy of 1% of the measured value.

The heat duty per unit driving force UA is calculated with Equation (7.3) $UA = \frac{\dot{Q}_w}{\Delta T}$. Where the water heat flux $\dot{Q}_w$ is calculated with (7.7) and ΔT is calculated with the logarithmic mean temperature difference (7.4) for Unit#B, Unit#C, Unit#D. Therefore is the uncertainty

in the heat duty per unit driving force calculated with Equation (7.A.4) for Unit#B, UnitC and Unit#D.

$$
\begin{aligned}
S_{UA}^2 &= \left(\frac{\partial UA}{\partial Q_w} S_{Q_W}\right)^2 + \left(\frac{\partial UA}{\partial T_{w,in}} S_{T_{w,in}}\right)^2 + \left(\frac{\partial UA}{\partial T_{w,out}} S_{T_{w,out}}\right)^2 + \left(\frac{\partial UA}{\partial T_{MH}} S_{T_{MH}}\right)^2 = \\
&\left[\left(\frac{1}{T_{w,in} - T_{w,out}}\right) \cdot \ln\left[\frac{T_{MH} - T_{w,out}}{T_{MH} - T_{w,in}}\right] \cdot S_{Q_w}\right]^2 + \\
&\left[\left[\frac{-Q_w}{\left(T_{w,in} - T_{w,out}\right)^2} \cdot \ln\left[\frac{T_{MH} - T_{w,out}}{T_{MH} - T_{w,in}}\right] + \frac{Q_w}{\left(T_{w,in} - T_{w,out}\right)} \cdot \frac{T_{MH} - T_{w,in}}{\left(T_{MH} - T_{w,out}\right)^2}\right] \cdot S_{T_{w,in}}\right]^2 + \\
&\left[\left[\frac{Q_w}{\left(T_{w,in} - T_{w,out}\right)^2} \cdot \ln\left[\frac{T_{MH} - T_{w,out}}{T_{MH} - T_{w,in}}\right] - \frac{Q_w}{T_{w,in} - T_{w,out}} \cdot \frac{1}{T_{MH} - T_{w,out}}\right] \cdot S_{T_{w,out}}\right]^2 + \\
&\left[\left[\frac{T_{w,out} - T_{w,in}}{T_{MH} - T_{w,in}} \cdot \frac{Q_w}{T_{w,in} - T_{w,out}}\right] \cdot S_{T_{MH}}\right]^2
\end{aligned}
\tag{7.A.4}
$$

Where the uncertainty in the water heat flux $\dot{Q}_W$ is calculated with (7.A.5) for Unit#B, UnitC and Unit#D.

$$
\begin{aligned}
S_{Q_w}^2 &= \left(\frac{\partial Q_w}{\partial \dot{m}} \cdot S_{\dot{m}}\right)^2 + \left(\frac{\partial Q_w}{\partial C_p} \cdot S_{C_p}\right)^2 + \left(\frac{\partial Q_w}{\partial \Delta T} \cdot S_{\Delta T}\right)^2 \\
&= \left(c_{p,w} \cdot \Delta T \cdot S_{\dot{m}}\right)^2 + \left(\dot{m} \cdot \Delta T \cdot S_{C_p}\right)^2 + \left(\dot{m} \cdot C_p \cdot S_{\Delta T}\right)^2
\end{aligned}
\tag{7.A.5}
$$

Where ΔT is defined as the difference between the inlet and outlet heating/cooling water.

Table 7.4 parameter uncertainties used to calculate the uncertainty in UA for Unit#B, Unit#C and Unit#D

$\dot{m}_w$ $\left[\frac{l}{\min}\right]$	$\dot{m}_{H_2}$ $\left[\frac{Nl}{\min}\right]$	$c_{p,w}$ $\left[\frac{J}{kg \cdot K}\right]$	T $[K]$	$T_{w,in} - T_{w,out}$ $[K]$
$0.02 \cdot \dot{m}_w$	$0.01 \cdot \dot{m}_{H_2}$	20	0.7	0.42

The two thermocouples $T_{w,in}$ and $T_{w,out}$ were calibrated to each other to yield a smaller uncertainty then they are subtracted. Common for Unit#B, Unit#C and Unit#D are that the measured inlet and outlet temperatures are the term that affects the uncertainty in UA the most. Common for the uncertainty calculations with these units was that the inlet and outlet water temperatures are the parameters dominating the uncertainty in UA. Typical UA values are; 18 ± 2 Unit#B, 4 ± 1 Unit#C and 40 ± 4 Unit#D. Table 7.4 summaries the parameters used in calculating the uncertainties of the heat duty per unit driving force coefficient for Unit#B, C and D.

Unit#A

Since the water heat flux $\dot{Q}_w$ is found from the energy balance (7.6) and the temperature difference ΔT is calculated with (7.5) for Unit#A. Equation (7.A.4) can not be used to estimate the uncertainty in UA. Instead Equation (7.6) is used for Unit#A.

(7.6)
$$S_{UA}^2 = \left(\frac{\partial UA}{\partial \dot{Q}_w} S_{\dot{Q}_w}\right)^2 + \left(\frac{\partial UA}{\partial T_{w,bath}} S_{T_{w,bath}}\right)^2 + \left(\frac{\partial UA}{\partial T_{MH}} S_{T_{MH}}\right)^2$$
$$= \left(\frac{S_{\dot{Q}_w}}{T_{w,bath} - T_{MH}}\right)^2 + \left(\frac{-\dot{Q}_w}{\left(T_{w,bath} - T_{MH}\right)^2} \cdot S_{T_{w,bath}}\right)^2 + \left(\frac{\dot{Q}_w}{\left(T_{w,bath} - T_{MH}\right)^2} \cdot S_{T_{MH}}\right)^2$$

The uncertainty in the water heat flux $\dot{Q}_W$ is calculated with Equations (7.A.7)-(7.A.10) for Unit#A.

Using the known uncertainty in the temperature and flow measurements, the uncertainty in the water's heat capacity was sat to $\pm 20 \frac{J}{kg \cdot K}$. However, for the cylindrical unit, which has no internal heat exchanger, the heat flux from the water to the reactor was calculated with Equation (7.6). This means that the heat flux to and from the reactor is estimated based on measured variables and an energy balance. The standard deviation in this estimated heat flux between the water bath and reactor was calculated with Equation (7.A.7).

(7.A.7)
$$S_{\dot{Q}_w}^2 = S_{\dot{Q}_m}^2 + S_{\dot{Q}_{reac}}^2 + S_{\dot{Q}_g}^2$$

The uncertainties of the different parameters in Equation (7.A.7) are a combination of the uncertainty in several measured values and are estimated using Equation (7.A.8)-(7.A.10).

(7.A.8)
$$S_{\dot{Q}_{reac}}^2 = \left(\frac{\partial \dot{Q}_{reac}}{\partial \dot{m}_{reac}} \cdot S_{\dot{m}_{reac}}\right)^2 + \left(\frac{\partial \dot{Q}_{reac}}{\partial \Delta H} \cdot S_{\Delta H}\right)^2$$
$$= \left(\Delta H \cdot S_{\dot{m}_{reac}}\right)^2 + \left(\dot{m}_{reac} S_{\Delta H}\right)^2$$

Equation (7.A.8) is used to estimate the standard deviation in the amount of heat released or consumed in the metal hydride gas solid reaction.

(7.A.9)
$$S_{\dot{Q}_g} = \left(\frac{\partial \dot{Q}_g}{\partial C_{P,g}} \cdot S_{C_{P,g}}\right)^2 + \left(\frac{\partial \dot{Q}_g}{\partial T_g} \cdot S_{T_g}\right)^2 + \left(\frac{\partial \dot{Q}_g}{\partial \dot{m}_g} \cdot S_{\dot{m}_g}\right)^2$$
$$= \left(T_g \cdot \dot{m}_g \cdot S_{C_{P,g}}\right)^2 + \left(C_{P,g} \cdot \dot{m}_g \cdot S_{T_g}\right)^2 + \left(C_{P,g} \cdot T_g \cdot S_{\dot{m}_g}\right)^2$$

Equation (7.A.9) is used to estimate the heat flux transported in and out of the reactor through the hydrogen gas. To be able to estimate the amount of energy used to change the temperature of the metal hydride powder and the reactor shell it self, the metal hydride reactor was divided into three control volume. The thermocouples shown in Figure 7.2 A are in the center of each control volume and their measured temperature is used as the control volumes averaged temperature. In addition, the thermocouple welded to the outside wall of the reactor was assumed to represent the average shell temperature. These measured temperatures and

estimated masses were used to calculate the amount of energy used to change the temperature of the metal hydride powder and the reactor. The uncertainty in this estimate is calculated with Equation (7.A.10).

(7.A.10)

$$S_{\dot{Q}_m}^2 = \left(\frac{\partial \dot{Q}_m}{\partial C_{P,MH}} \cdot S_{C_{P,MH}}\right)^2 + \left(\frac{\partial \dot{Q}_m}{\partial T_1} S_{T_1}\right)^2 + \left(\frac{\partial \dot{Q}_m}{\partial m_1} S_{m_1}\right)^2 + \left(\frac{\partial \dot{Q}_m}{\partial T_2} S_{T_2}\right)^2 + \left(\frac{\partial \dot{Q}_m}{\partial m_2} S_{m_2}\right)^2 + \left(\frac{\partial \dot{Q}_m}{\partial T_3} S_{T_3}\right)^2 + \left(\frac{\partial \dot{Q}_m}{\partial m_3} S_{m_3}\right)^2$$
$$+ \left(\frac{\partial \dot{Q}_m}{\partial T_r} S_{T_r}\right)^2 + \left(\frac{\partial \dot{Q}_m}{\partial m_r} S_{m_r}\right)^2 + \left(\frac{\partial \dot{Q}_m}{\partial C_{P,r}} \cdot S_{C_{P,r}}\right)^2$$
$$= \left(\left(\dot{T}_1 \cdot m_1 + \dot{T}_2 \cdot m_2 + \dot{T}_3 \cdot m_3\right) \cdot S_{C_{P,MH}}\right)^2 + \left(c_{p,MH} \cdot m_1 \cdot S_{T_1}\right)^2 + \left(c_{p,MH} \cdot \dot{T}_1 \cdot S_{m_1}\right)^2 + \left(c_{p,MH} \cdot m_2 \cdot S_{T_2}\right)^2 + \left(c_{p,MH} \cdot \dot{T}_2 \cdot S_{m_2}\right)^2$$
$$+ \left(c_{p,MH} \cdot m_3 \cdot S_{T_3}\right)^2 + \left(c_{p,MH} \cdot \dot{T}_3 \cdot S_{m_3}\right)^2 + \left(c_{p,MH} \cdot m_r \cdot S_{T_r}\right)^2 + \left(c_{p,MH} \cdot \dot{T}_r \cdot S_{m_r}\right)^2$$

The masses of metal hydride powder in the different control volumes $m_1 - m_3$ were estimated from the fraction between the total cross section of the reactor and the area of the control volume multiplied with the total amount of metal hydride powder. The uncertainties in the different masses were calculated with (7.A.3), assuming that the uncertainty in the total metal hydride powder mass is 10 gram and that the uncertainty in the radius of the filter element and reactor is zero. The uncertainty of the position of the different thermocouples, $X_{Thermocuple}$ was assumed to be 1 centimetre. The heat duty per unit driving force was calculated from a transient experiment and the uncertainty in the heat duty per unit driving force t will change as a function of time. Typically, the uncertainty will be higher in the end of the experiments when the heat flux is small and the temperature difference between the metal hydride storage unit and water bath is small. Uncertainty parameters used for calculating the uncertainty in UA for Unit#A is presented in Table 7.5

Table 7.5 parameter uncertainties used to calculate the uncertainty in UA for Unit#A

$c_{p,MH}$ $\left[\frac{J}{kg \cdot K}\right]$	ΔH $\left[\frac{J}{mol \cdot H_2}\right]$	M_{Tot} $[kg]$	$M_{reactor}$ $[kg]$	T $[K]$	$X_{Thermocuple}$ $[m]$	$\dot{m}_{H_2}$ $\left[\frac{Nl}{\min}\right]$
100	3000	0.01	0.01	0.7	0.01	$0.01 \cdot \dot{m}_{H_2}$

However, as long as the reactor absorb or desorbs more than $0.4\frac{Nl}{\min}$ of hydrogen a typical uncertainty will be approximately $UA \pm 1.5$. The most important contributions to the total uncertainty come from the uncertainty in ΔH with more than 60% of the total uncertainty followed by the heat capacity and temperature measurements..

Part 3: Behaviour of Metal Hydrides in Hydrogen Systems

8 METAL HYDRIDES SYSTEM INTEGRATION: BACKGROUND AND PRELIMINARY EXPERIMENTS

Nomenclature

A	Area	[m^2]
ELY	Electrolyser	[-]
EL	Electronic Load	[-]
FC	Fuel cell	[-]
I	Current	[A]
h	Heat transfer number	[$W/m^2 \cdot K$]
MH	Metal hydride	[-]
N	Number	[-]
P	Power	[W]
PEM	Proton Exchange Membrane	[-]
R	Thermal resistance	[W/K]
Re	Reynolds number	[-]
ΔT	Temperature difference	[K]
T	Temperature	[K]
$\dot{Q}$	Heat	[W]
U	Voltage	[V]
UA	Overall heat transfer number	[W/K]
η	Efficiency	[-]
ζ	Stoich	[-]

Subscripts

total	Total
base	Base
fin	Fin
net	Net
N	Number

8.1 INTRODUCTION

Hydrogen can be a viable energy storage option for power systems with intermittent power supply. Storage of hydrogen can be achieved in a combined system where hydrogen is produced electrolytically via water electrolysis, stored in a hydrogen storage, and converted back to power in a fuel cell. In such a system hydrogen is produced in periods with surplus electrical energy. Hydrogen can be stored for longer periods of time, for instance in periods with no renewable energy input, and later converted back to electricity (and water) through a fuel cell.

The main focus in the system part of this PhD-study has been to analyse the interaction between two of the key components in an integrated hydrogen storage system, namely the metal hydride and fuel cell, as illustrated in Figure 8.1. The scope of work included both laboratory experiments, component modeling and verification, and system simulation. A metal hydride storage unit suitable for thermal integration with a 1.2 kW water-cooled Proton exchange membrane (PEM) fuel cell (FC) was designed, built and implemented into the IFE system laboratory.

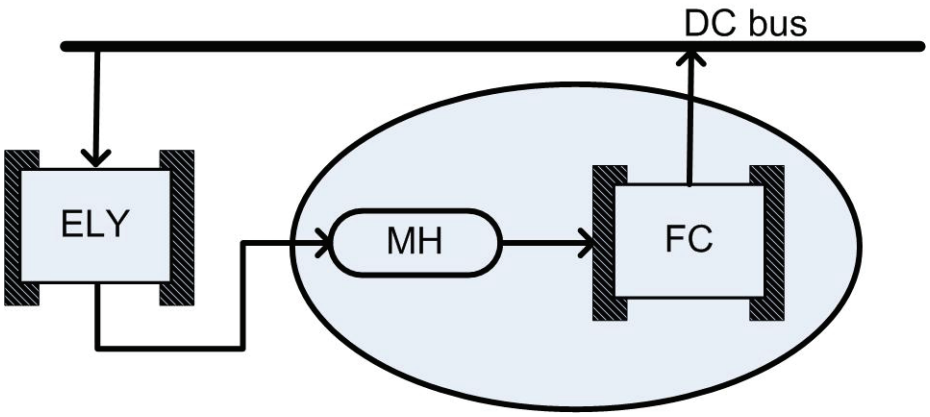

Figure 8.1 Principal sketch of the hydrogen subsystem in a hydrogen based energy system.

Storage of energy as hydrogen is more expensive and less efficient than most other electrical energy storage options. Comparison between hydrogen based energy system and other energy storage options, in terms of cost, energy density and energy efficiency is given in Figure 8.2-Figure 8.4 [1].

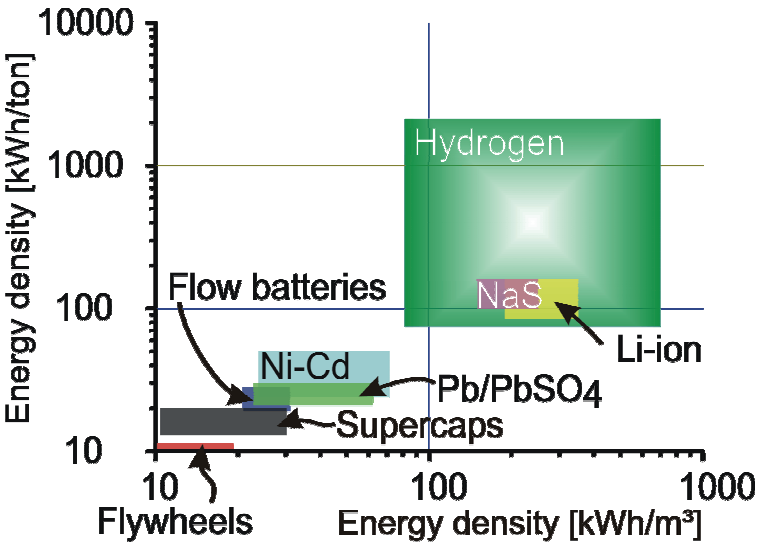

Figure 8.2 Plot of gravimetric energy density versus volumetric energy density for hydrogen and other energy storage alternatives.

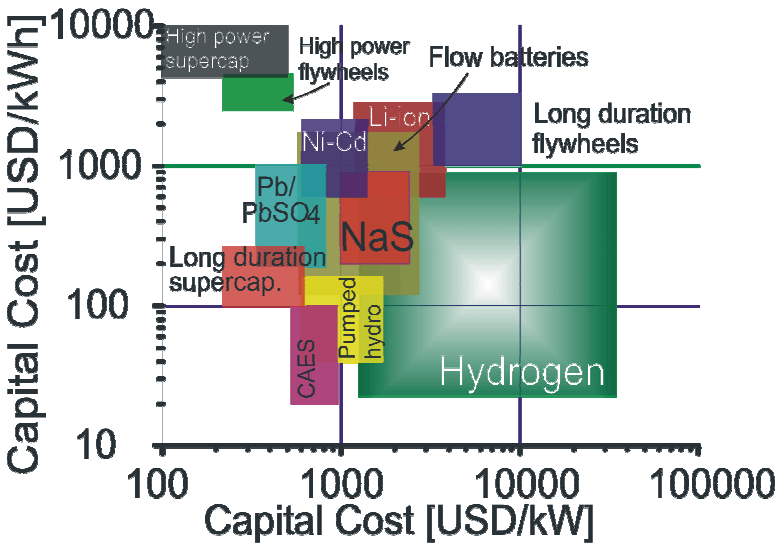

Figure 8.3 Plot capital cost per stored amount of energy versus capital cost pr energy delivery rate for different energy carriers.

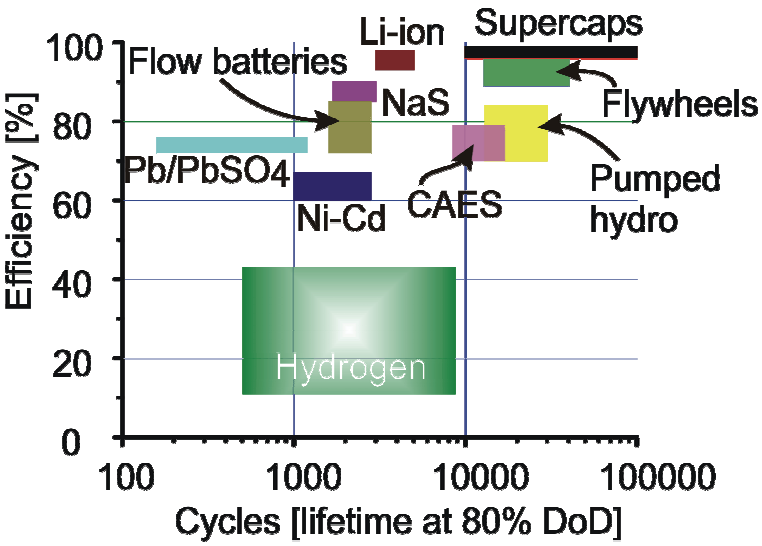

Figure 8.4 Plot of system efficiency for various energy systems versus system lifetime.

Data for the other the other electrical storage options used in Figure 8.2-Figure 8.4 were found in [2]. The hydrogen systems economical data were calculated based on data from [3,4]. The hydrogen system results were calculated based on experience from larger case studies [5] and smaller scale experimental data [6].

Figure 8.2 shows that hydrogen potentially has a high volumetric energy density, but the gravimetric energy density is at present lower than for most alternatives. Hydrogen also has a relatively low capital cost per amount of energy stored compared to other energy system at, but the capital cost pr kW delivered is still high compared to the other alternatives as indicated in Figure 8.3. Hydrogen will therefore be rather expensive compared to other energy carriers when the systems are scaled up. Figure 8.4 shows that the hydrogen systems efficiency is lower than for most other for most other energy systems. Energy systems based on hydrogen and renewable energy sources are therefore only competitive with other commercial alternatives if:

- A high security of supply is required
- High volumetric energy density is required, a relatively high capital cost pr kW power can be accepted. Such requirement are typical for remote area power energy system based on renewable energy sources, such as wind or solar power
- The customers are disconnected from the grid (e.g. due to expensive grid maintenance) or low quality on the electricity supply through the grid (uninterrupted power supply systems).
- To decrease local and global emission of climate gases, e.g. to vulnerable local environment and global greenhouse effect.

Thus, hydrogen based energy systems are only economical if alternative system costs are high, due to circumstances such as expensive fuel transport, or expensive or unreliable grid connections. The capital cost per kW can be reduced either by decreasing the component prize, increasing the component lifetime or system efficiency.

There are several ways to increase the system efficiency. First, a careful system design and control strategy must be developed [7]. Next, a significant engineering effort should be made in order to reduce the number auxiliary components [8]. Finally, once the system has been built and is operating properly, the control system should be optimized [9]. This has been the governing principal in the development and building of the renewable energy hydrogen system laboratory at IFE (discussed in more detail below). Hence, the system part of this PhD-study is closely linked to an ongoing activity at IFE, which started back in 1995.

Over the past 10-15 years there have also been a few other small-scale renewable energy hydrogen system demonstration projects around the world. A list of the most relevant projects are is provided in Table 8.1.

Table 8.1 Overview of domestic/residential RE–H2 and RE–MH projects and projects that might have an impact on the development of domestic/residential systems

Project	Country	Year [start- end]	Ref.
The Schatz Solar Hydrogen Project	USA	[89-]	[10]
NEMO 2: Advanced Energy Systems and Technologies Research Programme[1]	Finland	[93-98]	[11]
The Self-Sufficient Solar House in Freiburg	Germany	[92-]	[12,13]
Solar Hydrogen Plant on Markus Friedli Residential House[1]	Switzerland	[91-]	[14]
Solar-Wasserstoff-Bayern Hydrogen Demonstration Project at Neunburg vorm Wald,Germay	Germany	[92-99]	[15,16]
HYSOLAR: 10 kW Test and Research Facility	Germany	[89-]	[17]
PHOEBUS	Germany	[93-]	[18]
Takasago[1]	Japan	[2003-]	[19,20]

[1] system uses metal hydrides

8.2 RENEWABLE ENERGY HYDROGEN SYSTEM LABORATORY

The renewable energy hydrogen (RE/H_2) system laboratory test facility at IFE has a modular structure in order to achieve a high degree of flexibility with respect to type of components and systems to be investigated. Future expansion of the test facility has been taken into consideration by general purpose auxiliaries and using system components with a wide operation range. The test facility is designed for testing of individual hydrogen technology components, subsystems, as well as completes stand-alone power systems. A principal sketch of the hydrogen system lab at IFE is given in Figure 8.1.

The system laboratory currently consist of an wind turbine, power supply, lead acid battery bank, electronic load, electrolyser, air compressor, metal hydride storage unit, a fuel cell and several inverters and converters. The laboratory is now (2007) being upgraded with a PV-system, a Li-ion battery pack, and supercapacitors.

The control and data acquisition system is based on a PC with modular distributed I/O modules (NI Fieldpoint), two multifunctional PCI-DAQ boards, GPIB interface, mass flow metres/controllers, relays and valves for automatic and manual operation. The control and data acquisition software is developed in LabVIEW.

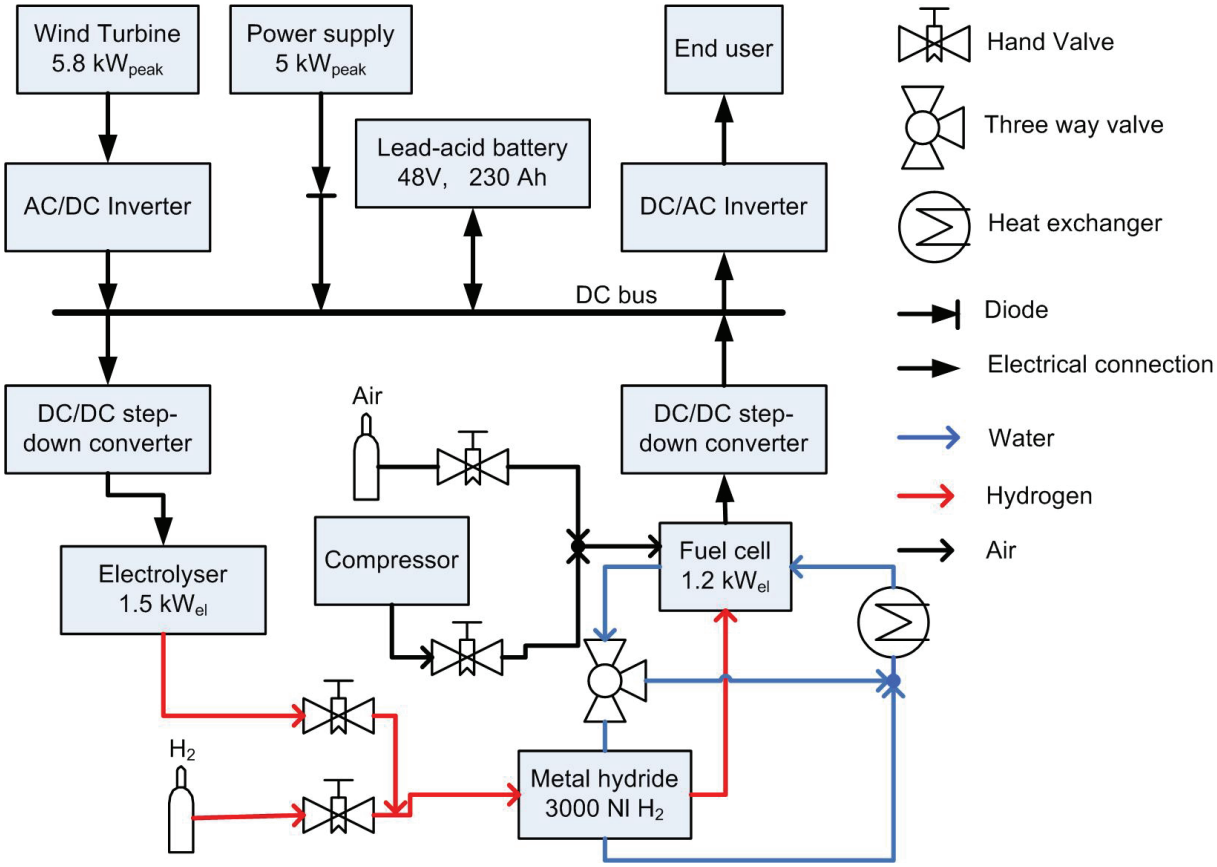

Figure 8.5. Principal sketch of the hydrogen system laboratory at IFE.

The battery bank used for short time energy storage is consist of four secondary lead acid batteries connected in series with a total electrical storage capacity of 230 Ah. A 5 kW wind turbine is connected to the laboratory grid in order to study the connection between the electrolyser and a wind turbine. The power supply is used to simulate the output of an array of solar panels and is capable of delivering 4800W. The user power demand is emulated using a programable electronic load, capable of withdrawing a maximum of 600 W from the system. In addition to the electronic load the laboratory set up also includes ohmic load consisting of eight ohmic elements capable of withdrawing 750 W. These two loads were operated together during testing of the fuel cell at higher power.

The 5 kW electrolyser operates at 16 bar and produces approximately 0.036 Nm^3/hour of hydrogen. The O_2 content in H_2 out from the electrolyser is in the range 0.01%-0.3%, in addition, the outlet hydrogen is saturated with water at 323 Kelvin when it leaves the electrolyser. In order to prevent degradation of the metal hydride due to the oxygen and water content in the hydrogen, the incoming hydrogen gas is passed through a hydrogen purification unit. The purification unit consist of an oxygen trap and a dryer. The oxygen trap contains a catalytic noble metal that combines traces of oxygen with hydrogen to formation of water. The water content in the hydrogen from the electrolyser and the water produced over the catalyst in the oxygen trap are removed by the dryer. The dryer consist of two filters, each containing 6 kg desiccant, that are used in alternation to ensure continuous operation. The dryer is designed to run with a maximum H_2 flow rate at 0.5 Nm^3/h. This component is not optimised for stand-alone power systems due to the high amount of energy consumed during

regeneration. Measurement of humidity in the hydrogen at the dryer output was performed using a flow- through electrolytic moisture analyser. The measured quality of the purified electrolytic hydrogen was found to be comparable to that of hydrogen 5.0.

The produced hydrogen is either stored in the air-cooled hydrogen storage filled with 85 kg of AB_2 type metal hydride unit (Hera) capable of storing 14 Nm^3 of hydrogen delivered by Hera [21], or in a prototype experimental unit developed by IFE, hereafter referred to as unit #5.

The stored hydrogen is used to fuel the 1.2 kW water-cooled PEM fuel cell. This fuel cell is thermally connected to unit #5. In addition to the metal hydride cooling loop, the fuel cell is connected to an external cooling loop to ensure that it will not overheat during operation.

The fuel cell is supplied with air by means of an air compressor (Vairex VV-520.03 INT) supplies the air used in the fuel cell. This air compressor meets the fuel cells purity demand and can supply 2-10 g/s of air, with pressure rations between 1.1 and 2.0, all the experimental work conducted on system level has focused on the interaction between the electrolyser, metal hydride and fuel cell. More details of the IFE hydrogen system are given in [6].

The research focus in the RE/H_2-system laboratory at IFE will for the next few years be on distributed grid-connected power systems based on photovoltaics and fuel cells, electrolytic hydrogen production, and hydrogen compression (for fuel cell vehicles) using metal hydrides.

8.3 PRELIMINARY EXPERIMENTS

In order to get a better practical understanding of the interaction between the fuel cell and metal hydride, some preliminary experiment were performed. These experiments were carried out in the metal hydride laboratory at IFE. This work was part of a project carried out by IFE with the European Space Agency (ESA) and Prototech a Norwegian consulting company. A simple experimental set up was designed. This set up consisted of an air cooled PEM fuel cell, an electronic load, a metal hydride storage unit, and a water bath supplying the metal hydride with cooling/heating water, as shown in Figure 8.6 (further details are found in [22].

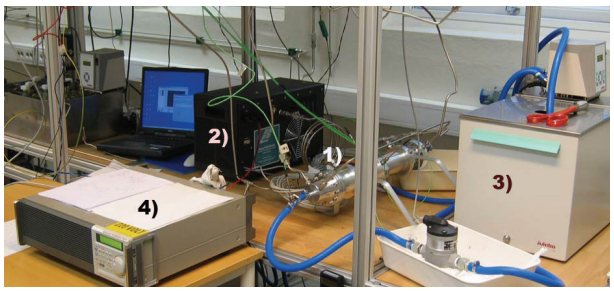

A

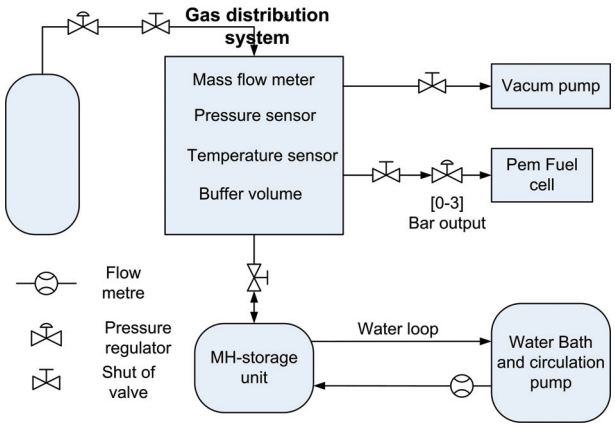

B

Figure 8.6.. A Photograph of the main components in the experimental set up. 1) MH storage, 2) PEM fuel cell, 3) thermal bath (providing water circulation through the MH storage unit), and 4) electronic load, and B schematic illustration of the experimental set up.

The following variables was measured during the experiments:

- Hydrogen pressure (bar)
- Hydrogen flowrate (Nl/min)
- Heating/cooling water water flow rate (l/min)
- Temperature of heating/cooling water at inlet and outlet of the metal hydride (K)
- Temperature of cooling water at inlet and outlet of the fuel cell (K)
- Temperature of the reacting gases (K)
- Fuel cell current (A)
- Fuel cell voltage (V)
- Internal metal hydride temperature (K)

The fuel cell produces heat during operation, while heat is required by the metal hydride to maintain its temperature during hydrogen desorption (due to endothermic gas solid reaction in metal hydride).

The amount of heat produced in the fuel cell is presented in Table 8.2. These values were calculated based on the lower heating value of hydrogen gas and an electrical fuel cell efficiency of 45%. The amount of heat consumed in the metal hydride was calculated based on and reaction enthalpy of 27 kJ per mol of hydrogen and the corresponding hydrogen flow.

Table 8.2 Heat produced in the fuel cell and consumed in the metal hydride at various percentages of fuel usage in the fuel cell operating at 500 W and an electrical efficiency of 45%.

FC fuel usage [%]	100	80	67	58	45	37	27
Heat produced in FC (LHV) [W]	423	423	423	423	423	423	423
Heat used in metal hydride [W]	-115	-143	-171	-199	-255	-311	-423

It can be seen from Table 8.2, that the fuel cell produces more heat than what is required by the metal hydride if the hydrogen flow rates are kept at reasonable stoich's. However, during operation some heat will always be lost to the surroundings.

In order to investigate the thermal interaction between the fuel cell (FC) and the metal hydride (MH) storage several experiments were performed. Some interesting results are shown in Figure 8.7.

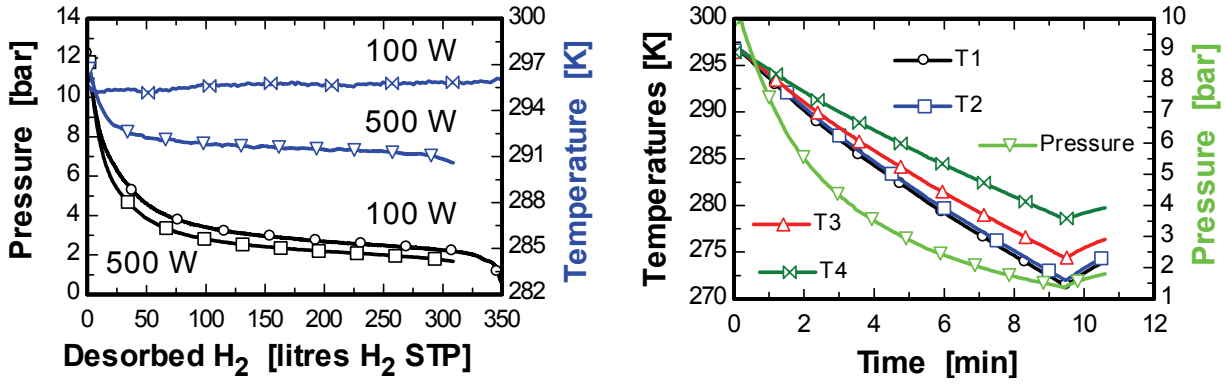

A B

Figure 8.7. Experimental results from the preliminary fuel cell metal hydride test runs. A) The average metal hydride temperature and metal hydride pressure as a function of amount of desorbed hydrogen, during fuel cell is operation at 500 W and 100 W and with a fuel efficiency of about 83%. The temperature and flow rate metal hydride heating water was 298 K and 0.75 litre per minutes. B) The metal hydride temperature and pressure without no water circulation and fuel cell operated at 500 W and a fuel efficiency of about 83%.

As seen from Figure 8.7A, fuel cell operation at higher power (500 W) output resulted in a decreased temperature of the metal hydride, and a subsequent decrease in the equilibrium pressure. This effectively reduced the amount of hydrogen available for the fuel cell. A specific run was performed without water circulating through the MH heat exchanger, both to simulate a local water-loop breakdown and to investigate the intrinsic behaviour of the metal hydride unit during near-adiabatic operation.

Figure 8.7B shows that at a fuel cell power output of 500 W (corresponding to a hydrogen flow rate of 6.4 litre STP / min), the temperature inside the MH unit drops from room temperature down to less than 273 K within 10 minutes. This dramatic drop in the temperature could lead to freezing of the water inside the heat exchanger. Thus, water-loop breakdown is critical (especially for a thermally isolated MH storage unit) and care should be taken in order to ensure proper and reliable water circulation.

8.4 DESIGN OF STORAGE UNIT AND CONTROL PROGRAM

8.4.1 Design of MH storage unit

The MH/FC interaction is a critical part of the hydrogen system and significantly influences the overall energy efficiency. Thus a good design of the MH storage unit depends on the fuel cell specification and operating behaviour. The metal hydride unit has to be designed and built

based on the FC specification and operating characteristic. The metal hydride unit described below was designed and built as part of this PhD-study.

The three main design criteria's for the metal hydride storage unit were:

1. **Hydrogen absorption**: Charge the metal hydride using the already installed PEM-electrolyser.

2. **Hydrogen desorption**: Run the fuel cell with hydrogen for at least 100 minutes at a fuel cell output of 60 A and a hydrogen gas pressures above 1.8 bar.

3. **Thermal characterization**: Measure temperature gradients inside metal hydride, in order to verify a heat and mass transfer model.

The storage unit was filled with an AB_5 type metal hydride powder, due to the high cycling stability and robustness of this alloy. The alloy can also be regenerated at moderate temperatures (573 K). The $LaNi_5$ based alloy was mixed with Ce to increase the plateau pressure at lower temperature, in order to better fit the fuel cell operation pressure.

The storage unit was filled with 18 kg of metal hydride powder. It was calculated that this amount of metal hydride powder would make it possible to design a metal hydride hydrogen storage unit capable of supplying a stoichometric hydrogen flow of 2 to a fuel cell operating at a constant current of 60 A for about 2 hours.

The MH storage unit was designed for research purposes in the laborator, and the weight of the unit was not an important design parameter. Thus, the storage unit was built using a stainless steal cylinder. The outer diameter of the reactor shell was 11.4 cm. A technical drawing of the designed unit is shown in Figure 8.8.

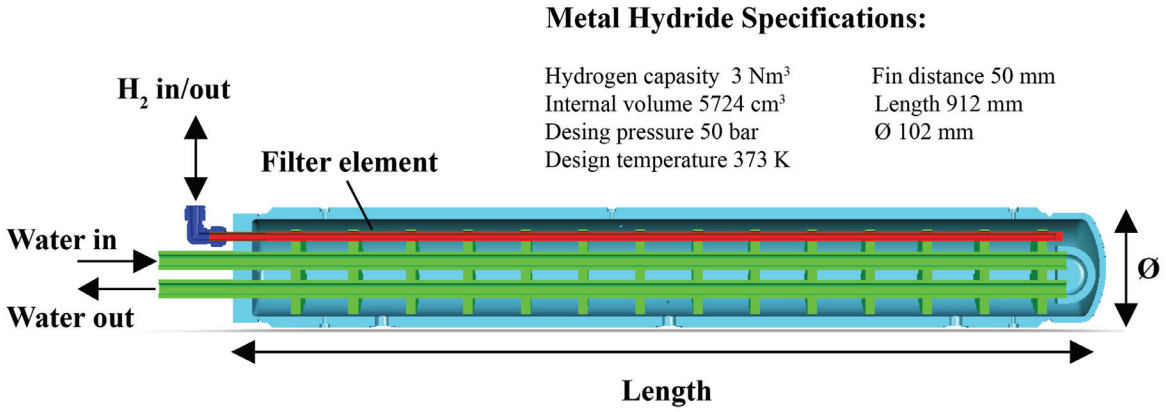

Figure 8.8 Technical drawing of Unit#5 (water-cooled metal hydride system unit designed, constructed, and tested at IFE).

Hydrogen is supplied through a filter element positioned in the upper centre of the storage unit. This ensures symmetry and simplifies thermal modelling of the storage unit.

The heating cooling water was circulated in a U bend cobber tube with an outer diameter of 1.9 cm, and 14 cobber fins were soldered on to the tube. The use of cobber tubes and silver soldering minimizes the thermal resistance in junction between the water pipe and the fins.

The fuel cell manufacturer specified the maximum temperature drop in the fuel cell inlet and outlet water to 5 Kelvin. To fulfil this demand the water pump was designed to give water flow rates between 3-4 litres pr minutes inside the closed metal hydride fuel cell water loop. These flow rates, yields Re>3800 in the metal hydride water tube and ensures good heat transfer at the waterside of the heat exchanger.

An important detail in the design of the MH-tank was to calculate the amount of metal hydride powder to be inserted into the storage unit. The expansion of the MH during hydrogenation had to be taken into account in the calculations. A packing density corresponding to 50% porosity when unhydrogenated and 20% swelling during hydrogenation was assumed. In addition 10 % void space when fully hydrogenated was added as safety margin. Before the reactor was filled with powder, it was leak tested and volume calibrated. The internal volume was found to be ca 5700 cm^3. Based on these assumptions, it was estimated that 18 kg of metal hydride powder would give approximately 10% void space when the powder was fully hydrogenated.

The system was designed with a U tube for circulation of cooling/heating water, instead of a horizontal water pipe going straight through the tank which would be easier to manufacture and to assemble. However, a very critical criterion for such tank is to build them leak tight for hydrogen. The shell of the reactor is a standard steal pipe and the risk for leakage is reduced when one end is welded and all the inlet and outlet pipes are collected in the other end, which is sealed with a screw chase with holes for inlet and outlet pipes. The heat exchanger was also sand blasted to remove the surface roughness created by the silver soldering of the fins to the cobber water pipe.

Due to special pre-treatment of the metal hydride powder the tank could be filled in an air atmosphere. Even though this simplifies the filling procedure, some problems with clogging might occur if the powder was to be filled through small filling holes positioned along the side of the reactor. To avoid this problem, it was made room for a filling rod with a diameter of 1 centimetre as shown in Figure 8.9. Another advantage of the filling rod was that it helped in getting the metal hydride powder evenly distributed through the storage unit, since a given amount of metal hydride powder could be inserted between each fin chamber. After filling the storage unit was rotated for 8 hours in a turning lathe to ensure uniform powder distribution.

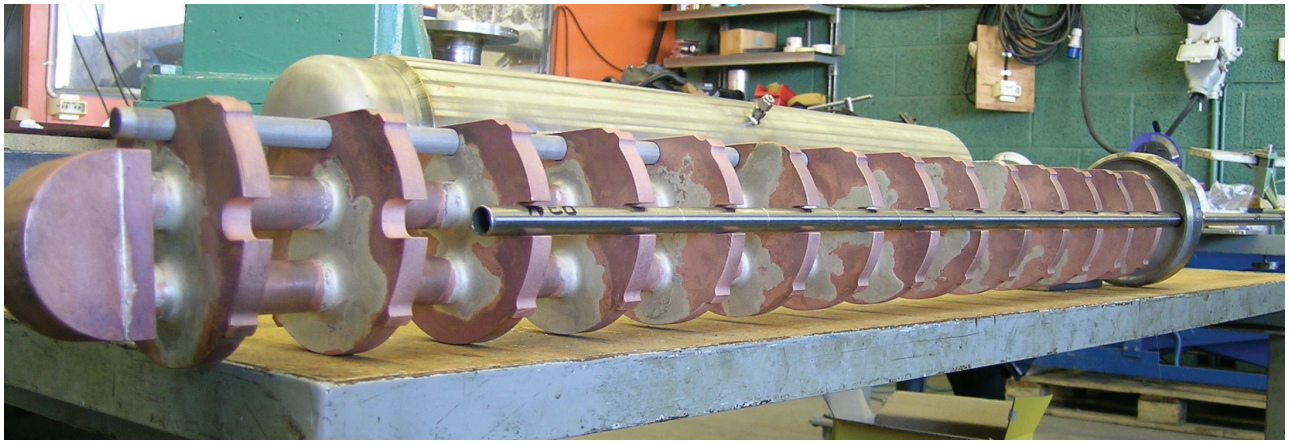

Figure 8.9 Unit#5 showing the heat exchanger and the filling pipe.

Figure 8.9 shows unit#5 with the filling rod inserted. Before the heat exchanger was constructed the fin distance needed to be estimated. Estimation of the heat fluxes, to be

removed or supplied to the system and the working temperature of the storage unit is the most important parameters then the fin distance is to be decided. The fuel cell cooling water temperature was estimated to be around 323-333 K, and the average temperature of the MH bed was specified to be above 303 K (to utilize the full storage capacity).

Based on a fuel cell output of 1000 W, stoichiometric flow of 1.8 and no re-circulation of hydrogen, the amount of hydrogen withdrawn from the metal hydride can be calculated. When this hydrogen flow is delivered by the metal hydride a given amount of heat is consumed in the metal hydride. This thermal energy demand can be calculated based on the reaction enthalpy and reaction rate. In principle, the heat exchanger must be capable of transferring at least the same amount of heat that is consumed in the gas solid reaction into the bed with temperature difference in the range of 20-25 K.

A simplified thermal analysis where the thermal resistance in the water pipe and through the cobber pipe are neglected yields the following expression for the overall heat transfer coefficient UA.

(8.1) $$UA = \frac{1}{R_{total}} = \frac{1}{R_{fin}} + \frac{1}{R_{base}} = \frac{N \cdot \eta_{fin} \cdot A_{fin} \cdot h}{1} + \frac{\left(A_{total} - N \cdot A_{fin,base}\right) \cdot h}{1}$$

Where N is the number of fins, η_{fin} is the fin efficiency A_{fin} is the surface area for one single fin, A_{total} is the total surface area of the water pipe, $A_{fin,base}$ is the surface area of the water covered by one fin pipe, and h is the wall to bed heat transfer coefficient.

The wall to bed heat transfer coefficient *h* is calculated with the correlation presented chapter 4 (of this thesis) derived with constant temperature as a boundary condition, and the steady state solution extracted after 9000 seconds. The energy balance between the theoretically quantity of energy transferred into the metal hydride bed and the quantity of heat consumed in the gas solid reaction in the metal hydride during fuel cell operation are calculated with Equation (8.2).

(8.2) $$\dot{Q}_{net} = UA \cdot \Delta T - \dot{Q}_{MH}$$

Where $\dot{Q}_{MH}$ is the quantity of energy consumed in the metal hydride storage unit during desorption. The calculated heat balances vs. number of fins are plotted in Figure 8.10.

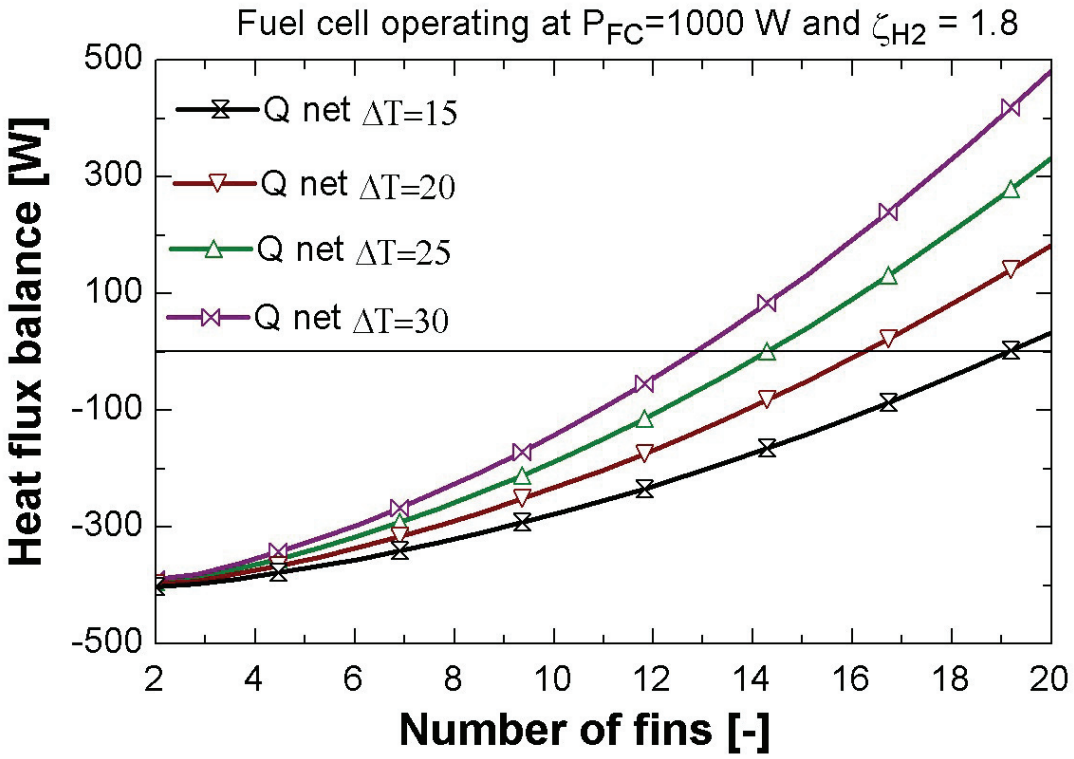

Figure 8.10 Calculated heat balances versus number of fins.

As shown in it Figure 8.10, the number of fins needed to achieve equilibrium between the consumed heat and heat theoretically possible to transfer decreases with increasing temperature difference. For Unit#5, a heat exchanger with 15 heat transfer surfaces (14 fins and a special U-bend) was chosen, this design correspond to a temperature difference between 20-25 K.

8.4.2 Control program

A LabVIEW control program for operation of the fuel cell and metal hydride was developed as part of this PhD. From a system operator point of view, the fuel cell is a much more demanding component than the metal hydride. This is because the fuel cell responds much faster to changes in operating parameters than the metal hydride. The control program was designed so that when the desired current, stoichiometric flow rates and fuel cell operating temperature were set, the operator could freely change the current set point. A safety routine was implemented for shutting down the fuel cell in a controlled manner if the minimum cell voltages drops below some critical values. This control program made it possible to study the interaction between the various laboratory components.

8.5 CONCLUSIONS

- A preliminary fuel cell/metal hydride experimental set up was built and some experiments were conducted.

- A control program was developed and tested.

- A water cooled metal hydride storage unit (unit#5) capable of storing 3 Nm^3 of hydrogen was built.

- The designed metal hydride storage unit was thermally integrated with a 1.2 kW water cooled PEM fuel cell.

References

[1] Vie, P, J, S, Miland H, Førde T, Pettersen A, G, Eriksen J, Ulleberg Ø. Renewable energy based hydrogen stand alone power systems. First International Renewable Energy Storage Conference (IRES I), Science Park Gelsenkirchen, Germany, 30 - 31 October, 2006.

[2] Electricity storage association, technology comparisons, http://electricitystorage.org/tech/technologies_comparisons.htm, (Sept 2007).

[3] Glöckner R. The HSAPS Market Analysis project. Ongoing EU-project (2002-2003), http://www.hsaps.ife.no, IFE, Kjeller, 2002.

[4] Glöckner R. HSAPS Market Analysis Project. Final report for EU/ALTENER-project (Contract No. 4.1030/Z/01-101/200), IFE/KR/E-2005/003, Institute for Energy Technology, Kjeller, NO-2027, 2005.

[5] Glöckner R, Kloed C, Nyhammer F, Ulleberg Ø. Wind/hydrogen systems for remote areas - A Norwegian case study. 14th World Hydrogen Energy Conference, Montreal, 9-14 June 2002.

[6] Ulleberg Ø, Yartys V, Vie P, Miland H, Eriksen J, Førde T, Lototsky MV. Hydrogen Storage in Solid Materials From Synthesis to Systems. IFE/KR/F-2006-226, IFE, 2006.

[7] Ulleberg Ø. Stand-alone power systems for the future : Optimal design, operation & control of solar-hydrogen energy systems. edn. Trondheim: Department of Thermal Energy and Hydropower Norwegian University of Science and Technology, 1998.

[8] Eriksen J. Experimental design of a data acquisition and control system for a small-scale PV-H_2 system. Faculty of Mathematics and Natural Sciences University of Oslo : Unipub, [Oslo], 2003.

[9] Miland H, Norges Teknisk-Naturvitenskapelige Universitet . Institutt for materialteknologi. Operational experience and control strategies for a stand-alone power system based on renewable energy and hydrogen. edn. Trondheim: Norwegian University of Science and Technology Faculty of Natural Sciences and Technology Department of Materials Technology, 2005.

[10] Schatz Solar Hydrogen Project http://www.humboldt.edu/~serc/realworld.html (04/08-07).

[11] Advanced Energy Systems and Technologies Research Programme http://www.tkk.fi/Units/NEMO/ (04/08-07).

[12] Stahl W, Voss K, Goetzberger A. The Self-Sufficient Solar House in Freiburg. Solar Energy 1994; 52(1): 111-125.

[13] Voss K, Goetzberger A, Bopp G, Haberle A, Heinzel A, Lehmberg H. The self-sufficient solar house in Freiburg - Results of 3 years of operation. Solar Energy 1996; 58(1-3): 17-23.

[14] Hollmuller P, Joubert J, M, Lachal B, Yvon K. Evaluation of a 5 kW(P) photovoltaic hydrogen production and storage installation for a residential home in Switzerland. International Journal of Hydrogen Energy 2000; 25(2): 97-109.

[15] Winter C, J. Solar Hydrogen, Energy Carrier for the Future Exemplified by 2 Field Programs - Hysolar and Solar-Wasserstoff-Bayern (Swb). Renewable Energy 1994; 5(1-4): 69-76.

[16] Winter C, J, Fuchs M. Hysolar and Solar-Wasserstoff-Bayern. International Journal of Hydrogen Energy 1991; 16(11): 723-734.

[17] Brinner A, Bussmann H, Hug W, Seeger W. Test-Results of the Hysolar 10 Kw Pv-Electrolysis Facility. International Journal of Hydrogen Energy 1992; 17(3): 187-197.

[18] Ghosh P, C, Emonts B, Jansen H, Mergel J, Stolen D. Ten yerars of operational experience with a hydrogen based renewable energy supply system. Solar Energy 2003; 75: 469-478.

[19] Ito H. R&D Progress of AIST-Takasago Hydrogen Integrated System. Personal communication, 6-9 March 2006.

[20] Okamoto H, Kawakami Y, Kozawa Y, Akai M. Total energy systems engineering by coring metal hydride tanks. Journal of the Hydrogen Energy System Society of Japan 2004; 29(2).

[21] Ergenics HERA solid state hydrogen energy solutions http://www.ergenics.com/ (04/08-07).

[22] Maehlen J, P, Eriksen J, Førde T. Testing the performances of the H storage unit with Proton Exchange Membrane Fuel Cell. IFE/KR/F-2005/210, IFE, 2005.

9 MODELLING AND SIMULATION OF A THERMALLY COUPLED ELECTROLYSER/METAL HYDRIDE/FUEL CELL SYSTEM

T. Førde, H. Miland and Ø. Ulleberg*

Institute for Energy Technology, P.O. Box 40, NO-2027 Kjeller, Norway

Key words: Hydrogen storage, system integration, metal hydrides, electrolyzers, fuel cells

Presented at Hypothesis VII

27-30 March 2007 Merida Mexico

9.1 ABSTRACT

This paper describes modelling and simulation work carried out at Institute for Energy Technology (IFE, Norway) on integrated electrolyser/metal hydride/fuel cell systems. A case study where hydrogen is produced via water electrolysis during night time (excess grid electricity), stored in a metal hydride, and converted back to electricity in a fuel cell during daytime, was simulated in detail using verified models with calibrated system parameters. The study, which was linked to an IEA-activity (Annex 18 of the Hydrogen Implementing Agreement) and a bi-lateral collaboration with the National Institute of Advanced Industrial Science and Technology (AIST, Japan), shows how it is possible to increase the overall hydrogen system efficiency by designing systems with close thermal integration between the various system components, particularly the metal hydride and fuel cell system.

Nomeclature

CH/HM	Hydrogen concentration in metal hydride (mol H/mol MH)	[-]
cp	Heat capacity	[J/kg·K]
$\dot{m}_{cw}$	Cooling water (i.e., heating water) flow rate	[kg/s]
$\dot{m}_{H2}$	Hydrogen mass flow rate (from electrolyzer or to fuel cell)	[kg/s]
$\dot{m}_{MH}$	Mass of metal hydride powder	[kg]
P	Power	$[W]$
PH2	Hydrogen gas pressure inside metal hydride storage	[bar]
PMHeq	Equilibrium pressure of metal hydride (bar)	[bar]
$\dot{Q}$	Heat	[W]
Tcw	Cooling water temperature (inlet or outlet) (°C)	[K]
TMH	Temperature of metal hydride	[K]
ΔT	Temperature difference	[K]

Subscript

cw	Cooling water
cool	Cooling
ELY	Electrolyser
FC	Fuel cell
MH	Metal hydride

9.2 INTRODUCTION

The storage of electricity in the form of hydrogen can only be justified if hydrogen storage systems with high overall energy efficiencies can be developed. The need for electrical storage varies with the application, from weekly energy storage in remote area photovoltaic (PV) power systems (e.g., telecom applications), to daily energy storage (night time to day time) in grid-connected systems (e.g. high cost markets, such as Japan).

The objective with this paper is to describe, via a modelling case study, how a thermally integrated electrolyser/metal hydride/fuel cell system can produce hydrogen at night time (excess grid electricity), store this hydrogen in a metal hydride system, and finally convert the hydrogen back to electricity in a fuel cell during daytime (Figure 9.1).

The original concept of a metal hydride based hydrogen storage system for load leveling of grid-electricity was developed by Dr. Yoshiyuki Kozawa (Gifu University, Japan), who in 2000 initiated modeling and experimental work on such system, that eventually lead to a detailed metal hydride system model and the building of a laboratory system at Takasago Thermal Engineering Company (Takasago, Atsugi) [1,2].

The behavior of a thermally coupled metal hydride and water cooled proton exchange membrane (PEM) fuel cell systems has also been studied by a few other groups [3], but the most significant effort has been made in Japan. In 2004, IFE initiated some modeling and simulation work on electrolyzer/metal hydride/fuel cell systems together with the National Institute of Advanced Industrial Science and Technology (AIST, Tsukuba), as part of an activity (Annex 18) within the International Energy Agency (IEA) Hydrogen Implementing Agreement (HIA) [4].

The fundamental metal hydride system models used in this study is based on a PhD-study [5,6], while other hydrogen energy system models have been developed over time. The modeling is closely linked to a small-scale laboratory at IFE for testing of autonomous renewable energy hydrogen (RE/H_2) systems. This RE/H_2-system laboratory currently consists of a 5 kW wind turbine, 5 kW PV-system emulator, 1.5 kW PEM (proton exchange membrane) electrolyzer, 14 Nm^3 metal hydride hydrogen storage system, and a 1.2 kW PEM fuel cell. The laboratory system is designed for testing of individual components, subsystems, and complete power system operation. In 2006, a new water-cooled PEM fuel cell unit was thermally integrated with a water cooled/heated metal hydride storage unit designed and built at IFE [7,8]. The work reported here is mainly based on work carried out at IFE.

9.3 SYSTEM DESCRIPTION

A schematic of the basic system simulated in this study is shown in Figure 9.1. The main purpose with this system is to utilize the differences in the electricity prizes to produce and store hydrogen during nighttime and convert it back to electricity via a fuel cell during daytime to serve a specific power demand. The basic design for the system simulated in this study was taken from the Takasago laboratory system: 15 kW PEM-electrolyzer, 3 × 210 kg AB_5 type metal hydride, and 5 kW_{el} PEM fuel cell. In the simulations described below two well-insulated water tanks were included, one for the electrolyzers side and another one for the fuel cell side (respectively, T1 and T2 in Figure 9.1).

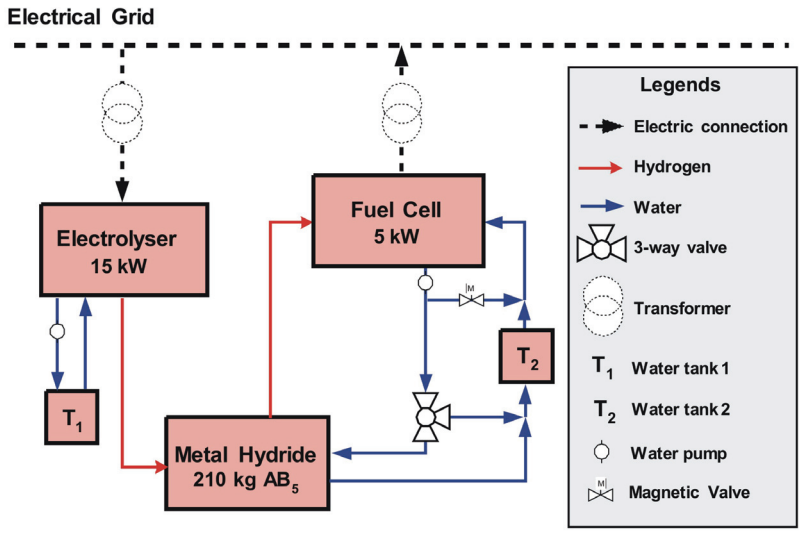

Figure 9.1 Schematic of the simulated electrolyzer/metal hydride/fuel cell system.

The size of the electrolyzer and fuel cell water tanks, found through simulations, was 100 and 1200 liters, respectively. Furthermore, the thermal management of the system was divided into two water loops:

- **Water loop 1 (to/from T1)**: High temperature heat transfer between electrolyzer and water tank 1 (e.g., hot tap water at ca. 333K).
- **Water loop 2 (to/from T2)**: Low temperature heat transfer between fuel cell, metal hydride, and water tank 2 (e.g., space heating at ca. 323K).

The water flow in water loop 2 can take several directions, as illustrated in Figure 9.1. For example, during start up of the fuel cell, it is possible to bypass water tank 2 and the metal hydride. Once the fuel cell has reached its operating temperature and produces excess heat, it is possible to optimize the thermal management by regulating the cooling water flow rate through the metal hydride (0-100%) before it goes into water tank 2.

9.4 SYSTEM SIMULATION TOOLS AND METHODOLOGY

The modeling and system simulations presented here were based on the HYDROGEMS-library, which is a collection of hydrogen energy models suitable for simulation of integrated hydrogen energy systems, particularly renewable energy systems (www.hydrogems.no). The models have been developed by IFE since 1995, were made publicly available for TRNSYS version 15 in 2002 [9], and were officially adopted into TRNSYS version 16 in 2005 (http://sel.me.wisc.edu/trnsys). IFE has developed a duplicate of the HYDROGEMS-library for the Engineering Equation Solver (EES) program (www.fchart.com) based on the same

source code as that developed for TRNSYS. In this particular simulation study EES was used as the simulation platform.

The basic theory behind the HYDROGEMS component models is thermodynamics, electrochemistry, and applied physics (e.g., electrical, mechanical and heat and mass transfer engineering). As a result the models are fairly physical and generic, but in order to make the models suitable for energy system simulations some simplifications have been made. This is done by using empirical relationships for current-voltage characteristics (*IU*-curves) for solar cells or electrochemical cells (e.g., fuel cells, batteries, electrolyzers), power curves for wind turbines, efficiency curves for electronic equipment (e.g. AC/DC-inverters), etc. Typical system model parameters are: (i) Component sizes (e.g. cell areas), (ii) System sizes (e.g., number of cells in series or parallel per module), and (iii) Limits (e.g., min/max of voltages, currents, temperatures etc.). Typical forcing functions required for renewable energy system simulations are wind speed (m/s), solar radiation (W/m^2), current (A) or power (W) demand, while typical variables calculated by the models are temperature (°C), pressure (bar), current (A), voltage (V), and flow rate (Nm^3/h).

The main objective with the work presented here was to develop an electrolyzer/metal hydride/fuel cell system simulation model, with focus on thermal integration and fuel cell sub-system control. Existing fuel cell and electrolyzer models from the HYDROGEMS-library could be used, but a new model suitable for system simulations needed to be developed (more details below). The fuel cell and electrolyzer models were simply calibrated based on experimental data (*IU*-curves, heat transfer characteristics, and thermal time constants) from IFE's RE/H_2 system laboratory and the Takasago laboratory system. The characterization of the metal hydride system was more involved (more details below).

In order to make a metal hydride model suitable for thermal energy system simulations it was necessary develop a fairly physical model that reflects both material and system specific properties, without introducing an excessive number of component model parameters. Thus, a new and simple zero dimensional metal hydride model suitable for hydrogen storage system simulations was developed. This model takes into consideration both material specific properties (pressure concentration isotherms, or *PCT*-curves, and kinetics of hydrogen reactions), as well as more general characteristics of the metal hydride system (heat and mass transfer). The basic metal hydride storage unit simulated in this study was based on an AB_5 type metal hydride powder. (Actual MH-systems normally contains several MH-units; in this case there were three MH-units). The main features of the zero dimensional metal hydride model developed can be summarized by the following general function:

(9.1) $f_{\text{MH-model}} = f(inputs : outputs) = f(\dot{m}_{\text{MH}}, \dot{m}_{\text{H2}}, p_{\text{H2}}, T_{\text{cw,in}}, \dot{m}_{\text{cw}} : p_{\text{MH,eq}}, C_{\text{H/MH}}, T_{\text{MH}}, T_{\text{cw,out}})$

where

$\dot{m}_{\text{MH}}$ = mass of metal hydride powder (kg)

$\dot{m}_{\text{H2}}$ = hydrogen mass flow rate (from electrolyzer or to fuel cell) (kg/s)

p_{H2} = hydrogen gas pressure inside metal hydride storage (bar)

T_{cw} = cooling water temperature (inlet or outlet) (K)

$\dot{m}_{\text{cw}}$ = cooling water (i.e., heating water) flow rate (kg/s)

$p_{\text{MH,eq}}$ = equilibrium pressure of metal hydride (bar)

$C_{\text{H/MH}}$ = hydrogen concentration in metal hydride (mol H/mol MH)

T_{MH} = temperature of metal hydride (K)

The *PCT*-curves for the AB_5 alloy used in the simulations of this study were based on measurements at four different temperatures performed in a dedicated experimental set up at IFE [10]. Values for the equilibrium pressures ($p_{\text{MH,eq}}$) in the zero dimensional metal hydride model were then linearly interpolated from tables generated by a more detailed (and experimentally verified) *PCT*-model developed by Lototsky [11]. A semi-empirical kinetic expression developed by Førde *et al.* [6] was used in the modeling of the reaction rates between the gas and solid for the selected AB_5 alloy. The heat and mass transfer properties of the modeled metal hydride reactor were scaled up from a small IFE-laboratory test reactor containing 2.3 kg of metal hydride powder and a brush type heat exchanger. A more detailed description of the heat and mass transfer properties and transient behavior of the reference reactor will be published in the near future [5].

9.5 RESULTS AND DISCUSSION

The assumed daily profile for the power flow to/from the simulated system (Figure 9.1) is shown in Figure 9.2. This load profile was generated by AIST on the basis of the actual energy consumption (measured data) for a typical Japanese hotel measured [2]. As seen from Figure 9.2, the electrolyzer operates at a constant power of 11.5 kW for 9 hours during nighttime, before the fuel cell starts up after 10 hours and operates for the next 14 hours at an average power of 2.9 kW (3.7 kW peak power).

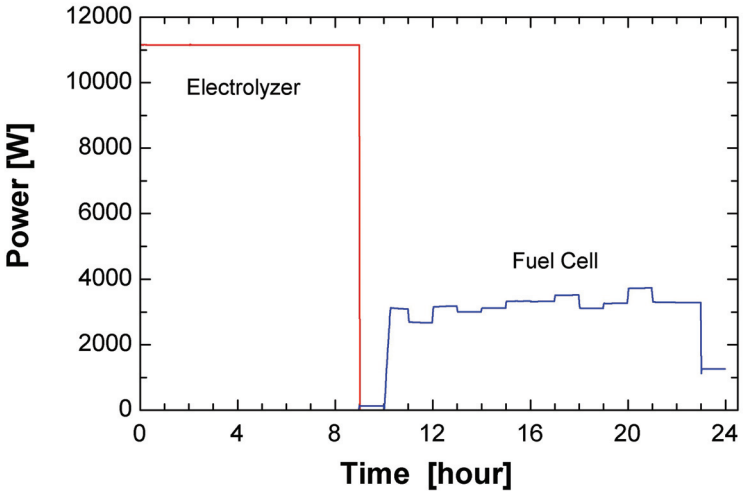

Figure 9.2 Power to electrolyzer from grid and power delivered from fuel cell back to the grid.

In the simulations described below it was assumed that all of the excess thermal energy produced by the fuel cell and metal hydride, minus the heat losses from these components to the surroundings, could be stored in the two water tanks and the metal hydride storage unit. The flow rate of the cooling water from the fuel cell to water loop 2 (fuel cell water loop) is calculated by the following equation:

(9.2)
$$\dot{m}_{\mathrm{cw,FC}} = \frac{\dot{Q}_{\mathrm{cool,FC}}}{C_{\mathrm{p,cw}} \cdot \Delta T_{\mathrm{FC}}}$$

where $Q_{\mathrm{cool,FC}}$ is the amount of heat removed from the fuel cell, $C_{\mathrm{p,cw}}$ is the heat capacity of cooling water, and ΔT_{FC} is the temperature difference between the inlet and outlet of the fuel cooling water. In this study ΔT = 5 K was assumed, which was in accordance to the specification of the actual water-cooled PEM fuel cell installed in the RE/H_2-system laboratory at IFE. Two different control strategies on how to regulate the water flow in the fuel cell loop were investigated in the system simulations described below:

- **Control Strategy A – No regulation of water flow to the metal hydride**: All of the fuel cell cooling water was first circulated through the metal hydride storage system and afterwards into water tank 2

- **Control Strategy B – Regulation of water flow to the metal hydride**: Fuel cell cooling water was circulated through the metal hydride storage system only if the metal hydride pressure was below a set point; a control pressure of 2 bar was used in this case study.

The temperatures and transient thermal behavior for the electrolyzer, metal hydride, fuel cell, and water tanks for the two different control strategies are shown in the two plots in Figure 9.3. In control strategy A (Figure 9.3, top plot) the temperature in the metal hydride

increases from ambient temperature (300 K) to 315 K over the 9-hour hydrogen charging period (at constant hydrogen production in electrolyzer, $\dot{m}_{H2,ELY}$ = 48 Nl/ min). The excess heat from the electrolyzer is used to heat up water tank 1, and the temperature increases from 300 K to 355 K (at constant electrolyzer cooling water flow rate, $\dot{m}_{cw,ELY}$ = 15 kg/min). The heat generated in the metal hydride during the hydrogen charging period (exothermic reaction) is transferred to water tank 2 (at a constant metal hydride cooling water flow rate, $\dot{m}_{cw,MH}$ = 2 kg/min), and the temperature increases to about 330 K over the same 9-hour time period. A comparison between control strategy A and B (Figure 9.3, top and bottom plots) confirms that the transient thermal behavior over the first 9-hour hydrogen charging period is independent of the control strategy. This is because there is no difference in the water regulation in water loop 1 (electrolyzer water loop).

After 9 hours, the fuel cell starts up and idles for one hour (at constant power, P_{FC} = 100 W). The hydrogen discharged from the metal hydride during this hour results in (due to endothermic reactions) both a temperature reduction (Figure 9.3) and a pressure reduction (Figure 9.4) in the metal hydride. The reduction in metal hydride temperature and pressure during this idling period depends on the control strategy. After 10 hours the fuel cell starts meeting the electrical load (Figure 9.1), and continues to do so for the next 14 hours (at average fuel cell power, $P_{avg,FC}$ = 2.9 kW_{el}). No water is circulated through the metal hydride or water tank 2 before the fuel cell has reached a minimum operating temperature of 328 K.

In control strategy A (Figure 9.3, top plot) the temperatures in the metal hydride storage unit and water tank 2 begin to rise after about 45 minutes. After another 2 hours the metal hydride has reached a steady state temperature of 326 K. The temperature in water tank 2 continues to rise throughout the fuel cell operation period, and ends up at 323 K. In control strategy B (Figure 9.3, bottom plot) no water circulates through the metal hydride before a set point pressure is reached, which in this case was 2 bar (Figure 9.4, bottom plot). As a result, the metal hydride temperature continues to decrease until it reaches 287 K, which happens after 17.5 hours. In control strategy B, the temperature in water tank 2 increases continuously (similarly to control strategy A), and ends up at 325 K (Figure 9.3, bottom plot).

Different sizes on the two water tanks were investigated in this study. The simulations showed that in order to reach a high temperature of 328 K it is necessary to install a fairly small 100 liters water tank on the electrolyzer side (water tank 1). If a higher temperature is required, the size of water tank 1 must be reduced even further.

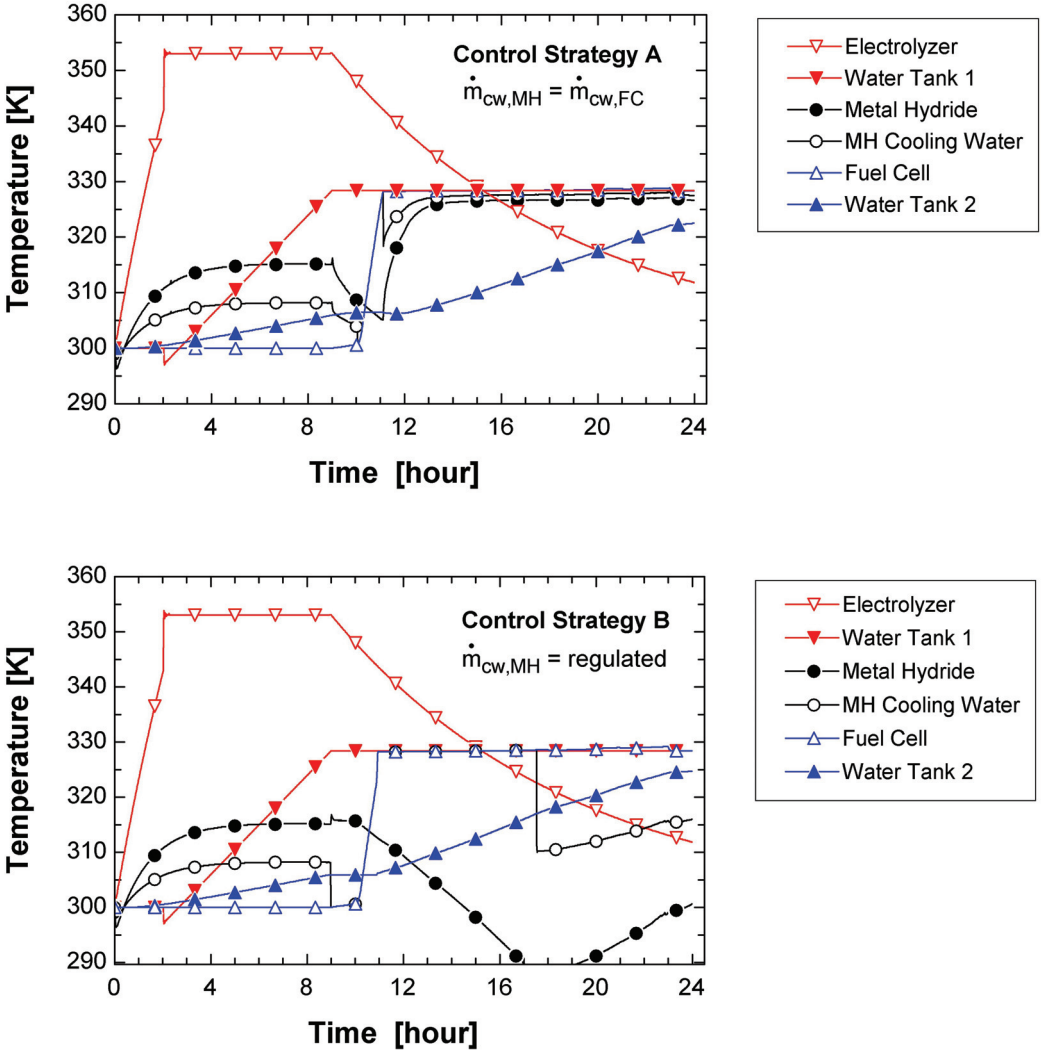

Figure 9.3 Temperature profiles for the electrolyzer, metal hydride, fuel cell, and the two water tanks for control strategy A (top) and control strategy B (bottom).

The objective with the fuel cell water loop (water loop 2) is to regulate the thermally coupled fuel cell and metal hydride system in the most energy efficient fashion. To illustrate this point, it was assumed that all of the fuel cell heat (minus losses to the surroundings) was regenerated in water loop 2, and that no auxiliary cooling was allowed. The simulations showed that water tank 2 must be very large, around 1200 liters, in order be able to absorb all of the excess heat from the fuel cell, and at the same time maintain a temperature lower than the nominal operating fuel cell temperature.

To fully understand the behavior of a thermally coupled electrolyzer/metal hydride/fuel cell system it useful to study the transient behavior of the hydrogen pressure and concentration in the metal hydride, as well as the flow rates in the fuel cell water loop (water loop 1). This behavior is illustrated in Figure 9.4. For both control strategies it can be observed that the hydrogen concentration in the metal hydride increases continuously as long as the electrolyzer operates and produces hydrogen, reaches its peak at 5.1 H/MH (mol H per mol metal atoms), and decreases continuously as long as the fuel cell operates.

It should be noted that the hydrogen gas pressure inside the metal hydride storage unit (p_{H2}) is almost equal to the equilibrium pressure of the metal hydride ($p_{MH,eq}$), due to relatively fast kinetics in the given operating temperature range. However, since the hydrogen pressure is strongly dependent on temperature, the evolution in pressure (p_{H2}) will depend significantly on the selected control strategy.

The development of the hydrogen gas pressure (i.e., metal hydride equilibrium pressure) is best illustrated by comparing the curves in the top and bottom plots of Figure 9.4. In control strategy A (Figure 9.4, top plot), water starts to circulate through the metal hydride already after 11 hours, and the hydrogen pressure increases continuously as long as the temperature increases. After a while the temperature stabilizes and the pressure decreases due to a decrease in the hydrogen concentration in the metal hydride.

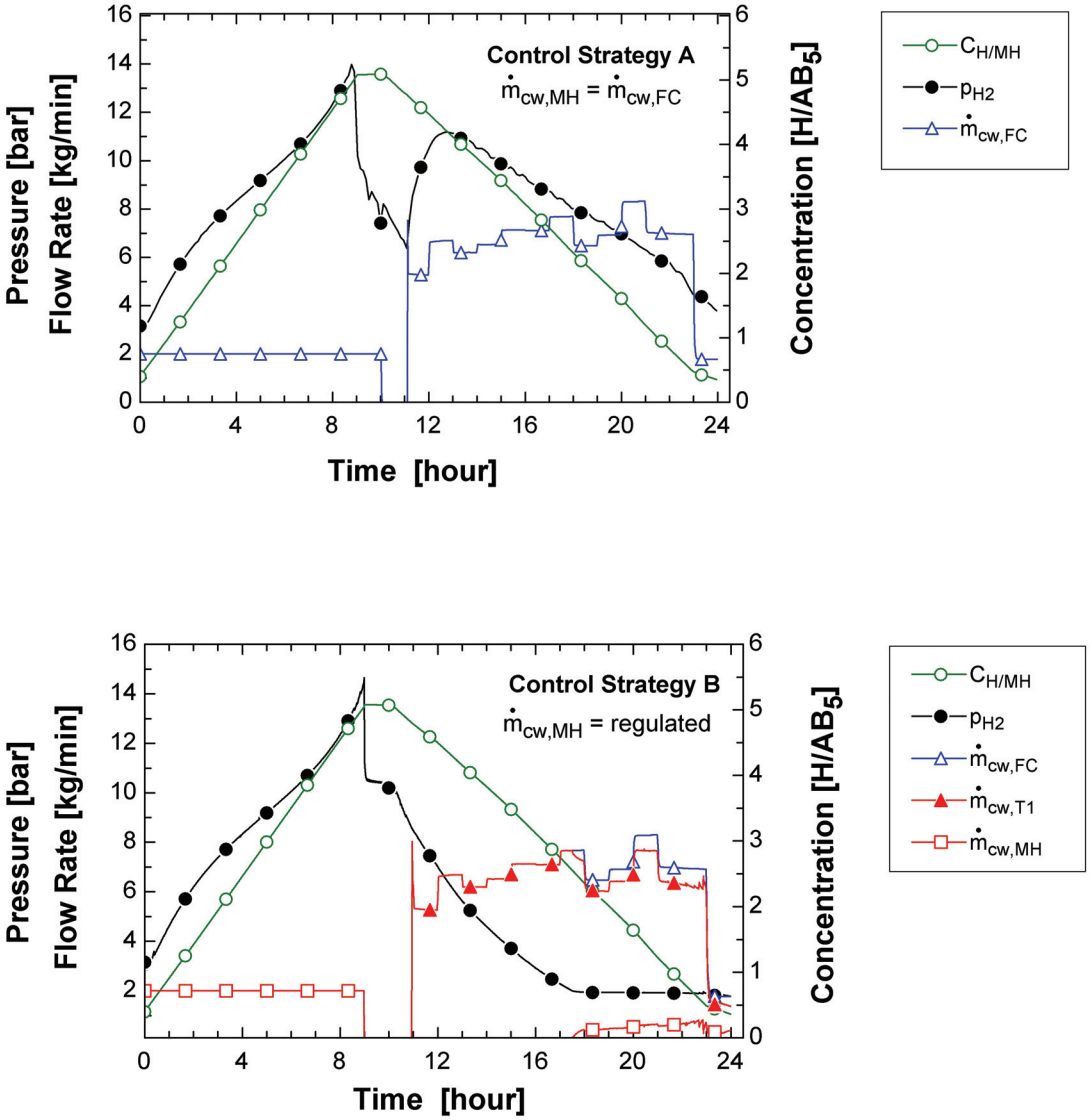

Figure 9.4 Metal Hydride pressure, hydrogen concentration, and water flows with control strategy A (top) and control strategy B (bottom)

In control strategy B (Figure 9.4, bottom plot), no water circulates through the metal hydride hydrogen storage unit before about 18 hours has passed. At this time a small part of the total

water flow from the fuel cell ($\dot{m}_{cw,FC}$) is directed to the metal hydride ($\dot{m}_{cw,MH}$), while the rest (majority of heat) is directed to water tank 1 ($\dot{m}_{cw,T1}$). The small water flow rate ($\dot{m}_{cw,MH}$ < 1 kg/min), leads to a slight increase in the metal hydride temperature, which in turn ensures a stable hydrogen gas pressure (p_{H2}) around 2 bar (regulation pressure).

Another alternative control strategy where no water passed through the metal hydride was also simulated. This control strategy (not plots shown here) resulted in a hydrogen gas pressure below 0.2 bar and a temperature below 260 K. This result confirms that thermal integration between the metal hydride and fuel cell is absolutely necessary for the system to function properly. It was found that a small part of the excess heat from the fuel cell can increase the hydrogen gas pressure in the metal hydride, which in turn makes it possible to use more of the stored hydrogen in the fuel cell. This result is in agreement with similar theoretical studies [3].

One of the main objectives with this study was to identify system designs and control strategies that yield high overall energy system efficiency. In order to evaluate the overall energy system efficiency the following simplified expression can be used:

$$\eta_{system} = \frac{\text{Energy Output (Electrical + Thermal)}}{\text{Energy Input (Electrical)}} = \frac{E_{FC} + Q_{T1} + Q_{T2}}{E_{ELY}} \tag{9.3}$$

where E_{FC} is the electrical energy delivered by the fuel cell (to the grid), E_{ELY} is the electrical energy delivered to the electrolyzer (from the grid), Q_{T1} is the thermal energy recovered from the electrolyzer and stored in water tank 1 and the metal hydride, and Q_{T2} is the thermal energy recovered from the fuel cell and stored in water tank 2 and the metal hydride. The electrical energy system efficiency is simply derived from Equation (9.3) by omitting the thermal terms (Q_{T1} and Q_{T2}) in the calculations.

The simplified efficiency equation above (Equation (9.3)) does not take into account the losses associated with auxiliary equipment, such as that associated with the air compressor for the fuel cell, hydrogen drying for the metal hydride, or power conditioning for the conversion to/from the electrical grid. Nevertheless, the efficiencies for a few different designs and control strategies were calculated for the 24-hour period above (Figure 9.2 - Figure 9.4).

The results showed that the electrical system efficiency was around 40%, independent of the selected control strategies, while the overall system efficiency was around 75%, also fairly independent of the selected control strategy. This high overall system efficiency assumes that the walls of the water tanks are well insulated, with a thermal conductivity, k = 0.05 W/mK, and that there were no heat losses from the pipes and interconnections.

9.6 CONCLUSIONS

Thermally coupled electrolyzer/metal hydride/fuel cell systems for stationary applications can have a high overall energy system efficiency. A system simulation model suitable for parametric studies and optimization of design and controls of such integrated metal hydride hydrogen systems has been developed. System simulations show how the electrolyzer, metal hydride, and fuel cell can be thermally coupled and operated together if sized properly. The

simulations also illustrate the importance of a thermal coupling between the metal hydride hydrogen storage and the fuel cell. A control strategy (control strategy B) that regulates the water flow through the metal hydride, and thereby ensures that the hydrogen gas pressure in the storage is sufficiently high, was demonstrated and evaluated.

Acknowledgements

The authors would like to thank the members of the IEA HIA Annex 18 group for facilitating relevant international meetings, workshops, and technical tours. A special thanks goes to our Japanese colleagues Hiroshi Ito and Makato Akai from AIST, for providing technical information and data on the Takasago hydrogen demonstration plant. We would also like to acknowledge the Research Council of Norway for providing the main funding for this study.

References

[1] Okamoto H, Kawakami Y, Kozawa Y, Akai M. Total energy systems engineering by coring metal hydride tanks. Journal of the Hydrogen Energy System Society of Japan 2004; 29(2).

[2] Ito H. R&D Progress of AIST-Takasago Hydrogen Integrated System. Personal communication, 6-9 March 2006.

[3] Jiang Z, Dougal R, A, Liu S, Gadre S, A, Ebner A, D, Ritter J, A. Simulation of a thermally coupled metal-hydride hydrogen storage and fuel cell system. Journal of Power Sources 2005; 142(1-2): 92-102.

[4] Ulleberg Ø, Ito H, Maack M, H, Ridell B, Miles S, Kelly N, Iacobazzi A. Modeling and Evaluation of Hydrogen Demonstration Systems. WHEC16 - World Hydrogen Energy Conference, Lyon, 2006.

[5] Førde T. Integration of Water-Cooled Metal Hydride Units into Hydrogen-based Stand-Alone Power Systems (tentative title). PhD thesis (to be submitted first half of 2007), Norwegian University of Science and Technology, Trondheim, 2006.

[6] Førde T, Maehlen J, Petter, Yartys V, A, Lototsky M, V, Uchida H. Influence of intrinsic hydrogenation/dehydrogenation kinetics on the dynamic behaviour of metal hydrides: A semi-empirical model and its verification. International Journal of Hydrogen Energy (2006), doi: 10.1016/j.ijhydene.2006.07.015 2006; In press.

[7] Vie P, J, S, Miland H, Førde T, Pettersen A, G, Eriksen J, Ulleberg Ø. Renewable Energy Based Hydrogen Stand-Alone Power Systems. First International Renewable Energy Storage Conference (IRES I), The case of energy autonomy: Storing Renewable Energies, Science Park, Gelsenkirchen, Germany, 30-31 October 2006.

[8] Ulleberg Ø, Yartys V, A, Vie P, Miland H, Førde T, Eriksen J. Hydrogen Storage in Solid Materials, from Synthesis to Systems (KMB-project: NFR-144075/212; period: 2001-2005). Final Report, IFE/KR/F-2006/226, IFE, Kjeller, 2006.

[9] Ulleberg Ø, Glöckner R. HYDROGEMS - Hydrogen Energy Models. WHEC 2002 - 14th World Hydrogen Energy Conference, Montreal, 9-14 June 2002.

[10] Sato M. Studies of hydrogen absorption and desorption processes in advanced intermetallic hydrides. Ph.D Thesis, University of Oslo, 2005.

[11] Lototsky M, V, Yartys V, A, Marinin V, S, Lototsky N, M. Modelling of phase equilibria in metal-hydrogen systems. Journal of Alloys and Compounds 2003; 356: 27-31.

10 THERMAL INTEGRATION OF A METAL HYDRIDE HYDROGEN STORAGE UNIT AND A PEM FUEL CELL STACK

T. Førde[1], J. Eriksen[2], A. Pettersen[3], Ø. Ulleberg, P. Vie[1,*]

1) Institute for Energy Technology, P.O. Box 40, NO-2027 Kjeller, Norway

2) Hydrogen Storage & System, P.O. Box 45,N0-2027 Kjeller Norway

3) Norwegian University of Life Sciences, P.O. Box 5003, NO-1432 Ås, Norway

10.1 ABSTRACT

A metal hydride storage unit and a polymer electrolyte membrane fuel cell stack were thermally integrated through a common water circulation loop. The low temperature waste heat dissipated from the fuel cell stack was used to enhance and ensure the release of hydrogen from the storage unit. A water-heated metal hydride (MH) tank has a smaller surface area than an air-heated MH-tank with external heating fins, and will therefore have the potential for significantly better kinetics for absorption and desorption of hydrogen.

The fuel cell stack and metal hydride storage unit were characterised and a strategy was tested and optimised for a fast start-up of the fuel cell stack. The main priority for the strategy was to maintain the metal hydride temperature at room temperature, while increasing the FC temperature to the specified operating temperature. The best strategy for this system was to increase the fuel cell temperature to at least 313 K before starting to heat the metal hydride storage unit to 303 K. Without thermal integration it was not possible to utilize the full hydrogen storage capacity of the metal hydride storage unit due to cooling of the tank.

*E-mail for corresponding author: Preben.vie@ife.no

Nomenclature

A	Area	$[m^2]$
c_p	Heat capacity	[J/kg·k]
c_U	Concentration	$[kg/m^3]$
C_{LMCD}	Logarithmic concentration difference	$[kg/m^3]$
D	Diffusion coefficient	$[m^2/s]$
D_h	Hydraulic radius	[m]
F	Faradays constant	[Coulomb/mol]
I	Current	[A]
K	Conductivity	[W/m·K]
L	Length	[m]
ΔH	Heat of reaction	[J/mol]
h_m	Convective mass transfer coefficient	$[mol/m^2 \cdot s]$ or $[kg/m^2 \cdot s]$
M	Mass	[kg]
$\dot{m}$	Mass flow	[kg/s]or [mol/s]
MA	Overall mass transfer number	$[m^3/s]$
M	Molar Mass	[g/mol]
m_f	Mass fraction	[-]
R	Universal gas constant	[J/mol·K]
R_o	Ohmic resistance	[ohm]
R_{mass}	Mass transfer resistance	$[m^{2\cdot}s/mol]$ or $[m^2 \cdot s/kg]$
P	Pressure	[bar]
Pr	Prandel number	[-]
Re	Reynolds number	[-]
Sh	Sherwood number	[-]
ΔS	Entropy	[J/K·mol]
T	Time	[s]
T	Temperature	[K]
$\dot{Q}$	Heat flux	[W]
UA	Overall heat transfer number	[W/K]
Z	Convergence criteria	[-]
ϑ	Efficiency	[-]
Υ	Weighting factor between $[0-1]$	[-]
λ	Concentration	$\left[{}^{H_2O}/_{SO_3^-} \right]$
Ψ	Water production	[kg/s] or [mol/s]

Subscript	
eq	Equilibrium
exchanger	Exchanger
FC	Fuel cell
G	Gas
in	In
H	Hydrogen
MH	Metall hydride
out	Out
prod	Produced
reac	Reaction
sat	Saturated
W	Water

10.2 INTRODUCTION

The significance of hydrogen as an environmentally sound energy carrier has been manifested through various roadmaps and demonstration projects around the World [1-8]. Most recently, the European Parliament adopted a written declaration [9] on establishing a green hydrogen economy founded on five key factors for energy independency including hydrogen fuel cell technology for storage of renewable energy and smart power grids.

The requirements for hydrogen storage are different for different applications. Low total weight is essential for mobile applications, but is usually not important for stationary applications, where compactness is normally more important. Hydrogen is most commonly stored as gas, liquid or reversibly absorbed in a metal hydride powder. Hydrogen can also be stored chemically, but at a higher energetic cost. Storage of hydrogen in metal hydrides is advantageous due to a high volumetric density at low pressures. The volumetric density can be more than twice that of liquid hydrogen. Due to the weight of the metal hydride itself conventional metal hydrides have lower weight densities than storage of hydrogen as gas or liquid. Therefore, hydrogen storage as gas or liquid is more advantageous when low weight is vital for the application.

The hydrogen desorption from the metal hydride is endothermic. Due to poor thermal conductivity within the metal hydride bed, heat transfer is often the rate controlling variable for the desorption process. During operation a fuel cell produces excess heat. This heat can be utilised in the metal hydride and will improve the kinetics of the hydrogen desorption reaction from the metal hydride storage unit (MHU).

Before a metal hydride storage unit is designed and implemented into a hydrogen system, the system's hydrogen flow rate requirements must be identified. A carefully designed system is essential to assure proper heat transfer from the fuel cell to the metal hydride unit. The MHU's heat transfer properties can be improved by increasing the effective thermal conductivity of the metal hydride granulates by: (a) adding nickel or aluminium foam into the metal hydride bed [10,11], (b) inserting metal matrices of aluminium foams and copper nets [12], (c) compacting metal hydride powder with an expanded graphite [13]; or by improving the tanks design: (a) internal heat exchanger [14] (b) by adding an external heat exchanger [15].

The interaction between a metal hydride storage unit and a proton exchange membrane fuel cell (PEMFC) has been studied both through simulations and experimental work by various authors. Bossi et al. [16] experimentally studied a system containing a PEM fuel cell, a battery bank, a metal hydride hydrogen storage unit, and an electronic load. The metal hydride storage unit was filled with 50 kg of metal hydride powder and had an internal heat exchanger, but was not thermally integrated with the fuel cell. They found that heat transfer between the metal hydride powder and cooling/heating medium was a critical issue and that thermal integration between the fuel cell and H_2 storage unit was feasible. Wilson et al. [17] showed experimentally that two cylindrically shaped metal hydride tanks with a hydrogen storage capacity of 280 Nl (were able to fuel a 1.0 kW PEMFC. The metal hydride tanks had external heat transfer and the hot fuel cell excess air was blown past the MHU. A hydrogen system containing an electrolyser, MHU, and PEM fuel cell was studied through simulations by Førde et al.[18]. The effect of various strategies for circulation of the fuel cell cooling water through the metal hydride storage unit was investigated and overall system efficiency

was calculated. Jiang et al. [19] and MacDonald et al. [20] studied the interaction between a fuel cell and a metal hydride reactor. The previously studied reactors had internal heat exchangers [19], as well as external heat exchangers [20]. In summary, the studies [18-20] conclude that proper design of the metal hydride reactor is important in order to obtain a reliable overall system.

The study descriped in this paper included the building, characterization, and testing of a metal hydride unit with an internal heat exchanger. The metal hydride unit was then thermally integrated with a water cooled PEM fuel cell. The objective with the study was to demonstrate how heat from a PEM fuel cell can enhance the release of hydrogen from the metal hydride storage, and how critical system control parameters can affect the start-up and operation of the combined MH/PEMFC-system.

10.3 EXPERIMENTAL SET UP

The experiments reported in this paper were performed at Institute for Energy Technology's laboratories for Hydrogen Storage and Hydrogen Energy Systems.

10.3.1 Metal hydride storage unit

Apparatus

The metal hydride hydrogen storage unit was designed for kinetic and thermal measurements of adsorption and desorption of hydrogen in a "larger" storage unit. In addition, the unit was designed for integration with a water-cooled PEM fuel cell stack. Hence, the heat-transfer medium was water. The metal hydride unit was designed to supply hydrogen for at least 3 hours of peak fuel cell power. The unit was manufactured at Institute for Energy Technology's workshop. A schematic drawing of the unit is shown in Figure 10.1.

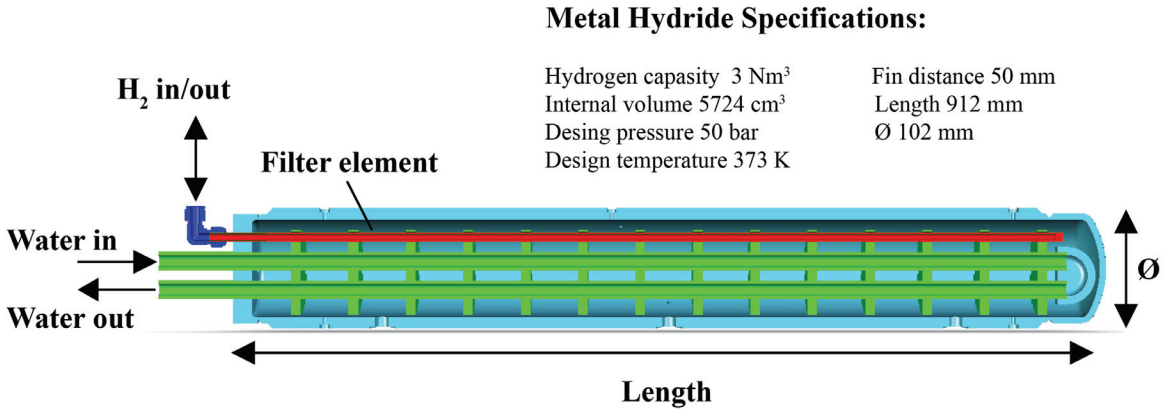

Figure 10.1. The water-cooled metal hydride storage unit (designed, constructed, and tested at IFE).

The outer shell of the MHU was a stainless steel (SS-316) cylinder with an outer diameter of 11.4 cm and a total weight of 40 kg. Hydrogen is distributed in the tank through a filter element positioned in the top of the tank. The water is circulated in an internal u-shaped copper tube below the filter element. Copper fins (1 cm thick) were soldered to the water tube with 5 cm spacing, in order to effectively distribute and remove heat from the metal hydride

bed. The internal temperature of the metal hydride bed was measured with 6 K-type thermocouples. 4 thermocouples monitored the radial temperature gradients and 2 thermocouples were positioned axially between two fins in the centre of the reactor. In addition, the metal hydride gas pressure was measured.

The MHU was filled with 17.5 kg of AB_5 type metal hydride powder from LABTECH Int. CO Ltd Alloys Research and Manufacturing [21]. The alloy was a Ce modified $LaNi_5$ type. After filling, the storage unit was rotated for 8 hours in a turning lathe to ensure uniform powder distribution.

10.3.2 Characterisation

Both the MHU and the MH-powder was characterised. The volume of the MHU with and without MH-powder was calibrated using argon gas. The MH-powder was activated under vacuum and 373 K for 4 hours. Then the unit was cycled several times with hydrogen to reach reversible hydrogen capacity. During operation of the metal hydride storage unit, the flow rate and inlet and outlet temperatures of the circulating water were measured.

The metal hydride alloy powder was characterised with respect to pressure, concentration, and temperature (*PCT*-isotherms) and kinetic behaviour. The *PCT*-isotherms were measured in a Sievert-type experimental set up described in detail by Sato [22]. The alloy's kinetic behaviour was measured using a stepwise technique [23]. The sample was heated to 523 K under vacuum for 2 hours, and then cycled several times with industrial grade hydrogen of 99.9999% purity, until nominal hydrogen storage capacity was reached. The temperature of the sample and hydrogen pressure were monitored every 20 ms. The rate of desorption or absorption of hydrogen was measured volumetrically by monitoring the increase or decrease of hydrogen gas pressure.

10.3.3 PEM fuel cell system

Apparatus

The fuel cell stack was a water-cooled PEMFC-stack manufactured by HTI Biel, Switzerland [24-26] (Figure 10.2A). The nominal power was 1.2 kW at 333 K and 1.2 bar, with 22 cells and an active area of 170 cm². The membrane and electrode assembly was a Pmembrane H300 from Umicore[2]. An internal air humidifier is included in each single cell [27] (Figure 10.2B). In the humidifier dry inlet air is humidified with water transported from the hot exhaust air through a proton-conducting membrane. The water transport was modelled and the results were included in the fuel cell stack control program improving the control of the water balance in the fuel cell stack.

Air was supplied to the stack by a Vairex VV- 520.03 INT dry-vane compressor[3], and hydrogen was supplied from the MHU (described in Section 10.3.1) through a mass flow controller. The cooling water was circulated with a Bosch DC pump, type PCA 12V, at rates

[2] now SolviCore AG

[3] VAIREX Corporation, Boulder, Colorado, USA: http://www.vairex.com

between 3.5 to 5 l/min. The stack temperature was controlled by a "tube in tube" heat exchanger, additionally cooling the stack by tap-water. Each single cell voltage was monitored continuously in addition to inlet and outlet temperatures of the reactants and cooling water.

A B

Figure 10.2: The 1.2 kW water-cooled PEM fuel cell from HTI Biel. A) The fuel cell stack. B) A detail of the internal humidification channels for inlet air on one cell plate.

10.3.4 Operation and characterisation

The PEM fuel cell stack was operated with an outlet cooling water temperature of maximum 333 K and at 1.5 bar_a, maximum. To optimize the system efficiency, the air compressor was operated at a minimum pressure giving a back-pressure of maximum 1.1 bar_a of the fuel cell. The suggested minimum reacting gas stoichiometries of hydrogen and air were respectively 1.2 and 1.8. In the experiments described here the stoichiometric flows for hydrogen and air was, 1.5 and 2.0, respectively, as this gave the most stable stable fuel cell operation,

The minimum single cell voltage during operation was 0.6 V, giving a minimum stack voltage of 13.2 V. The gas channels were purged occasionally, or if one of the cell voltages dropped below the minimum cell voltage. The maximum allowable temperature drop through the stack was 5 K.

The stack was characterised during steady-state operation at different electrical currents and temperatures. Measurements of polarisation curves at 313, 323 and 333 K were performed. The polarisation curves were measured after stable operation at maximum current in minimum 15 minutes by reducing the current step-wise down to open circuit voltage (OCV).

10.4 RENEWABLE HYDROGEN ENERGY SYSTEM

Apparatus

The thermal integration of the MHU and PEM fuel cell stack was performed at Institute for Energy Technology's Renewable Hydrogen Energy Laboratory. The structure of this laboratory is presented in Figure 10.3 and the components are specified in Table 10.1. The system is operated by a in-house developed control and data acquisition program (National

Instruments LabVIEW). Further details of the laboratory are available in other sudies and reports [28,29].

The integration of the MHU and PEM fuel cell stack was obtained by a common water circulation loop. The cooling water leaving the PEM fuel cell stack can either pass through the MHU at various flow rates controlled by a three-way valve or go directly to the heat exchanger. The minimum controllable water flow rate through the MHU was 20% of the total water flow rate.

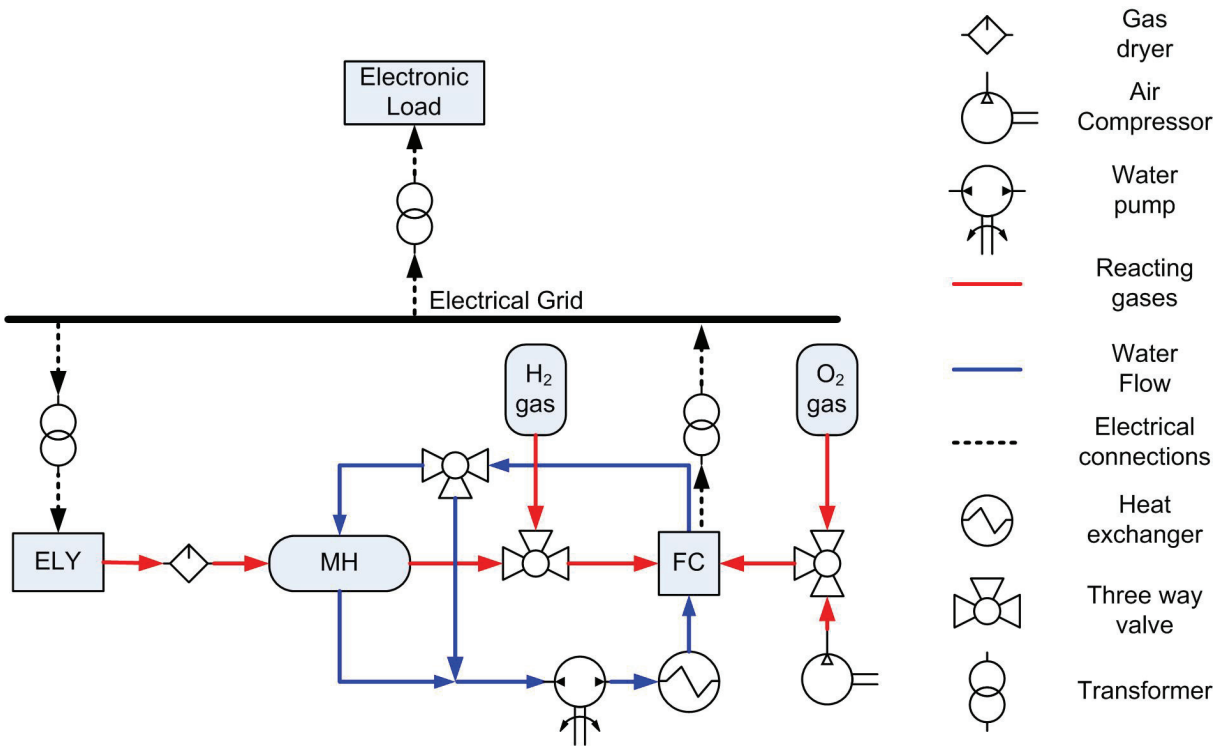

Figure 10.3: Schematic diagram of the Renewable Energy Hydrogen System Laboratory at IFE.

Table 10.1. The components of the Renewable Hydrogen Energy Laboratory

Component	**Specification**
PEM electrolyser	Fraunhofer ISE, prototype nr 02, 15 bar, 348 K, 390 l_N/min H_2
Oxygen tratp (Gas drier 1)	Deoxon, Alltech Associates
Hydrogen dryer (Gas drier 2)	MG03, AquaGas
Metal hydride storage	Chapter 10.3.1
PEM fuel cell stack system	Chapter 10.3.3
Load	PLZ-603W (Kikusui Electronics)
Three-way valve	Bürkert BR-10 type 10/MC60
Heat exchanger	Tube-in-tube, SS-316 Outer tube OD Ø19 mm, Inner tube OD Ø9.5mm, L= 1 m.

10.4.1 Characterisation and operation

The MHU and PEMFC stack was operated in start-up cycles from room temperature and up to fuel cell operation temperature. During the start-up sequences the three-way valve was operated at different levels and control schemes (Table 10.2).

Table 10.2: Experimental set up for start-up cycles of the MHU and PEM stack start-up experiments

Name	MH-valve value
Closed	0
Minimum flow	20
Open	100
Batch	0/20

10.5 RESULTS AND DISCUSSION

10.5.1 Metal hydride

Metal hydride alloy

The metal hydride alloy powder used in the MHU was a Ce modified $LaNi_5$ type of material. The MHU's ability to supply and store hydrogen depends on the material properties in the storage alloy and the design of the storage unit. To predict the behaviour of the MHU it is therefore very important to understand the alloys behaviour at a particle level. It must be possible to fill the MHU with hydrogen at the production rate and pressure of the electrolyzer. The MHU must also be able to supply more than 90% of its capacity with a high enough pressure and flow rate to the fuel cell stack

The metal hydride alloy powder's filling and draining properties was characterised with respect to *PCT*-isotherms and kinetic behaviour. Data from *PCT*-measurements on a 0.9057 g metal hydride sample was used as basis for the system design calculations. The *PCT*-isotherms (283, 298, 333 and 323 K) for adsorption and desorption of hydrogen in this sample is presented in Figure 10.4. The pressure plateau for this particular metall hydride alloy is observed to be between 1 and 20 bar for all measured temperatures and hydrogen concentrations.

In the reference renewable energy hydrogen system laboratory described above (Figure 10.3), hydrogen is produced via water electrolysis at 15 bar. Thus, the MHU needs to operate at a temperature < 298 K, in order to be fully charged up with hydrogen (ref. the 15 bar line in Figure 10.4A). The fuel cell needs a hydrogen pressure of minimum 1.2 bar to operate. A minimum pressure of 2 bar was required to ensure proper control of the hydrogen flow . The MHU temperature needs to be > 298 to take full advantage of most of the stored hydrogen (ref. the 2 bar line in Figure 10.4C). At lower hydrogen to metal atomic ratios the equilibrium pressure drops below one bar, and this hydrogen is therefore not available for use in the fuel cell. The enthalpies and entropies of absorption and desorption were calculated from $\Delta H_{absorption} = -28$ kJ/mol, $\Delta H_{desorption} = -27$ kJ/mol, $\Delta S_{absorption} = 105 \frac{\text{J}}{\text{Kmol}}$ and $\Delta S_{desorption} = 103$ J/Kmol (Figure 10.4 B and D to)

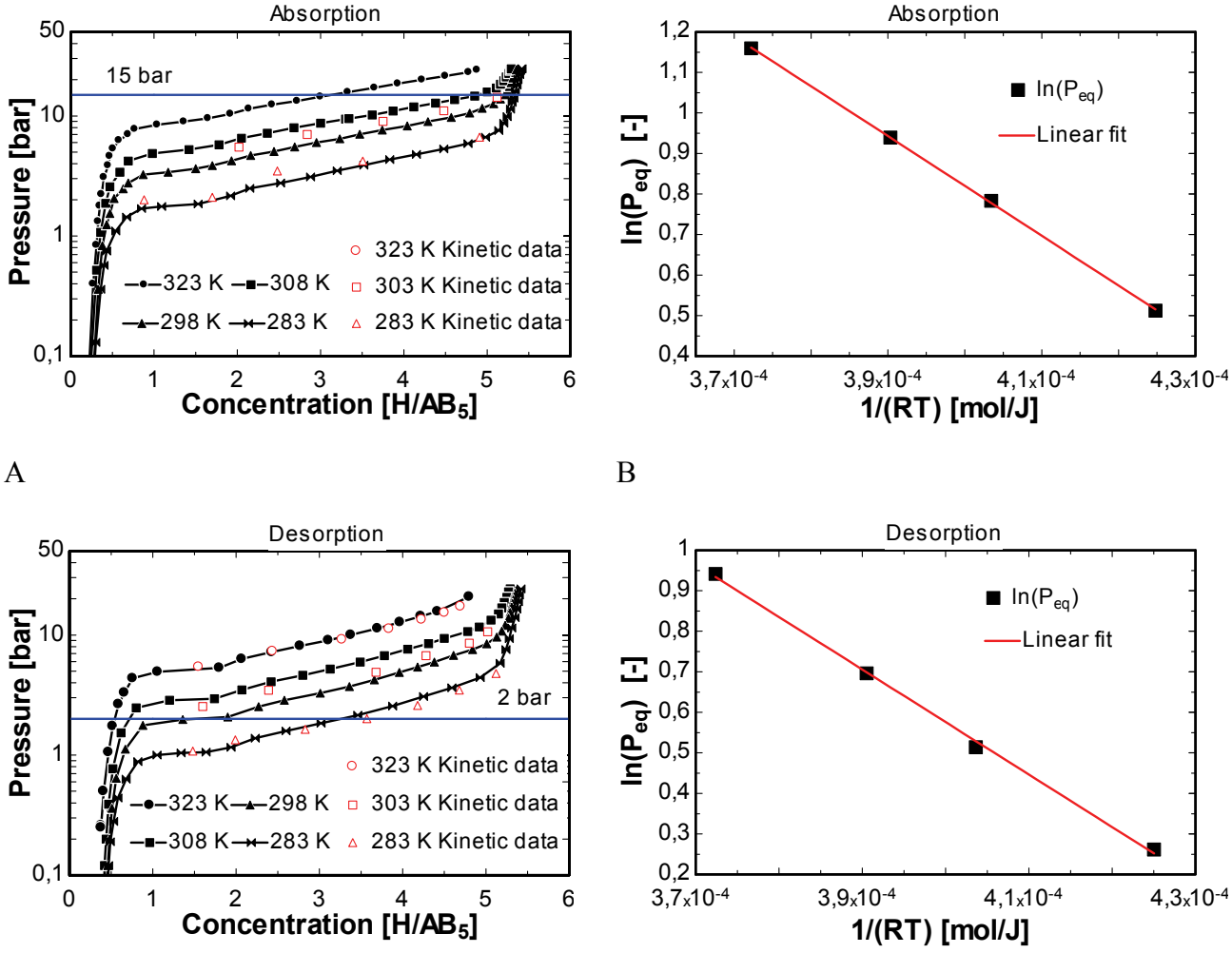

Figure 10.4: PCT isotherms of hydrogen absorption (A) and desorption (C) at 10, 25, 35 and 323 K. The corresponding Van't hof plots are presented in graphs B and D.

The alloy's kinetic behaviour was measured and analysed by step by step methods presented respectively by Wang [23] and Førde [30]. To obtain isothermal sample temperatures during the experiment, a small MH sample (0,323 g) was mixed with nickel powder (1.87 g, 99.999% purity). The nickel was used as an additional thermal mass and increased the thermal conductivity and heat capacity of the sample system. Hydrogen absorption by the nickel powder was negligible at the given pressures and temperatures. The *PCT*-data from the samples used in the kinetic measurements (Figure 10.4) were measured in the same experimental set up as the other *PCT*-data. The data collected deviated slightly from the the other *PCT*-data. This deviation can be explained by experimental errors due to smaller test-samples.

The results from the experiments on the kinetics of the selected metal hydride material are preliminary, and further experiments are required to increase their accuracy. Nevertheless, a few trends and preliminary conclusions can already be observed: The pressure dependent term of the rate constant (K) was found to be proportional to the logarithm of the gas pressure, and the "pre-exponential" factor (n) was respectively 1 and 2 for desorption and absorption of hydrogen (more details are given in appendix A). The derived activation energies for the

hydrogen absorption and desorption reactions were calculated to respectively 12 kJ/mol and 30 kJ/mol. The correlation coefficient (r^2) was larger then 0.83. These preliminary results indicate that the alloy's intrinsic kinetic is fast, and that the alloy's properties are very similar to the alloy investigated by Førde et. al. [30].

Metal hydride storage unit

The capacity of the metal hydride storage unit (MHU) was measured to approximately 2.9 Nm³ and 260 g of hydrogen. This corresponds to a storage density of 1.5 wt% with respect to the MH alloy and 0.4 wt% with respect to the complete storage tank. This is enough to supply the fuel cell with hydrogen for approximately 3 hours at nominal power. The internal volume of the tank was measured to 5.7 litres, giving an overall void density for the tank of about 3 g/cm³.

It is relatively straighforward to run experiments and calculate the energy balance for hydrogen absorption or desorption in metal hydrides. The main heat fluxes are: the heat production or consumption due to the gas solid reaction $\dot{Q}_{H_2}$, the heating or cooling heating water energy $\dot{Q}_w$, and the amount of energy used to change the temperature of the reactor shell itself $\dot{Q}_m$. The overall heat transfer number for the tank UA_{w-MH} was calculated to be 25 ± 5 W/K at steady state conditions (based on average from 4 temperature measurements made within the MHU).

10.6 PEM FUEL CELL SYSTEM

The PEM fuel cell stack was characterised through polarisation curves at different temperatures, see Figure 10.5A. There was a very small difference between the current voltage characteristic for the three measured temperatures of the cooling water. This small difference is quite typical at higher fuel cell voltages. A larger difference is expected at higher current densities and lower cell voltages than measured in this paper. The measured performance at 333 K was in accordance with the performance when tested at HTI Biel prior to its shipment to IFE.

The efficiency of the fuel cell and fuel cell system is presented in Figure 10.5B. The output power was calculated from the measured current and voltage from the fuel cell. The input power for the fuel cell was calculated including the measured hydrogen flow and the higher heating value of hydrogen. The auxiliary power for the compressor and water circulation pump was included in the calculation of the overall fuel cell system efficiency. The efficiencies was calculated based on fuel cell temperature of 333 K, a stoichiometric air flow of 2, and a stoichiometric hydrogen flow of 1.5, and an electrical current of > 20 A. The results are shown in Figure 10.5B.

The experiments show that the hydrogen flow rate had a constant value of 4 Nl/min at currents < 20 A. Due to the lower hydrogen flow rate limit, the fuel cell efficiency has a maximum value of 42% at 280 W. The maximum system efficiency (32%) occurs at a higher power rating (450 W). This decrease in efficiency is mainly due to the air compressor work, which has a very low efficiency at low flow rates and needs a minimum power to start the compressor. The cooling water pump work (constant flow rate) also reduces the overall efficiency.

It should also be noted that the energy balance for the stack was well defined and more than 90% of the produced heat was removed through the cooling water and could be utilized by other system components.

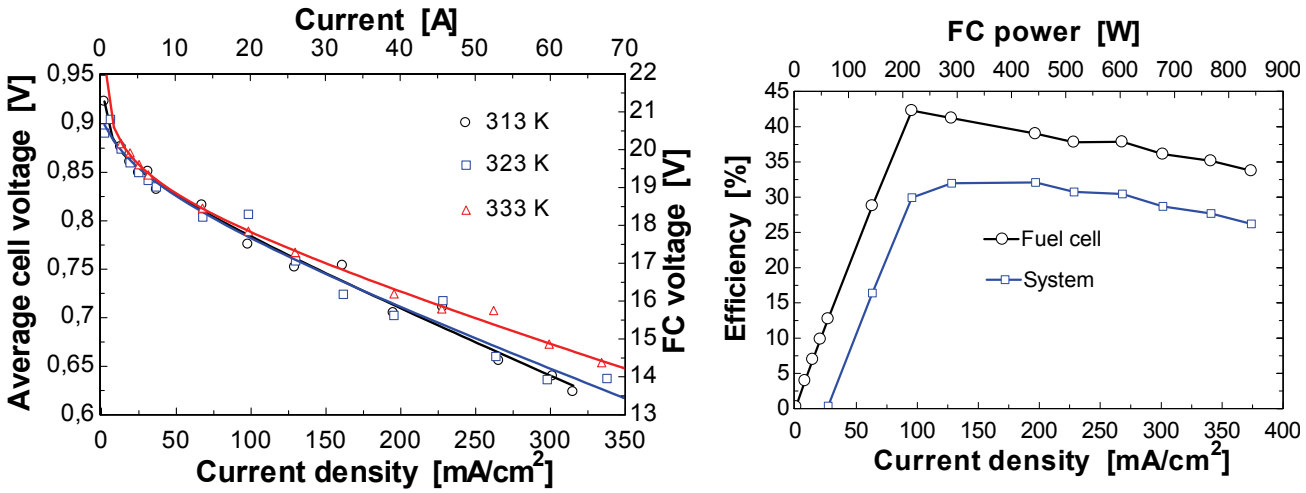

A B

Figure 10.5: The measured current voltage characteristic is presented for fuel cell outlet water temperatures of 313, 323 and 333 K (A). The fuel cell and fuel cell system efficiency is presented in graph B relative to current density and power output from the fuel cell. The fuel cell water temperature at the outlet was 333 K.

10.7 INTEGRATION OF METAL HYDRIDE H_2 STORAGE UNIT AND PEM FUEL CELL

The MHU and PEM fuel cell stack was successfully integrated through a common water circulation loop and a 3-way valve controlling the amount of water entering the MHU from the fuel cell, see Figure 10.3. From Figure 10.6 it can be observed that the fuel cell produces sufficient amounts for the desorption of hydrogen in the metal hydride. At steady-state fuel cell operating conditions the 3-way valve regulates the system so that the MHU's temperature is always > 298 K.

An example of a start-up of the PEM fuel cell stack with the MHU fully integrated is presented in Figure 10.7. As expected we observe a heating of the MHU during the test period, but there is first a slight cooling due to the low heat production the first 5 minutes in the stack and the demand for minimum 4 Nl/min hydrogen when running the fuel cell system Figure 10.7A). At the same time it can be observed that the temperature of the fuel cell starts to increase immediately when the load is connected. Temperature distribution within the MHU is expected; the temperatures are high close to the tubes for circulating water and low further away from the centre of the MHU.

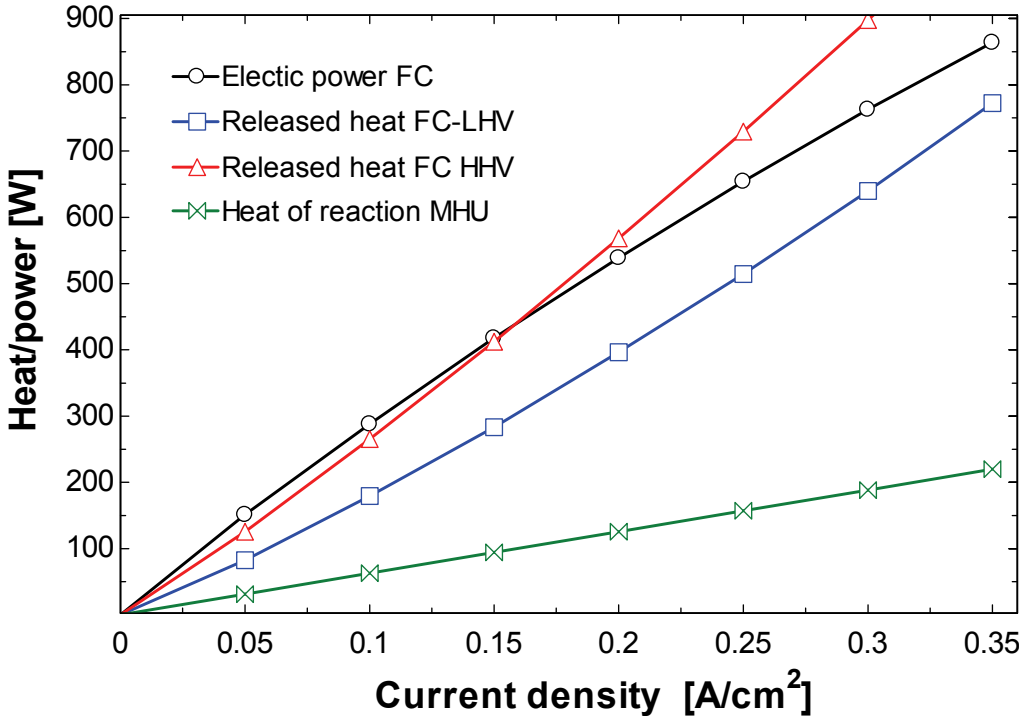

Figure 10.6: Comparison of produced heat in the fuel cell and minimum heat required to desorption of hydrogen in the metal hydride The values were calculated based on the measured polarisation curve for the fuel cell and heat of desorption for the MH-alloy.

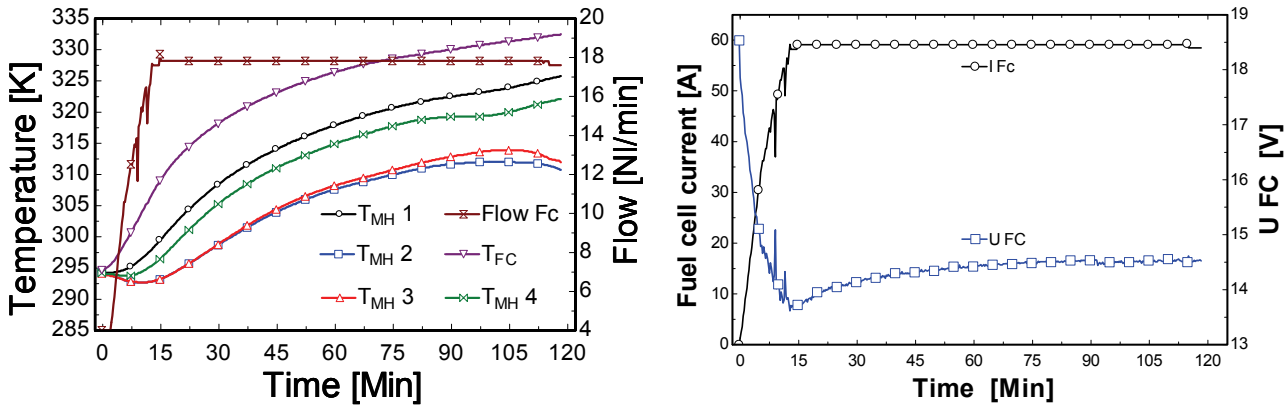

A B

Figure 10.7: 4 different temperatures within the MHU and the fuel cell cooling water outlet temperature are presented in graph A at start-up of the PEM fuel cell stack. The fuel cell voltage and current is presented in graph B. The position of the 3-way valve was at 100 %. $T_{MH}1$ was closest to the heat exchanger tubes, $T_{MH}4$ a bit further away, and $T_{MH}2$/$T_{MH}3$ was farthest away from the tubes.

The start-up time for the system was optimised with respect to the temperatures of fuel cell and MHU. The fuel cell should obtain its operational temperature and hence highest efficiency as soon as possible, while the MHU should preferably not cool down below 25 C to ensure a stable hydrogen flow from the tank. 4 different start-up regimes were tested experimentally (Table 10.2). The results are presented in Figure 10.8.

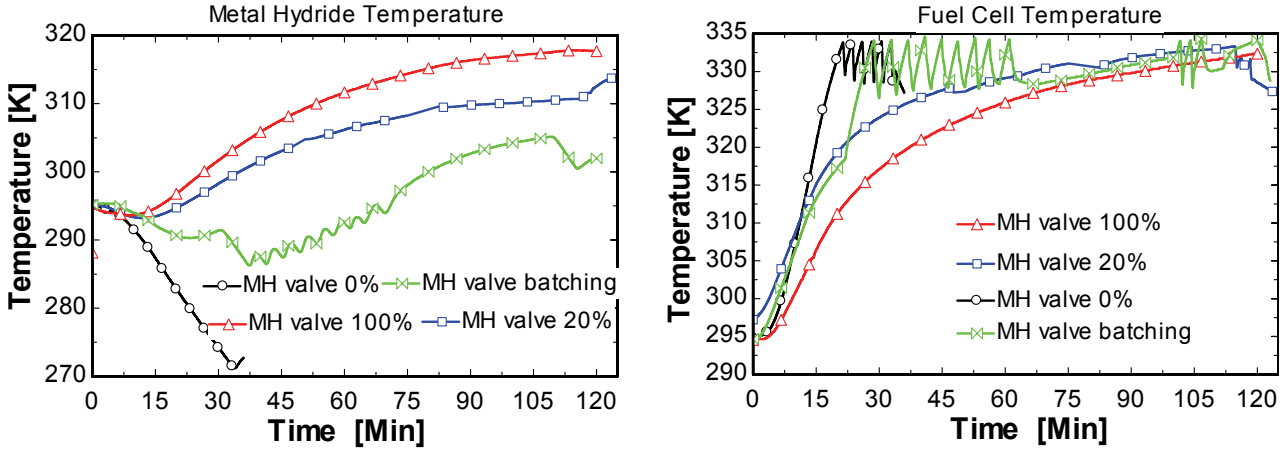

A B

Figure 10.8: Start-up of the fuel cell system and MHU with 4 different start-up strategies. Figure A shows the average metal hydride temperature with different flow rates of heating water in the metal hydride water loop. Figure B shows the average temperature of the inlet and outlet fuel cell cooling water with different water flow rates in the metal hydride loop.

The experiments demonstrated that the MHU cools down to 273 K after 30 minutes when the MHU was not integrated with the fuel cell stack (MH valve 0 %). At the same time the fuel cell temperature increases to 323 K within 20 minutes. When the MHU is fully integrated with the fuel cell (100 % MH valve), the fuel cell temperature is 323 K after about 90 minutes, and the MHU's temperature is approx. 313 K. Maximum fuel cell temperature was obtained faster (70 minutes), as expected, when less heat from the FC was used to heat the MHU (20 % MH valve). However, this is still somewhat slowed than desired. Therefore, the MH-valve was controlled through an on/off process where the valve was cycled between 0% and 20% open. This option was chosen due to limitations in the minimum flow through the MH-valve. For this case we observe that the fuel cell temperature is 333 K after 25 minutes and the MHU temperature is never lower than 288 K. This control option is not ideal, but ensures both a fast start-up of the fuel cell stack with only 5-10 minutes longer start-up period than the non integrated fuel cell and a MHU-temperature that ensures enough hydrogen supply.

Based on these experiments the chosen start-up procedure should be the on/off switching between 0 % and 20 % open MH-valve. However, from Figure 10.9 it can be observed that the fuel cell power increases in a similar manner for 4 experiments. This is due to the fact that the fuel cell performance is only slightly better at 333 K than 313 K, see Figure 10.5. Therefore the start-up case with the MH-valve in constant 20% open would be preferable due to ease of control and less power needed to control the MH-valve motor. It should also be noted here that a too high operating temperature in the MHU should be avoided, as this may lead to severe underpressure in the MHU after cool-down to ambient temperature.

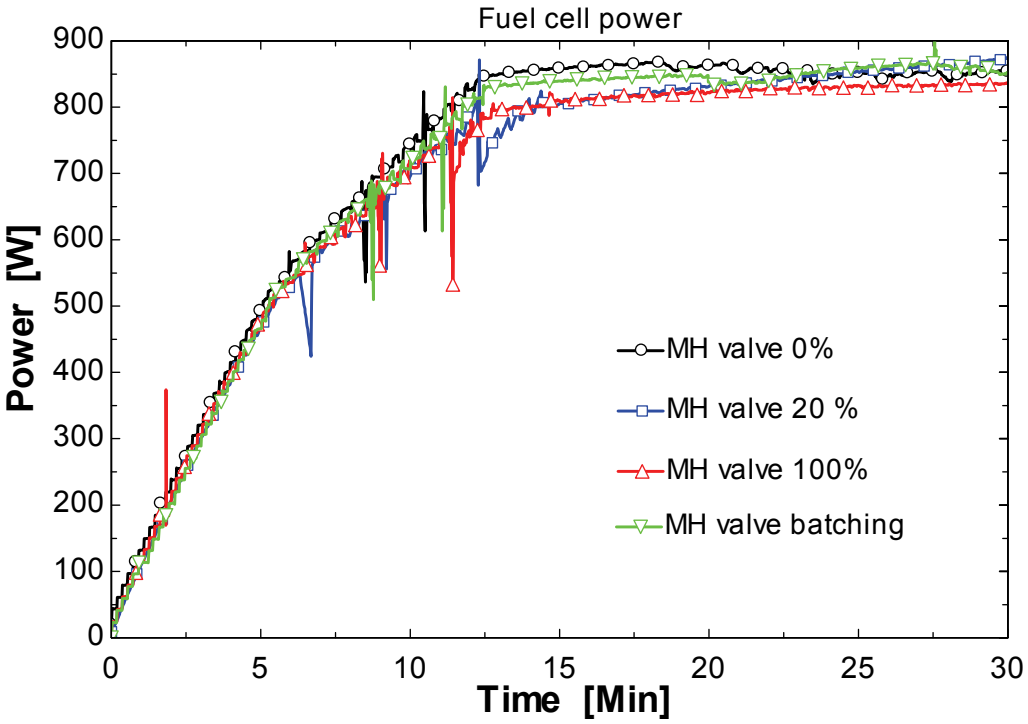

Figure 10.9: Fuel cell power as a function of time is presented for the 4 different start-up strategies. Only the first thirty minutes of the experiments are shown due to small variations in the last ninety minutes of the experiments.

10.8 CONCLUSIONS

A metal hydride storage unit was designed and thermally integrated with a water-cooled PEM fuel cell. Without thermal integration between the fuel cell and the metal hydride storage unit it was not possible to utilize the full hydrogen storage capacity in the metal hydride hydrogen storage unit. The metal hydride temperature was identified as a useful system control parameter. The temperature of the metal hydride unit during desorption (discharging) of hydrogen from the specific metal hydride unit investigated in this study should be above 298 K. This ensures suitable hydrogen flows and pressure to the fuel cell, and a maximum utilization of the metal hydride's hydrogen storage capacity. The experiments confirms preliminary results of kinetic analyses, and demonstrates that the intrinsic kinetic properties of the metall hydride alloy selected was more than fast enough for integration with a low-temperature PEM fuel cell.

Different control strategies for regulating the water flow from the fuel cell to the metal hydride were investigated in a series of experiments. The results demonstrated how the amount of cooling water recovered from the fuel cell and heat exchanged with the metal hydride affected the time for the fuel cell to reach its operating temperature. The main conclusion is that the ramp-up of the fuel cell power was not significantly influensed by the control strategy, provided . However, in order to ensure full utilization of the hydrogen storage capacity in the metal hydride it is necessary to keep the average metal hydride temperature above a certain temperature. Hence, chosing the correct control strategy is important for the overall MH/FC-system operation over time..

Acknowledgements

The authors acknowledge funding of the project “Hydrogen Storage in Solid Materials, from Synthesis to System” from the Research Council of Norway (NFR) and industrial partners. The industrial partners were Hydro ASA, Statkraft SF, and Raufoss ASA. The project was supported through the “Energy for the Future” program, and later through the “Clean Energy for the Future” (RENERGI) program within NFR.

References

[1] The Schatz Solar Hydrogen Project. http://www.humboldt.edu/~serc/realworld.html, (04/08-07) 2007.

[2] Advanced Energy Systems and Technologies Research Programme http://www.tkk.fi/Units/NEMO/ 4 Aug 2007.

[3] Stahl W, Voss K, Goetzberger A. The Self-Sufficient Solar House in Freiburg. Solar Energy 1994; 52(1): 111-125.

[4] Voss K, Goetzberger A, Bopp G, Haberle A, Heinzel A, Lehmberg H. The self-sufficient solar house in Freiburg - Results of 3 years of operation. Solar Energy 1996; 58(1-3): 17-23.

[5] Hollmuller P, Joubert J, M, Lachal B, Yvon K. Evaluation of a 5 kW(P) photovoltaic hydrogen production and storage installation for a residential home in Switzerland. International Journal of Hydrogen Energy 2000; 25(2): 97-109.

[6] Winter C, J. Solar Hydrogen, Energy Carrier for the Future Exemplified by 2 Field Programs - Hysolar and Solar-Wasserstoff-Bayern (Swb). Renewable Energy 1994; 5(1-4): 69-76.

[7] Brinner A, Bussmann H, Hug W, Seeger W. Test-Results of the Hysolar 10 Kw Pv-Electrolysis Facility. International Journal of Hydrogen Energy 1992; 17(3): 187-197.

[8] Gosh P, C, Emonts B, Jansen H, Mergel J, Stolen D. Ten years of operational experience with a hydrogen-based renewable energy supply system. Solar Energy 2003; 75: 469-478.

[9] Gurmai Z, W, A, Prodi V, Guidoni U, and Turmes C. Written Declaration on Establishing a Green Hydrogen Economy and a Third Industrial Revolution in Europe through a Partnership with Committed Regions and Cities, SMEs and Civil Society Organisations. 2007.

[10] Chen Y, Sequeira C, Chen C, Wang X, Wang Q. Metal hydride beds and hydrogen supply tanks as minitype PEMFC hydrogen sources. International Journal of Hydrogen Energy 2003; 28: 329-333.

[11] Levesque S, Ciureanu M, Roberge R, Motyka T. Hydrogen storage for fuel cell systems with stationary applications-- I. Transient measurement technique for packed bed evaluation. International Journal of Hydrogen Energy 2000; 25(11): 1095-1105.

[12] Nagel M, Komazaki Y, Suda S. Effective thermal conductivity of a metal hydride bed augmented with a copper wire matrix. Journal of the Less Common Metals 1986; 120(1): 35-43.

[13] Klein H-P, Groll M. Heat transfer characteristics of expanded graphite matrices in metal hydride beds. International Journal of Hydrogen Energy 2004; 29(14): 1503-1511.

[14] Oi T, Maki K, Sakaki Y. Heat transfer characteristics of the metal hydride vessel based on the plate-fin type heat exchanger. Journal of Power Sources 2004; 125(1): 52-61.

[15] MacDonald B, D, Rowe A, M. Impacts of external heat transfer enhancements on metal hydride storage tanks. International Journal of Hydrogen Energy 2006; 31(12): 1721-1731.

[16] Bossi C, Del Corno A, Scagliotti M, Valli C. Characterisation of a 3 kW PEFC power system coupled with a metal hydride H_2 storage. Journal of Power Sources 2007; 171(1): 122-129.

[17] Wilson P, R, Bowman J, R, C, Mora JL, Reiter JW. Operation of a PEM fuel cell with $LaNi_{4.8}Sn_{0.2}$ hydride beds. Journal of Alloys and Compounds 2007; In Press, Corrected Proof.

[18] Førde T, Miland H, Ulleberg Ø. Modeling and Simulation of a Thermally Coupled Electrolyzer/Metal Hydride/Fuel Cell System. HYPOTHESIS VII, Merida, Mexico, 27 – 30 March 2007.

[19] Jiang Z, Dougal R, A, Liu S, Gadre S, A, Ebner A, D, Ritter J, A. Simulation of a thermally coupled metal-hydride hydrogen storage and fuel cell system. Journal of Power Sources 2005; 142(1-2): 92-102.

[20] MacDonald B, D, Rowe A, M. A thermally coupled metal hydride hydrogen storage and fuel cell system. Journal of Power Sources 2006; 161(1): 346-355.

[21] LABTECH Int.CO.Ltd Alloys Research and Manufacturing. http://labtech.solo.blg/, 2007.

[22] Sato M. Studies of hydrogen absorption and desorption processes in advanced intermetallic hydrides. edn. [Oslo]: Ph.D Thesis from Department of Chemistry Faculty of Mathematics and Natural Sciences University of Oslo : Unipub, 2005.

[23] Wang X-L, Suda S. A dehydriding kinetic-study of $LaNi_{4.7}Al_{0.3}$ hydride by a step-wise method. J. Less-Common Metals 1990; 159((1-2)): 83-90.

[24] PowerPacProject IMES ETH Zürich. http://www.powerpac.ethz.ch/index1.htm, 4 Oct 2007.

[25] Labor für Brennstoffzellen. http://labs.hti.bfh.ch/index.php?id=752, 4 October 2004.

[26] Ruge M. Entwicklung eines flüssigkeitsgekühlten Polymer-Elektrolyt-Membran-Brennstoffzellenstapels mit einer Leistung von 6,5 kW. PhD, ETH Zürich, Zürich, 2003.

[27] Santis M, Schmid D, Ruge M, Freunberger S, Büchi F, N. Modular stack-internal air humidification concept-verification in a kW stack. Fuel Cells 2004; 4(3): 214-218.

[28] Miland H. Operational Experience and Control Strategies for a Stand-Alone Power System based on Renewable Energy and Hydrogen. PhD, Norwegian University of Science and Technology, Trondheim, 2005.

[29] Eriksen J, Miland H, Førde T, Tranøy Y, Aaberg R, J, Glöckner R. "Integrated Hydrogen Systems" - Report on the Installation and Testing of a PV/H_2 Energy System with

Metal Hydride Storage. IFE/KR/F-2003/027, Institute for Energy Technology, Kjeller, Norway, 2003.

[30] Førde T, Maehlen J, P, Yartys V, A, Lototsky M, V, Uchida H. Influence of intrinsic hydrogenation/dehydrogenation kinetics on the dynamic behaviour of metal hydrides: A semi-empirical model and its verification. International Journal of Hydrogen Energy 2007; 32(8): 1041-1049.

Appendix A10.1: Kinetics and thermal equations

Metal hydride hydration and dehydration reaction rate

A semi-empirical model was developed by Førde [30] describing the hydration and dehydration rates for the metal hydride powder. The model splits the rate constant K into a pressure dependent $K(P)$ and temperature dependent $K(T)$ term :

(A 10.1) $$\mathrm{K} = \mathrm{K(P)} \cdot \mathrm{K(T)} = \mathrm{K(P)} \cdot \mathrm{K_0} \exp\left(-\frac{\mathrm{E_a}}{\mathrm{RT}}\right)$$

Where E_a is the activation energy, R is the gas constant, and K0 is the rate constant for the temperature dependent term. The rate constant is related to the reacted fractions (X) for hydration or dehydration and the pre-exponential factor n through an equation based on the Avrami-Erofeev equation:

(A 10.2) $$\frac{\left[-\ln(1-\mathrm{x})\right]^{\frac{1}{\mathrm{n}}-1}}{\mathrm{n}(1-\mathrm{x})} \cdot \frac{\mathrm{dx}}{\mathrm{dt}} = \mathrm{K}$$

The dimensionless reacted fraction X is determined for absorption and desorption, from:

(A 10.3) $$\mathrm{X} = \frac{\mathrm{C} - \mathrm{C_1}}{\mathrm{C_2} - \mathrm{C_1}}$$

(A 10.4) $$\mathrm{X} = \frac{\mathrm{C_2} - \mathrm{C}}{\mathrm{C_2} - \mathrm{C_1}}$$

Were C is the actual hydrogen concentration, and C_1 and C_2 are the concentration limits of the initial and final states of the reaction, respectively.

Metal hydride storage unit heat transfer coefficient

The thermal characteristics and the effective heat transfer within the metal hydride storage unit can be represented by the overall heat transfer coefficient, UA. To calculate this number an energy balance is required:

(A 10.5) $$\dot{Q}_m = \dot{Q}_{reac} + \dot{Q}_{\mathrm{H_2}} + \dot{Q}_w$$

$\dot{Q}_m$ is the heat flux used to change the temperature of the reactor shell and the metal hydride bed described in Equation(A 10.5), $\dot{Q}_{reac}$ is the amount of energy consumed or produced in the chemical gas solid reaction (A 10.7), $\dot{Q}_{H_2}$ is the amount of energy transferred in and out of the

reactor with the hydrogen gas (A 10.8)and $\dot{Q}_w$ is the amount of energy transferred in and out of the reactor with the heating and cooling water (A 10.9).

(A 10.6) $$\dot{Q}_m = C_{\mathrm{P},reactor} \cdot m_{reaclor} \cdot \frac{\partial T_{reactor}}{\partial t} + C_{P,MH} \cdot m_{MH} \frac{\partial T_{MH}}{\partial t}$$

(A 10.7) $$\dot{Q}_{reac} = \dot{m}_{H_2} \cdot \Delta H$$

(A 10.8) $$\dot{Q}_{H_2} = \dot{m}_{H_2,g} \cdot c_{p,H_2} \cdot \left| T_{surrounding} - T_{MH} \right|$$

(A 10.9) $$\dot{Q}_w = \dot{m}_w \cdot C_{P,w} \cdot \left(T_{w,in} - T_{w,out} \right)$$

Where Cp is heat capacity, m is mass, T is temperature, $\dot{m}_{H_2,g}$ is the amount of hydrogen entering or leaving the reactor defined negative for desorption and positive for absorption, ΔH is the reaction enthalpy, and $\dot{m}_w$ is the flow rate of the circulating water.

The overall heat transfer coefficient UA_{w-MH} can now be calculated from Equation (A 10.9) and(A 10.10).

(A 10.10) $$\dot{Q}_w = UA_{w-MH} \cdot \frac{T_{w,out} - T_{w,in}}{\ln\left(\frac{T_{MH} - T_{w,out}}{T_{MH} - T_{w,in}} \right)}$$

Appendix A10.2: Water balances

Water balances

Control of the water balance in the Proton exchange membrane fuel cell (PEM-FC) is important. If water is removed too fast the fuel cell may dry out, resulting in lower H^+ ionic transportability and higher ohmic resistance. The cell can also be cracks/rupture if it dry out. However, too low water removal rates could also cause problems, due to flooding. Flooding introduces a high mass transfer resistance between the reacting gases. Water is transported into and out of the fuel cell with the reacting gases, and is produced at the cathode. A general figure illustrating the different ways of water transport in a PEM fuel cell is shown in Figure A 10.1.

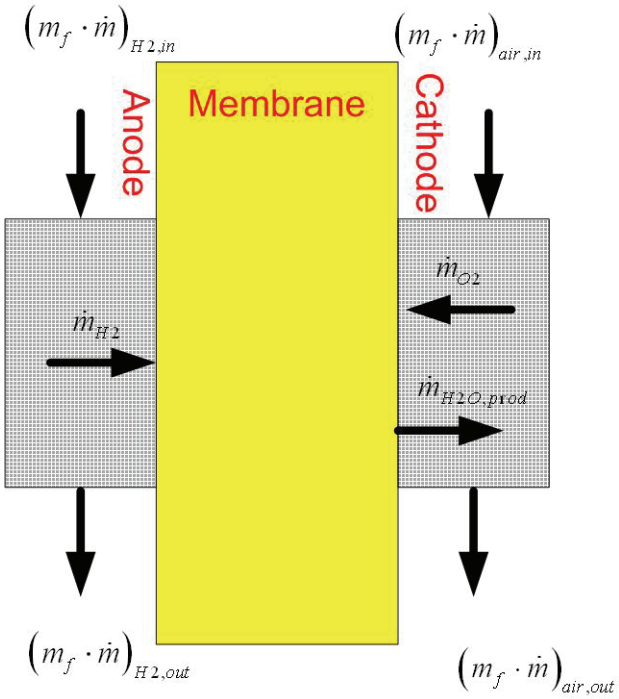

Figure A 10.1 Sketch of the flows and production of water in a PEM fuel cell

Water is transported through the membrane, due to a concentration gradient and due to electro osmotic drag from the transport of H^+ ions moving from the anode to the cathode. The governing Equations which describe the water balance in a general PEM fuel cell is given below Equations (A 10.11) and (A 10.12).

(A 10.11) $$\frac{\partial m_w}{\partial t} = \left(m_f \cdot \dot{m}\right)_{Air,in} - \left(m_f \cdot \dot{m}\right)_{Air,out} + \left(m_f \cdot \dot{m}\right)_{H_2,in} - \left(m_f \cdot \dot{m}\right)_{H_2,out} + \dot{\psi}$$

Where the change in fuel cell water contents $\frac{\partial m_w}{\partial t}$ is a function of the inlet and outlet air and hydrogen flow $\dot{m}$ and and water vapour mol fraction m_f and the amount of water produced at the cathode of the fuel cell ψ, which is calculated by Equation (A 10.12).

(A 10.12) $$\psi = \frac{I}{2 \cdot F}$$

Where I is the fuel cell stack current and F is the Farradays constant. During steady state operation with moderate stoichometric flows the outlet gas can be assumed to be saturated.

However, for the fuel cell discussed in this paper is it not straightforward to estimate the product $\left(m_f \cdot \dot{m}\right)_{Air,in}$ used in the water balance Equation (A 10.12). The incoming air denoted $\dot{m}_{Dry}$ in Figure A 10.2 used in the fuel cell stack it is pre humidified in a parallel flow mass exchanger, with the fully saturated $\dot{m}_{wet}$ air which already has passed through the fuel cell stack. Every bipolar stack has its own mass exchanger as shown in Figure 10.2B consisting of

12 different channels with length spanning from 16 to 13 cm and depth and with of 0.1 cm. A rough analysis of this pre humidifier is performed to be able to estimate the mol fraction of the incoming air.

The fully developed concentration profile for water vapour will have the principle shape shown in Figure A 10.2, where $C_{\infty,1}$ and $C_{\infty,2}$ are the water concentration in the wet and dry air. $C_{U;1}$ and $C_{U;2}$ are the concentrations at the surface of the Nafion membrane.

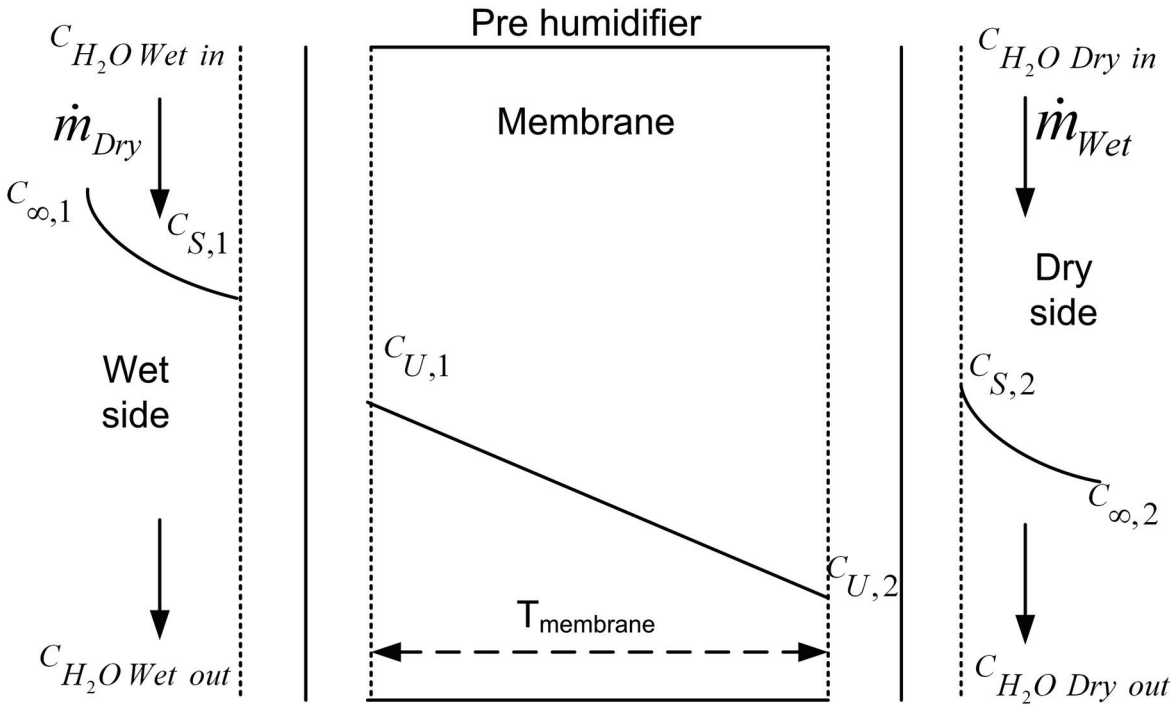

Figure A 10.2 Principal sketch of the concentration profile in the parallel flow mass exchanger

The next step in analysing the mass exchanger is to draw an electrical analogy Figure A 10.3, splitting the transfer of water vapours into several small steps.

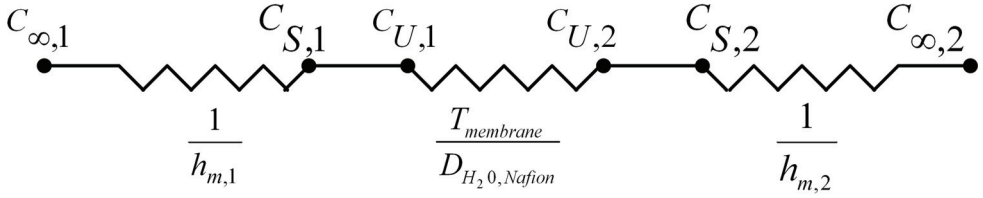

Figure A 10.3 Equivalent mass transfer circuit for a series mass exchanger

The electrical analogy simplifies the mass transfer into three separate processes, a convective transport from the bulk concentration to the interface between air and membrane, a diffusive transport through the membrane and a convective transport from the interface membrane-air towards bulk concentration. Assuming fully developed laminar flow in the channels, using the heat and mass transfer analogy gives 3.66 as a lower limit for the Sherwood number. The

convective mass transfer number calculated with (A 10.13) based on this lower limit, and has the value of 0.097[m/s]. The corresponding mass transfer resistance $\frac{1}{\overline{h}_m}$ will have the value of 10.26. Estimates of the maximum and minimum air flow are calculated assuming that the fuel cell is producing 100 and 5 ampere, respectively with an air stoich of 2.4. These airflows will give Reynolds number spanning in the range from [17-370], in the pre-humidifiers air channels.

(A 10.13) $$\overline{h}_m = \overline{Sh} \cdot \frac{D_{H_2O,Air}}{D_h}$$

To calculate the resistance corresponding to the diffusion of water through the membrane it is necessary to find a value for the diffusion coefficient of H_20 in Nafion. [30] and [31] has published values for the diffusion coefficient of H_2O in nafion, as a function of water activity. Both authors describes an decrease in the coefficient with higher activity, [30] measures diffusion coefficients in the interval [2Exp(-11),1Exp(-13)], while [31] presents a correlation for the diffusion coefficient presented in (A 10.14).

(A 10.14) $$D_{H2O} = 10^{-10} e^{\left[2416 \cdot \left(\frac{1}{303} - \frac{1}{T}\right)\right]} \cdot \left(2.563 - 0.33\lambda + 0.0264\lambda^2 - 0.000671\lambda^3\right)$$

Where λ is the number of water molecules per charge carrying specie $\left[RSO_3^-\right]$. A correlation connecting λ to the activity defined as $\frac{P_{H_2O}}{P_{H_2O}^{sat}}$, are published by [31] this correlation is presented in (A 10.15) . The maximum value of λ increases with temperature.

(A 10.15) $$\lambda = 0.0043 + 17.81 \cdot \frac{P_{H_2O}}{P_{H_2O}^{Sat}} - 39.85 \cdot \left(\frac{P_{H_2O}}{P_{H_2O}^{Sat}}\right)^2 + 36.0 \cdot \left(\frac{P_{H_2O}}{P_{H_2O}^{Sat}}\right)^3$$

Using Equation (A 10.14) to estimate the diffusion coefficient and a membrane thickness $T_{membrane}$ of 50 μm the diffusion resistance $\frac{T_{membrane}}{D_{H_2O,Nafion}}$ can be calculated to be of approximately 102880, indicating that $R_{mass,Diffusion} >>> R_{mass,convection}$. However, to do a mass transfer analysis of the pre humidifier we also need a way to approximate water concentration at the surface of the Nafion membrane CU, as indicated in Figure A 10.2. This is done with Equation (A 10.16)

(A 10.16) $$\left|H_2O\right| = \lambda \cdot \left|SO_3 -\right|$$

The proton exchange membrane is an Nafion 117 type with an molar weight of 1100 [gram/mol SO_3-] [30]. The density of the membrane depends of the water content but an average can be taken to be 2.05 g/cm^3 based on [32], the weight and the concentration of SO_3- in the membrane are calculated to 3.25 [gram] and 0.00186 [mol/cm^3].

If the lower limits for the Sherwood number are used in the calculation of the convective mass transfer resistance the size of the membrane resistance be will at least 1000 times greater than

if we assume a membrane thickness of 50 μm. To simplify the analysis we will therefore neglect the convective mass transfer term and assume that the water vapour concentration at the $C_{S,1}$ and $C_{S,2}$ surfaces equal the concentrations in centre of the incoming and out coming air flows. We have also neglected the fact that the incoming and outgoing air will change temperature as it flows through the pre-humidifier and assumed that the temperatures are constant through the entire pre humidifier. The relative humidity of the inlet dry air is calculated from the state of the ambient air at 298 K and a relative humidity of 70%. The wet air in, is assumed to be either fully saturated, or to have a relative humidity of 0.8. The flow rates of the gasses are found from the current production and stoich relationships.

With the given assumptions is an algorithm calculating the outlet concentrations of H_2O in the dry and wet airflow developed and described below.

Algorithm:

1. Calculate the vapour pressure at room temperature.
2. Calculate $C_{H_2O\ Dry\ in}$.
3. Calculate $C_{H_2O\ Wet\ in}$.
4. Guess on $C_{H_2O\ Dry\ out}$.
5. Calculate the mass and mol fraction of the dry water vapour in an outlet air.
6. Calculate the mass and mol fraction of the wet inlet air.
7. Calculate the mass fraction of the wet outlet air with the mass balance $\dot{m} = \dot{m}_{Dry}\left(m_{f,Dry\ out} - m_{f,Dry\ in}\right) = \dot{m}_{Wet}\left(m_{f,Weti\ n} - m_{f,Wet\ out}\right)$.
8. Calculate $C_{H2OwetOut}$ and corresponding water vapour pressure of the wet gas out.
9. Calculate $C_{U1,\ in}$ $C_{U1,\ out}$, $C_{U2,\ in}$, $C_{U2,\ out}$ and with Equation(A 10.16).
10. Calculate the average membrane diffusion coefficient.
11. Calculate the simplified overall mass transfer number $MA = \frac{D_{H_2 0,Nafion} \cdot A_{exchanger}}{L_{exchanger}}$.
12. Calculate $C_{LMCD} = \frac{\left(C_{H_2O\ Wet\ in} - C_{H_2O\ Dry\ in}\right) - \left(C_{H_2O\ Wet\ out} - C_{H_2O\ Dry\ out}\right)}{\ln\left[\frac{C_{H_2O\ Wet\ in} - C_{H_2O\ Dry\ in}}{C_{H_2O\ Wet\ out} - C_{H_2O\ Dry\ out}}\right]}$.
13. Calculate $\dot{m}_{calculated} = MA \cdot C_{LMCD}$.
14. Calculate the outlet water vapour mass fraction $m_{f,Dry\ out\ calculated}$ and concentration $C_{H_2O\ Dry\ out,\ calculated}$ from the relation $\dot{m}_{Calculated} = \dot{m}_{Dry}\left(m_{f,Dry\ out\ calculated} - m_{f,Dry\ in}\right)$ and the ideal gas law.
15. If $\left|C_{H_2 0\ Dry\ out,calculated} - C_{H_2O\ Dry\ out,\ guessed}\right| < Z$, guess on a new $C_{H_2O\ Dry\ out}$ with the under relaxing $C_{H_2O,Dry out,gussed,new} = \Upsilon \cdot C_{H_2O,Dry out,calculated} + (1-\Upsilon) \cdot C_{H_2O,Dry out,guessed}$ and return to 5. Else finished.

The simulations indicate that the relative humidity of the incoming air ranges from 0.2-0.5 with a temperature of 333 K depending on the air flow rates. Based on the results from the

analysis of the pre-humidifier a water balance is performed with (A 10.11) the results is shown in Figure A 10.4.

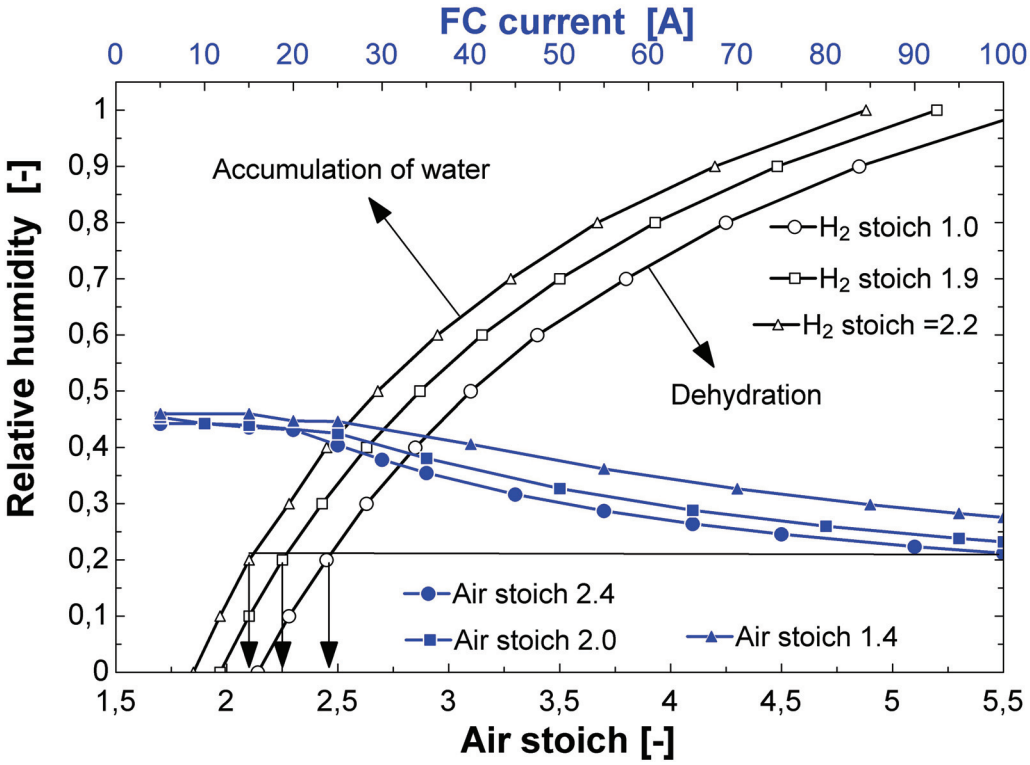

Figure A 10.4 The black lines with unfilled dot shows where the fuel cell will produce either surplus or deficient water as a function of air stoich at different hydrogen stoichs', the incoming air is at 298 K with a relative humidity of 70%. The incoming hydrogen is assumed to be completely dry. The out flowing gases are assumed to be fully saturated and to have a temperature of 323 K. The blue lines with filled dots show the calculated relative humidity of humidified incoming air.

As shown in Figure A 10.4 (black lines with unfilled dot's) the risk for dehydration will rise with higher air and hydrogen stoichs. In the water balance calculations we have assumed that the inlet air has a temperature of 323 K, that the inlet hydrogen flow are compleately because it comes from the metal hydride storage unit and that the exit hydrogen and air flows are fully saturated at a temperature of 333 K. The vertical lines (blue with filled dot's) indicate the relative humidity of the inlet fuel cell air after it has passed the pre-humidifier as a function of fuel cell current. The estimations of the fuel cell inlet air relative humidity are based on the assumptions and the equations presented above.

The simplified analysis indicate that even if as much as hundred ampere is pulled from the fuel cell it can be operated with 2.3 air and 1.9 H_2 stoich and still avoid dehydration.

PART 4: Conclusions and Recommendation for Further Work

11 MAIN RESULTS, SUMMARY AND RECOMMENDATIONS FOR FURTHER WORK

Hydrogen combined with renewable energy sources and efficient fuel cells will play an important role in future society. Development of hydrogen storage solutions is one of the key challenges before a hydrogen economy can be established. The most safe storage solution is solid-state storage. These thoughts were the background and motivation for the work done in this thesis. The main result and recommendations for further work are given below.

11.1 MAIN RESULTS

Chapter 3

This chapter deals with the kinetic of the gas solid reactions in a metal hydride. Several models of the kinetic reactions in the powder materials are available in the literature. These models describe the gas-solid reactions differently: stepwise models (simulates all the partial steps in the reaction), shrinking core models (describes the reaction as a diffusion process), nucleation and growth models, combination of nucleation and growth and shrinking core models and empirical models (where the reaction rate depends on some selected parameters without any physical meaning). The main aim for the work described in Chapter 3 of the thesis was to develop an expression suitable for using in heat and mass transfer models. This means that the expression should be as simple as possible. The model should also describe the reaction rate independently of the initial particle state. It should also be possible to identify the modelling parameters from experiments performed with an experimental set up used for PCT measurement (Sivert type of apparatus). This type of experimental set up is quite common in laboratories dealing with metal hydrides.

Investigation of the kinetics of an $La_{0.83}Ce_{0.10}Pr_{0.04}Nd_{0.03}Ni_{4.40}Al_{0.60}$ alloy and its corresponding hydride has been performed. A method and an analytic approach allowing for an adequate description of the experimental kinetic data, performed in a volumetric experimental set up was proposed. That is, a semi-empirical correlation suitable for heat and mass transfer modelling and engineering design of metal hydride storage units was proposed and verified experimentally.

The results show that the developed kinetic expression reproduces the experimental data with high accuracy when thermal effects are negligible and pressure variations are small. This expression is rather precise and simple enough to use in a heat and mass transfer analysis. The experimental procedure and analytic data treatment methodology described in Chapter 3 yield activation energies and Avrami pre- exponential factors close to the values published in literature.

Chapter 5

A cylindrical reactor filled with the AB_5 type $La_{0.83}Ce_{0.10}Pr_{0.04}Nd_{0.03}Ni_{4.40}Al_{0.60}$ alloy was investigated with respect to the rates of hydrogen charging and discharging. The unit was able to deliver more than 80 % of its capacity towards a 1.1 bar gas pressure with a constant flow rate of 0.001224 H/M per sec if the water bath temperature exceeded 293 K. The charge and discharge times for this reactor were dependent on both charging and discharging pressure and surrounding water bath temperature in the temperature range from 293-313 K. A one-dimensional transient heat and mass transfer model was developed, reproducing the reaction rates and temperature fields in the reactor with good accuracy. A sensitivity analysis indicated that the activation energy, effective thermal conductivity and heat of the reaction were the most sensitive parameters for this system. All simulations showed that the reaction was fastest at the beginning of a charge/discharge cycle and close to the external heat transfer surface. The performed experiments and simulations indicate that the charging and discharging processes are reaction controlled in the first part of the experiments while the later parts of the experiments are heat transfer controlled.

Chapter 6

Experimental results together with heat and mass transfer models, for a metal hydride unit storing 340 litre of hydrogen are presented. Charging and discharging experiments were performed at four different temperatures and with different pressures and flow rates. The experiments were carried out with two types of heat exchangers: a brush and a tube type. Two transient heat and mass transfer models are developed and experimentally verified. A zero dimensional model for the configuration with the brush type heat exchanger and a more complex two-dimensional model assuming thermal non equilibrium between the gas and solid phase are developed for the tube type heat exchanger.

The results show that the charge and discharge times for this reactor filled with this AB_5 type of MH powder are linearly dependent on the charging and discharging pressure and temperature. The performance regarding the charge and discharge times and the ability to deliver hydrogen at a constant flow rate is considerably better for the brush type heat exchanger. The simulations with the heat and mass transfer model assuming thermal non equilibrium, indicate that the validity of this assumption are dependent on the surface area and the correlation used for the solid to gas heat transfer number.

Chapter 7

The performance of four different metal hydride storage units is characterized and analysed. A relationship between charge/discharge pressure and charging/discharging times are found. The brush type heat exchanger is a good and economic alternative to use as a heat exchanger.

The AB_5 type of metal hydrides powder used in this investigation is capable of delivering more than 90% of its total capacity with a flow rate of 0.085 H/AB_5 pr min, with 303 K heating water towards a 1.1 discharge pressure if the product of the overall heat transfer number and heat transfer surface is above 20 W/K**.** The overall heat transfer number affects the charging and discharging times and depend on the reactors heat transfer surfaces.

Chapter 9

This paper investigates a hydrogen subsystem through simulation, which takes advantage of variation in grid electricity cost between day and night. Hydrogen are utilized during daytime to produce electricity to supply a given user profile. During night electricity are bought from the grid and given to an electroylser producing hydrogen, stored in a metal hydride storage unit.

The simulation shows how it is possible to increase the overall hydrogen system efficiency by designing systems with close thermal integration between the various system components, particularly the metal hydride and fuel cell system. Two different strategies for circulation of the fuel cell cooling water were investigated. The results showed that the electrical system efficiency was around 40%, independent of the selected control strategies, while the overall system efficiency was around 75%, also fairly independent of the selected control strategy.

Chapter 10

A hydrogen system containing a 1.2 kW water-cooled PEM fuel cell thermally connected to a metal hydride storage unit containing 18 kg of AB5 type metal hydride powder is experimentally investigated. A simple control program making it possible to operate the fuel cell and metal hydride storage unit is developed. The fuel cell current-voltage characteristic is found, and an energy balance is established. The PCT curves for the metal hydride powder used in the storage unit are experimentally characterised. The heat transfer characteristic and energy balance for the metal hydride storage unit is studied experimentally. Finally, the thermal interaction between the fuel cell and storage unit is studied experimentally for different start up strategies. The temperature of the metal hydride storage unit was kept above 303 K to insure that most of the stored hydrogen could be supplied to the fuel cell. There are small differences in the fuel cell current-voltage characteristic in the temperature range 313-333 K which makes the fuel cell performance relatively independent of the different water circulation strategies. The performed experiments indicate that the measured metal hydride temperature is the best control parameter for controlling the flow rates of the circulating heating and cooling water, due to slow thermal response of such systems.

11.2 SUMMARY

Part one

A brief introduction to the governing theory of gas solid reactions was given. A status for hydrogen storage and its future goals were presented. Further on in Chapter 3 a semi-empirical kinetic model suitable for heat and mass transfer models was suggested, and a method and analytic approach allowing for an adequate description of the experimental kinetic data, performed in a volumetric experimental set up was proposed and verified. The experimental procedure and analytic data treatment methodology described yield activation energies and Avrami pre-exponential factors in agreement with the values published in the literature.

Part two

The theory describing heat and mass transfer in a porous bed is presented together with an review of the heat transfer parameters of importance for metal hydride storage units. A zero dimensional model describing the performance of a MH storage unit is developed. A more

complex one dimensional heat and mass transfer model assuming thermal equilibrium between the gas and solid is also developed. This one dimensional model is also used to perform a parameter sensitivity analysis. Finally, a two dimensional model assuming thermal non-equilibrium between the gas and solid is also developed. Four different metal hydride reactors containing from 0.85 to 2.4 kg of the same MH powder were experimentally investigated. Three of the reactors had internal heat exchangers. The reactors charging and discharging times and the ability to deliver a constant hydrogen flow rate at different conditions were investigated. An energy balance were performed and used to analyse and compare the reactors. Relationships between the time it takes to charge and discharge the reactors and charging/discharging pressures and the reactors overall heat transfer number were identified.

Part three

The interaction between the electrolyser, metal hydride storage unit and fuel cell is studied though system simulations. The zero dimensional model developed in part two of the thesis is used in these system simulations. A metal hydride storage unit containing 18 kg of MH powder was designed and built. This unit was integrated thermally with a water cooled PEM fuel cell. The fuel cell stack and metal hydride storage unit were characterised and a strategy was tested and optimised for a fast start-up of the fuel cell stack.

11.3 RECOMMENDATIONS FOR FURTHER WORK

New knowledge and improved technology together with experimental experience and improved knowledge of the system requirements are often a basis for asking new questions and searching for better component design and system performance.

Part one

The main focus in part one was to develop an expression suitable for using in heat and mass transfer modelling. This expression was verified through experiment performed in the IFE laboratory. However, the developed experiment has only been used to describe the behaviour of AB_5 type of material. As a first step the developed expressions ability to describe the kinetics of other materials reaction rate should be investigated. Further, the developed expression could be improved by accounting too the rate changing as the reaction proceeds. For example the initial reaction rate could be controlled by surface processes and later on changing into a diffusion-controlled reaction as the process reach equilibrium. Particle size, distribution and geometry are also parameter what could be included in the kinetic expression. However, as discussed in Chapter 3 different groups have reported deviating results regarding the kinetics of quite similar materials. This can be due to several factors as discussed in Chapter 3. These deviations in the way of performing kinetic experiments and how to report the results show that it is a need for developing an international approved standard for how kinetic results should be reported and experiments should be performed.

Part two

The major goal of part two and of this thesis was to improve the understanding of the behaviour of metal hydride storage units through modelling and experiments. A set of governing equations has been formulated and compared to experimental results. However, the modelling should be expanded to other types of materials (not only AB_5 types of metal hydrides), operating at higher temperatures and pressures. In addition a three dimensional heat

and mass transfer model of the IFE designed metal hydride storage unit should also be developed. The experimentally verified set of equations should also be used to do more parametric studies. Like for example modelling the performance of a storage unit with different fin distances. The improvement in the reactors charging and discharging times should be compared to the increased manufacturing costs and the increased system weight due to larger heat exchangers. In addition there is a need for simple zero dimensional models of both metal hydride storage units, compressors and heat pumps, which are suitable for system simulations, based on different types of storage materials. How the metal hydride storage units will behave when scaled up are not investigated and should be given some attention in the future. Units with other types of material and heat exchanger surface geometries should also be tested in the laboratory. A problem not discussed in this thesis is the filling of the storage units with metal hydride powder; easy and complete filling of the storage unit with metal hydride powder is important.

Part three

The metal hydride technology needs to be developed further before it can compete with compressed and liquid hydrogen and can meet the goal for public accepted and efficient energy storage. The main focus in this part of the thesis was to study the component interface between the electrolyser, the metal hydride storage unit and the fuel cell with special focus on the thermal interaction. This was done through simulations of a hydrogen subsystem, using already developed models of the fuel cell and electrolyser and the present developed metal hydride model. A metal hydride storage unit was also designed and implemented with a water-cooled fuel cell. In the future more experiments should be done to optimise the metal hydride unit start up procedure. The developed control program should also be improved so the start up time of the fuel cell is decreased. This could, for example, be done by deciding the maximum step up current based on both the measured temperature and gradient of the minimum, maximum and averaged cell voltage. A control system able to control the amount of water circulating through the metal hydride storage unit should also be implemented in the laboratory set up. However, another very important step towards using metal hydride and hydrogen systems in commercial applications is to identify suitable applications for using hydrogen systems from both a technical and economical point of view. These identified systems should be thoroughly investigated through simulations, laboratory experiments and economical analyses. Since larger demonstration plant is an important step towards the hydrogen society. One very promising application for metal hydrides not discussed in this thesis is to use metal hydrides to compress hydrogen, in for example, a hydrogen filling station. Where metal hydrides could replace or operate in parallel and series with commercial compressors. The metal hydride compressor could perform the first step from 10 to 150 bar driven by for thermal energy from the electrolysers waste heat and heat supplied from, for example, a solar collector. In the future both an economical and technical analysis of such system should be performed. Another important problem not discussed in this thesis is the problems with the water content in the hydrogen produced by the electrolyser. If the hydrogen is not dried before it is loaded into the metal hydride storage unit in can cause a rather large problem for the metal hydride. This problem should be solved either by developing very effective drying processes or with further material research developing metal hydrides accepting higher water content.